MULTI-DECADAL SPACE-BASED OBSERVATIONS OF BASALTIC EFFUSIVE ERUPTIONS FROM MODIS INFRARED DATA

A DISSERTATION SUBMITTED TO THE GRADUATE DIVISION OF THE UNIVERSITY OF HAWAIʻI AT MĀNOA IN PARTIAL FULFILLMENT OF THE REQUIREMENTS FOR THE DEGREE OF

DOCTOR OF PHILOSOPHY

IN

GEOLOGY AND GEOPHYSICS

August 2018

By

Estelle Bonny

Dissertation Committee:

Robert Wright, Chairperson

Peter Mouginis-Mark

Sarah Fagents

Matthew Patrick

Jennifer Griswold

Keywords: effusive eruption, satellite, remote sensing, infrared, discharge rate, MODIS

ACKNOWLEDGEMENTS

These past three-and-a-half years of my life were incredible and challenging in many ways and I can't believe it's already coming to an end. It took me a while to decide to get a PhD in volcanology, but after volunteering at the Hawaiian Volcano Observatory, I was convinced that this was the kind of job I want to do in my life. I would like to thank everyone who was around me and supported me during both the happy and stressful times.

I am very grateful to my advisor, Rob Wright, who gave me the opportunity to pursue my goal and took me on as his PhD student. As only his second full time PhD student, he never failed in guiding me through my research and making sure that I was on track. I also want to thank all members of my dissertation committee. Pete Mouginis-Mark always helped improve my projects by encouraging discussion, and also served on my comprehensive exam committee. Matt Patrick helped me organize a visit at HVO for a week, and it was an amazing learning experience to work with him. Finally, Sarah Fagents and Jennifer Griswold always gave me great feedback and helped improve my research projects. I also want to thank the members of my comprehensive exam committee: Mike Garcia, James Foster and Scott Rowland, who always pushed me to look outside my realm of expertise.

I am grateful for the opportunity to collaborate with Icelandic colleagues, Thor Thordarson, Inga Jónsdóttir, Ármann Höskuldsson and Stephanie Groecke with whom I had great discussions about the Holuhraun eruption and who shared their field datasets with us.

I do not want to forget Julia Hammer, who was the instructor for GG 101, "Dynamic Earth", during my semester as a Teaching Assistant. She was always very helpful, pushing us to improve each lab by using our experience in the classroom to guide us. I also want to thank Tom Shea who trusted me as a co-leader for the GSA "Geological Overview of Kīlauea Volcano" field trip to the Big Island, and also as an instructor for one of his "Lava Flow Rheology and Morphology" classes. I am grateful to the UH Graduate Student Organization, for providing a travel grant in support of the GG 601 " Explosive Volcanism" field trip to New Zealand. This field trip, led by Bruce Houghton, was an unforgettable two weeks of learning about explosive volcanism.

I would also like to thank Harold Garbeil for help with programming, Eric Pilger for acquiring large datasets necessary for my projects, and Ethan Kastner for always fixing my computer problems. I cannot forget all the administrative personnel who made the paperwork much easier: Alison, Mars, Grace, Vi, Karynne, Rena, Lily, Susan and Leona. Thank you also to Marcie, who guided me in communicating with the public about my work.

Thank you to all anonymous reviewers that greatly improved two of my chapters, and Andy Harris who gave us invaluable comments.

Finally, I know life would have been much harder without the help of my many friends. First of all, my officemates: Caroline, Macey, Melissa, Andrea, David, Tayro, Myriam, Lingzhi, and Katie R. I also can't forget Erin, for the best coffee breaks, and Liz for her help with my cover letters. Mahalo also to all the visiting students: Emeline, Marie, Clémence, Hannah, Elishevah, and Lily. Additionally, I'm grateful to all the GG family: Kate, Sam, Liz (the birthday quartet), Alyssa, Harrison, Kendra, Brett, Nick, Samantha, Emily, Chris, Wendy, and Katie T.

Thank you to all my awesome surf buddies, especially Darwina, as well as Echo, my numerous housemates, and Cody!

A special thanks to my Hawaiian Ohana, the Trusdells, who made me feel at home and loved far away from home.

A la famille Bonny et Leone,

A Maman, Papa, Marion, et Julia. Merci pour votre soutien continue même depuis l'autre cote de la planète, je sais que vous êtes fière de moi. Je vous aime fort!

Et surtout à Violaine, ma sœur jumelle, tu sais comme la vie serait tellement moins belle sans toi.

Merci ☺

This work was supported financially by the National Aeronautics and Space Administration (NNX14AP34G and NNX14AP37G).

ABSTRACT

Lava discharge rate, the volume of lava emitted from a vent at any given time, is a critical parameter that volcanologists use to study effusive eruptions. It not only gives us information about the eruption dynamics but also is a key control on how far lava can flow. Thermal infrared satellite remote sensing has shown advantages for deriving lava discharge rate and monitoring temporal changes during an eruption, with a higher temporal resolution than in-situ measurements. In this dissertation, I use NASA's MODIS (Moderate Resolution Imaging Spectroradiometer) sensor to study 104 basaltic effusive eruptions over a 15-year time period, to retrieve time-averaged discharge rates (TADR). I first show that the theoretical asymmetrical shape of TADR time-series can be used to predict the end of lava flow-forming eruptions from space. Then, I investigate the 2014-2015 Holuhraun eruption, Iceland, the country's largest basaltic effusive eruption in the past 200 years. I compared the satellite- and ground-based TADR for this exceptional six month-long eruption. Final flow volumes estimated from both techniques were in good agreement. However, systematic differences between satellite and field TADR estimates the first 30 days of the eruption indicated that the satellite-derived method, and some of the assumptions on which it is based, need to be revised to reconcile these differences for lava flows that are areally extensive and highly radiant. Finally, I tested three different thermal satellite-based methods to retrieve TADR (Harris et al., 1997a; Wright et al., 2001a; and Coppola et al., 2012) to determine whether they yield comparable results, and assess the absolute accuracy of these approaches. I used the global TADR time-series database of basaltic effusive eruptions to estimate final flow volumes (by integrating the TADR time-series), which can be very well constrained at the end of an eruption unlike instantaneous discharge rates. Using final

flow volumes from the literature and inferred volumes from satellite images, we demonstrated that the Harris et al. (1997a) method yields TADR closer to reality. However, we showed that the accuracy of TADR could be improved by updating the coefficient method (Wright et al., 2001a) with our eruption database.

TABLE OF CONTENTS

LIST OF TABLES

LIST OF FIGURES

LIST OF ABBREVIATIONS

Abbreviation/Variable	Definition
a	coefficient
A_{lava}	area of active lava within a pixel
A_{pixel}	pixel area
A_{tot}	total surface area of active lava at a given point in time
ASCII	text file
ASTER	Advanced Spaceborne Thermal Emission and Reflection Radiometer
AVHRR	Advanced Very High Resolution Radiometer
c	speed of light
C_L	latent heat of crystallization
C_p	lava specific heat capacity
C_{rad}	radiant density
CE	Common Era
COSMO-SkyMed	Constellation of Small Satellites for Mediterranean basin Observation
DEM	Digital Elevation Model
DRE	Dense-Rock Equivalent
EOS	Earth Observing System
f	pixel fraction occupied by active lava
G	acceleration of gravity
GOES	Geostationary Operational Environmental Satellite
GPS	Global Positioning System
GVN	Global Volcanism Network
GVP	Global Volcanism Program
h	Planck's constant

h_c	convective heat coefficient
HVO	Hawaiian Volcano Observatory
IFOV	Instantaneous Field of View
InSAR	Interferometric Synthetic Aperture Radar
IR	infrared part of the electromagnetic spectrum
k	Boltzmann constant
KSAT	Kongsberg Satellite Services
L	spectral radiance
L_4	spectral radiance at 4 µm
$L11_{cor}$	corrected spectral radiance at 11 µm
$L11_{MOD}$	measured at-satellite radiance
L_U	upwelling spectral radiance
Landsat	Land remote sensing satellite
LOWTRAN	Low Resolution Atmospheric Transmission
LST	Land Surface Temperature
M	spectral radiant exitance
M_{rad}	radiative heat loss
M_{conv}	convective heat loss
MIR/MWIR	Midwave Infrared
MODIS	Moderate Resolution Imaging Spectroradiometer
MODTRAN	Moderate Resolution Atmospheric Transmission
MODVOLC	hotspot detection algorithm
MOR	Mean Output Rate
NEΔT	Noise-Equivalent Temperature Difference
NIR	Near Infrared
NTI	Normalized Thermal Index
nsig	number of standard deviation

Q_{end}	critical effusion rate at which an eruption ends
$Q_{f,t}$	effusion rate at any time t
Q_{max}	maximum lava effusion rate
RADARSAT-2	Radar Satellite 2
Sentinel-1	radar imaging satellite
SWIR	short wave Infrared
T	temperature
T_{back}	background temperature
T_{lava}	integrated lava surface temperature
t_{end}	time of the end of eruption
$t_{end,\ pred}$	predicted time of the end of the eruption
TADR	Time-Averaged Discharge Rate
$TADR_{MOD}$	Time-Averaged Discharge Rate from MODIS
$TADR_g$	Time-Averaged Discharge Rate from field measurements
TIR	long wave infrared
UAF	University of Alaska Fairbanks
USGS	United States Geological Survey
UTC	Coordinated Universal Time
VIS	visible
VRP	Volcanic Radiative Power
X	coefficient
X_{2007}	coefficient from Harris et al., (2007)
X_{new}	new coefficient
X_{SiO2}	silica content
wt%	weight percent
μm	micrometers
λ	wavelength

λ	decay constant in chapter 2
τ	transmissivity
σ	Stefan-Boltzmann constant
ε	emissivity
ρ	lava density
ρ_{air}	air density
Φ	average crystal fraction
$\Delta L4$	radiance emitted by active lava at 4 μm
Δt	time difference between the predicted end and the observed end of eruption
Δt_{10}	time difference with 10% of the TADR data
ΔT	temperature difference between eruption temperature and flow cessation temperature
$\Delta TADR$	difference between the TADR from Method-3 and Method-1

CHAPTER 1

INTRODUCTION

1.1 Dissertation overview

Lava flows are the most common volcanic features on the surface of the Earth. Many questions remain for volcanologists to grasp the full complexity of processes that govern lava flow emplacement, morphology and the temporal evolution of the effusive eruptions that result in the emplacement of flows. This dissertation aims to show how satellite thermal remote sensing can help further our understanding of lava flow-forming eruptions. Satellite images provide a long-term database for volcanoes worldwide, and can be used to help improve our knowledge of this type of volcanic eruption. Lava flows are dynamic and change quickly over time, and near-real time monitoring and measurement is important: remote sensing provides this observational capability. Three research chapters are presented here, and each contains its own introduction. In this chapter, I provide a brief overview of three concepts required to understand how these chapters relate to each other, and place the work they contain in context: the nature of thermal infrared satellite measurements, the nature of effusive eruptions and the hazards associated with their products, and finally the key physical parameter that links all of the chapters together − the lava effusion rate.

1.2 Observing lava flow-forming eruptions using thermal infrared remote sensing

Here, I define what is remote sensing and how light can be emitted by a hot target, such as an active lava flow, at the surface of the Earth. Remote sensing can be passive or active. Active remote sensing is when an instrument emits electromagnetic radiation towards the Earth's surface onto the target of interest, such as radar measurements, to measure and investigate Earth surface targets. Passive remote sensing, the more common form of remote sensing and the focus of this dissertation, involves detecting sunlight that is reflected from Earth's surface, or light emitted by Earth's surface by virtue of its temperature. A hot material (temperature above absolute zero; Schott, 2007) is thermally excited, which creates shaking or vibration of electrons within the material and produces a "particle" of light, called a photon, as the atom returns to its

ground state from an excited state. The energy of a photon (J) is proportional to its frequency (hertz) multiplied by Planck's constant h (6.63×10^{-34} J s). This emitted light can be detected using remote sensing instruments and yields information on the properties of the material such as its temperature and/or composition. The light emitted by the target is received at the satellite and then divided into spectral bands (for example, by using filters). Here, I define what we mean when referring to the infrared (IR) part of the electromagnetic spectrum. It can be decomposed in four groups: 1) the near infrared (NIR) from 0.7 to 1.1 μm; 2) the shortwave infrared (SWIR) from 1.1 to 3.0 μm; 3) the midwave infrared (MIR) from 3.0 to 5.0 μm; and 4) the longwave infrared (TIR) is from 5.0 to 20 μm (Harris 2013). In this dissertation, I use the term thermal infrared to define measurements in both the MIR and TIR, which is the part of the electromagnetic spectrum where light is emitted by any thermal phenomenon such as volcanic activity.

How much light is available for us to measure from space? The Sun illuminates the Earth and emits a spectrum almost equivalent to that of a blackbody, an idealized surface with the ability to perfectly absorb and reradiate all incident electromagnetic flux (Schott, 2007). The Sun's surface has a temperature of about 5900 K and using Planck's blackbody radiation law (following Equations 1.1, 1.2 and 1.3) we can estimate the amount of light that a surface emits at different wavelengths and as a function of temperature. Max Planck defined in 1901 the relationship that allows an estimate of the spectral radiant exitance M(λ) of a blackbody, the radiant flux emitted by a surface per unit area of that surface (W m^{-2} m^{-1}), for a given wavelength and temperature.

$$M(\lambda) = 2\pi hc^2 \lambda^{-5}[(\exp(hc/\lambda kT) - 1)]^{-1} \quad (1.1)$$

$$\text{or } M(\lambda) = c_1 \lambda^{-5}[(\exp(c_2/\lambda T) - 1)]^{-1} \quad (1.2)$$

$$\text{with } c_1 = 2\pi hc^2 = 3.74 \times 10^{-16} \text{ W m}^{-2} \text{ and } c_2 = hc/k = 1.44 \times 10^{-2} \text{ m K} \quad (1.3)$$

where c is the speed of light (2.99×10^8 m s^{-1}) and k is the Boltzmann constant (1.38×10^{-23} J K^{-1}).

The radiant flux received by the Earth (spectral irradiance) from the Sun at the top of the atmosphere is less than that which leaves the Sun because of the inverse square law that governs

the decay of intensity of light with distance from the source. Moreover, not all of this light reaches the Earth's surface because of the atmosphere. The amount of light available at the top of the atmosphere (exoatmospheric solar irradiance) decreases after going through the atmosphere as certain frequencies of light are preferentially absorbed by molecules of gas. The amount of light that the atmosphere absorbs is defined as the transmissivity $\tau(\lambda)$, a unitless parameter with values of between zero and one, with one meaning that all light is transmitted and zero that all light is absorbed (Figure 1.1).

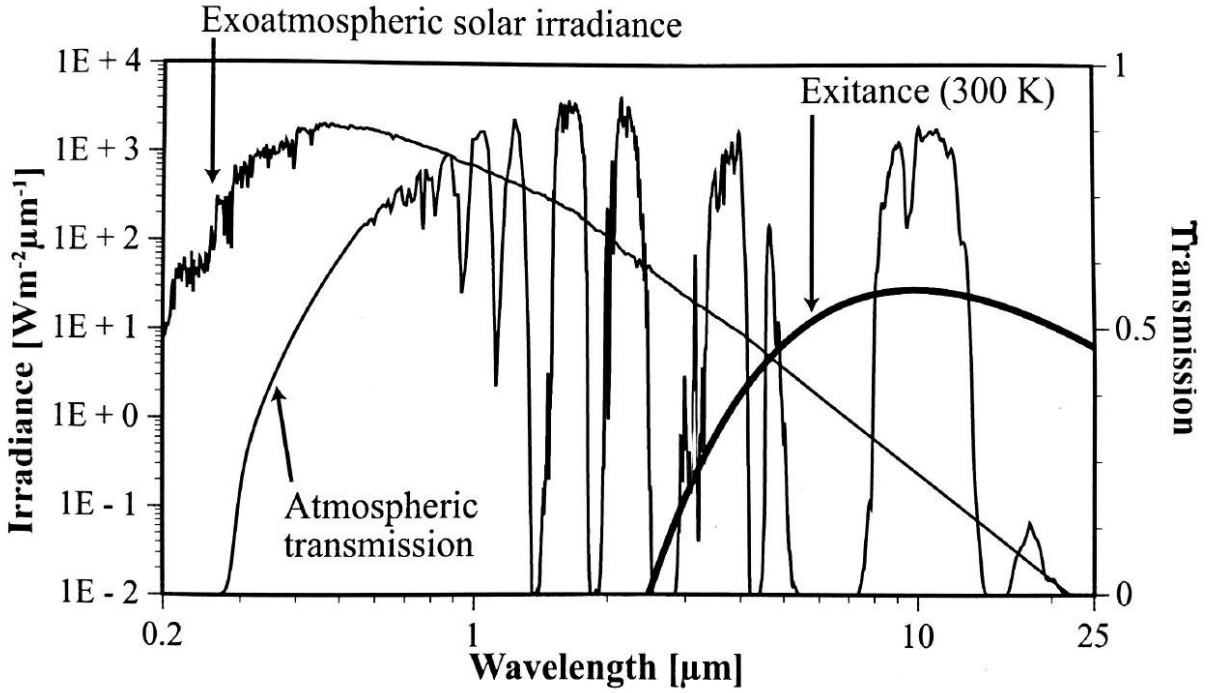

Figure 1.1. Measured top of the atmosphere solar irradiance (exoatmospheric solar irradiance), the transmissivity of the atmosphere and the exitance from a 300 K blackbody as a function of wavelengths (Schott, 2007).

Satellite remote sensing measurements can only be made when the atmospheric transmission is close to one. Each time $\tau \sim 1$, it creates an atmospheric window that is used for satellite remote sensing measurements. However, the light reaching the surface of the Earth is not all completely reflected back; some will travel through the atmosphere one more time before it reaches any sensor orbiting in space. Another important limitation is that not all materials on the Earth's surface emitting in the thermal infrared are real blackbodies. This is taken into

account by considering the emissivity of the target ε(λ), which defines how well an object radiates energy compared to a blackbody (Schott, 2007), which would have an emissivity of 1.

The amount of light we measure when performing remote sensing is termed spectral radiance L(λ). The spectral radiance is equal to the spectral exitance divided by pi (strictly this is true only when considering a Lambertian surface). A common unit for spectral radiance is W m^{-2} sr^{-1} m^{-1} and this introduces the unit of steradian (sr), an angle that allows the measurement to be independent of the distance (no matter how close we are from our target, it will not change the energy we detect). The more common unit for spectral radiance L(λ) in satellite remote sensing is W m^{-2} sr^{-1} μm^{-1}, when we divide by 10^6.

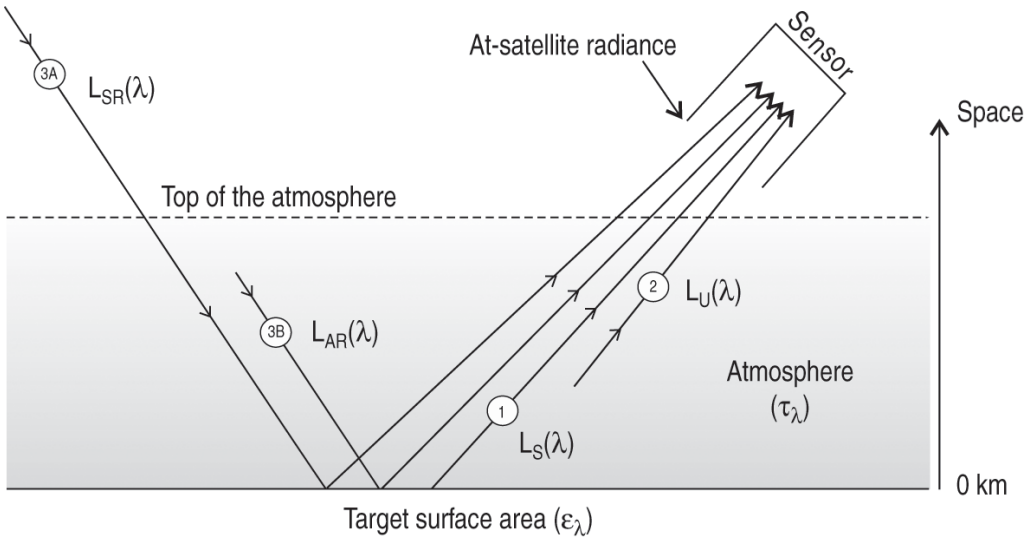

Figure 1.2. Schematic of the energy paths considering the effects the atmosphere has on the measurement from the sensor (Cracknell and Hayes, 1991). 1) The spectral radiance emitted by the target $L_S(\lambda)$; 2) the atmospheric upwelling radiance $L_U(\lambda)$; 3A) the reflected radiance of the target from the Sun $L_{SR}(\lambda)$; and 3B) the downwelling radiance $L_{AR}(\lambda)$ − light emitted by the atmosphere down onto the target which is then reflected back to the sensor.

When studying an active lava flow on Earth from space, we need to remember that there is more than just the energy emitted by the lava flow reaching the sensor (Figure 1.2). In the case of a target emitting thermal radiation, we first have to consider: 1) the target self-emission due to

its temperature as we described above − this is the radiance $L_S(\lambda)$ we are interested in measuring to learn more about active lavas; 2) the upwelling radiance emitted by the atmosphere itself $L_U(\lambda)$; and 3) the solar radiance reflected by the surface $L_{SR}(\lambda)$ and the atmospheric downwelling radiance $L_{AR}(\lambda)$ which is then reflected back to the sensor. Of these energy paths some are more important than others, and relative importance varies with observation conditions. For example, wavelength of interest and the time of day is important and allows us to neglect some of the energy paths, such as the reflected solar radiance during nighttime acquisition.

1.3 History of satellite thermal remote sensing and the MODIS instrument

NASA's MODIS is the MODerate Resolution Imaging Spectroradiometer and has been orbiting the Earth since December 1999 onboard Terra and since May 2002 on the Aqua satellite. This instrument is something of a successor to (continuation of) the AVHRR (Advanced Very High Resolution Radiometer) class of remote sensing instruments, which was initially designed for meteorological studies. However, this class of instrument proved significant for active volcano monitoring given their spectral range and their high temporal resolution (about two images every day). Thermal remote sensing of active volcanism with the AVHRR class sensors started early in the 1960s (Dozier, 1981; Matson and Dozier, 1981) with simple hotspot detection. A hotspot, in the context of this thesis, represents any point on the Earth's surface with an anomalously high temperature due to a volcanic source. The use of AVHRR data for volcanic hotspot detection in publications increased from one every few years to a few each year in the 1990s. This happened thanks to a key paper from Rothery et al. (1988) evaluating the potential use of SWIR and TIR data to study volcanic hotspots. Also during the 1990s, the University of Alaska Fairbanks (UAF) remote sensing group was the first to use satellite thermal data (AVHRR) for operational monitoring to detect and track volcanic hotspots. Later on, Harris et al. (1997a, b) and Oppenheimer et al. (1998) reviewed the volcanological applications of this class of instruments and highlighted the importance of the low spatial but high temporal resolution instruments. In 1991, the EOS (Earth Observing System) program was launched to observe and monitor the Earth as an environmental system (Mouginis-Mark et al., 1991; 2000; Ramsey and Flynn, 2004). This program helped boost the number of studies using thermal remote sensing for volcanic activity. MODIS was one of the four instruments designed during the EOS program with thermal infrared channels allowing the study of active volcanoes.

Over time, technological improvements associated with ground segments allowed the reception, processing and storage of satellite images to happen in a much faster and easier way and at reduced cost (Harris, 2013). This helped Harris et al. (1995a, b, c) to create the first automated detection algorithm for hotspot using AVHRR data from Mt Etna (Italy) and Krafla (Iceland) volcanoes. Following closely, the first global near-real time system, MODVOLC, was developed (Wright et al., 2002). MODVOLC is an automated near-real time algorithm for identifying hotspots using MODIS data that detects and records in near-real time any location on Earth that is anomalously hot compared to a normal non-volcanic state. The main measurement recorded is the spectral radiance of each anomalous pixel in every image. High temporal resolution enables tracking of the change of volcanic activity over time and allows the creation of time-series (Glaze et al., 1989; Oppenheimer et al., 1993; Wooster and Rothery, 1997). Therefore, the main advantages of satellite remote sensing are: 1) the temporal resolution; 2) the synoptic view with the potential to image more than one volcano; 3) the continuous data available during the lifetime of a sensor; and 4) the wide range of sensors allowing a worldwide view of every existing volcano. Since many active volcanoes are remote, this is an important tool for volcanologists.

MODIS possesses 36 spectral bands from the visible (VIS) to the longwave infrared (TIR) with resolutions ranging from 250 m to 1 km, including 10 wavebands suitable for hotspot detection. The first two bands have a spatial resolution of 250 m (VIS to NIR), the next five bands have a resolution of 500 m (VIS to NIR) and the 29 other bands have a resolution of 1 km (VIS to TIR). The fact that the MODIS instrument is carried on two satellites (Terra and Aqua) allows imaging of the entire Earth every 1-2 days (Masuoka et al., 1998). Terra and Aqua are sun-synchronous, near polar orbiting satellites at 705 km in altitude with Terra being part of EOS AM-1 (passing north to south at 10:30 am at the equator) and Aqua the EOS PM-1 (crossing the equator south to north at 1:30 pm). Therefore, the MODIS instrument is well designed for the detection of active volcanism around the world and forms a very extensive database (Wright and Flynn, 2004) with better spectral resolution and calibration than AVHRR. This provides the volcanological community with a large database of active volcanism detection with information on spectral radiance measurements for over 15 years.

1.4 Effusive volcanic activity

Volcanic activity can be of many different types, but is mainly split into two categories: effusive and explosive (Francis and Oppenheimer, 2004). The main difference between the two styles arises from the presence or absence of magma fragmentation. The important parameter driving fragmentation is the gas content. Most explosive events occur when the dissolved gas exsolves as it rises in a viscous magma that does not let gas escape, building pressure and resulting in the fragmentation of magma into small particles (tephra) in a sudden manner. By contrast, in volcanoes with less viscous magma, gas can escape easily and lava can be extruded or flow passively in lava flows or domes, producing effusive eruptions with no fragmentation. However, the range of possible activity is actually continuous between these two eruptive styles with no clear separation (Francis and Oppenheimer, 2004). Here, we define effusive activity following Parfitt and Wilson (2008) "*an effusive eruption is an eruption in which lava flows away from a vent as a coherent liquid"*. Lava flows are often basaltic, i.e., low silica content, with low viscosity and high temperature flowing in a sustained manner for hours to days and up to months. We focused on basaltic activity because it is the most abundant, i.e., more than half of volcanoes are formed with basaltic magma composition (Walker, 2000), basaltic flows can travel for greater lengths than more silica-rich magmas and are found in all tectonic settings. A large majority of effusive activity occurs underwater, unseen by most at mid-oceanic ridges (three quarters of the Earth's magma output is emitted at divergent plate boundaries; Simkin and Siebert, 1994), and only visible at the surface in Iceland and East Africa. Therefore, effusive eruptions occurring at the surface give us the opportunity to observe and study lava flow emplacement to understand their dynamics.

Lava flows are the most common volcanic feature on the Earth's surface (Kilburn, 2000), covering about 70% of it, and frequently found on other terrestrial planets. Understanding how they form and emplace is therefore crucial to study our planet's surface evolution as well as the deeper conditions that allow melt formation. A lava flow comes from magma that gently oozes from the ground and slowly moves downslope. It can form different flow morphologies such as ʻaʻā or pāhoehoe (Hawaiian terms used around the world, introduced in the 19th century). ʻAʻā lava is defined as a flow with irregular surfaces covered by small cooler crust fragments, usually forming lava channels. Lipman and Banks (1987) divided ʻaʻā flows into four different types

depending on magma rheology and flow rates (from slabby, to scoriaceous, clinkery and blocky). A pāhoehoe flow is defined as a smooth and continuous surface, usually having lower velocity than ʻaʻā flows, commonly inflating, and forming lava tubes. Through these tubes, the interior of the flow is insulated and can flow for greater distance than ʻaʻā flows. As for eruption style, there is a continuous range between the two lava flow types and the transition from pāhoehoe to ʻaʻā generally reflects an increase in viscosity. As lava is erupting at the surface, it starts to cool and loses heat to the atmosphere and the ground due to the large temperature difference (e.g., basaltic lava is between 1000-1200°C and the atmosphere usually ~15°C).

Lava fountains and small explosive events might also produce associated lava flows if the magma composition has a low viscosity, high temperature and high enough supply rate. This volume flux, also called effusion rate or lava discharge rate, is one of the most important parameters used by volcanologists to study lava flow propagation since it controls how far the lava flow will go and potentially how long it will last. It is also a principal input for lava flow modelling (Wright et al., 2008). Thermal infrared imaging is greatly suited for observations of effusive eruptions because of the high temperature surface of lava flows and satellite remote sensing can make synoptic measurements even over flows covering tens of square km and over long duration. Based on the MODIS archive of thermal infrared measurements, I aim to build a time-series database of lava discharge rates for every basaltic effusive eruptions on the globe from the time the instrument became operational in 2000 until the end of 2014. In this dissertation, I focus on effusive activity i.e., lava flows around the world, with a basaltic composition during a 15-year time-period. The only volcano I did not consider in this work is Kīlauea, Hawaiʻi because of its more complicated setting and its continuous state of activity at Puʻu ʻŌʻō since 1983.

1.5 Lava flow hazards

Although lava flows are relatively slow-moving, they still pose important hazards for the population living nearby. Lava flow-producing eruptions are usually considered less dangerous than explosive eruptions due to their calmer and slower evolution. However, lava flows can still travel far (a few kilometers to many tens of kilometers) for long periods of time, blocking roads, destroying properties and burning infrastructure, causing great disturbance to the population as seen during the current Kīlauea eruption (Figure 1.3). Field measurements of lava effusion rate

can therefore be hazardous and remote sensing methods allow for safer and easier access to make the same measurement.

Figure 1.3. Picture taken by USGS HVO on June 4, 2018 around 6 am from the Kīlauea eruption that started on May 3, 2018 in the lower east rift zone. It shows one of the ocean entries that destroyed many vacation homes in the Kapoho neighborhood.

Some lava flows can be fluid enough to reach high velocity such as in Nyiragongo on January 10, 1977 in Congo. The lava lake present at the summit of the volcano suddenly drained and formed a very fluid pāhoehoe flow at about 15 km/h that burnt 70 people (Kilburn, 2000). Mauna Loa, in Hawai‘i, produced a lava flow in 1950 that reached the ocean from the flank of the volcano (~3 km a.s.l.) in about three hours (Finch and MacDonald, 1953). However, other lava flow-forming eruptions occur in locations remote enough that no roads or people are harmed, such as the recent Holuhraun eruption, Iceland, in 2014-2015. The principal hazards of basaltic lava flows arise from the destruction of infrastructure such as houses, roads and hospitals. Lava flows slowly enough (in general) to allow people to safely evacuate but there is a probability that the residents will not be able to access their house and belongings or lose them entirely when they return. Additional hazards may come from fragments falling from lava fountains, or explosions when lava comes into contact with water at an ocean entry or burns vegetation (Peterson and Tilling, 2000). Furthermore, if a lava flow covers agricultural lands it

might be problematic for the population relying on that food supply. Long-lasting lava flow eruptions have been known to affect the climate, such as the Laki eruption in 1783-1784. The eight-month emission of lava produced such high amounts of sulfur dioxide and fluorine that Iceland and Northern Europe were affected. The gas emission from this eruption resulted in loss of livestock and crops, producing famine and disease and eventually the death of many people (Francis and Oppenheimer, 2004).

1.6 Lava discharge rate

An important parameter that we are interested in is: How far a lava flow will go. Will it flow for a few hundred meters or for many kilometers? Where will it spread? How fast does it cool? Many factors come into play to answer these questions, such as magma composition, topography, and viscosity. Walker (1973) however, proposed that if all factors are equal, the intensity of the eruption is more important than the viscosity of the flow to estimate the final length of the flow. Here, the intensity refers to the effusion rate. Malin (1980) contested his findings using a larger set of data (including that of Wadge, 1978) by saying there was not in fact a direct relationship between flow length and effusion rate but rather with flow volume. Pieri and Baloga (1986) later clarified the connection and reported the linear relationship that exists between effusion rate and the lava flow surface area rather than its length (obviously the flow area will increase as the flow length does). They introduced a thermal loss model for lava flows to explain this proportionality between these two factors.

Pieri and Baloga (1986) was the stepping-stone for the first method to estimate effusion rate using thermal satellite remote sensing. Harris et al. (1997a) discovered that the low spatial resolution thermal images available at the time could be used to infer the area of active lava flow during an eruption. Knowing the active lava flow area at each satellite acquisition, the lava effusion rate could be calculated consistently during an eruption. Following this, two other thermal remote sensing methods to estimate effusion rate were developed. First, Wright et al. (2001a) clarified and simplified the first method by recognizing that the physics-based model was in fact nothing more than an empirically derived constant relating active lava area to effusion rate. Coppola et al. (2012) developed another method also based on a thermal balance model. Harris et al. (2007) reviewed the current methods to estimate effusion rate from ground-based measurement, geophysical techniques and the thermal satellite-based method, as well as

clarifying the nomenclature. Figure 1.4 highlights the definition of effusion rate and the different terms, such as eruption rate or time-averaged discharge rate, to which I will refer in the rest of this dissertation. Before the Harris et al. review paper in 2007, it was not clear exactly what authors were referring to when citing lava effusion rates in published papers. Since an increase in volume flux cannot be translated to the surface instantaneously, it is important to take into consideration the time over which the measurement was made. Therefore, to clarify this I will follow the definition of Harris et al. (2007) using lava effusion rate or discharge rate as a general term and using time-averaged discharge rates for a specific value of volume flux averaged over the time elapsed since the previous measurement.

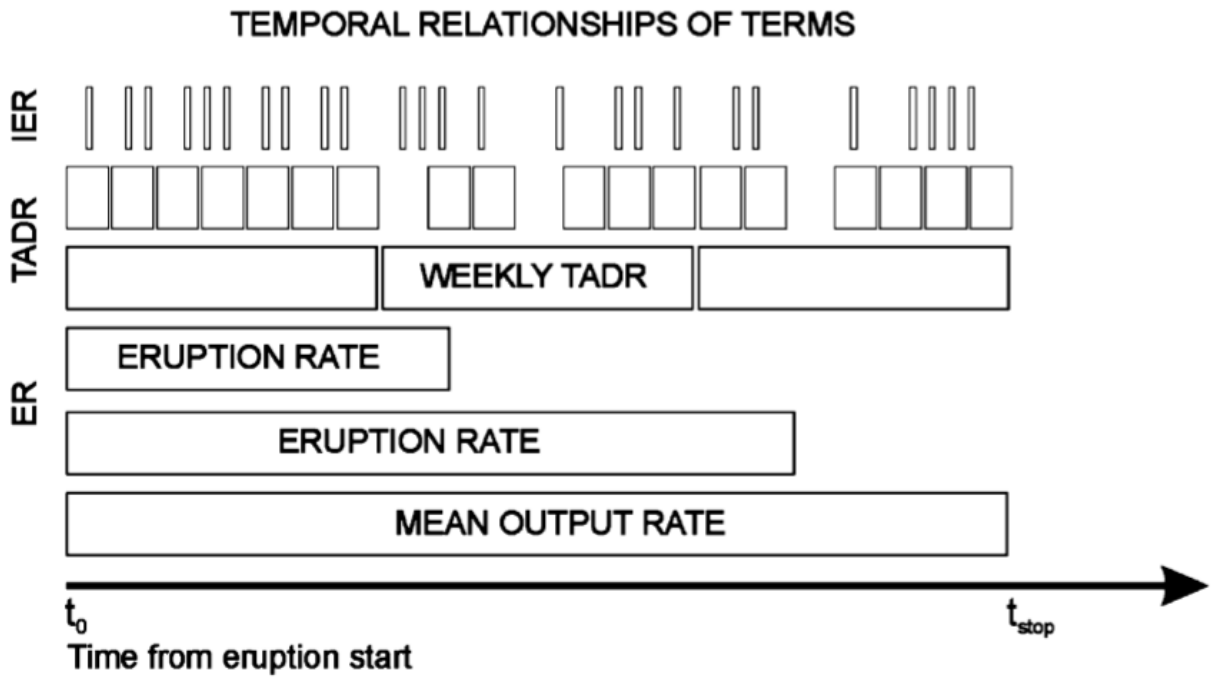

Figure 1.4. Lava supply rate nomenclature I will use throughout this dissertation as taken from Harris et al. (2007). IER stands for Instantaneous Effusion Rate, TADR is Time-Averaged Discharge Rate, ER is the Eruption Rate, t_0 is the onset of the eruption and t_{stop} is the time at which the eruption end.

1.7 Dissertation organization

In this dissertation, I focus on estimating lava discharge rates of basaltic lava flow-forming eruptions around the globe for a 15-year time period using satellite thermal remote

sensing. This work is based on data available through the MODVOLC system. I concentrate on using the previously defined methods published in the literature to estimate lava discharge rate, TADR. In Chapter 2, I show how these TADR time-series can be used as the basis for a simple method for predicting the end of lava flow-forming eruptions. In Chapter 3, I use the TADR estimated from satellite-derived and compare my results with in-situ data estimated by my Icelandic colleagues to better understand the eruptive dynamics of an unusually large and well monitored effusive eruption that occurred at Holuhraun, Iceland in 2014-2015. Finally, in Chapter 4, I compare the different techniques currently available to volcanologists in the published literature to assess their accuracy, both relative to each other and absolute. As with most scientific work, the following three research chapters were not done in isolation but with the collaboration of many. My advisor wrote the proposals and contributed ideas for each chapter. I analyzed the data and wrote Chapter 2, which was then reviewed by my advisor (R. Wright). In Chapter 3, my Icelandic co-authors (T. Thordarson, A. Höskuldsson, I. Jónsdóttir) provided the ground-based data and contributed ideas to this research project. I prepared the figures and tables and I. Jonsdottir provided Figure 3.1 and information for Table 3.1. I wrote this chapter and all four of my co-authors reviewed it and accepted it. For the last chapter, I analyzed the data and wrote this research project, which was reviewed by my advisor.

The first project (Chapter 2) consists of using our discharge rate time-series database along with the theory of Wadge (1981) to see if I could use the shape of these time-series to predict when an effusive eruption would end. Wadge (1981) recognized a trend typical for basaltic episodic eruptions in the effusion rate time-series (based on seven volcanoes), that is asymmetric with a fast and sharp increase of effusion rate reaching a maximum quickly and then slowly decreases exponentially over time. This was one of the early works that recognized and characterized how effusion rate time-series could be used to gain insight into the dynamics of effusive eruptions. This logarithmic behavior of the waning period during an effusive eruption was tested with our multi-decadal database to see if it could be used as a predictive tool for the end of effusive eruptions. Since lava flows pose a hazard for populations that can be sustained for long periods of time (days to months), it would be useful information to have. This work has been published in Bulletin of Volcanology under the title “Predicting the end of lava-flow-forming eruptions from space”.

In the third chapter, I had the opportunity to study the most recent Icelandic eruption that started in August 2014 and continued for the next six months. This case study used the satellite remote sensing methods to estimate lava discharge rate and compared it with the large datasets available from ground-based measurements. This eruption turned out to be one of the largest basaltic effusive eruption in the past 200 years and was the focus of my third chapter. I was able to compare the satellite-based method of lava discharge rate against measurements taken on the ground for the entire duration of the eruption. This chapter, which was recently accepted in the Journal of Geophysical Research Solid Earth, is entitled "The volume of lava erupted during the 2014 to 2015 eruption at Holuhraun, Iceland: a comparison between satellite- and ground-based measurements".

Finally, a large part of this PhD (Chapter 4) was concentrated on establishing whether or not the three different satellite thermal remote sensing methods of estimating lava discharge rate (Harris et al., 1997a; Wright et al., 2001a; Coppola et al., 2012) are equivalent. I suspected that each method would give different results, although it seemed that many studies used one method as if it did not affect the results. Using the same database of worldwide basaltic effusive eruptions, I estimated lava discharge rate time-series with the three different methods and looked at the relative differences in TADR for all 104 eruptions, at 34 volcanoes, over the last 15 years. Chapter 4 is entitled "An assessment of three satellite-based methods to estimate lava discharge rates during effusive basaltic eruptions" and aims to identify the most accurate method of the three. To do so, I used our lava discharge rate time-series to retrieve the final flow volume that was produced during each eruption. I then compare this satellite-derived volume with published values of final flow volume that can be accurately defined at the end of an eruption (particularly by geophysical methods). Realizing that the methods following a physics-based model could not assimilate all complexities of the discharge rate calculation, I decided to go back to a simpler coefficient relationship. I therefore propose new coefficient values to estimate lava discharge rate for a larger number of volcanoes that give more accurate final flow volumes and lava discharge rates.

CHAPTER 2

PREDICTING THE END OF LAVA-FLOW-FORMING ERUPTIONS FROM SPACE

Published as: Bonny, E., R. Wright (2017), Predicting the end of lava flow-forming eruptions from space, Bulletin of Volcanology, 79:52, DOI 10.1007/s00445-017-1134-8.

Abstract

Although the volcanological community places great emphasis on forecasting the onset of volcanic eruptions, knowing when an effusive eruption will end is just as important in terms of mitigating hazards. Wadge (1981) postulated that the onset of an episodic, lava flow-forming basaltic eruption is characterized by a rapid increase in effusion rate to a maximum, before decaying over a longer period of time until the eruption ends. We used thermal infrared remote sensing data acquired by NASA's MODerate Resolution Imaging Spectroradiometer (MODIS) to derive time-averaged discharge rate (TADR) time-series using the method of Harris et al. (1997a) for 104 eruptions at 34 volcanoes over the last 15 years. We found that 32 eruptions followed the pattern described by Wadge (1981). Based on the MODIS-derived maximum lava discharge rate and a decay constant that best fits the exponential waning phase (updated as each new MODIS TADR observation is added to the time-series) the time at which the discharge equals zero, and thus the point at which effusion ends, can be predicted. The accuracy of the prediction improves with the number of data points so that, in the ideal case, the end of effusion can be retro-casted before half of the eruption duration has passed. This work demonstrates the possibility of predicting when an eruption will end using satellite-derived TADR time-series acquired in near-real-time during that eruption. This prediction can be made after an eruption has reached its maximum lava discharge rate and the waning phase of the Wadge trend has begun. This approach therefore only applies to the case of eruption from a chamber undergoing an elastic release of energy during lava flow emplacement, and we provide examples of eruptions where it would not be applicable.

2.1 Introduction

The volcanological community has focused much attention on predicting when an eruption will begin (Linde et al., 1993; Sparks, 2003; Marzocchi and Woo, 2007; Marzocchi and Bebbington, 2012; Pallister et al., 2013), mainly taking cues from seismicity (Harlow et al., 1996; Brenguier et al., 2008), ground deformation (Voight et al., 1998; Segall, 2013), thermal emissions (Pieri and Abrams, 2005; Van Manen et al., 2013) or gas emissions (Baubron et al., 1991; Aiuppa et al., 2007). However, accurately forecasting when an eruption will end is similarly important in terms of hazard mitigation. This is especially true for lava flow-forming eruptions that can threaten population centers down slope of vents. For example, accurate forecasting could help in terms of evacuation management, allowing decisions to be made as to when it is likely going to be safe for people to move back to their homes. Although much more research has been conducted on forecasting eruption onset than eruption cessation, the recent work of Hooper et al. (2015) is a notable example of an effort to forecast the end of an eruption (Bárðarbunga 2014-15) using deformation measurements. Attempts to use satellite data to define (but not predict) the end of an effusive eruption have also been carried out, such as Aries et al. (2001), who showed that Advanced Very High Resolution Radiometer (AVHRR) 3.9 μm radiance undergoes a sharp decline at the cessation of effusion. This can be used as a proxy for eruption termination and is due to the fact that exposure of the highly radiant flow interior through cracks in the flow surface ends when the flow is no longer moving.

Here we present a method for using satellite-based infrared data, acquired in near-real-time during lava-flow-forming eruptions, to predict when such eruptions will end. Wadge (1981) suggested that lava effusion rate (instantaneous volume flux of lava, in m^3/s) during effusive basaltic eruptions, when plotted against time, follows a typical asymmetric trend (Fig. 2.1). Wadge explained this temporal evolution in effusion rate in terms of rapid increase in lava flux after the onset of an eruption, with maximum lava discharge rate reached within the first few hours to days. This period of waxing flow is due to release of the magma chamber overpressure and gas exsolution. Effusion rate then decreases logarithmically over the rest of the eruption period due to the elastic release of energy from the magma chamber as it re-equilibrates with the lithostatic pressure.

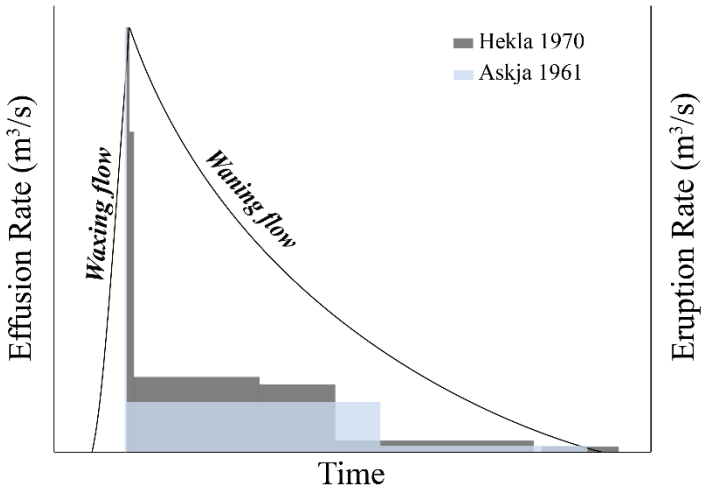

Figure 2.1. Wadge (1981) theoretical model (black solid line) and two examples of his limited dataset from Hekla 1970 and Askja 1961. He used eruption rates (volume of lava erupted during a certain period of time and divided by that time) to approximate the variation of effusion rate due to the insufficient number of effusion rate measurements available at that time.

This simple logarithmic decay of volume flux with time is expressed as a relationship between the effusion rate at any time during the eruption ($Q_{f,t}$), the maximum lava discharge rate (Q_{max}) and a decay constant (λ) by

$$Q_{f,t} = Q_{max} e^{-\lambda t} \tag{2.1}$$

as shown in Fig. 2.1. This typical asymmetric trend in effusion rate, hereafter referred to as a "Wadge curve", has been recognized during many eruptions, including effusive events at Etna and Krafla (Harris et al., 1997a; 2000), Nyamuragira, Piton de la Fournaise and Sierra Negra (Wright and Pilger, 2008). However, Coppola et al. (2017) and Harris et al. (2000; 2011), pointed out that at Piton de la Fournaise and Etna respectively, this asymmetric trend does not occur for all effusive eruptions. The work described here assumes that most lava-flow-forming eruptions exhibit this relatively simple behavior, and that fitting a synthetic curve with the form of Equation 2.1 to an effusion rate time-series acquired during the waning phase (i.e., after the point of maximum discharge) will allow prediction of the end of the eruption (i.e., predicting when the lava discharge rate approaches zero). Crucially, our method uses effusion rate time-

series constructed from multi-temporal thermal infrared satellite measurements. As these measurements can be made as often as several times per day during eruptions anywhere on Earth, the end of an eruption can be predicted in near-real time relatively soon after eruption onset, and updated as the eruption progresses and more satellite data are acquired.

We note, here, that infrared satellite data do not yield the instantaneous effusion rate, but instead yield a time-averaged discharge rate (TADR, Wright et al., 2001a; Harris and Baloga, 2009; Harris, 2013). Following Harris et al. (2007), lava effusion rate is defined as the instantaneous measure of lava flux from a vent at any given time, whereas TADR is the volumetric output averaged over some longer time period. Ultimately, the TADR becomes the Mean Output Rate (MOR) if estimated at the end of an eruption from the total volume of erupted lava over the entire eruption duration. Here, we assume that our maximum TADR derived from the satellite data is equivalent to the maximum lava discharge rate defined by Wadge (1981; i.e., Q_{max}). We have used satellite-based TADR measurements made over the last 15 years to test how well such a method works. Specifically, we used data acquired by the MODIS (MODerate Resolution Imaging Spectroradiometer) instruments, which have been operational since December 1999 (on NASA's Terra satellite), and since May 2002 (on NASA's Aqua satellite). This archive yields data for 104 effusive basaltic eruptions at 34 different volcanoes (Fig. 2.2).

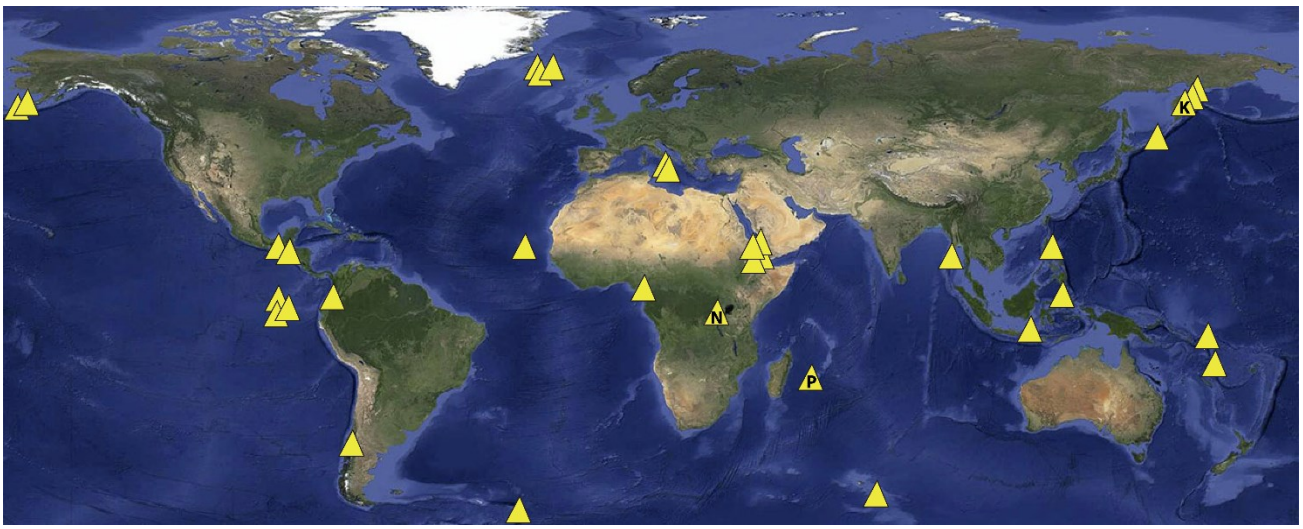

Figure 2.2. Map of the 34 volcanoes where MODIS detected at least one effusive basaltic eruption in the last 15 years (for the period 2000-2014, inclusive). P stands for the Piton de la Fournaise, Réunion; N is for Nyamuragira, DR Congo; and K is for Kizimen, Russia.

2.2 Methods

2.2.1 Estimating time-averaged discharge rate from infrared satellite data

We used MODIS satellite data from both the Terra and Aqua spacecraft, focusing on data from a single thermal infrared channel with a central wavelength at 11.03 μm (band 31). MODIS band 31 spectral radiance data for any hot-spot detected by MODVOLC (Wright et al., 2002) are freely accessible online (http://modis.higp.hawaii.edu), and it is this database that we use. MODIS samples spectral radiance from the Earth's surface in the thermal infrared (Fig. 2.3) with an instantaneous field of view (IFOV) equivalent to 1 km^2 on the ground at nadir (although this increases to about 2 × 5 km at the edge of the ~2500 km wide sensor field of view).

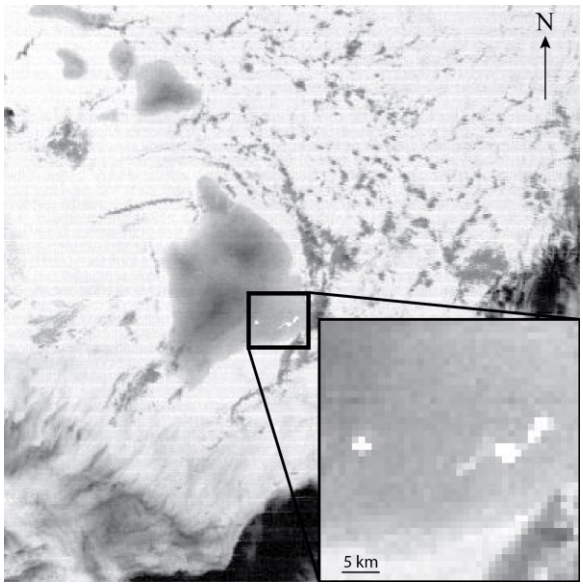

Figure 2.3. MODIS Terra image of the Big Island on October 3 2014 at 08:45 UTC from Band 21. Insert shows full-resolution (1 km per pixel) image of Pu‘u ‘Ō‘ō lava flow.

TADR is estimated by applying the method from Harris et al. (1997a; 1997b; 1998; 2000; and 2007) to the satellite spectral radiance, which is, in turn, based on the work of Pieri and Baloga (1986) who found a direct proportionality between lava discharge rate and the surface area of the resulting active lava flow. At-satellite spectral radiance in band 31 must be corrected for atmospheric effects (i.e., transmission losses as the signal passes upwards through the atmosphere, and an upwelling radiance component that the atmosphere itself emits towards the

sensor) and surface emissivity. The corrected spectral radiance ($L_{11,\,cor}$) is an estimate of the spectral radiance leaving the ground surface contained within each pixel. A two-component radiance mixture model, in which each pixel is assumed to contain a fraction of active lava surrounded by a colder background (representing the ground over which the active lava is flowing), is employed. To estimate the area of active lava within each pixel, the temperature of the lava flow surface, T_{lava}, must be assumed and Harris et al. (1997a) use 100°C as a lower estimate of the likely average temperature of an active lava flow surface (a cold case) and 500°C as a likely upper estimate (a hot case).

For the background temperature, T_{back}, we use the approach of Wright et al. (2015), rather than that of Harris et al. (1997a). T_{back} is estimated for each volcano in our dataset using the MODIS Land Surface Temperature (LST) product. This product (MOD11C3 and MYD11C3 for Terra and Aqua respectively) is downloadable from https://search.earthdata.nasa.gov/ and takes the MOD11C1 and MYD11C1 daily global LST dataset and computes a monthly average surface temperature for every 0.05° latitude/longitude (points are 5.6 km apart at the equator), after excluding cloudy values (via the MODIS cloud product). We then use each monthly average temperature value to compute a decadal average (2000-2010 for Terra and 2002-2012 for Aqua) for each point on Earth's surface. For each calendar month, surface temperature averages were quantified for each MODIS overpass time (i.e., MODIS Aqua and Terra nighttime and daytime datasets), which produces a T_{back} robust to seasonal variations in surface temperature and cloud contamination.

2.2.2 How many eruptions conform to the idealized effusion rate behavior described by Wadge (1981)?

We examined the TADR time-series of each eruption in our dataset (Fig. 2.2) to determine which ones displayed the waxing-waning trend defined by Wadge (1981). The relatively simple logarithmic decay that occurs during the waning phase of basaltic effusive eruptions enables us to compare the Wadge (1981) model to our satellite-derived time-averaged discharge rates. More than simply visualizing each time-series, we modelled a Wadge curve to compare the model with our space-based observations.

We rearrange Equation 2.1 to derive the time decay constant λ and to estimate a Wadge curve following

$$\lambda = \ln\left(\frac{0.1\%\ Q_{max}}{Q_{max}}\right) / t_{end} \quad (2.2)$$

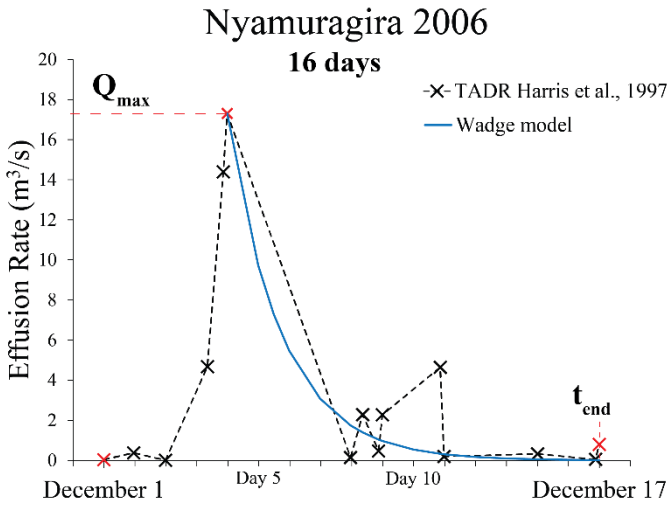

Figure 2.4. Example of satellite-derived TADR time-series from Nyamuragira eruption in 2006 that displays a Wadge-type curve, illustrating the maximum lava discharge rate Q_{max} and the last MODIS measurement that defines the end of the eruption (t_{end}).

In this case, the only required values are the maximum lava discharge rate Q_{max} and the time of the end of eruption (t_{end}) taken as the time of the last TADR measurement calculated from our thermal infrared satellite data (Fig. 2.4). This approach is only possible when t_{end} is known, i.e., when the effusion has already ended, which does not enable the creation of a predictive tool. A technique for prediction will be described in the section 2.2.3. Due to the asymptotic behavior of logarithmic decay, defining the end of the eruption is challenging. For consistency throughout, we considered the eruption to have ended when the time-averaged discharge rate reached a critical value (Q_{end}), selected to be 0.1% of the maximum lava discharge rate Q_{max}. This cut-off was found to be representative of the time at which eruptions in our dataset ended (i.e., the TADR after which radiance from the flow surface was insufficient to generate a detectable thermal anomaly). Choosing this value normalizes each eruption threshold to its maximum lava discharge rate and therefore the critical value varies for different eruptions and volcanoes. Thermal infrared TADR data can be calculated using the hot case (T_{lava}=500°C)

or the cold case (T_{lava}=100°C). Since the critical limit is a percentage of Q_{max}, the estimated decay constant is equal in both cases, and only the hot case is used in this study.

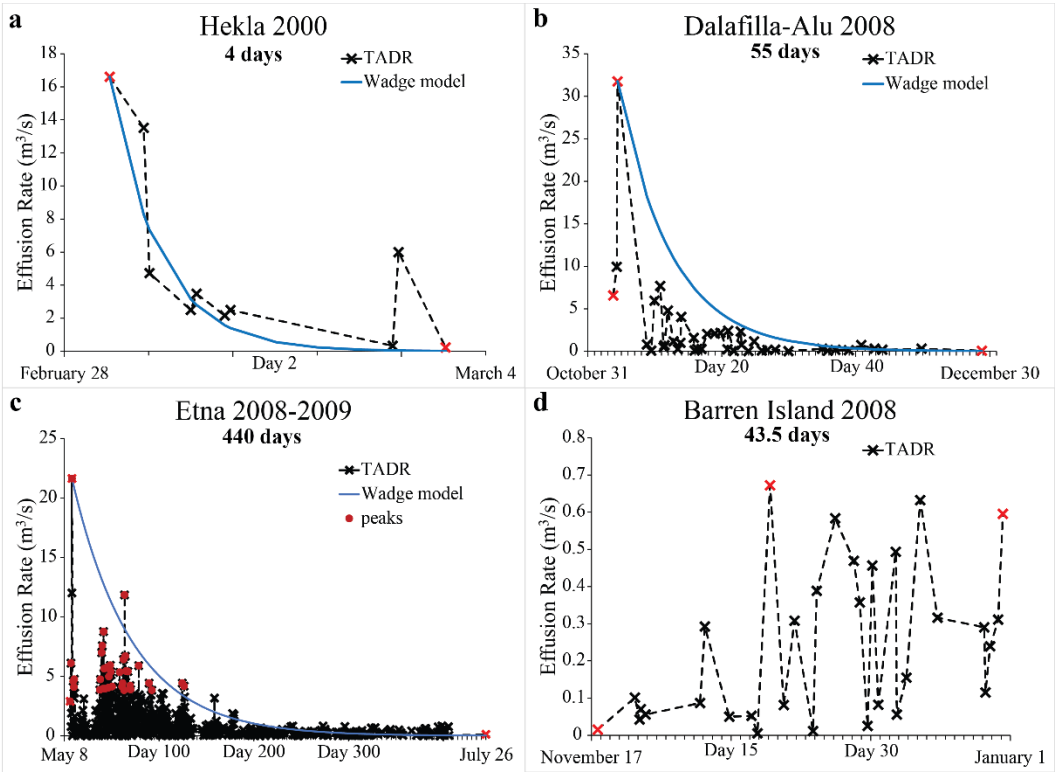

Figure 2.5. Examples of different TADR time-series with the Wadge model curve drawn for comparison. a) Wadge type, b) Half-Wadge, c) double pulse, d) undefined.

If the modelled Wadge curve (as calculated from Equation 2.2) followed the satellite data in a given eruption, it was called a Wadge-type eruption (Fig. 2.5a). If the modelled curve was higher than the MODIS-derived discharge rate during the entire eruption and also exhibited a plateau of low TADR after about half of the eruption duration, it was classified as a Half-Wadge-type eruption (Fig. 2.5b). We distinguished another group of eruptions having more than one maximum lava discharge rate (usually two), but still showing a logarithmic decay behavior that we called “double-pulse” type (Fig. 2.5c). All other eruptions were classified as undefined because no trend was visible and/or the TADR actually increased towards the end of the eruption (Fig. 2.5d). This increase was previously noticed by Wadge (1981) for some episodes at Kīlauea, which can be explained for this open-vent system by the backflowing of lava freezing the

conduit resulting in lava pouring out for a longer period. All 104 eruptions in our dataset were placed in one of these four groups (Fig. 2.5 and 2.6), and only a third of the total conformed to the idealized Wadge-type eruption.

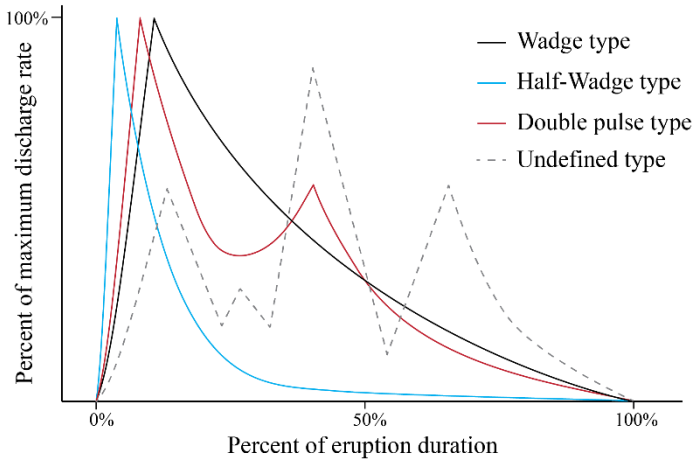

Figure 2.6. Schematic of different lava discharge rate time-series types.

2.2.3 How soon after the maximum lava discharge rate is attained can we predict the end of an effusive eruption?

For Wadge-type eruptions, the simple decay trend of the waning phase can be exploited to predict the end of an eruption. We predict when our end-of-eruption criterion is met (i.e., Q_{end} = 0.1% of Q_{max}) by fitting an exponential function (following Equation 2.1) to our TADR time-series. We estimate the decay constant that best fits the waning phase of the eruption based only on our MODIS-derived satellite data with no "a priori" knowledge of the time at which the eruption ended (t_{end}). Once the maximum lava discharge rate had been reached (i.e., the eruption has entered its waning phase) the time at which TADR falls below the cessation criteria is predicted using only the MODIS data available at that time, and compared to the known end-date of the eruption. Clearly, few data are available at first. As the eruption progresses, and new satellite data become available, we update the best-fit decay constant as new MODIS TADR observations are added to the time-series (i.e., the amount of data available to constrain the prediction increases with time). By re-computing each time a new TADR is added to the time-series, we are able to simulate how the method would work in near-real-time during an eruption.

Our results are expressed in two ways. First, we determine how the prediction of effusion cessation evolves as the amount of TADR data used to compute the prediction increases. Specifically, once Q_{max} was observed, we progressively add roughly 10% of the total TADR data to the time-series, and fit a new exponential curve to our satellite measurements each time (e.g., 10% of the data, 20%, 30%, up to 100%). For each "data step", the predicted end ($t_{end,\ pred}$) is then defined as the time at which the TADR reaches the critical value (Q_{end}) and compared (in terms of days) with the observed eruption end (t_{end}) corresponding with the last TADR data point detected by MODIS. Second, we express our predictions in terms of percent of eruption duration, which allows for a simpler comparison between eruptions since the TADR measurements are not acquired at regular intervals, or equally spaced in time (e.g., 50% of the total TADR observations after Q_{max} does not always equal 50% of the eruption duration). The best-fit of our data was found in a least-square sense (difference squared between the exponential curve and the satellite data). The difference between the predicted end and the observed end is expressed in terms of Δt (in days or % eruption duration) for each time at which a new TADR estimate is added to the time-series:

$$\Delta t = t_{end,pred} - t_{end} \tag{2.3}$$

Δt is positive when the predicted cessation is after the observed end of effusion and negative when it predates the observed end. Fig. 2.7 provides an illustration of the method where Δt_{20} is a schematic representation for the Δt that is predicted using 20% of the TADR data.

After the initial TADR calculation, we account for possible cloud contamination. Sub-pixel clouds are hard to identify and can cause low at-satellite spectral radiance, which produces an artificially low TADR estimate. For the eruptions in our dataset that have a well-defined TADR time-series (i.e., a large amount of data available), we attempt to exclude some cloud-contaminated values by only selecting the peak TADR measurements, or local maxima in discharge rate, that are one standard deviation above the median of all such local maxima (one *nsig* criterion). In some cases, this greatly reduces the number of data points available for prediction (sometimes to as few as two TADR observations), and in this case we use all TADR estimates classified as "peaks". For other eruptions, mainly those of short duration, the amount of TADR available can be so limited that no cloud-screening is feasible and all TADR estimates are used.

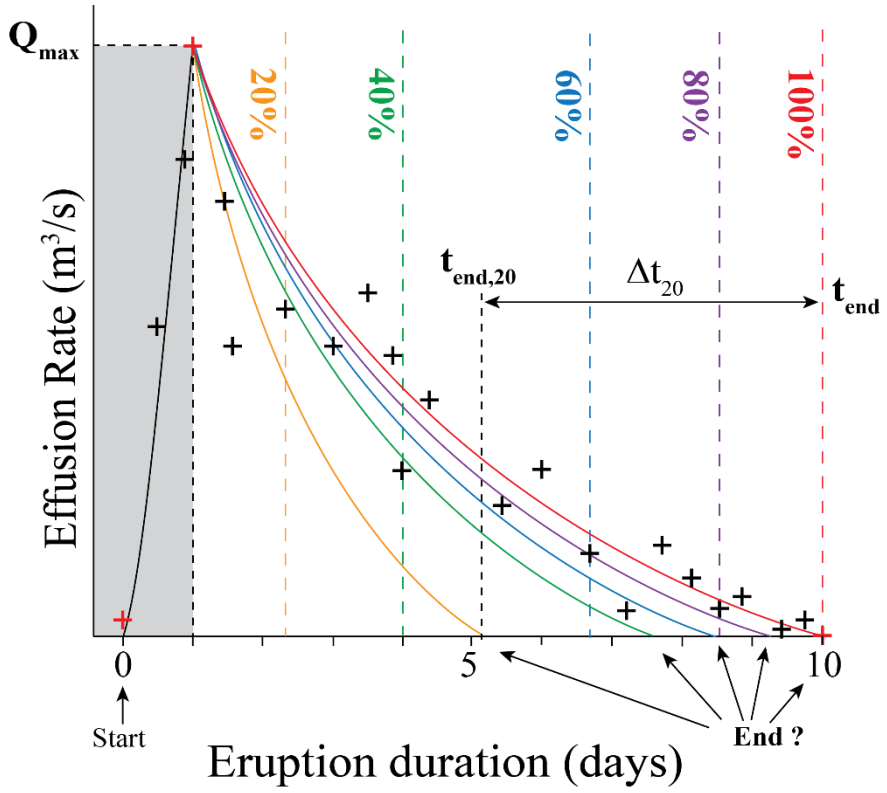

Figure 2.7. Cartoon of the method used for predicting the end of the eruption in this chapter. The colors of each exponential curve represent a different fit of a given amount of data (in percent) and give a different predicted end (when the effusion rate gets to ~0 m^3/s noted as End), with the associated Δt (Δt_{20} represents the Δt that is predicted using 20% of the TADR data). The red crosses represent three important points: the first is the onset of the eruption, the second is the maximum lava discharge rate Q_{max} and the last is the last TADR data point or the observed eruption end t_{end}. All of the data above are thermal infrared remote sensing data from MODIS. Notice that the fit with 40% of the data (green line) after Q_{max} is equal to 40% of the eruption duration but this is not always the case.

2.3 Results

Of the 104 eruptions studied, 32 eruptions strictly followed the typical Wadge curve, eight exhibited a double pulse in TADR, 13 corresponded to a Half-Wadge type, and 51 were undefined and did not show any trend at all (Fig. 2.5). Of the 32 eruptions, only half could be

used (the remainder comprised of fewer than five TADR data points) and our predictions are summarized in Table 2.1. The table shows the evolution of the prediction for each eruption, as we increased the amount of TADR estimates available and updated the best-fit exponential curve. Although we divided the time-series into percentiles of data used to compute the curves, far more relevant is how soon after the eruption began can the end-of-eruption prediction be made, and how good is that prediction. For this reason, Table 2.1 gives both measures: Δt, both in terms of days and percent of eruption duration; and the time since the onset of eruption at which the prediction could be made (also in terms of days and percent of eruption duration). For example, to illustrate how the data in the table are to be interpreted, in the case of the Piton de la Fournaise eruption of December 2005, our best prediction (bold in the table) was that the eruption would last 9 days (it lasted 10 days, for a Δt of -1). This prediction would have been possible on day 3 of the eruption (or after 30% of eruption duration had elapsed) at which time 30% of the MODIS data that would ultimately define the total TADR curve for the eruption had been acquired. For the Kizimen eruption of 2011, a good prediction (Δt within 7%) is possible on day 47 (or after 22% of the eruption had passed, at which time 70% of the MODIS data had been acquired) that the eruption would last 198 days (it lasted 212 days, for a Δt of -14 days). And if we had waited until 48% of the eruption had elapsed (day 102), our best prediction was that the eruption would last 211 days which is within 1% of the actual eruption duration. At this time, 90% of the MODIS data that would ultimately define the TADR curve for the eruption had been acquired.

To illustrate the viability of our predictive tool, we concentrate on three case studies: one eruption of short duration from Piton de la Fournaise in December 2005, one of medium duration from Nyamuragira in 2000, and one of long duration from Kizimen in 2011 (each volcano is denoted as P, N and K, respectively in Fig 2.2). For each graph shown (Figs. 2.8, 2.9, and 2.10), the green horizontal line represents the critical limit, Q_{end} that defines the end of the eruption. Figs. 2.8, 2.9, and 2.10 all include an inset figure, which summarizes how the end-of-eruption prediction changes (i.e., improves as we move up and closer to a Δt of zero along the y-axis) as we use more satellite data to constrain the prediction (i.e., as the eruption progresses, moving right along the x-axis). The more rapidly the curves in this figure approach a Δt of zero, the better.

2.3.1 Piton de la Fournaise 2005

Piton de la Fournaise is a stratovolcano located in La Réunion Island, in the Indian Ocean. MODIS detected a lava-producing eruption that started on December 26th, 2005 and ended on January 4th, 2006, for a total duration of 10 days. The maximum lava discharge rate was reached on December 27th at 20:49 UTC, about a day after the eruption started, with a TADR of 8 m^3/s (Fig. 2.8). Since we only have 15 satellite TADR measurements during the waning phase, we decided to keep every data point to apply our predictive tool.

Once two measurements after Q_{max} were obtained, in this case 1.5 days after the onset of the eruption (here 15% of the eruption duration), we began fitting an exponential curve to our data, which predicted that the eruption would last only three days instead of the observed 10 days (Δt of -seven days, dark blue diamond in Fig. 2.8f inset). After adding three more TADR estimates, three days past the onset of the eruption, our method predicted that the eruption would last nine days, which is accurate to within one day of the observed end of eruption (Δt = -1 day, light blue in Fig. 2.8f inset). This new prediction was six days closer to the observed end than the prediction made with two data points and happened to be the most accurate prediction after 30% of the eruption duration had elapsed. Using data from four days after the eruption onset, we predicted that the eruption would last eight days; in fact, it lasted 10 days (Δt = -2 days, purple diamond in Fig. 2.8f inset). A few hours later, with one more TADR observation, we reached the best-fit curve (same prediction with 100% data) which yielded an eruption that would end after 8.5 days (Δt of -1.5 days). As we increase the amount of TADR used and the eruption progresses, the prediction does not necessarily get better, but our best end-of-eruption prediction (within a day) could be estimated only three days after the eruption started (equivalent to 30% of the observed eruption duration). This result is significant in terms of hazard mitigation for this type of episodic basaltic eruption with a prediction of the eruption cessation seven days in advance.

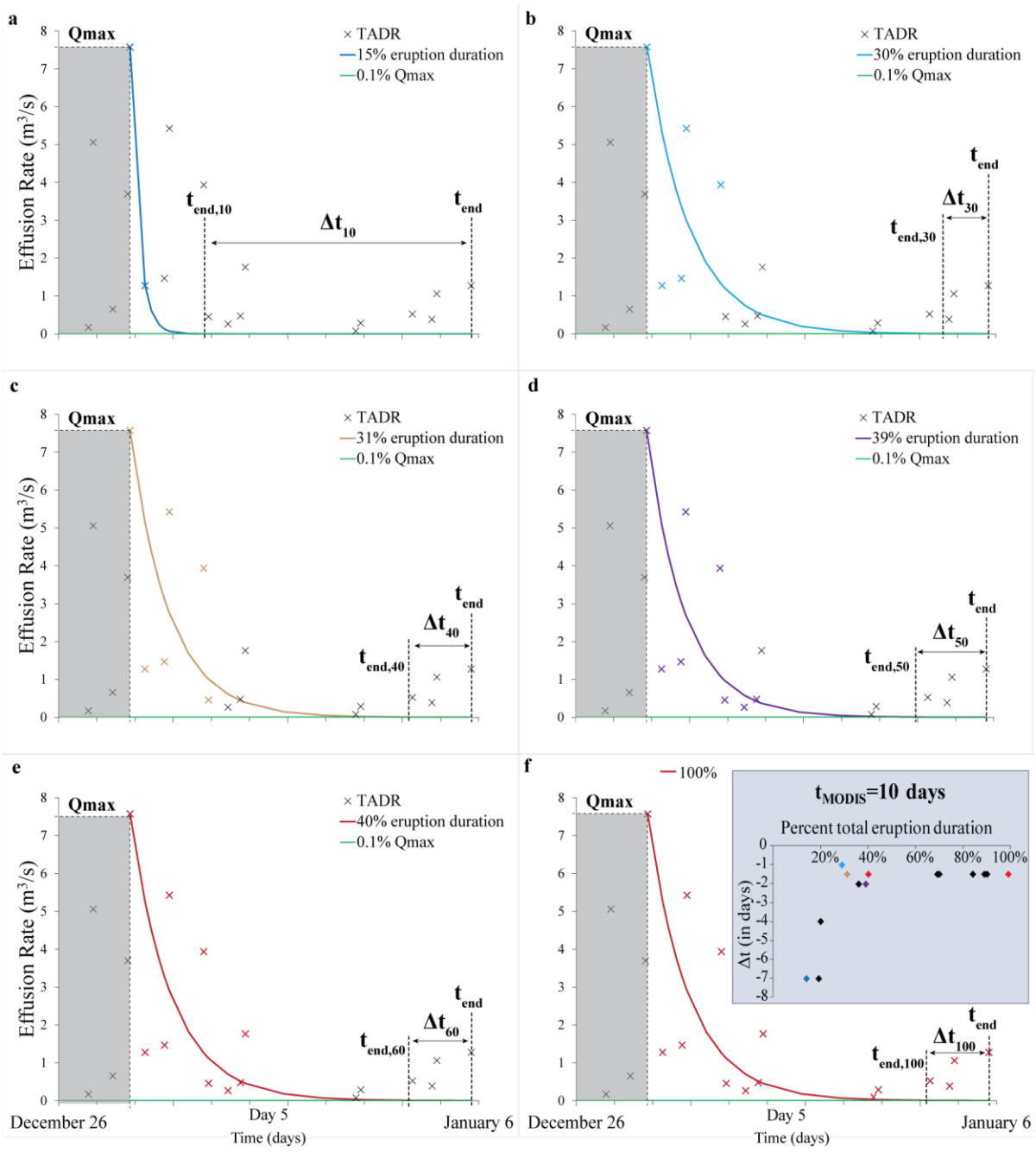

Figure 2.8. The December 2005 eruption of Piton de la Fournaise as observed by MODIS (eruption duration is 10 days). All axes have the same scale and legend. Δt_{10} represents the Δt that is predicted using 10% of the TADR data. f) Inset shows the evolution of the prediction as we increased the amount of data used to fit equation 2.1 from a to f (15% eruption duration to 100%), and the colors of the TADR data points (crosses) and curves match to show which data were used to generate each prediction.

2.3.2 Nyamuragira 2000

Nyamuragira is a shield volcano in DR Congo, and is the most active volcano in Africa (Smets et al., 2010). An eruption was recorded by MODIS on February 25th, 2000 that lasted until April 23rd, 2000, totaling 58 days. The eruption produced a lava flow, bombs, cinder and ash (GVN, 2000). The maximum lava discharge rate was detected on February 26th at 20:50 UTC only one day after the beginning of the eruption with a TADR of 17 m^3/s (Fig. 2.9). In this case, we used all the identified peaks to increase the amount of data available (providing us with eight data points instead of the three points that would have been available had we enforced the one *nsig* criterion).

For Nyamuragira, 7.5 days after the onset of the eruption (13% of the eruption duration), our method (with 25% of data or two TADR values) predicted that the eruption would last 54.5 days, close to the observed end (Δt = -3.5 days; blue diamond in inset in Fig. 2.9d). However, 14 days after the onset of the eruption (with three TADR values or after 24% of the eruption duration had passed), we predicted that the eruption would end after 50.5 days (Δt = -7.5 days). Our best prediction (also the final estimate) was that the eruption would last 59 days and this was found after 24 days into the eruption (41% of eruption duration) at which time 60% of the MODIS data that would ultimately define the total TADR curve for the eruption had been acquired. The eruption actually lasted 58 days, one day before the predicted end (Δt = 1 day, red diamond in inset in Fig. 2.9d). Therefore, for Nyamuragira we have a good prediction (Δt within 6%) a week into the eruption (i.e., after only 13% of the eruption had elapsed), and reached the most accurate prediction (to within one day) before half of the eruption had passed.

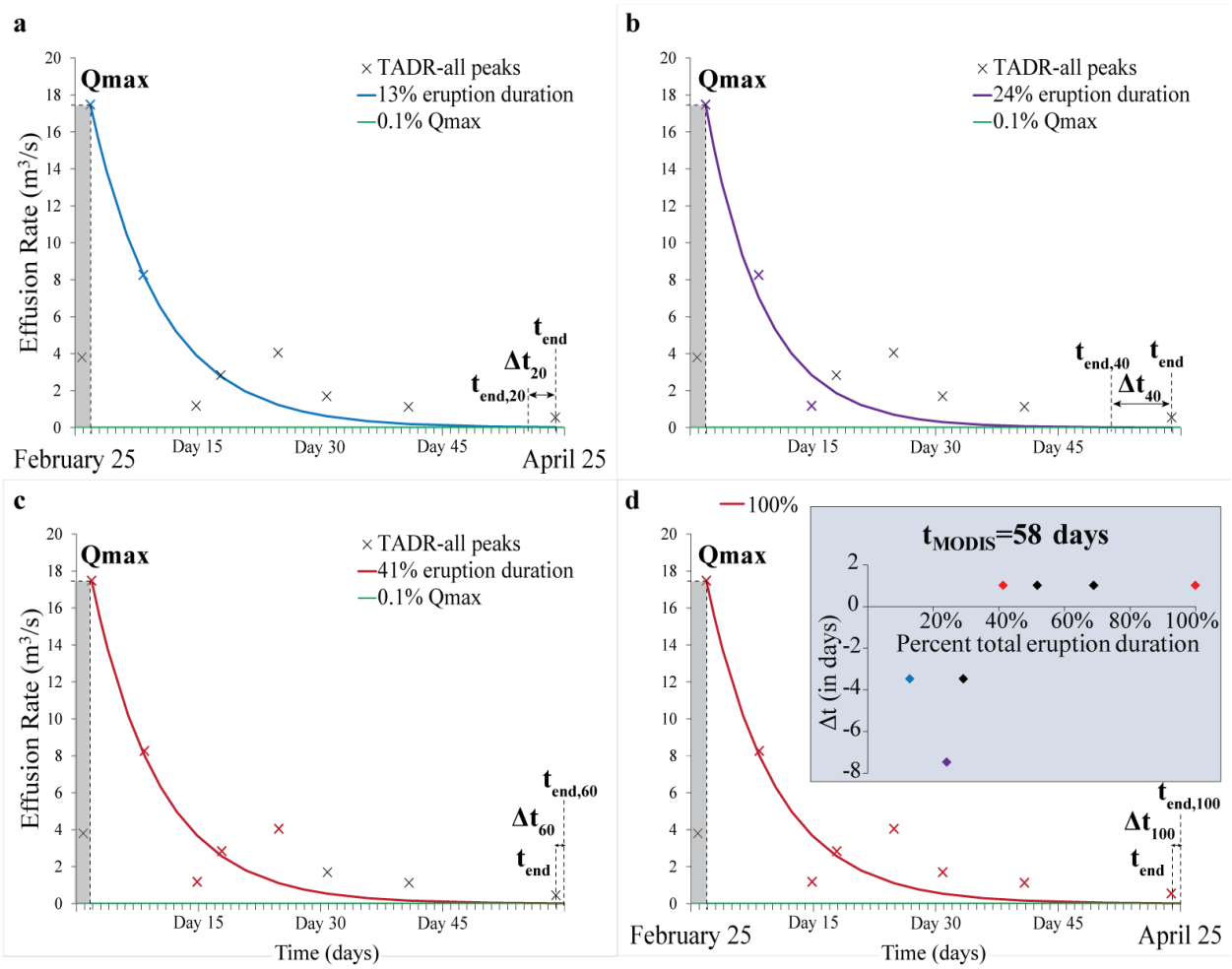

Figure 2.9. The Nyamuragira 2000 eruption (with a duration of 58 days) TADR time-series as detected by MODIS. d) Inset shows the evolution of the end of eruption prediction as we increased the amount of data used to fit equation 2.1 from a to d (13% to 100% of eruption duration). All graphs have the same scale and legend if not indicated and the colors of the TADR data points (crosses) and curves match to show which data were used to generate each prediction. Δt_{20} represents the Δt that is predicted using 20% of the TADR data.

2.3.3 Kizimen 2011

Kizimen is a stratovolcano in Kamchatka, Russia, and we focused on the first phase of the eruption that started on March 1st, 2011 and ended on September 29th, 2011 (GVN, 2011). In the second phase of this eruption (starting on October 3rd), the TADR time-series did not exhibit

the typical Wadge trend, so we only used the first phase with our predictive tool. The first phase lasted 212 days and reached a maximum lava discharge rate on March 1st at 15:25 UTC, which is the first point that MODIS detected, with a TADR of 12 m^3/s (Fig. 2.10). During this long duration eruption, we retrieved many estimates of TADR that allowed us to use the identified peaks (one *nsig* criterion) as defined in section 2.2.3 (15 peaks were found).

For Kizimen, 15 days after the onset of the eruption or 7% of the eruption duration (with two TADR values) our method predicted that the eruption would last 91 days, which is about 4 months shorter than the observed duration of 212 days (Δt = -121 days, blue diamond in Fig. 2.10f). With six TADR values (or 40% of data), we predicted that the eruption would end after 169 days; in fact, it lasted 212 days. This prediction would have been possible on day 29 of the eruption (or after 14% of eruption duration had elapsed) at which time 40% of the MODIS data that would ultimately define the total TADR curve for the eruption had been acquired. However, after 19 more days (47.5 days after the eruption onset or 22% eruption duration), our method predicted that the eruption would last 198 days, which is accurate to within 14 days (Δt = -14 days or 7% the eruption duration, brown diamond in Fig. 2.10f) of the observed end. At 102 days after the eruption onset (about half the eruption duration), our method predicted that the eruption would end after 210 days which is two days from the observed end. The prediction does not change once we add more data to our method. This case study shows that after only 14% of the eruption had elapsed (day 29), the end of the effusion could be predicted with a 20% accuracy (Δt = -20% eruption duration, which represents 43 days before the observed end). However, if we wait until 22% of the eruption has passed, a highly accurate end-of-eruption prediction can be made with a Δt of -7%. This could be further improved to a two day offset in the prediction with half of the eruption duration.

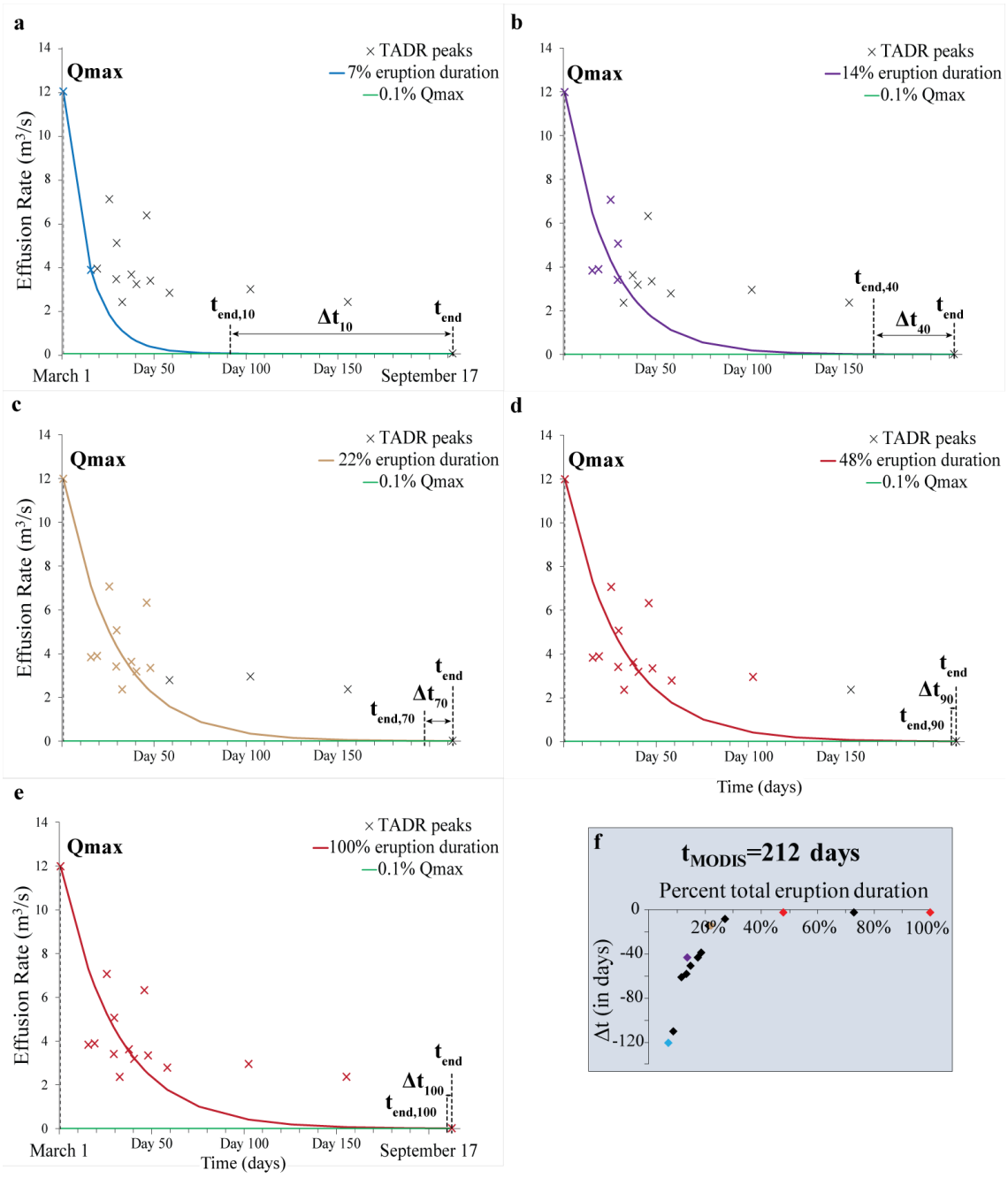

Figure 2.10. The Kizimen 2011 eruption, phase 1 from March 1st to September 29th. TADR were calculated from MODIS data and the eruption duration is 212 days. f) Evolution of the end of eruption prediction as we increased the amount of data used to fit equation 2.1 from a to e (7% to 100% of eruption duration). All graphs have the same units and legend and the colors of the TADR data points (crosses) and curves match to show which data were used to generate each prediction. Δt_{10} represents the Δt that is predicted using 10% of the TADR data.

2.4 Discussion and conclusions

Our initial goal was to determine a decay constant that best described all 104 eruptions in our dataset that would be "globally applicable" and then to use this global value to retro-cast the end of basaltic effusive eruptions. However, we observe too wide a range of decay constant values and thus a single average decay constant would not be valid for all eruptions. Focusing on a single volcano, the same issue arises: each eruption from a specific volcano has a unique TADR time-series trend that we cannot generalize (Harris et al., 2011; Coppola et al., 2017*).*

Using the ideal case defined by Wadge (1981), it is possible to predict in advance when effusion will cease if the waxing/waning behavior of the TADR time-series follows this trend. One limitation of this technique is that it may not be obvious initially whether the eruption will exhibit the Wadge-type TADR behavior, although the satellite data themselves could be used to make this determination as the TADR curve is compiled. The method we present is also potentially useful for other types of eruption, like the double pulse. In this case, the predictions would simply be reset after the secondary TADR peak. The detection of the maximum lava discharge rate Q_{max} is of great importance, and missing it would prevent a reliable forecast, especially when there are insufficient data and no observations close to the true time of Q_{max} to compensate. How many of our time-series were not classified as 'Wadge-type' eruptions simply because MODIS did not sample the key maximum lava discharge rate? We experimented with what would happen when removing Q_{max} from our TADR time-series for some eruptions in our dataset and observed three different outcomes: i) the Wadge curve could not be defined anymore, ii) the Wadge curve was still visible but the prediction was degraded, or lastly, and perversely, iii) the prediction improved. Improved temporal resolution of the satellite data acquisitions (perhaps by merging data from multiple platforms) would help ameliorate the detection of Q_{max}.

Another limitation arises from the thermal cooling behavior of a lava flow. Some lava flows can continue to radiate heat for a long period even after the flow has stopped advancing and can still be "hot" enough to be detectable by space-based sensors. The end of an eruption is therefore hard to define and often there is a discrepancy between the start and end date recorded depending on the techniques used, e.g., satellite measurements, the Global Volcanism Network database and literature on specific eruptions. For consistency throughout this work, we decided to use only our thermal infrared remote-sensing data for reference in our predictive tool.

However, the work of Aries et al. (2001) and Wright et al. (2001b) shows that precipitous decreases in emitted short-wave and mid-wave infrared (SWIR and MWIR, respectively) radiance accompany the time at which an active lava flow stops moving. In short, when the flow stops moving fresh cracks on the flow surface (which expose the hotter flow interior that contribute greatly to the observed SWIR and MWIR radiance) are not created to replace cooling lava in older cracks. As such, defining the end of an eruption using thermal infrared satellite data should be somewhat robust provided the detection method using the SWIR or MWIR spectral intervals.

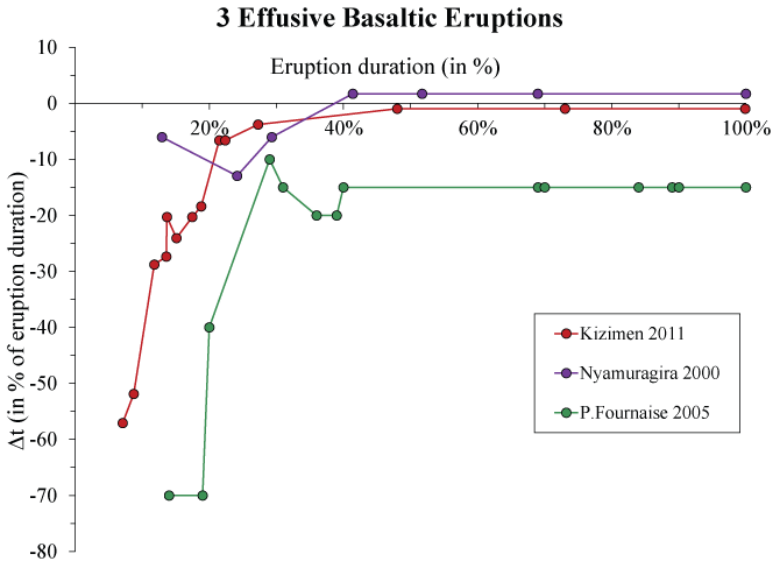

Figure 2.11. Summary for the three episodic basaltic effusive eruptions detected by MODIS discussed in detail in this chapter. Both axes are in percentage of eruption duration to allow for comparison of the predictions.

The TADR that marks the end of eruption has been assumed arbitrarily as 0.1% of the maximum lava discharge rate since it worked best for most of the Wadge type eruptions. But one can argue that a fixed value should be used at all time, such as the 2-3 m^3/s that Wadge mentioned in his 1981 paper. But with technologic advancements, it is now possible to resolve much lower values of discharge rates so we decided on a lower critical value. In Table 2.1, we summarize all the predictions made with the method described here. To generalize our estimates for all the eruptions, we relied on the estimate of Δt in percent of the eruption duration. We

found that the end of an eruption could be predicted (to within Δt of 25% of the observed duration) as early as 13% after it begins, and no later than 94% (Fig. 2.11 shows a summary of our three case studies). Each data point shows how the residual between the predicted end and the actual end of the eruption changes (moving "up" along the y-axis, as a percent of eruption duration) as more data are available to compute the prediction (i.e., after eruption onset, expressed as percent of eruption duration). Obviously, the more rapidly the curve approaches a Δt of zero, the sooner after eruption onset the end of eruption can be predicted. The closer the curve approaches the Δt of zero, the more accurate that prediction is. Generally, less than half of the eruption duration (average of 43%) allows for our best prediction. It can be seen that TADR time-series have peaks and troughs (Figs. 2.4, 2.5, 2.8, 2.9 and 2.10) and therefore the prediction of the end of effusion does not always improve with time.

In summary, once an effusive eruption starts, and the TADR time-series conforms to the Wadge-type model, we can use thermal infrared satellite remote sensing data to predict the cessation of effusion with high accuracy before the eruption is half over, and with reasonable accuracy even earlier after the eruption onset. In the future, applying this technique to an ongoing eruption in real-time, instead of retrospectively, would be of great interest for lava flow hazard mitigation. Its key contribution would be to reduce the damaging uncertainty that results from not knowing when multi-month-long lava flow eruptions will end. In the next chapter, we focus on a single case study in Iceland, the six month long eruption at Holuhraun, to see how accurate the thermal remote sensing method to retrieve lava effusion rate is compared to field-based methods. However, this eruption did not conform to the Wadge-type model and we could not test our predictive tool.

Table 2.1. Summary of the 16 Wadge eruption predictions. In bold is the "best" prediction (the smallest Δt) and in italic is a reasonably good prediction (the earliest prediction with a Δt at or less than 25% of the eruption duration), and in bold italic is when both the good and best prediction are coincident. Δt is in days and in percent of the eruption duration. The same is given for the time since eruption onset at which the prediction could have been made (in days and in percent of the eruption duration). The empty cells are for non-available data. Each eruption uses a different amount of TADR data to make our prediction and (a) stands for using all the TADR available without screening for low values, (p) is for all the available "peaks" TADR and (n) is for the plus one *nsig* criterion.

	P. Fournaise Dec '05 10 days (a)				**Nyamuragira '00 58 days (p)**				**Kizimen '11 212 days (n)**				**Cameroon '00 48.5 days (a)**			
	Δt		Time since eruption onset		Δt		Time since eruption onset		Δt		Time since eruption onset		Δt		Time since eruption onset	
% data	days	%	days	%	days	%	days	%	days	%	days	%	days	%	days	%
10	-7	-70	1.5	15					-121	-57	15	7				
20	-7	-70	2	19	*-3.5*	*-6*	*7.5*	*13*	-110	-52	18.5	9	-33	-68	16.5	34
30	***-1***	***-10***	***3***	***30***					-58	-27	29	14	-33	-68	18.5	38
40	-1.5	-15	3	31	-7.5	-13	14	24	*-43*	*-20*	*29*	*14*	-33	-68	20.5	42
50	-2	-20	4	39	-3.5	-6	17	29	-43	-20	37	17	-33	-68	21	43
60	-1.5	-15	4	40	**1**	**2**	**24**	**41**	-39	-18	40	19	-33	-68	22.5	46
70	-1.5	-15	7	70	1	2	30	52	-14	-7	47.5	22	-12.5	-26	23	47
80	-1.5	-15	8.5	85					-8	-4	58	27	***-12***	***-25***	***32***	***66***
90	-1.5	-15	9	90	1	2	40	69	**-2**	**-1**	**102**	**48**	-12	-25	39	80
100	-1.5	-15	10	100	1	2	58	100	-2	-1	212	100	-12	-25	48.5	100

Table 2.1. (Continued) Summary of the 16 Wadge eruption predictions.

	Etna July '01 21.5 days (a)				**Etna Nov '07 1 day (a)**				**Reventador '07 62 days (a)**				**Stromboli '07 34 days (p)**			
	Δt		Time since eruption onset		Δt		Time since eruption onset		Δt		Time since eruption onset		Δt		Time since eruption onset	
% data	days	%	days	%	days	%	days	%	days	%	days	%	days	%	days	%
10	-11.5	-53	6	28									-26.5	-78	2	6
20	-10	-47	7.5	35												
30	-7	-33	9	42									-23.5	-69	6	18
40	-6	-28	10.5	49	***1***	***0***	***0.4***	***40***	***-7.5***	***-12***	***12***	***19***	-14.5	-42	12	35
50	-6	-28	11.5	53									-11.5	-33	16	47
60	*-4*	*-19*	*13*	*60*	1	0	0.5	50	-11	-18	15	24	-10	-29	19	56
70	**-3.5**	**-16**	**14.5**	**67**									-9	-26	28	82
80	-3.5	-16	16.5	76	1	0	0.9	90	-11	-18	15	24				
90	-3.5	-16	19	88									***-8***	***-23***	***32***	***94***
100	-3.5	-16	21.5	100	1	0	1	100	-11	-18	62	100	-8	-23	34	100

Table 2.1. (Continued) Summary of the 16 Wadge eruption predictions.

	Hekla '00 4 days (a)				**Klyuchevskoy '08-09 67.5 days (n)**				**Llaima April '09 10 days (a)**				**Nyamuragira '06 16 days (a)**			
	Δt		Time since eruption onset		Δt		Time since eruption onset		Δt		Time since eruption onset		Δt		Time since eruption onset	
% data	days	%	days	%	days	%	days	%	days	%	days	%	days	%	days	%
10									-5.5	-55	1.8	18				
20	10	250	0.4	10	***-5.5***	***-8***	***30***	***44***	-5	-50	2	20	-6	-38	8	50
30	*1*	*25*	*0.5*	*13*	-18.5	-27	30	44	-4.5	-45	2.5	25	*-1.5*	*-9*	*8.4*	*53*
40	**0.5**	**13**	**1**	**25**	-19.5	-29	30.5	45	-3	-30	2.9	29	-1.5	-9	8.9	56
50	1	25	1	25					***0***	***0***	***3***	***30***	**0**	**0**	**9**	**56**
60	1	25	1.4	35	-20.5	-30	31	46	0.5	5	3.5	35	1.5	9	10.9	68
70	1	25	1.4	35	-17.5	-26	31.5	47	1.5	15	4	40	1.5	9	11	69
80	1	25	3.4	85	-12.5	-19	32.5	48	2	20	4.9	49	1.5	9	14	88
90	1	25	3.4	85	-5.5	-8	33	49	2.5	25	6.9	69	1.5	9	15.9	99
100	1	25	4	100	-5.5	-8	67.5	100	2.5	25	10	100	1.5	9	16	100

Table 2.1. (Continued) Summary of the 16 Wadge eruption predictions.

	P. Fournaise Aug '04 61.5 days (p)				**P. Fournaise July '06 21.5 days (a)**				**P. Fournaise April '07 29 days (p)**				**P. Fournaise Oct '10 21 days (p**			
	Δt		Time since eruption onset		Δt		Time since eruption onset		Δt		Time since eruption onset		Δt		Time since eruption onset	
% data	days	%	days	%	days	%	days	%	days	%	days	%	days	%	days	%
10	-28.5	-46	20	33	-20.5	-95	2	9	***-2***	***-7.5***	***10.5***	***37***				
20					***-3***	***-14***	***4.5***	***21***	-7	-25	13	46	-12.5	-60	2	10
30	-27	-44	25	41	7	33	5.5	26	-7	-25	14.5	51	*-2*	*-10*	*4*	*19*
40	***-11.5***	***-19***	***27.5***	***45***	5	23	6	29	-6	-21	16.5	58	1	-5	5	24
50					7	33	10.5	49	-5	-18	20.5	72	**0**	**0**	**5.5**	**26**
60	-11.5	-19	43.5	71	8	37	14.5	67	-5	-18	21.5	75	1.5	7	8.5	40
70	-11.5	-19	47.5	77	8	37	15.5	73	-4.5	-16	23.5	82	2.5	12	12	57
80					10.5	49	16.5	77	-4.5	-16	27	94	3.5	17	15.5	74
90	-11.5	-19	54.5	89	12	56	20	93	-4.5	-16	28.5	99	3.5	17	16	76
100	-11.5	-19	61.5	100	12	56	21.5	100	1	1	29	100	3.5	17	21	100

CHAPTER 3

THE VOLUME OF LAVA ERUPTED DURING THE 2014 TO 2015 ERUPTION AT HOLUHRAUN, ICELAND: A COMPARISON BETWEEN SATELLITE- AND GROUND-BASED MEASUREMENTS

Published in Journal of Geophysical Research Solid Earth as: Bonny, E., Thordarson, T., Wright, R., Höskuldsson, A., & Jónsdóttir, I. (2018). The volume of lava erupted during the 2014 to 2015 eruption at Holuhraun, Iceland: A comparison between satellite- and ground-based measurements. Journal of Geophysical Research: Solid Earth, 123. https://doi.org/10.1029/2017JB015008.

Abstract

The 31 August 2014 to 27 February 27 2015 (180 days) eruption at Holuhraun created the largest lava flow field in Iceland since the 1783-1784 Laki eruption. Emplacement of a basaltic flow field of this magnitude onto an effectively flat surface (<0.1°) is a rare occurrence. Lava discharge rate, a fundamental variable that controls flow field emplacement, allows us to estimate the total volume of lava erupted when integrated over time. Thus, discharge rate data are important for volcano monitoring and lava flow modeling. Here we compare discharge rates estimated using data from NASA's MODerate Resolution Imaging Spectroradiometer (MODIS) and the method of Harris et al. (1997a, b, 2007), with estimates of discharge rates derived from comparing intermittent ground-based measurements of flow field volume. The Time-Averaged Discharge Rates (TADR) reveal a pulsed increase in the first few days of the eruption. Although the trends of the satellite- and ground-based discharge rates are similar, the ground-based estimates are systematically higher than the satellite-derived estimates (about two to three times higher) in the first 30 days of the eruption, and relatively close (within 30%) for the next 20 days. Conversely, during the final 130 days the satellite-based estimates are systematically higher than the ground-based estimates (about two times higher). This difference likely arises from the assumption of the lava flow surface temperature used in the space-based calculation, which may

not be entirely representative of this uniquely large and intense basaltic eruption. However, the satellite-based technique yields a total erupted volume of about 1.21 km^3, in remarkably good agreement with the 1.2 km^3 (84 km^2 lava flow field) derived from field observations and mapping.

3.1 Introduction

Constraining lava discharge rate is important to understand the dynamics of effusive eruptions (Wadge, 1981; Harris et al., 2000; Coppola and Cigolini, 2013) and is a critical input parameter for most lava flow modeling (Harris and Rowland, 2001; Wright et al., 2008). The use of satellite thermal remote sensing to estimate discharge rates is of great importance as it provides a near-real time data acquisition and thus improves volcano monitoring with a global view of the eruption site. The 2014-2015 eruption at Holuhraun on Dyngjusandur in North Iceland produced a basaltic lava flow field, with a volume in excess of 1 km^3 and covering 84 km^2 (Pedersen et al., 2017), making it the largest lava-producing eruption in Iceland since the 1783-1784 Laki event (volume, 15 km^3; area, 600 km^2; Thordarson and Self, 1993). To put this into perspective, the area covered by the 2014-2015 eruption almost equals the size of Manhattan Island, New York (87.5 km^2). As such, this event provides a unique opportunity to the volcanological community to observe the formation of an areally extensive and volumetrically substantial basaltic lava flow field emplaced on effectively flat ground (<0.1° slope). To retrieve lava discharge rates from space, we chose the method of Harris et al. (1997) based on the 1991-1993 eruption at Mount Etna. They found that satellite measurements of eruption rate and flow volume were in agreement with ground-based data. However, this eruption was a much smaller eruption than Holuhraun and relied only on ten field-based discharge rates over 1.5 years. Therefore, testing that this method can also be applied to larger eruption, and yields discharge rates and a final flow volume in agreement with ground-based measurements, is a principal goal.

The 2014-2015 lava-producing eruption at Holuhraun (Figure 3.1) was preceded by an increase in seismicity at and north of the Bárðarbunga central volcano in mid-August. One of the seismic swarms propagated 7.5 km to the southeast away from Bárðarbunga (Ágústsdóttir et al., 2016). Fifteen hours later a new seismic swarm began 3 km to the east of the location where the

southeast migrating seismic swarm had ended. This new swarm migrated to the north-northeast over a distance of 42 km (Sigmundsson et al., 2015; Gudmundsson et al., 2016). Around 05:00 on 31 August 2014 lava began to pour from a 1.8-km-long fissure that had opened up along the cone row of the 1797 CE Holuhraun eruption (= Holuhraun I event), coinciding with the northern terminus of the north-northeast seismic swarm.

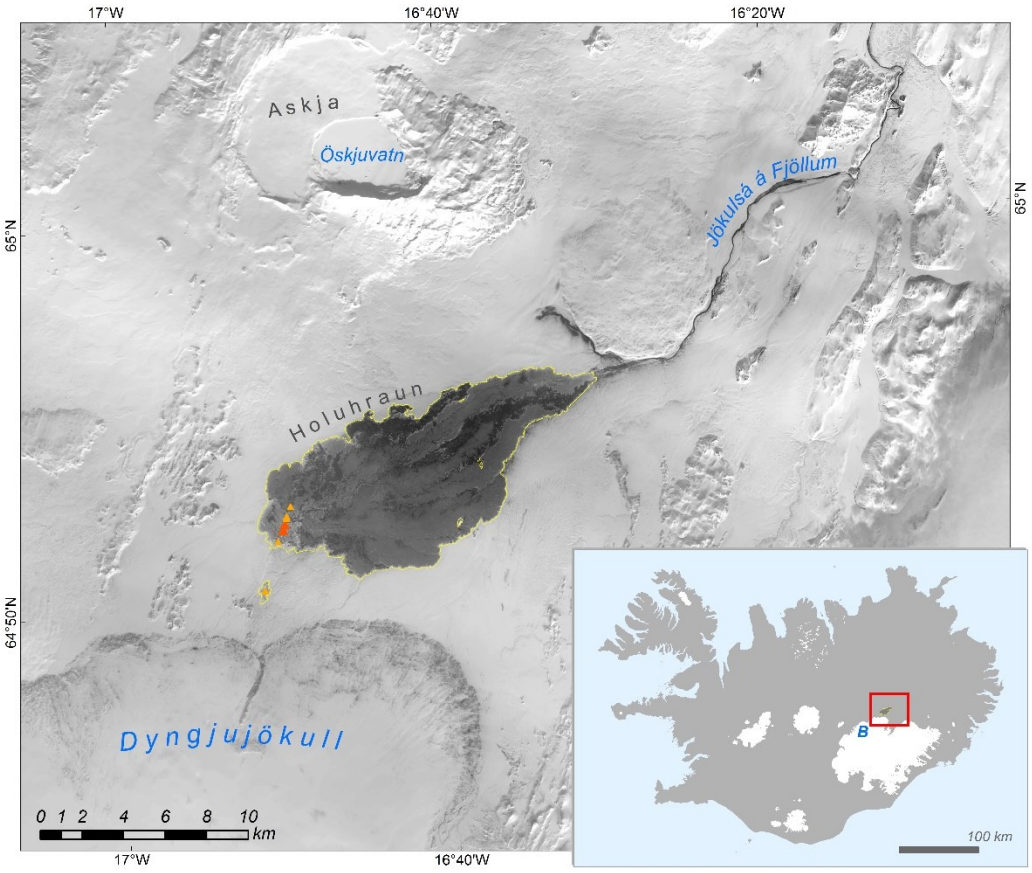

Figure 3.1. Outlines of the 2014-2015 Holuhraun lava flow field at the end of the eruption are represented in yellow. The different volcanic vents are shown with triangles, and the main vents that were active the longest, which merged into one, are colored in red. Background based on a Landsat 8 satellite image from USGS/NASA and a base from the National Land Survey of Iceland (IS50V lmi.is). The inset shows Iceland with the location of Bárðarbunga central volcano (B) and the eruption site.

The erupting fissure was located 18 km south of the Askja central volcano and 40 km to the northeast of the Bárðarbunga central volcano. Although the eruptive fissure opened on the

southern segment of Askja fissure swarm, the magma composition (Sigmarsson and Halldorsson, 2015) implied a Bárðarbunga system affinity, similar to its predecessors the Holuhraun I and Holuhraun II (circa 1867 CE) events (Hartley and Thordarson, 2013). The Volcanology and Natural Hazard Group of the Institute of Earth Sciences, at the University of Iceland, and the Iceland Meteorological Office monitored on a daily to weekly basis a number of eruption source parameters for the duration of the eruption (six months). Monitoring of the eruptive activity included measurements of the flow field growth (i.e., area and thickness) and mapping of lava types (e.g., Pedersen et al., 2017), the nature of the volcanic tremor (Eibl et al., 2017), seismicity and deformation (e.g., Sigmundsson et al., 2015; Gudmundsson et al., 2016), volcanic gas emissions and their environmental impact, as well as comprehensive petrological investigations (e.g., Gíslason et al., 2015; Hartley et al., 2018; Bali et al., 2018). However, in this study we are only concerned with the flow field area and thickness (detailed in the next section), the most relevant parameters to estimate lava discharge rates from the field. The eruption was also well monitored from space, by a variety of remote sensing instruments such as MODIS (MODerate Resolution Imaging Spectroradiometer; ~four times/day), Landsat 8 (once every 16 days), and Synthetic Aperture Radar (Sentinel-1, RADARSAT-2 and COSMO-SkyMed), documenting the extent and spreading of the lava as well as the amount of thermal energy it radiated (Table 3.1). In our case, we focused on MODIS thermal infrared (TIR) data to measure and build a time series of lava discharge rates. The high-latitude location of Iceland allows acquisition of more satellite images than at the equator, which makes it complementary to ground-based measurements. This large and intense basaltic eruption is a valuable opportunity for case study due to the wide range of data acquired both remotely and in the field.

In this chapter, we present results obtained from satellite thermal remote sensing and measurements of the flow field geometry at particular times during the eruption, each dictating how the magma discharge varied during the 2014-2015 eruption at Holuhraun. These types of measurements have been carried out successfully on smaller flow fields, and therefore, a study of well-documented large volume effusive eruption is a good test case for the robustness of the thermal remote sensing method. The main objectives are to i) estimate the time-varying discharge rate, using satellite and ground-based measurements; ii) use this to estimate the final volume of lava erupted; iii) illustrate the correspondence (and noncorrespondence) of TADR

estimates made using these two different techniques and discuss their origins; and iv) identify the nature of the time versus discharge rate relationship to establish whether the temporal evolution of lava discharge during this eruption matched that of similar large eruptions in the recent past.

Table 3.1. Detailed information about the satellite images used in our study.

Radar images		
Sentinel-1[a]	6, 8, 13, 23, 25, 27, and 30 October 6, 11, 18, 20, 23, and 30 November 5, 12, 17, 22, 24, and 29 December 3, 5, 7, 10, 15, 17, 22, 24, 29, and 31 January 3, 5, 10, 12, 15, 17, 22, and 27 February	
RADARSAT-2[b]	1 January 2015 and 1 March 2015	
COSMO-SkyMed[c]	30 September 2014 and 1 November 2014	
MODIS	**Terra**	**Aqua**
Launched	December 1999	May 2002
Altitude	705 km	
Equatorial crossing time	10:30 descending orbit	13:30 ascending orbit
Complete coverage	Every 24 hour at the equator	
Scan angle from nadir	+/- 55°	
Swath width	2330 km	
Pixel size in the TIR	1x1 km at nadir, 2x4.8 km at the edge of the swath	
Band 31 Saturation	130°C	70°C
Band 31 NEΔT	0.05°C	

[a] Images freely available for download at the Sentinel Data Hub
[b] Images ordered through KSAT in Tromso, Norway
[c] Images from collaboration with the Institute of Earth Sciences group (Freysteinn Sigmundsson - Iceland Super Site).

3.2 Data description

3.2.1 Ground-based measurements: flow field geometry

On-site observations on the extent and thickness of lava flow field were obtained from accurate georeferenced positioning of the flow field margins along with systematic flow thickness measurements. For the first two weeks of activity (until 15 September 2014), the Icelandic Coast Guard flew over the flow field, and both LANDSAT-8 and EO-1 images were acquired, supporting the field observations and allowing the entire flow field to be mapped. The

position of the flow margins was determined by a Global Positioning System (GPS) mounted on 4 × 4 vehicles that were driven along the flow margins to outline the aerial growth of the lava on a daily basis. When high-resolution satellite-derived visible, radar and thermal images became more readily available, they were used to determine the outlines of the flow field, and its evolution in space and time, and to verify the earlier on-site mapping of flow margins (e.g., Pedersen et al., 2017).

The on-site thickness measurements were obtained in three ways: (a) by direct thickness measurements of the flow margins that were carried out for the duration of the eruption, including several topographic profiles taken perpendicular to the flow margins to a point where the lava surface became level; (b) by occasional theodolite-based thickness measurements of the flow margins and the flow interior at specific locations; and (c) on one occasion using shadow-lengths on a satellite radar image in conjunction with simultaneous on-site measurements. During the first fifteen days of the eruption, the first lava flow was actively growing via inflation and did not manifestly change after that (Table 3.2). Therefore, we derived a sensible mean thickness for the lava flow field, which for the bulk of the eruption was ~17 m (= 14 m when calculated as Dense Rock Equivalent, DRE). The obtained lava flow area multiplied by the mean DRE flow thickness (14 m thick for all eruption except the 14 first days) yields an estimate of the volume of erupted lava, and we have measurements at 33 occasions over the 6-month long eruption. The combination of thickness measurements, GPS tracking and satellite and airplane imagery allows for lava flow field geometry reconstitution and forms our ground-based measurements.

Table 3.2. Summary of the ground-based thickness measurements during the eruption with the time of day when available.

Date	Time (UTC)	Thickness (m) DRE
31 August 14	5:15	0
1 September 14	6:18	4
1 September 14	14:00	5
2 September 14	14:00	7
3 September 14	14:53	9
4 September 14	18:22	11
5 September 14	15:00	11.5
6 September 14	17:38	12
7 September 14	13:00	12.75
7 September 14	19:40	13
11 September 14	18:00	14
15 September 14	7:31	14
17 September 14	18:40	14
20 September 14		14
26 September 14		14
30 September 14		14
7 October 14		14
10 October 14		14
17 October 14		14
19 October 14		14
23 October 14		14
31 October 14		14
9 November 14		14
15 November 14		14
20 November 14		14
26 November 14		14
30 November 14		14
11 December 14		14
12 December 14		14
18 December 14		14
29 December 14		14
4 January 15		14
27 February 15		14.34

3.2.2 MODIS thermal infrared satellite data

Remote sensing observations are based on the MODIS instrument carried by NASA's Terra (launched in December 1999) and Aqua satellites (May 2002). MODIS makes measurements in 36 spectral bands from visible to thermal infrared (TIR) wavelengths (Table 3.1). For lava flow studies, we are interested in the latter to make measurements of thermal emission. At the equator, one satellite achieves complete coverage of the Earth every 48 hours but this temporal resolution is improved by having two near-identical sensors on two satellites in different orbits, yielding a complete coverage of the Earth's surface every 24 hours. At high latitudes (>50°), adjacent swaths start having significant overlap, and in the case of Iceland, it means that each MODIS instrument could acquire an image of the lava flow field four to five times every 24 hours (Masuoka et al., 1998). This implies that lava discharge rate could potentially be calculated between eight and ten times per day if highly radiant lava flow surfaces were detected. We found that we had observations ranging from 1 to 8 times every 24 hours for this eruption. Although MODIS has a spatial resolution of 1 km² at nadir (making it of limited value for mapping lava flows), its temporal resolution makes it a good tool to estimate TADR, allowing to track its temporal changes. MODIS also provides a synoptic view of the entire flow field (instead of only a certain part of the flow, which is usually the case with field measurements), thanks to its wide image swath of 2330 km. This is due to its large scan angle of +/-55°, which increases the size of one pixel (A_{pixel}) from 1 km² at nadir to almost 10 km^2 at the edge of the swath (2 × 4.8 km) and this was accounted for in our data processing.

The MODVOLC algorithm (Wright et al., 2002, 2004; Wright, 2015; http://modis.higp.hawaii.edu) detects and quantifies thermal anomalies indicating high surface temperatures on Earth's surface. This freely available and downloadable database was used here to discern this Icelandic lava flow and estimate lava discharge rate based on the measured spectral radiance at a given wavelength λ (L_λ, W m^{-2} sr^{-1} μm^{-1}). For each 1 km² patch of ground identified as containing active lava hereafter called "anomalous" pixel, the emitted spectral radiance is recorded in five bands (Bands 21, 22, 6, 31 and 32). The MODVOLC algorithm "flags" a pixel to be anomalous if it exceeds a certain Normalized Thermal Index (NTI) value, which is defined as the ratio of the radiance $(L_4-L_{12})/(L_4+L_{12})$, but more simply it detects surfaces that are anomalously hot (hotspots). More information on the exact time and date of

acquisition in UTC, the satellite geometry (satellite zenith and azimuth) and geographic location of the pixel is also included in an ASCII text file on the MODVOLC website platform.

3.3 Methods

In the case of remotely-sensed measurements, the discharge rate computed is representative of the effusion rate that prevailed over some period of time prior to satellite overpass (Wright et al., 2001a; Harris and Baloga, 2009), called Time-Averaged Discharge Rate (TADR), and not the instantaneous effusion rate (Harris et al., 2007). Intermittent estimates from field-based surveying techniques can also be used to deduce TADR, which we report here for the ground-based data. Lava discharge rate changes during an eruption, but a single value called the mean output rate can be estimated at the end of the eruption where the final flow volume is divided by the entire period of eruption. Such values are used to compare eruption intensities around the world.

3.3.1 Space-based lava discharge rate retrievals, $TADR_{MOD}$

Time-averaged discharge rates from satellite measurement, $TADR_{MOD}$, are computed based on the spectral radiance recorded by MODVOLC. We used the approach that was derived from Harris et al. (1997a, 1997b, 2007) with the work of Wright et al. (2001a) and also referred to as the coefficient method. In Figure 3.2, a schematic of the method used is shown, as well as the streak of white pixels trending left to right that denotes the 2014-2015 lava flow field at Holuhraun (the bright pixels are those that contain active lava, the high temperature of which yields elevated spectral radiance for these ground targets). To replicate the method of Harris et al. (1997a, 1997b), we used MODIS band 31 with a central wavelength of 11 μm (10.78 - 11.28 μm**)**. Saturation in the TIR occurs when the presence of highly radiant surfaces overwhelms the capacity of the detectors. Band 31 saturates at an integrated temperature of about 130°C for Terra and 70°C for Aqua with a small noise equivalent temperature variation ($NE\Delta T = 0.05$), and we found that we reached these temperatures at Holuhraun with the Aqua instrument (presence of saturated pixel) but not the Terra instrument. The measured MODVOLC spectral radiance at a wavelength $\lambda = 11$ μm for each anomalous pixel, $L11_{MOD}$, is the at-satellite radiance. $L11_{MOD}$ needs to be corrected for atmospheric effects, both from upwelling radiance $Lu(\lambda)$ and

transmittance $\tau(\lambda)$ ($Lu(\lambda)$ is 0.009 W m^{-2} sr^{-1} μm^{-1} and $\tau(\lambda)$ is 0.87 taken from a standard MODTRAN (Moderate Resolution Atmospheric Transmission) U.S. atmosphere following Harris, 2013), and for the emissivity of the target $\varepsilon(\lambda)$ (0.989 for basaltic lava; Harris et al., 1997a).

$$L_{11,\ cor} = \frac{L11_{MOD} - Lu(\lambda)}{\tau(\lambda)\varepsilon(\lambda)} \quad (3.1)$$

One 1 km² MODIS pixel may not be completely filled by the active lava flow, and so will also contain ground radiating at an ambient background temperature. As a result, the spectral radiance detected from such a pixel is a weighted average of the radiance emitted from the active lava and that emitted from the adjacent ground. This mixed pixel spectral radiance can be defined where one pixel is composed of two radiating components, the active lava surface occupying a fraction f of the pixel and the colder background occupying the corresponding (1-f) pixel fraction (Figure 3.2, inset):

$$L_{11,\ cor} = f\ L(\lambda, T_{lava}) + (1 - f)L(\lambda, T_{back}) \quad (3.2)$$

where f is the fraction of active lava surface in a single pixel, T_{lava} is the temperature of the active lava surface and T_{back} is the background temperature. As a result, the fraction of active lava within each pixel can be estimated by using

$$f = \frac{L_{11,\ cor} - L(\lambda, T_{back})}{L(\lambda, T_{lava}) - L(\lambda, T_{back})} \quad (3.3)$$

There are two unknowns, $L(\lambda, T_{back})$ and $L(\lambda, T_{lava})$. T_{back} is typically estimated by finding lava-free pixels adjacent to the flow in the remote sensing image. However, if such pixels are cloud contaminated (and subpixel clouds are very difficult to identify), T_{back} can be too low, causing f to be too high. Thus, we adopt a different approach for estimating T_{back} following Wright et al. (2015). The MODIS Land Surface Temperature (LST) product (MOD11C3 and MYD11C3 for Terra and Aqua, respectively) provides monthly estimates of ground surface temperature for every 0.05° latitude/longitude (a pixel is 5.6 × 5.6 km at the equator), by compositing each individual MODIS image acquired by each MODIS sensor in each calendar month pixel by pixel. These data are screened for cloud contamination. To derive a robust estimate of T_{back} (i.e., the ambient temperature of the ground at Holuhraun in the absence of

active lava), we used ten years' worth of these monthly LST products to derive the decadal average background temperature at Dyngjusandur.

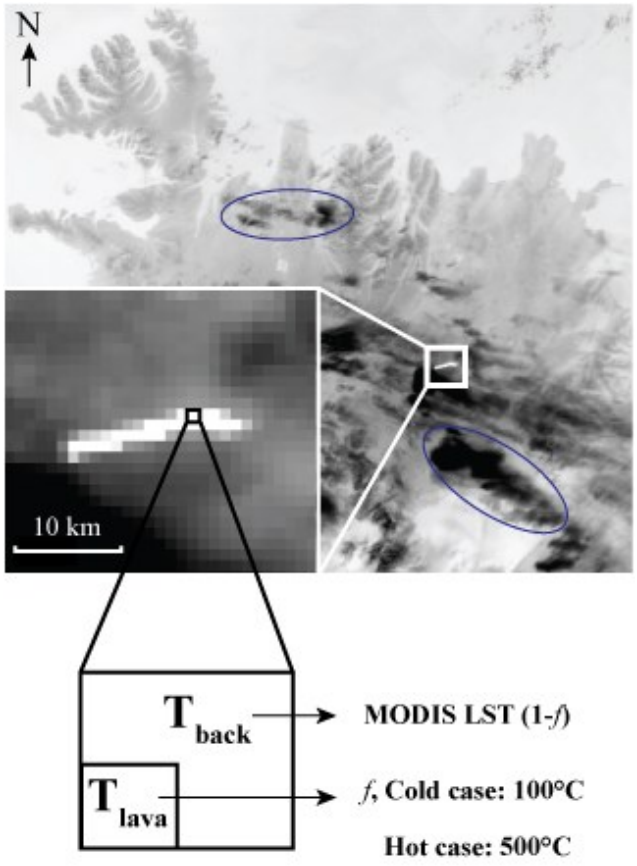

Figure 3.2. MODIS Terra image band 31 (11µm) of Bárðarbunga eruption on 12 September 2014 at 22:35 UTC. The bright pixels show the location of anomalous pixels; in this case it corresponds to active lava flows, at the time of acquisition coming from the Holuhraun fissure (flows from west to east). We highlight the presence of black opaque clouds in this image using dark blue circles. The scheme below shows the two main sources of radiance coming from a single anomalous pixel and summarizes the data used in each case.

Therefore, we compiled a different T_{back} value for each calendar month, day and night, each instrument, and utilize the corresponding value for our TADR calculation. In Table 3.3, we show the results for the Terra instrument and we can see that the surface temperatures vary only slightly over the 10 year period we looked at (the standard deviation is smaller than the seasonal variation and makes this method reliable).

Table 3.3. Background temperature defined for Holuhraun in the case of Terra instrument averaged over a 10-year period (2001-2010) in degrees Celsius. The results for the Aqua instrument are very similar and we chose not to show them here.

	Terra nighttime		Terra daytime	
	Mean	Standard deviation	Mean	Standard deviation
January	-12.75	1.63	-12.45	2.18
February	-13.05	3.4	-10.95	3.02
March	-11.95	2.98	-8.75	3.47
April	-9.55	2.05	-2.85	2.45
May	-6.95	1.52	2.65	2.75
June	-2.55	1.46	15.75	6.38
July	-1.35	1.58	19.95	2.72
August	-1.65	1.39	13.85	4.65
September	-4.15	1.73	2.55	3.01
October	-8.85	2.14	-6.25	1.48
November	-11.55	1.9	-11.05	1.56
December	-11.45	1.72	-11.45	1.47

For the second unknown T_{lava}, a large number of studies (Harris et al., 1997a, b, 1998, 2000; Harris and Neri, 2002) looking at small basaltic eruptions use a lava surface temperature of 100 and 500°C to represent the upper and lower average surface temperatures. These assumed temperatures yield satellite-derived discharge rates that are consistent with ground-based measurements. For a given pixel, when using T_{lava} as 100°C, hereafter referred as the "cold case", the estimate of active lava area will be higher than the area calculated assuming T_{lava}=500°C, hereafter referred as the "hot case". This is because a larger area of "cool" lava is required to generate the same at-satellite spectral radiance than a smaller area of "hot" lava. Following Planck's law, we converted this temperature to radiance to use in our pixel-mixture model

$$L(\lambda, T) = c_1 \lambda^{-5}[(\exp(c_2/\lambda T) - 1)]^{-1} /10^6 \quad (3.4)$$

in W m^{-2} μm^{-1} sr^{-1} where c_1 and c_2 are constants; $c_1 = 2hc^2 = 1.19 \times 10^{-16}$ in W sr^{-1} m^{-2} and $c_2 = hc/k = 1.44 \times 10^{-2}$ in m K, λ is the wavelength in μm, T is the temperature in Kelvin, h is Planck's constant, c is the speed of light, and k is the Boltzmann constant.

The area of active lava (A_{lava}) within each thermally anomalous MODIS pixel can then be calculated using $A_{lava} = fA_{pixel}$ with A_{pixel} being the pixel size. Summing for each thermally anomalous pixel detected at each unique observation time (i.e., within each image) yields an estimate of the active lava area at that time. From the active lava area, and for each anomalous pixel detected at each satellite acquisition, we can estimate the lava discharge rates from the following linear relationship between the area of active lava with a coefficient X (Wright et al., 2001a; Harris, 2013).

$$TADR_{MOD} = X\, A_{lava} \tag{3.5}$$

where $X = [\varepsilon\sigma(T_{lava}^4 - T_{back}^4) + h_c(T_{lava} - T_{back})]/\rho(C_p\Delta T + \Phi C_L)$ (3.6)

in which ε is the emissivity of the target surface, σ is the Stefan-Boltzmann constant, h_c is the convective heat coefficient, ρ is the lava density, C_p is the lava specific heat capacity, ΔT is the difference between the temperature at which lava erupted and the temperature at which the flow ceased to flow, Φ is the average crystal fraction grown in cooling through ΔT, C_L is the latent heat of crystallization and T_{back} is the background surface temperature. Coefficient values are hard to define, and Harris et al. (2007) presented coefficients for a limited group of volcanoes covering the felsic to mafic compositional range. We thus decided that the value for Etna and Krafla volcanoes was likely applicable to Bárðarbunga knowing that the flows erupted at each are mafic (Hartley et al., 2018; Harris et al., 2000). The coefficient X we used here defined for Etna and Krafla volcano is between 2.1 and 33 × 10^{-6} m/s. The lower coefficient value was used with the larger area estimate (from the cold case) and the higher coefficient value with the smaller area estimate (from the hot case). The higher coefficient yields higher estimates of discharge rate ($TADR_{MOD}$ high) than the lower coefficient ($TADR_{MOD}$ low), even though the area computed is smaller. We were able to make estimates of $TADR_{MOD}$ on 866 occasions during the 180 days of the eruption at Holuhraun (anomalous pixels were detected every day except on 10 occasions), from which our time series is constructed, documenting the entire duration of the flow field formation.

The measurement of the spectral radiance L_λ recorded by MODVOLC is very precise; however, using satellite data introduces some uncertainties in the retrieval of lava discharge rate. There are three main sources of uncertainty (in order of importance): i) presence of clouds above the target, ii) the satellite zenith angle, and iii) saturation of the band of interest. First, cloud contamination is known to be an inherent problem for infrared time series using low spatial resolution data. Visual examination would allow identification of completely cloud covered pixels above the lava flow field, but not subpixel clouds or transparent ash and gas plumes. MODIS has a cloud mask product that unfortunately does not perform well over bare rock surface such as lava flow fields (Koeppen et al., 2011). The presence of cloud, above all, or a small part of an active lava flow, can produce a "dip" in the spectral radiance measured from space and therefore a low TADR. We indeed notice that 90% of the very low values of TADR in our time series (<1 m^3/s) are contaminated by opaque clouds (black clouds in Fig. 3.2). Second, an increase in satellite zenith angle can also produce lower value of spectral radiance (Harris et al., 1997a; Coppola et al., 2010) and affect the TADR time series with anomalously low values, although we minimize this by using the area of the pixel corresponding to the satellite zenith angle. Both clouds and large satellite zenith angles are responsible for very low radiance values in part of our dataset, and we therefore decided to only use a subset of the data for the rest of this paper using the peak TADR (explained in more detail in the next section). Finally, the saturation of the instrument at certain wavelengths can also introduce some errors in the estimation of lava discharge rate. Each wavelength saturates at different temperatures (as mentioned earlier), and if the surface radiates energy that is higher than the limit of the detectors, the spectral radiance detected reaches its maximum possible value. Therefore, the calculated lava discharge rate is a minimum and underestimates the true value. In our case, the 11 μm radiance rarely saturates (only found with Aqua sensor due to its lower saturation limit) and in cases when it does sature, we use the maximum possible radiance value to estimate the lava discharge rate, knowing that it is an underestimate.

3.3.2 Flow field volume determinations

The bulk volume of the 2014-2015 lava flow field is obtained by differencing the pre- and post-eruption digital elevation models (based on aerial photographs from before (2013) and

after (2015) the eruption with an approximately 1-m-resolution; Höskuldsson et al., 2016; Jónsdóttir et al., 2016). The daily to weekly ground-based dataset (i.e., lava area and thickness) is used to calculate the flow field volume at any given time during the eruption. However, pristine lava contains voids. In case of ʻaʻā and rubbly pāhoehoe dominated flow fields, such as that of 2014-2015 at Holuhraun, the voids are both air-filled space between clasts in the flow-top and basal rubble, as well as in vesicles within the rubble clasts and the top portion of the coherent lava. On-site field observations indicate that on average, up to a quarter to one third of the flow thickness contains about 60% voids and vesicles, which implies that in bulk the flow field has between 15 and 20% of void space. Hence, the dense rock equivalent (DRE) volume for the 2014-2015 Holuhraun lava flow field is obtained by multiplying the bulk volume by factors of 0.8 to 0.85. The difference between two DRE volume estimates divided by the time elapsed between them gives the ground-based time-averaged discharge rate ($TADR_g$) with an estimated error of 15% arising from both lava thickness and void space estimates.

The satellite-based volume of lava erupted can be obtained by integrating the area under the curve of lava discharge rates against time. As mentioned in the previous section, clouds, which partially obscure the active flow field from the sensor, can result in a reduction in spectral radiance L_λ below that which was actually emitted by the lava surface. Integrating the area under the entire cloud-contaminated $TADR_{MOD}$ time series underestimates the lava volume. Therefore, we only used the peak values in the discharge rate time series to compute lava volume. Peaks in our $TADR_{MOD}$ estimates were found by identifying the local maxima in the data and then retaining only those peaks that were *n* sigma (*nsig*) above the standard deviation of all peaks in the time series. We found that one *nsig* usually identifies correctly the most important peaks in the lava discharge rate data, where the peaks identified are all above 46 and 75 m^3/s for the cold and hot cases, respectively. Out of the 866 scenes investigated in this study, a total of 46 peak values of $TADR_{MOD}$ were identified (red and green symbols in Figure 3.3) and it is this subset of data that we used to estimate the final flow field volume. The volume was then estimated by integrating the area under the peaks starting at the first MODIS acquisition point (31 August at 12:30 UTC) and stopping at the last MODIS acquired point (21 February at 12:45 UTC) using a trapezoidal summation ($(t_2-t_1)\times[(TADR_2+TADR_1)/2]$). The volume estimated from those

discharge rates is a dense rock equivalent (DRE) volume that corresponds to the total volume of lava produced without including void spaces.

3.4 Results

One can note that the onset of the eruption is detected at slightly different times with satellite- or ground-based measurements. The first anomalous pixel recorded by MODIS is on 31 August at 12:30 UTC, but field measurements estimated the start of effusion more than seven hours earlier that day (05:15 UTC). A gap in satellite acquisition between ~5:00 and 12:00 UTC might be responsible for this delay. The eruption was continuous until 27 February 2015; however, MODVOLC only detected hot spots up until 21 February 2015. The $TADR_{MOD}$ observations identified as "peaks" (red and green symbols in Figure 3.3) were used to calculate a total erupted volume of 0.7 km^3 to 1.21 km^3 (cold and hot cases, respectively), which yields a mean output rate of 46.5 m^3/s and 80.5 m^3/s (based on 174 days with MODIS). The total bulk volume for the flow field estimated from the ground-based measurements (i.e., DEM difference) is 1.44 km^3 (Höskuldsson et al., 2016; Jónsdóttir et al., 2016). The corresponding DRE volume for the 2014-2015 Holuhraun lava flow field is 1.2 ± 0.1 km^3 (assuming mean bulk lava void space of 15 to 20%). The range in DRE volumes obtained here is in good agreement with the volume calculated for the hot case using MODIS. This yields a mean output rate for the entire eruption of ~80 m^3/s, which compares well to the remote sensing retrieved value.

3.4.1 Comparison of the performance of the two techniques

3.4.1.1 Time-averaged discharge rates

In Figure 3.3, we see that TADR from both space- and ground-based measurements generally follow the same pattern of increase and decrease although individual peaks and troughs do not match perfectly. The slight differences in their positions can happen for several reasons: a) the temporal resolution is different between the two methods, with the satellite-based method having a higher resolution (maximum of eight observations per 24 hour) than field measurements; b) the measurement frequency in both data series is variable, and therefore,

TADR can represent different time periods. Weather and accessibility can hamper ground-based observations, and hotspot satellite detection can fail if the scene is completely filled by clouds; c) the space-based measurements are easily underestimated due to partial cloud or plume cover, as well as d) saturation of the band detectors over highly radiant surfaces.

Figure 3.3b focuses on the comparison of TADRs from both methods, and we concentrated on the first 50 days of the eruption in the inset. We first discuss ground-based estimates ($TADR_g$) and then describe the results from space ($TADR_{MOD}$). This is followed by a more comprehensive consideration of the different pulses over time (black arrows). The first maximum in $TADR_g$ detected is 1.5 days after the eruption begins (270 ± 40 m^3/s) and is stable for a day before rising to 405 ± 60 m^3/s on day 3. It dropped to 375 ± 55 m^3/s a day later before a new pulse (peak and trough) is visible on days 5 and 6, with 490 ± 75 m^3/s and 370 ± 55 m^3/s, respectively. The maximum $TADR_g$ for the entire eruption is reached on day 8 of the eruption, in the evening of 7 September, when the discharge rate was 560 ± 85 m^3/s. Then the rate dropped over a period of a week to a new low of 30 ± 5 m^3/s on day 15 of the eruption, and at this point, the eruption almost stopped (http://www.vedur.is/skjalftar-og-eldgos/frodleikur/greinar/nr/2996#sep12). This change is linked to termination of the flow 1 advance around 15 September and onset of flow 2 in the days that followed (Pedersen et al., 2017). On day 20, the $TADR_g$ rose again to 440 ± 65 m^3/s and then slowly decreased in the next 30 days to 130 ± 20 m^3/s.

Concentrating now on the satellite-based peak $TADR_{MOD}$ estimates for the hot case (T_{lava}=500°C values are closer to the ground-based estimates early in the eruption), we notice that the first peak is reached on day 2 with 115 m^3/s and slightly rises to 120 m^3/s on day 5. It then decreases to about 100 m^3/s a day later before $TADR_{MOD}$ increased again to reach the maximum. This maximum $TADR_{MOD}$ was attained on 9 September 2014 at 03:00 UTC, about a day after the maximum that was detected in the field, with a value of 216 m^3/s. A new pulse is visible on days 11 and 12, with a peak up to 140 m^3/s and again on days 16 to 20 (peak at 145 m^3/s). After that, the estimated $TADR_{MOD}$ stays relatively constant around 95 m^3/s until a new pulse appears on days 30-32 with a peak at about 150 m^3/s. It then again slowly rises until a new high is attained on day 50 when both ground and space TADR estimates are almost the same at ~130 m^3/s.

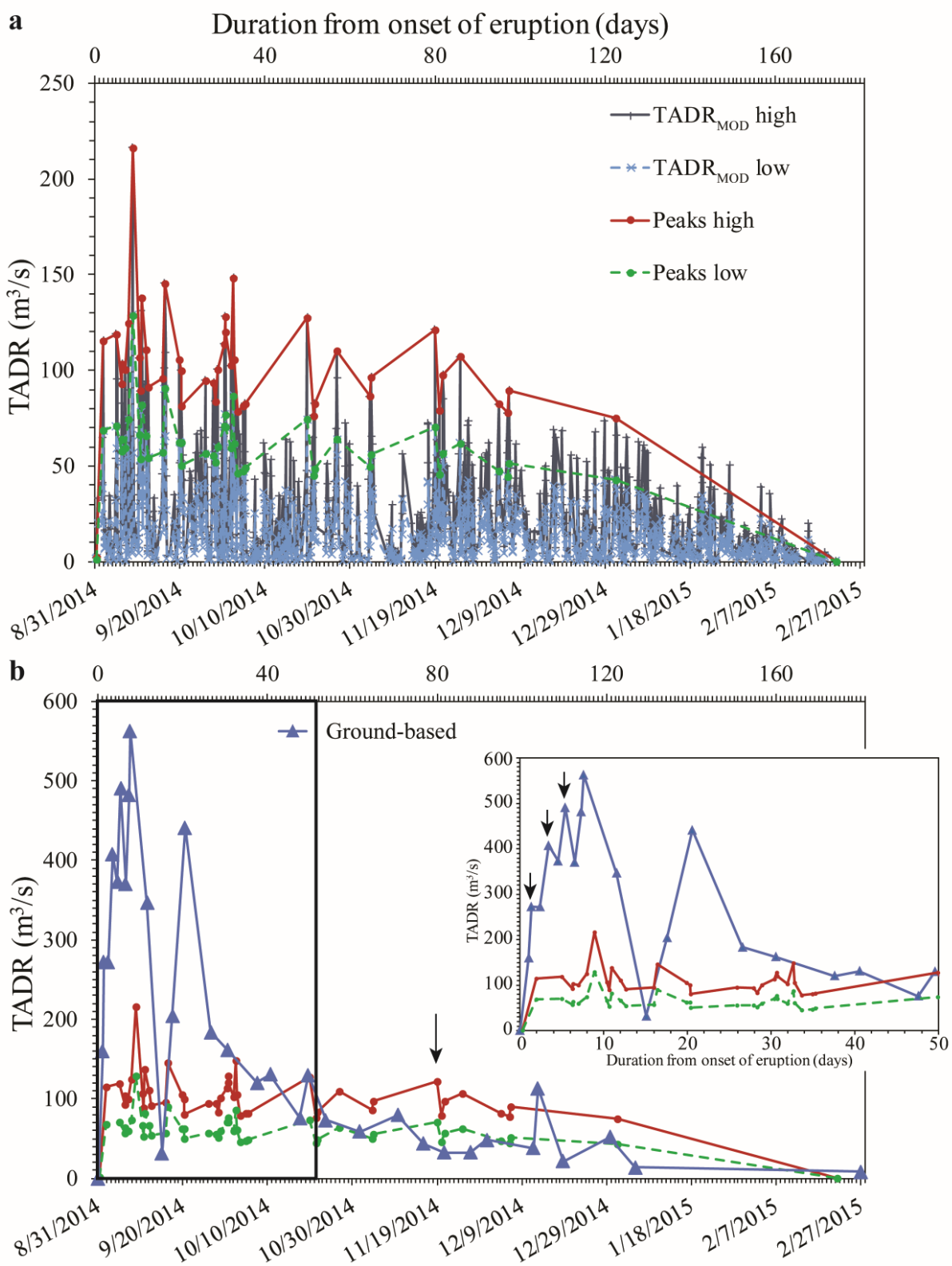
a
Duration from onset of eruption (days)
0
40
80
120
160
250
200
150
100
50
0
TADR (m³/s)
TADR_MOD high
TADR_MOD low
Peaks high
Peaks low
8/31/2014
9/20/2014
10/10/2014
10/30/2014
11/19/2014
12/9/2014
12/29/2014
1/18/2015
2/7/2015
2/27/2015
b
0
40
80
120
160
600
500
400
300
200
100
0
TADR (m³/s)
Ground-based
600
500
400
300
200
100
0
TADR (m³/s)
0
10
20
30
40
50
Duration from onset of eruption (days)
8/31/2014
9/20/2014
10/10/2014
10/30/2014
11/19/2014
12/9/2014
12/29/2014
1/18/2015
2/7/2015
2/27/2015

Figure 3.3. a) Satellite-based lava discharge rates from the 2014-2015 eruption at Holuhraun estimated with the low and high coefficient values (in light blue and black, corresponding to the cold and hot cases, respectively) with the identified peaks in discharge rate (one *nsig* criterion; in red and green curves). b) TADR results from both satellite- (red and green curves) and ground-based (dark blue curve) data with the black box being the focus of the inset zooming in the first 50 days of the eruption (notice the different y-axis scale). We only showed the peak TADR from both high and low coefficients to facilitate comparison with the ground-based values. In both graphs the onset of the eruption is taken on 31 August at 05:15 UTC, as detected from the ground; the secondary x-axis shows the number of days since the start of the eruption; the blue triangles are lava discharge rates from field measurements and were corrected to be DRE discharge rates. The black arrows highlight pulses in TADR.

We can now compare the different TADRs from both methods highlighting the key differences. Starting with day 2, MODIS underestimates the initial peak in discharge from field observations (115 m^3/s compared to 270 m^3/s), due to a storm-like cloud atop Iceland hiding the highly radiant lava flow. Second, a peak in $TADR_{MOD}$ was not recorded during the ground-based observations on days 3 and 4 because the flow is partly obscured by the eruptive plume and clouds. Generally, aside from an offset between the two TADR, they both follow the same step-like increase somewhat concurrently until the maximum discharge rate was reached on days 8-9. Third, the high ground-based discharge rates on days 18 and 20 (205 and 440 m^3/s, respectively) were not detected by MODIS, due to cloudy conditions and pixel saturation, respectively. Five pixels in the 11 μm band were saturated, which happens only in very rare occasions, resulting in a probably large underestimation of the $TADR_{MOD}$ on that date. For the first 30 days of the eruption, we see that the $TADR_g$ values are two to three times higher than $TADR_{MOD}$, except on day 15 when $TADR_g$ is exceptionally low in this early stage and is only partly captured by the satellite observations (Fig. 3.3). Finally, from day 30 onwards, the correspondence between the ground-based dataset and the space-based hot case TADR improves and the estimates are relatively close (within ~30%).

Overall, the hot case $TADR_{MOD}$ estimates are closer to the ground-based measurements for the first 50 days (although still producing underestimates it in the first 30 days or so), and

then the cold case estimates provide better agreement with ground-based measurements for the rest of the eruption. Notable features are stepwise (or pulse-like) rather than smooth gradual changes in the discharge rate to reach a maximum in the first 8-9 days of the eruption. The broad rise in the middle of the eruption as seen with a peak in $TADR_{MOD}$ on 19 November at 120 m^3/s (hot case) is not captured by the ground-based measurements.

3.4.1.2 Volume of erupted lava

Figure 3.4 shows the cumulative volume for the entire eruption from both ground-based measurements and satellite thermal infrared data (only from the identified peaks in red and green in Figure 3.3). For the entire eruption, the ground-based estimates are higher than those obtained from MODIS (typically two to three times higher for the hot case estimates (T_{lava}=500°C), and about four times higher in terms of the cold case for the first 50 days). It is only at the last MODIS acquisition that the space-based estimate meets the ground-based measurements and becomes slightly higher. The volume of the flow field detected from the ground exhibits a sharp increase in $TADR_g$ after day 15, which is not discernable in the satellite-based data, arising from the very low discharge rate on this day (30 m^3/s). The total volume for this eruption from ground-based measurements (1.2 km^3 DRE) is almost exactly the same as the total DRE volume calculated from space with the hot case (1.21 km^3) but 40% higher than the DRE volume based on the cold case (0.7 km^3). The total DRE volume shows that the space-based estimate calculated with the hot case is closer to that taken from the ground.

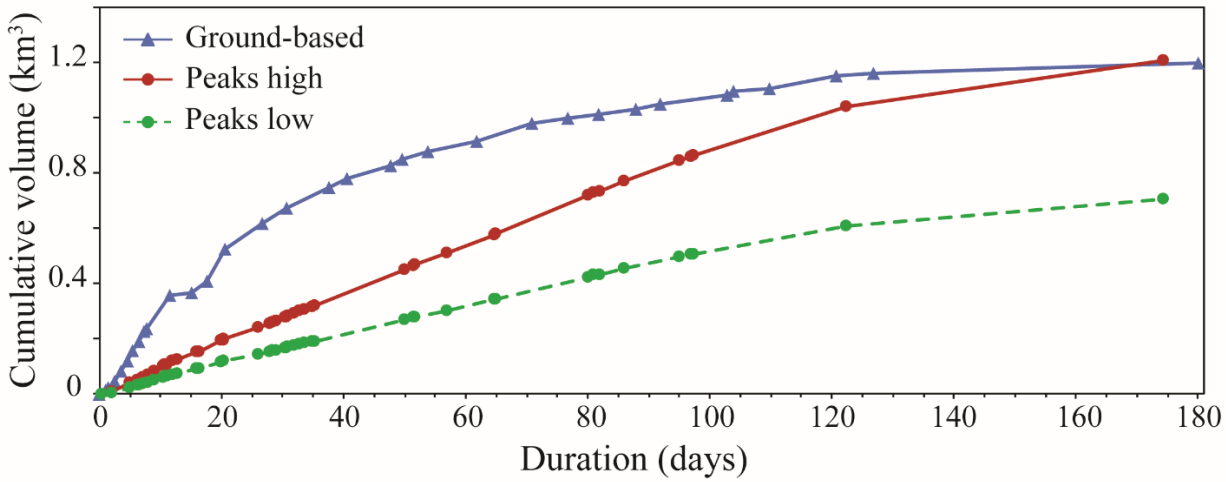

Figure 3.4. Cumulative volume for the entire duration of the eruption from space- (red and green curves from the high and low coefficients, respectively) and ground-based (dark blue curve) measurements.

3.5 Discussion

3.5.1 Discrepancies between the two methods used to retrieve TADR and flow volume

We found that the lava discharge rates retrieved using the satellite- and ground-based methods rarely agree with each other for the first 50 days, although the final flow volume is in good agreement. Where are these differences in lava discharge rates coming from? In our detailed comparison of the TADR during the first 50 days of the eruption, we saw that $TADR_g$ was two to three times higher than $TADR_{MOD}$ for the first 30 days. We inspected some of the MODIS images producing peaks in $TADR_{MOD}$ and found that some still seemed to be cloud contaminated (an inherent source of error when using optical remote-sensing data). The presence of clouds during the acquisition of a MODIS image clearly affects the measured at-satellite spectral radiance and can cause an underestimate of the true TADR. However, this large offset between the two methods cannot be explained by cloud contamination alone. The main assumption in the satellite method is the lava surface temperature. In the method we use here, we assume that the lava surface temperature ranges between 100° and 500°C and find that the flow volume retrieved with the hot case is in better agreement with the ground-based measurements. Interestingly, during the 1991-1993 Etna eruption, Harris et al. (1997a) found that the cold case estimate of discharge rates was closer to field estimates than those obtained via the hot case, presumably, because the flow surface in that eruption (for which discharge rates peaked at approximately 20 m^3/s), radiated little energy. The intense 2014-2015 eruption at Holuhraun, covering a much larger area and with TADRs an order of magnitude higher, is likely to have produced a more radiant flow surface than the 1991-1993 Etna eruption. For this reason, a higher assumed T_{lava} is more appropriate for such an intense eruption. This most likely explains why the hot case of $TADR_{MOD}$ yields estimates of discharge rate and flow volume that are closer to the values obtained from our ground-based dataset (although the $TADR_{MOD}$ hot case still significantly underestimates the lava discharge rate at the beginning of the eruption). We also

note a cross-over at about day 50 where the ground-based TADR became closer to the cold case than the hot case. This is probably due to the decrease in lava surface temperature through cooling and the drop in discharge rate, with a change of lava transport from open channel to lava ponding and lava tubes leading to a reduction in the rate of thermal renewal of the flow surface, and hence less exposure of higher temperature material to the sensor from the flow interior.

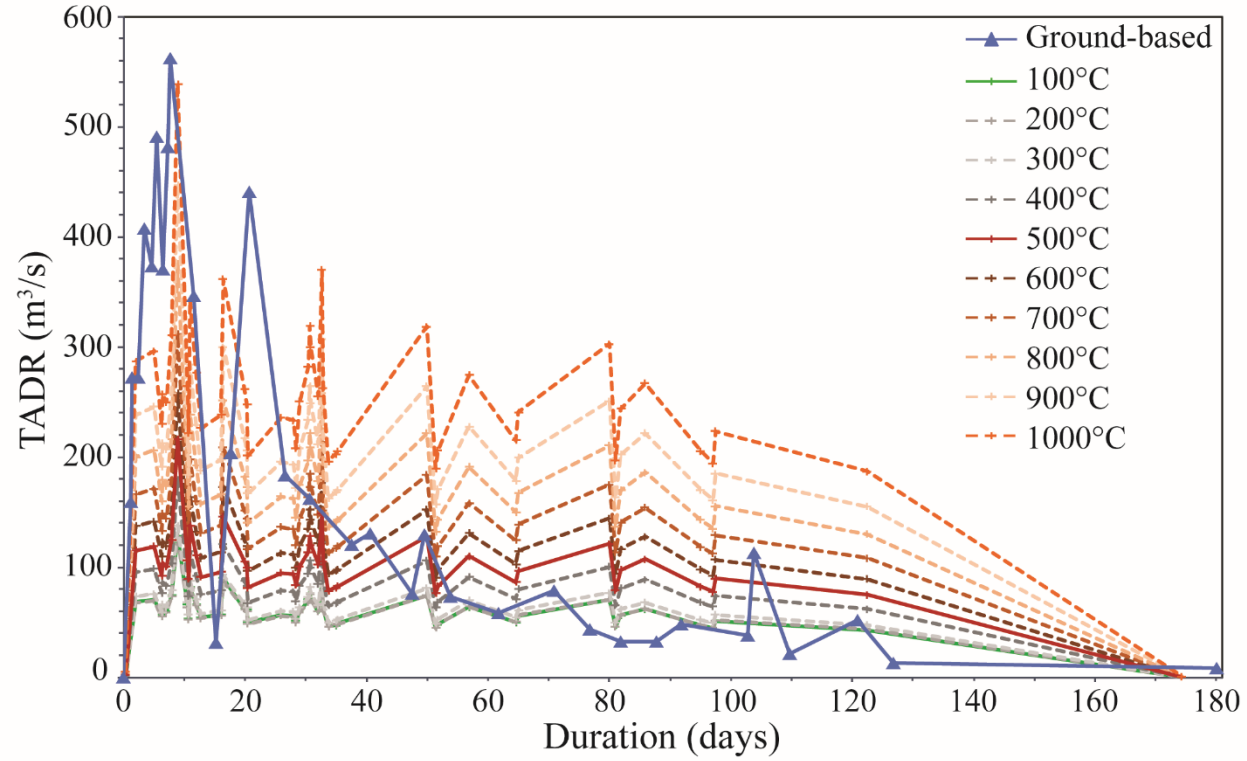

Figure 3.5. TADR time series (peaks only) for different values of T_{lava} compared with the ground-based TADR in blue triangles. In red and green curves are the same TADR as from Figure 3.3 (100°C corresponds to the cold case or low coefficient and 500°C corresponds to the hot case or high coefficient).

This raised our interest in the influence of different lava surface temperatures on the estimated TADR, and we decide to experiment with this parameter (Figure 3.5). It is interesting to see that the maximum $TADR_{MOD}$ can be forced to match the maximum ground-based TADR by changing the lava surface temperature to 1000°C instead of 500°C. In summary, it seems that a lava surface temperature of 1000°C would be more appropriate for the calculation of TADR for

the first 30 days, then for the next 20 days a temperature of 500°C would be better and finally from day 50 to the end of the eruption a temperature of 100°C fits best the ground-based measurements. Therefore, we see here that early on, the incandescent part of the flow field (vent plus open lava channels) was large and the thermal remote sensing TADR hot case is more appropriate. After day 50, it seems that the cold case becomes more representative of the prevailing lava flow surface temperature. We therefore hypothesize that it would be ideal to change the value of the assumed T_{lava} at different time during the eruption to have the best correspondence with ground-based estimates. However, this solution is not practical/realistic because it requires advance knowledge of when to change the lava surface temperature and which value to use, which is not feasible in near-real time unless there is a field team on site making observations of any changes in thermal emissions (or another remote sensing mission). In general, using the hot case thermal remote sensing method at 500°C still proves to be a good assumption to estimate a final flow volume in agreement with ground-based data. However, this method apparently underestimates the value of TADR at the beginning of the eruption but then overestimates it toward the end.

The alternative solution to visual examination of each satellite image is to use a subset of data points that we trust to be from a mostly clear satellite acquisition using the maximum TADR (peaks). Thus, eliminating most anomalous values of TADR allows us to retrieve a final flow volume that corresponds to the ground-based measurements. Considering the cumulative volume curves in Figure 3.4, we can see that both satellite- and ground-based methods show different trends over time. It is almost linear for the cumulative volume estimated from $TADR_{MOD}$ while the volume derived in the field has a more first-order exponential distribution. We are more familiar with the latter for episodic effusive basaltic eruptions (Wadge, 1981) and therefore believe that the more linear trend observed with the remote sensing method is an artifact from the method used to subset our dataset using only the main peaks in TADR.

3.5.2 Volcanological interpretation

Wadge (1981) proposed that the time evolution of discharge rates during basaltic eruptions can be defined as an asymmetric curve with a short waxing phase rising to an initial maximum and a much longer waning phase explained by the slow, somewhat exponential,

release of elastic strain energy stored in the magma chamber until reequilibration with lithostatic pressure. As seen in Figures 3.3a and 3.5, we found that the 2014-2015 eruption at Holuhraun does not display the typical Wadge model curve for the reconstructed TADR. Instead, we see a stepwise buildup of the lava discharge via a set of two to three distinct pulses until the maximum TADR is reached on days 8-9. There is also a more subtle and gradual rise and fall in the space-based TADR during the period mid-October to mid-December and peaking in mid-November. Therefore, the 2014-2015 eruption does not exhibit the simple waxing/waning behavior postulated by the Wadge model but follows a more convoluted pattern. We know from Gudmundsson et al. (2016) that the simultaneous subsidence of the Bárðarbunga caldera was not stepwise, at least not on this timescale, and we can therefore rule it out as the cause for the pulsating lava discharge during about the first 20 days of the eruption. Other possible explanations for this pattern include the following: i) a number of fluid dynamic studies show that a steady input of magma into a conduit can result in a pulsating discharge rate (Melnik and Sparks, 1999; Melnik, 2000; and Barmin et al., 2002); ii) the nature of magma extraction from the storage zone. If, as the petrology suggests (Guðfinnsson et al., 2015; Halldórsson et al., 2015), the magma produced in 2014-2015 is erupted from a mushy storage zone with a melt fraction, the extraction of melt from such a zone can be envisioned to become pulsating if the rate of extraction from the zone closest to the conduit feeding the eruption is slightly higher than the recharge of melt into that zone. iii) irregularities and changes in conduit geometry (Wilson and Head, 1981; Wylie et al., 1999; James et al., 2006a; Parcheta et al., 2015). Constrictions in the conduit feeding the eruption or variations in conduit shape and size could result in pulsating discharge.

Although the first two points provide viable mechanisms for producing pulsating lava discharge as observed in the early stage of the eruption, they do not explain why it stopped. This stepwise increase is only seen during about the first 20 days, which makes the third process more plausible, especially because it coincides with the stepwise evolution of the vent system from full-scale linear vent (day 1), to several discrete vents distributed along the length of the fissure, decreasing in number with time (days 2-19), to eruption from a single source vent (day 20; e.g., Eibl et al., 2017). A detailed investigation of the exact mechanism by which this happens is beyond the scope of this paper. With more data becoming available for volcanoes around the

world, we note that the simple physical theory defined by Wadge does not always apply in every case (Bonny and Wright, 2017). For example, it is hard to find a single pattern for the eruptions of Etna, Sicily (Harris et al., 2000 and 2011); it seems that about 50% have a fast increase in discharge rate which slowly decreases over time, the rest having different shapes and patterns.

The broad secondary pulse in TADR between day 50 and about day 100 (centered on day 80 and highlighted by a black arrow in Fig. 3.3b) is another point of interest, although it does not appear in the ground-based data. Pedersen et al. (2017) show that a large pond existed in the main lava distributary for the flow field situated about 1 km down from the vents, from mid-October to end of November/early December (Figure 3.6b). Hence, the presence of this pond coincides with the timing of the increase in discharge. Therefore, we interrogated our datasets to try to decide whether this is a real increase in the lava discharge from the vents or an artifact from the presence of the lava pool. We know that the TADR calculation is based on its proportionality with the area of active flow. We do need to keep in mind that the method used here to estimate TADR relies on the assumption of a range of lava surface temperatures. Using these assumed temperatures, an estimate of the area can be calculated but we do not directly measure the area of active lava. A larger estimated area would yield a higher TADR for a given surface temperature. However, the same TADR could be calculated from a smaller area of active lava with a higher radiant surface (i.e., hotter temperature).

One way to test this hypothesis is to look at the number of saturated pixels. In Figure 3.6a, we can see that the ratio of the number of saturated pixels over the total number of anomalous pixels at 11 μm detected in each MODIS acquisition is correlates well with high TADR. Especially during the increase in lava discharge during the middle of the eruption, the ratio is consistently high with values reaching up to 0.33, meaning that 33% of the pixels in that image were saturated. During this relative increase in $TADR_{MOD}$, we also see that $TADR_g$ is slowly decreasing, which suggests that the lava surface area measured in the field did not increase. This indicates that the apparent high discharge rate detected from space is not produced by an increase in area but an increase in lava temperature. Therefore, it seems that this small increase in TADR can be explained by the presence of a lava pool (its surface is hotter and its spectral radiance higher than the cooling preexisting lava flow) and rules out the possibility of this being an event of magma recharge. We can illustrate this by examining photographs from

that time, which highlight the presence of a large lava pond at the surface of the flow field exposing fresher, hotter lava to the detector (Fig. 3.6b, Pedersen et al., 2017).

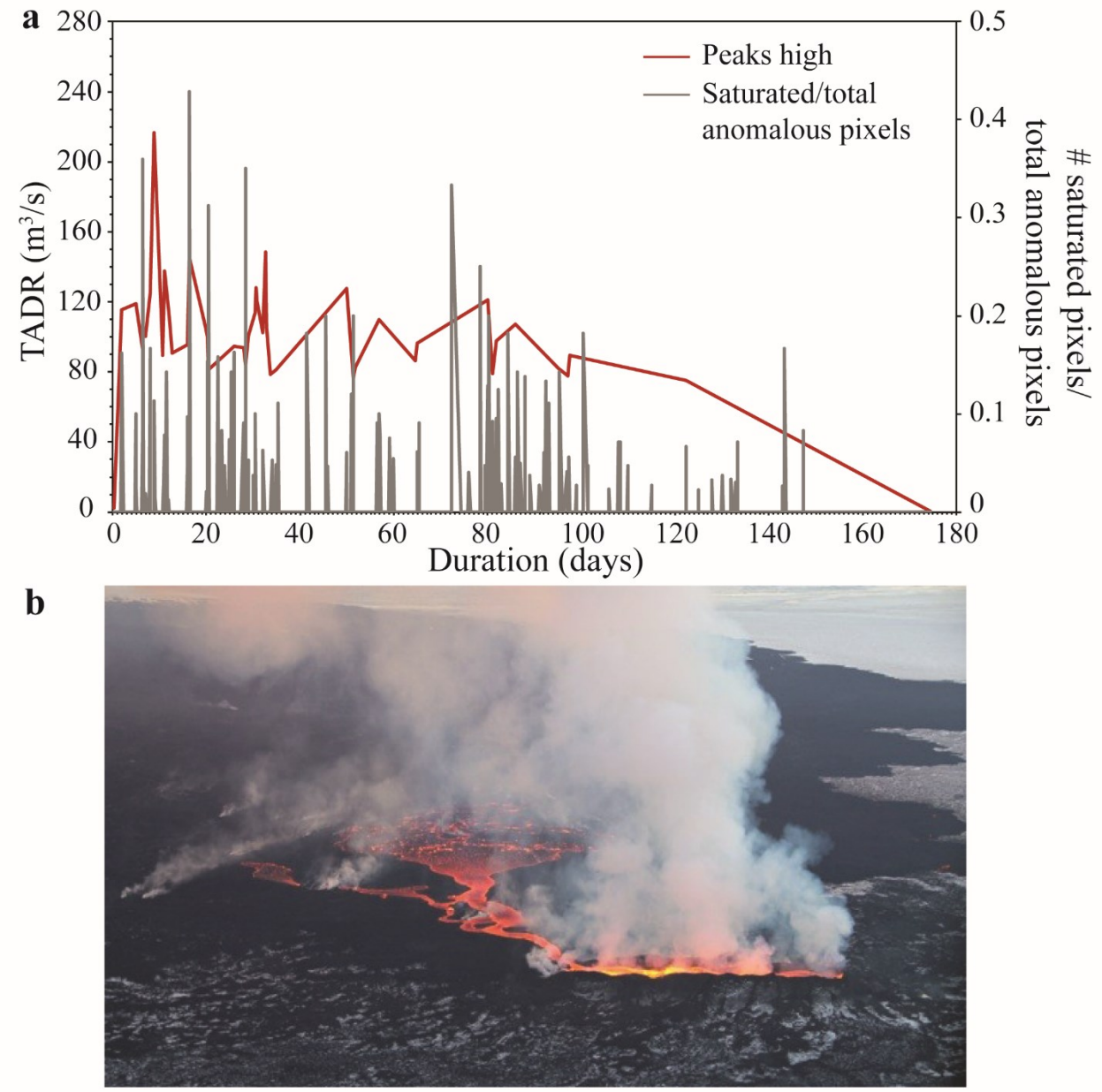

Figure 3.6. a) Space-based TADR (peaks only) estimated by the high coefficient for the 2014-2015 eruption at Holuhraun and the ratio of saturated pixels over the total number of anomalous pixels in band 31 detected by MODIS. b) Photogaph of the lava pond in the background from 8 December 2014 (day 99) taken by Gro Pedersen.

3.6 Conclusions

Estimates of changing lava discharge rates during an eruption are important for monitoring and understanding an eruption and its dynamics. However, we know that it is a very difficult parameter to measure well. We focused here on two methods, from satellite- and ground-based measurements, and both have assumptions and uncertainties associated with them. In terms of ground-based measurements, the estimation of the lava flow thickness is the main source of error. For the thermal remote sensing method, the main assumption is the lava surface temperature and uncertainties in our results come from cloud contamination, satellite zenith angle, and saturation (which all produce possible underestimation of discharge rate). Despite all sources of errors, we consider the ground-based measurements of lava discharge rates and final flow volume to be the most accurate values. For this eruption, we found that the ground-based DRE volume of 1.2 km^3 (DEM difference) is closer to the "hot case" satellite DRE volume estimate of 1.21 km^3. The good agreement between these two final flow volumes provides encouragement that the remote sensing method yields robust estimates of lava flow volume (Figure 3.4). This almost certainly relies on the eruption being of sufficient duration that a large enough temporal sample can be obtained, such that anomalously low, cloud-contaminated TADRs can be excluded from the time-series. Although we see discrepancies in the TADR time series between the two methods, we can reconcile them if we consider changing the lava surface temperature for the early stages of the eruption considering that this was a very large and intense eruption. We therefore consider that a higher lava surface temperature could be used early in the eruption for such unusual effusive activity but the 100-500°C temperature range is a good assumption for the overall eruption.

CHAPTER 4

AN ASSESSMENT OF THREE SATELLITE-BASED METHODS TO ESTIMATE LAVA DISCHARGE RATES DURING EFFUSIVE BASALTIC ERUPTIONS

In preparation for publication as: Bonny E., R. Wright. An assessment of three satellite-based methods to estimate lava discharge rates during effusive basaltic eruptions. To be submitted to the Journal of Volcanology and Geothermal Research.

Abstract

As basaltic lava flows spread, the area of active lava changes with time during eruptions. Satellite images can be used to quantify this change, and estimate the supply rate at which the lava is erupted, and ultimately the total volume. The lava effusion rate, defined as the instantaneous volumetric flux of lava from the vent, is of great utility in lava flow forecasting and the understanding of eruption dynamics. Three methods that use infrared satellite data to estimate time-averaged discharge rates (TADR) are prevalent in the literature: i) Harris et al. (1997; Method-1), ii) Wright et al. (2001a; Method-2) and iii) Coppola et al. (2012; Method-3). While each method claims to yield TADR, they are in fact based on a) the use of spectral radiance measurements made at contrasting wavelengths (4 μm vs 11 μm), and b) different assumptions. As such, there are strong reasons to believe that these methods should not provide equivalent estimates of TADR, even when using the same satellite data for the same eruption. Here, we show how well these methods agree with each other, by using NASA's MODerate Resolution Imaging Spectroradiometer (MODIS) to estimate discharge rates for 104 basaltic effusive eruptions from 34 volcanoes over the last 15 years. We used freely accessible MODIS data from the MODVOLC system (Wright et al., 2002) that detects volcanic "hot spots" anywhere around the world, with complete coverage every day. TADR time-series from each

method were calculated for all eruptions. Ground-based measurements of discharge rate have large (and usually unquantifiable) errors. We instead use the final volume of lava erupted, which can be precisely constrained at the end of an eruption (e.g., literature values obtained via geodetic surveys or Interferometric Synthetic Aperture Radar (InSAR) measurements), to validate satellite-derived estimates of final flow volume (by integrating the TADR curves). We found that in general the method of Harris et al. (1997a) correlates better with the literature estimates than the method of Coppola et al. (2012). However, the envelope of TADR resulting from application of Method-3 more often encompasses the literature values than Method-1 (5% more often than Method-1); this is because Method-3 yields a larger range of TADR. The final flow volumes estimated using Method-3 are often overestimates (60% of the eruptions) of the recorded final flow volumes. We discuss the reasons for these discrepancies and investigate how and when the satellite-derived discharge rates (and volume estimations) correlate better (or worse) with published data. This work sheds light on the evolution of the method for estimating lava discharge rates from infrared satellite data over time from first a physics-based model (Harris et al., 1997a) to a simplified coefficient method (Wright et al., 2001a) and back to another physics-based model (Coppola et al., 2012). Finally, we define new coefficient values for 14 basaltic volcanoes in our database that improve final flow volume and hence TADR results by 30-50% compared to Harris et al. (2007) coefficient values.

4.1 Introduction

Lava effusion rate is defined as the instantaneous volumetric flux of lava from a vent at any given time, invariably expressed in m^3/s. This is an important parameter that controls the length of a lava flow (Walker, 1973) and can help us better understand the dynamics of effusive activity (Harris et al., 1998). The work of Walker (1973) and Wadge (1978; 1981) showed that the lava effusion rate produced during an eruption was proportional to the length of the flow. This conclusion was later recast by Pieri and Baloga (1986) as the effusion rate being proportional to the area of the flow (clearly a flow cannot lengthen without increasing in surface area). Lava effusion rate is also a critical input parameter for lava flow modelling (Crisp and Baloga, 1990; Wright et al., 2008). A large number of techniques has been developed to estimate lava effusion rate, including field-based methods using measurements of lava channel geometry

and flow speed (Calvari et al., 2003), electromagnetic methods (Kauahikaua et al., 2003), photogrammetric methods (James et al., 2006b; 2007), measurements of thermal emissions made by hand-held cameras (Harris et al., 2005; Calvari et al., 2005), and thermal emission measurements made by satellites (Harris et al., 1997a; Coppola et al. 2012).

For the last technique, the resultant estimate is not of the instantaneous effusion rate, as the area of lava emitting at a given temperature at the moment of satellite overpass is not function of instantaneous changes in flux at the vent, but rather the antecedent effusion rate averaged over some period of time prior (Wright et al., 2001a). This has been referred to as the time-averaged discharge rate (TADR; Harris et al., 2007). Three different methods in the literature are commonly cited when computing TADR from infrared satellite data. Two are based on physics-based model of heat and mass balance (Harris et al., 1997a; Coppola et al., 2012), while another simply assumes that TADR is related to the area of active lava at the moment of image capture by an empirically-tuned constant (Wright et al., 2001a). To the non-specialist it may appear that, if using the same satellite data for the same eruption, it is reasonable to expect each method to yield the same TADR, and that these methods are interchangeable. The purpose of this study was to determine to what extent this is true, as there are good reasons to believe that it is not. Most obviously, a method that uses measurements of thermal emission from an active flow made at 4 μm (e.g., Coppola et al., 2012) should yield a different TADR than one which makes the same measurement at 11 μm (e.g., Harris et al. 1997a; Wright et al., 2001a), because the relationship between emitted spectral radiance (L) and flow surface temperature (T) is $L \sim T^4$ at 4 μm and $L \sim T^2$ at 11 μm (Wooster et al., 2003). The latter is expected to more reliably document the area of active lava, the former is more sensitive to the exposure of high temperature lava in cracks in the crust. Each of the three methods also rely on different assumptions.

Using thermal infrared remote sensing (here we use both midwave infrared from 3.0 to 5.0 μm and longwave infrared from 5.0 to 20 μm), we can measure the spectral radiance emitted by anomalously hot pixels contained in images of active lava flows. This enables us to derive time-averaged discharge rates repeatedly over the duration of the eruption, and to build a time series for 104 eruptions over the last 15 years using each of the aforementioned methods. Method-1 (Harris et al., 1997a) uses measurements of spectral radiance at 11 μm to estimate the

thermal emission from the lava flow surface at the moment of image capture. This heat loss is then compared to the amount of energy available to support this cooling (via cooling of the mass of lava, and crystallization) to estimate the volume flux (discharge rate). This was based on a study of Etna volcano using Advanced Very High Resolution Radiometer (AVHRR) images. They found a good agreement with ground-based estimates of lava flux as well as with the total volume of lava emitted during the 1991 to 1993 eruption. Later on, this method proved to be accurate for other eruptions and became widely used (Harris et al., 1998, Harris et al., 2000, Lautze et al., 2004, Morgan et al., 2013). However, Wright et al. (2001a) found that Method-1 could be simplified since the only variable in this physics-based model is the area of active lava flow, and they formulated Method-2. The linear relationship between the area of active lava and discharge rate is defined by a coefficient usually characteristic of a given volcano (Harris et al., 2007) and this agrees with the idea that the discharge rate is proportional to the area of the active flow (Pieri and Baloga, 1986). Finally, Coppola et al. (2012) defined a new physics-based method to estimate discharge rates by using the 4 μm spectral radiance from MODerate Resolution Imaging Spectroradiometer (MODIS) images instead of 11 μm. The use of 4 μm measurements of thermal emission from the flow surface allows the radiant energy to be directly estimated (Kaufman et al., 1998; Wooster et al., 2003). This radiative energy was then scaled against a coefficient (which is claimed to vary with the silica content of the lava in question) to yield TADR. It can be argued that discharge rate retrieval using thermal remote-sensing has evolved from a physics-based model to a simpler linear relationship to a new physics-based model.

We used the database freely available from the MODIS archive (since 2000 on Terra and 2002 on Aqua satellites) to calculate TADR time-series for each basaltic effusive eruption that was detected by the MODVOLC algorithm (http://modis.higp.hawaii.edu/, Wright et al., 2002). TADRs were calculated for 104 discrete eruptions detected at 34 volcanoes over a 15-year period (2000 to 2014 inclusive) with each of the three methods. Use of the MODVOLC dataset allows us to provide the same input data to each method (i.e., the same thermally anomalous pixels were used, such that the effects of the method alone on TADR estimation can be isolated). This chapter quantifies the differences in TADR estimation that result from the application of these seemingly equivalent methods. Furthermore, we can also determine which method gives results

closest to reality. Ground-based measurements of time-averaged discharge rate can be subject to large errors (Harris et al., 2007) and have a much sparser temporal resolution, or even are absent, at remote volcanoes (Patrick et al., 2003). As such, it is perhaps pointless to compare an effusion rate derived in-situ with one derived from space as which one is more accurate is open to debate. One parameter that can be very well constrained at the end of an eruption is the final flow volume. Therefore, we have integrated our satellite-derived TADR measurements to yield an estimate of final flow volume, and compared this to final volumes (derived from, for example, InSAR or geodetic surveying) published in the literature.

4.2 Methods

4.2.1 Three nominally equivalent methods for estimating TADR from infrared satellite data

Below we describe each method and apply them as closely as possible to the ways described in the original papers, and any differences are noted. In the original papers the authors used different methods for segmenting the images (i.e., identifying which 1 km pixels contained active lava and would be used to compute TADR), compensating for atmospheric effects, and estimating the temperature of the ground surrounding the active lava (amongst other things). It is important to note that we "feed" each method the same data, obtained from the MODVOLC data archive. As such, issues related to cloud contamination affect each method equally, and do not contribute to any differences observed between the methods. Furthermore, we estimate the temperature of the ground surrounding each active lava pixel using a single dataset for each method (Wright et al., 2015). Essentially, we isolate the impact that the method (and its inherent assumptions) have on the estimation of TADR, from the data and its pre-processing.

4.2.1.1 Method-1: Harris et al. (1997a, 1997b and 1998)

The first method follows from a series of papers published by Harris et al. (1997a, 1997b, 1998) based on measurements of the spectral radiance emitted at 11 μm. The spectral radiance from the satellite detects not only the energy emitted by the hot lava flow on the ground but also the upwelling radiance emitted by the atmosphere; therefore, the 11 μm at-satellite radiance has to be corrected to infer the radiance coming from the active lava flow alone. This is done by

correcting the measured spectral radiance for each pixel ($L11_{MOD}$, measured at-satellite radiance) for the emissivity of the target $\varepsilon(\lambda)$ and atmospheric effects using the following equation

$$L11_{cor} = \frac{L11_{MOD} - L_u(\lambda)}{\tau(\lambda)\varepsilon(\lambda)} \quad (4.1)$$

$L11_{cor}$ is the corrected spectral radiance at 11 μm, $L_u(\lambda)$ is the upwelling atmospheric radiance and $\tau(\lambda)$ is the transmissivity of the atmosphere at wavelength λ. Those parameters are defined for the combination of surface type (basalt), atmosphere (standard), scan angle (nadir), wavelength and elevation of the eruption on the volcano. These parameters were defined for each volcano (Table A.1) based on the graphs found in Figures 2.17 and 2.15 from Harris (2013), corresponding to the upwelling radiance and transmissivity variations with elevation in the thermal infrared based on a MODTRAN US standard atmosphere.

A MODIS pixel is 1 km² at nadir (equivalent to the instantaneous field of view of the AVHRR data used by Harris et al., 1997a) and therefore it is rarely completely filled by active lava (incandescent part of the flow). However, it is the spectral radiance from the lava that is relevant to the estimation of TADR. This is taken into account by assuming that the corrected radiance ($L11_{cor}$) is a combination of that emitted by the hot active lava within the pixel and that radiated by the ground adjacent to the flow (two-component model). In Figure 4.1, we can see an image from MODIS Terra at 11 μm on December 5, 2012 during the Tolbachik eruption, where the bright pixels identify the lava flow field. For each such pixel the at-satellite radiance is assumed to be given by

$$L11_{cor} = f\, L(11, T_{lava}) + (1 - f)\, L(11, T_{back}) \quad (4.2)$$

$L11_{cor}$ is the pixel-integrated radiance at 11 μm wavelength corrected for emissivity and atmospheric effects, L(11,T) is the spectral radiance emitted by a blackbody at temperature T and at a wavelength of 11 μm. The f is the portion of the 1 km² pixel occupied by the active lava flow assumed to radiate at temperature T_{lava} and is estimated with following equation

$$f = \frac{L11_{cor} - L(11, T_{back})}{L(11, T_{lava}) - L(11, T_{back})} \quad (4.3)$$

T_{back} is the temperature used to characterize the low temperature component of the pixel (cold ambient surfaces surrounding the lava; computed using the approach described in Wright et al., 2015).

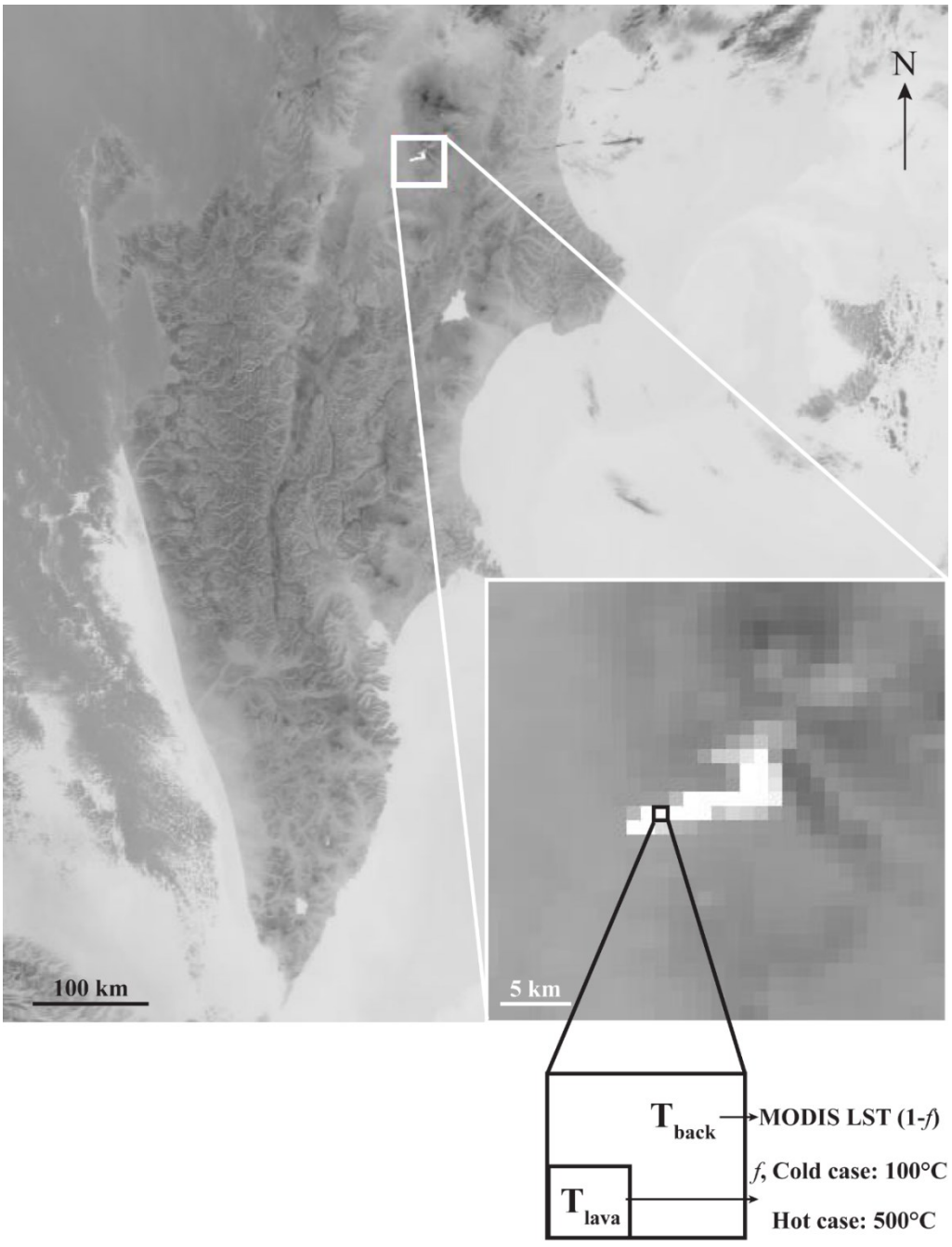

Figure 4.1. MODIS image of the Kamchatka peninsula on 12/05/2012 at 00:25 UTC showing the lava flow field (bright pixels) during the Tolbachik eruption. This image is from band 31 or at 11 μm with a zenith angle of 15° and the inset gives a schematic view of how Method-1 from Harris et al. (1997a) works.

The area occupied by active lava in each pixel (a precursor to calculating TADR) can then be estimated if the temperature of the lava surface can be assumed. Harris et al. (1997a) assumed that the integrated surface temperature of an active lava flow (i.e., the weighted average of the temperature of the crust and any fractures in that crust exposing the flow's hot interior) can be inferred to range between 100°C (referred to as the cold case hereafter) to 500°C (hot case hereafter). We can then deduce the area of active lava for those two cases (100°C and 500°C) by multiplying the fraction *f* of active lava of each anomalous pixel by the corresponding pixel area A_{pixel} (i.e., 1 km^2 at nadir increasing to ~2 x 5 km at the edge of the swath)

$$A_{lava} = f \times A_{pixel} \tag{4.4}$$

By summing A_{lava} for all anomalous pixels detected at a given satellite acquisition, we obtain the total surface area of active lava ($A_{tot} = \Sigma A_{lava}$) at a given point in time for two different lava surface temperatures (T_{lava}, 100°C and 500°C). It is important to note that the area estimated at 100°C will be larger than at 500°C for the same measured spectral radiance because the energy emitted by a low temperature surface is smaller than at a higher temperature, as described by Planck's law. From the active lava area and for each anomalous pixel detected at each satellite acquisition we can estimate the rate of heat loss by the flow through radiation M_{rad} and convection M_{conv} (in W) by using

$$M_{rad} = A_{tot}\varepsilon\sigma\left({T_{lava}}^4\right) \tag{4.5}$$

$$\text{and } M_{conv} = 0.14\, A_{tot}\, k(g\alpha\rho_{air}/\mu\kappa)^{1/3}(T_{lava} - T_{back})^{4/3} \tag{4.6}$$

where σ is the Stefan-Boltzmann constant (5.67×10^{-8} W m^{-2} K^{-4}), ε is the emissivity of the target surface (0.989 for basalt), g is the acceleration of gravity (9.8 m s^{-2}), k, μ, κ, α and ρ_{air} are thermal conductivity, dynamic viscosity, thermal diffusivity, cubic expansivity, and density of air. All these values are set for air at the mean temperature of air and lava, using T_{air} of 0°C from Kays and Crawford (1980) who compiled the air properties at different temperatures. Harris et al. (1997a) assume that the conductive contribution is negligible compared to the radiative and convective heat loss, thus the total heat loss is $M_{tot} = M_{rad} + M_{conv}$ or

$$M_{tot} = A_{tot}\left[\varepsilon\sigma\left({T_{lava}}^4\right) + 0.14\, k(g\alpha\rho_{air}/\mu\kappa)^{1/3}(T_{lava} - T_{back})^{4/3}\right] \tag{4.7}$$

Finally, lava discharge rates are calculated at 100°C and 500°C by dividing the rate of heat loss from the surface of the active flow by the heat that was available per unit volume due to cooling and crystallization, using the following equation

$$TADR = \frac{M_{tot}}{\rho[Cp\Delta T + C_L\Phi]} = \frac{[Mrad + Mconv]}{\rho[Cp\Delta T + C_L\Phi]} \quad (4.8)$$

where ρ is the lava density (in kg m^{-3}), C_p is the lava heat capacity (in J kg^{-1} K^{-1}), C_L is the latent heat of crystallization (2.9×10^5 J kg^{-1}). ΔT is the difference between the lava core temperature at the vent (eruption temperature) and when it stops flowing (the point at which the flow core cools to a point at which further forward motion is rheologically impossible); this is assumed to be 150 K by Harris et al. (1997a). Φ is the average crystal fraction caused by cooling through ΔT (here we used 45%; Table A.2 shows all values used in Method-1 calculations). We have attempted to remain faithful to the original method of Harris et al. (1997a), substituting only values of the upwelling radiance and the transmissivity for MODTRAN instead of LOWTRAN (sourced from Harris, 2013). The hot case yields a higher estimate of TADR than the cold case, even though the area computed is smaller. This is because the radiative heat loss term contains the temperature raised to the power of four and therefore has bigger influence on the TADR estimates for the hot case. The final product is a minimum time-averaged discharge rate for the cold case (T_{lava} = 100°C) and a maximum TADR for the hot case (T_{lava} = 500°C).

4.2.1.2 Method-2: After Wright et al. (2001a) and Harris et al. (2007)

Based on the first method, and looking at Equations 4.7 and 4.8, only one parameter is variable in the estimation of discharge rate and that is the active lava flow area (Wright et al., 2001a). All other parameters in the retrieval of TADR are either assumed or estimated, but kept constant for a given volcano. Therefore, Equation 4.8 can be reduced to a linear relationship between active lava area and lava discharge rate by a constant X (Figure 4.2).

$$TADR = X.A_{tot} \quad (4.9)$$

where X is in m s^{-1}, which can be decomposed as m/c to be similar to Equation 4.8 where m is equal to $\left[\varepsilon\sigma\left({T_{lava}}^4 - {T_{back}}^4\right) + h_c(T_{lava} - T_{back})\right]$ in W m^{-2} corresponding to the rate of heat loss per unit area and c is equal to $\rho(Cp\Delta T + \Phi C_L)$ in J m^{-3} corresponding to the heat available to the flow per unit volume.

So X follows

$$X = \left[\varepsilon\sigma\left({T_{lava}}^4 - {T_{back}}^4\right) + h_c(T_{lava} - T_{back})\right]/\rho(Cp\Delta T + \Phi C_L) \quad (4.10)$$

where all constants are the same as previously defined and h_c is the convective heat transfer coefficient. The coefficient X is slightly different than what it is following Method-1 because the manner in which the discharge rate estimation accounted for different heat loss mechanisms has evolved over time (Harris et al., 1998, 2000, Harris and Neri, 2002; and Harris et al., 2007; more details in section 4.3.1.6).

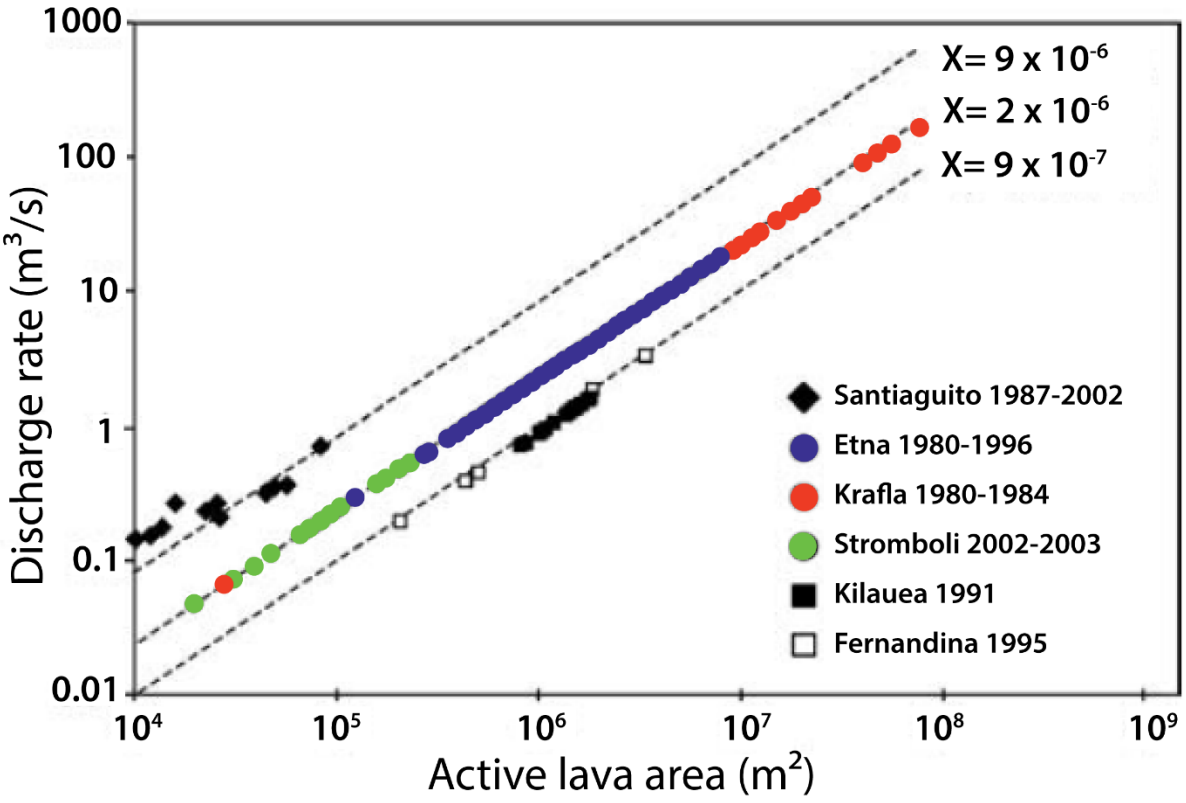

Figure 4.2. Discharge rate against active lava area showing the linear relationship between the two. This has been modified from Harris et al. (2007) and summarizes Method-2. The values of coefficient X are shown in the top right corner but only the minimum values for clarity.

For this method, also referred to as the "coefficient method", we multiplied the total area of active lava (A_{tot}) found previously with Harris et al. (1997a) by a coefficient X. Harris et al. (2007) defined carefully the coefficient X for six different volcanoes (Etna, Krafla, Stromboli,

Kīlauea, Fernandina and Santiaguito; Figure 4.2), which are linearly related to TADR. The main reason for the different values arises from the different lava composition, with X increasing from mafic to more felsic lavas. We organized our 34 volcanoes in three different groups, choosing the closest values from either Etna, Kīlauea or Stromboli for their given lava composition (Table 4.1), and estimated the corresponding TADRs. The coefficient varies, so we used its minimum value to multiply with the area of active lava estimated with the cold case, and the maximum value was used with the area estimated from the hot case.

Table 4.1. Coefficients X used for Method-2 depending on the volcano of interest following values from Harris et al. (2007).

	Kīlauea	Etna, Krafla	Stromboli
X ($\times 10^{-6}$ m s^{-1})	0.9 - 29	2.1 - 33	2.1 - 26
Volcanoes	Cameroon, Cerro Azul, Dalafilla-Alu, Fernandina, Jebel at Tair, Manda Hararo, Nabro, Nyamuragira, Sierra Negra	All the others (24)	Stromboli

4.2.1.3 Method-3: After Coppola et al. (2012 and 2013)

Coppola et al. (2012) estimate the radiance emitted by the active lava at 4 μm using

$$\Delta L4 = \sum_{i}^{n_{alert}} [L4_{MOD} - L(4, T_{back})] \quad (4.11)$$

where $L4_{MOD}$ is the 4 μm radiance detected by MODIS and $L(4,T_{back})$ is the radiance from the ambient temperature surrounding the active lava in the pixel also at 4 μm (Figure 4.3). Coppola et al. (2012) then estimate the Volcanic Radiative Power (VRP, the radiative heat loss of the lava surface) in watts using the equation established by Wooster et al. (2003) where

$$VRP = \left[\left(\sigma A_{pixel}\right)/a\right]\Delta L4 \quad (4.12)$$

where A_{pixel} is the size of the pixel, σ is Stefan-Boltzmann constant, *a* is a coefficient (3.0×10^{-9}) and for pixel at nadir (1 km^2) this equals to $1.89\times10^{7}\times\Delta L4$.

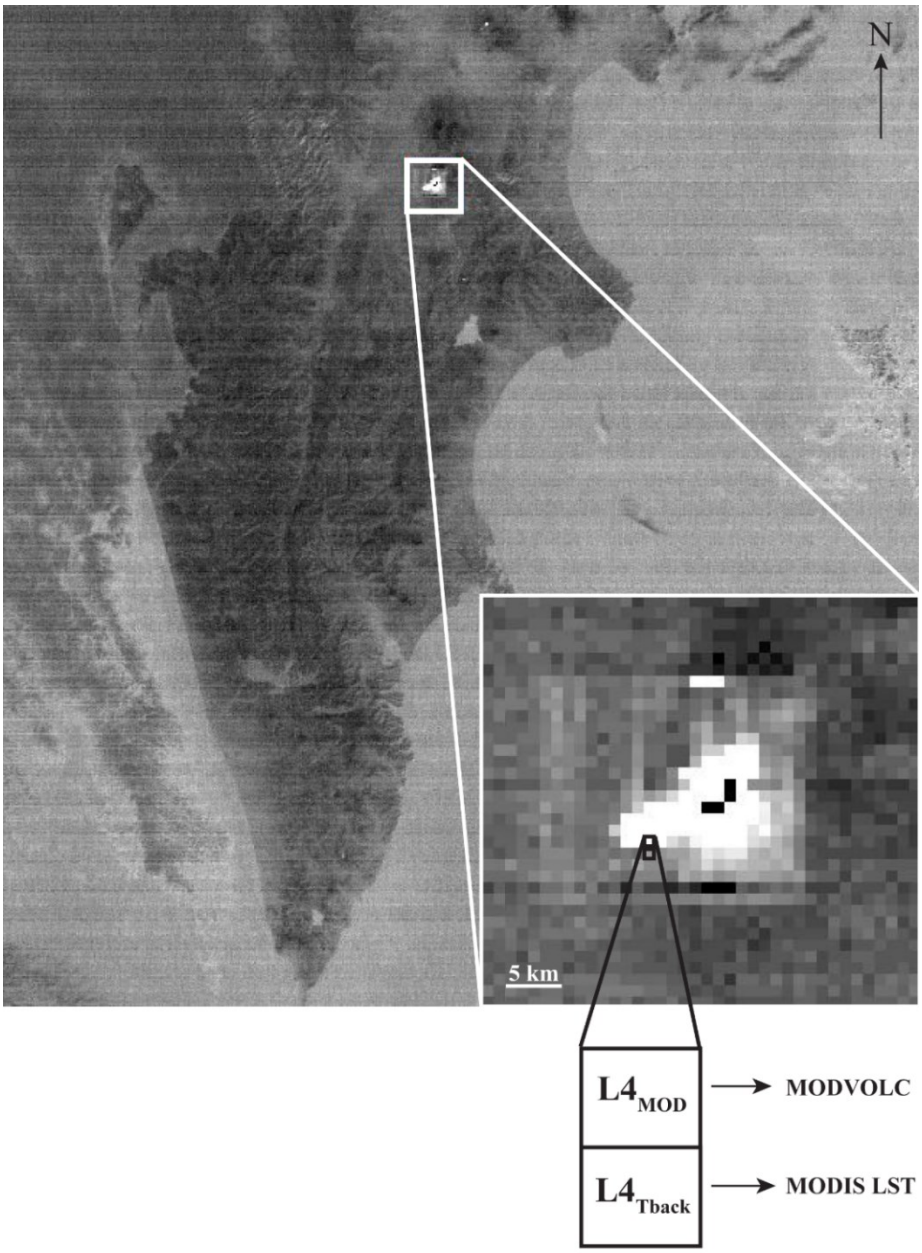

Figure 4.3. MODIS image of the Kamchatka peninsula on 12/05/2012 at 00:25 UTC showing the lava flow field (bright pixels) during the Tolbachik eruption (same satellite acquisition as Figure 4.1 but showing a different wavelength). You can see a few black pixels that are saturated (reached the maximum radiance detectable). This is from band 21 (the 4 μm channel) and the inset summarizes how Method-3 from Coppola et al. (2012) works.

The time-averaged discharge rate (in $m^3\ s^{-1}$) is then calculated from

$$TADR = \frac{VRP}{C_{rad}} \tag{4.13}$$

where C_{rad} is the defined as the "radiant density" (Coppola et al., 2013) in J m^{-3} estimated from the SiO_2 content of the lava flow (X_{SiO2} in weight percent, i.e., wt%, which is variable for different eruptions, but we used an average value for each volcano taken from the literature).

$$C_{rad} = 6.45 \times 10^{25} \times (X_{SiO_2})^{-10.4} \tag{4.14}$$

For example, the silica content used to estimate C_{rad} for Etna is 47.9 wt% and 46.5 wt% for Fimmvörðuháls, Iceland. This empirical parameter was defined using the discharge rates estimated from 28 eruptions based on FLIR data (Coppola et al., 2010).

Table 4.2. Summary of the silica content values used for each volcano with Method-3 (many of these values were compiled by Coppola et al., 2013).

Volcano name	**$XSiO_2$ (wt%)**
Nyamuragira (Head et al., 2011)	45.4
Eyjafjallajokull, Hekla, Holuhraun (Sigmarsson et al., 2011)	46.5
Etna (Coulson et al., 2010), Chirpoi, Fogo, Heard, Karangetang, Kizimen, Klyuchevskoy, Lopevi, Pavlof, Rinjani, Tinakula, Veniaminof	47.9
Fernandina (Allan and Simkin, 2000), Cameroon, Cerro Azul, Dalafilla-Alu, Jebel at Tair, Manda Hararo, Nabro, Sierra Negra	48.5
Piton de la Fournaise (Vlastélic et al., 2007)	49.4
Pacaya (Morgan et al., 2013), Stromboli (Cigolini et al., 2008)	50.0
Barren Island (Sheth et al., 2009), Fuego (Lyons et al., 2010), Montagu Island (Patrick et al., 2005)	51.0
Llaima (De Maisonneuve et al., 2012), Tolbachik (basaltic trachy-andesite, Edwards et al., 2013)	53.0
Mayon (basaltic andesites, McDermott et al., 2005)	54.7
Reventador (Samaniego et al., 2008)	55.0

This parameter was calculated within +/- 50% to include the variation in this empirical equation as it was defined in Coppola et al. (2013). This results in a minimum and maximum TADR considering the range of silica content. Table 4.2 shows the silica content values that we used for different volcanoes.

4.2.1.4. Initial comments on the similarities and dissimilarities of the three methods

Table 4.3 summarizes the main characteristics of all three methods described above. All three methods give an envelope of TADR within which the "true" value is assumed to lie. This is due to the fact that the emitting temperature of the active lava must be assumed in order to compute flow area (Method-1 and Method-2) and to accommodate limits to the C_{rad} parameter in Method-3. All methods isolate the radiance emitted by the active lava flow from that emitted by the adjacent substrate (i.e., background radiance term is subtracted from the at-satellite signal) but do so in different ways (Figure 4.4).

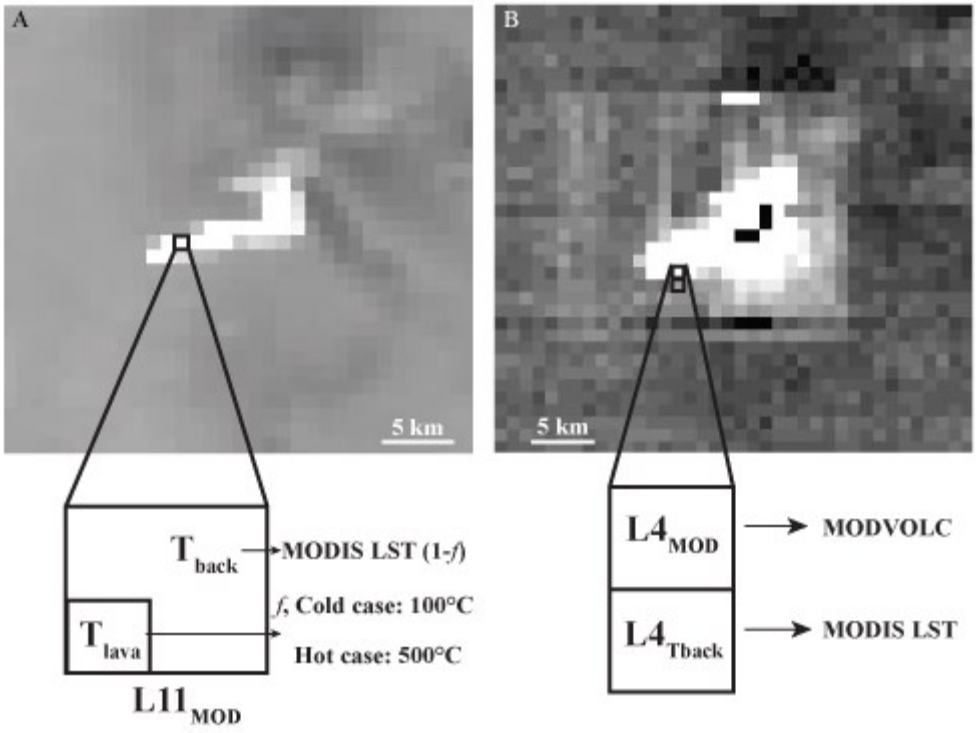

Figure 4.4. Comparison of the insets from Figures 4.1 and 4.3 showing the technique to estimate TADR using Method-1 and Method-2 (A) against Method-3 (B). The image is taken during the Tolbachik eruption on 12/05/2012 at 00:25 UTC.

Table 4.3. Summary of the main characteristics of the three methods described in this chapter to calculate lava discharge rates.

	Method-1 ***Harris et al., 1997a***	**Method-2** ***Wright et al., 2001a***	**Method-3** ***Coppola et al., 2012***
Wavelength (μm)	11	11	4
Anomalous pixels used in TADR calculation	Sourced from MODVOLC		
T_{back}	Derived from MODIS LST (Wright et al., 2015)		
ε and atmospheric corrected	Yes	Yes	No
Two-component model	Yes	Yes	No
Rate of heat loss (W)	$M_{rad} = A_{lava}\varepsilon\sigma\left({T_{lava}}^4\right)$ $M_{conv} = 0.14\, A_{lava}k(g\alpha\rho/\mu K)^{1/3}(T_{lava} - T_{air})^{4/3}$	m*	$VRP = (\sigma A_{pixel}/a)\Delta L4$
Heat available (J m^{-3})	$\rho(Cp\Delta T + \Phi C_L)$	c[+]	$C_{rad} = 6.45 \times 10^{25} \times (X_{SiO_2})^{-10.4}$

*m is defined as $\left[\varepsilon\sigma\left({T_{lava}}^4 - {T_{back}}^4\right) + h_c(T_{lava} - T_{back})\right]$

[+]c is defined as $\rho(Cp\Delta T + \Phi C_L)$

A major difference lies in the estimation of surface heat loss. Harris et al. (1997a; Method-1) define it as the sum of radiation and convection whereas Coppola et al. (2012; Method-3) assume only radiative heat loss. The radiative heat loss in Method-1 is defined as $A_{lava}\varepsilon\sigma\left({T_{lava}}^4\right)$ and in Method-3 as $[(\sigma A_{pixel})/a]\Delta L4$. In the latter method, it is defined as Volcanic Radiative Power (VRP) and has an uncertainty of +/- 30%, although only for temperatures between 350°C and 1200°C (Wooster et al., 2003). Outside of this temperature range, VRP (Fire Radiative Power as originally defined by Kaufman et al., 1998) becomes much more uncertain, so it must be assumed that VRP is inaccurate in many cases for older, cooler lavas with surface temperature below 350°C. Method-1 takes the position that the instantaneous discharge rate can be calculated from a knowledge of the ratio of the rate of heat loss from the flow surface to the heat available to sustain these losses through cooling and crystallization of the volume of lava. Method-2 assumes that the temporal changes in the area of active lava during an eruption is a function of antecedent effusion rate (TADR) and that estimation of TADR from active lava area relies merely on adoption of the appropriate constant of proportionality. Method-3 relies on the same physics-based model as Method-1; however, they consider their estimate of time-averaged discharge rate to follow the definition of Harris et al. (2007).

The heat available to the flow is defined as a parameter called the radiant density C_{rad} in Method-3 (Coppola et al., 2012) with units of J m^{-3}, which is equivalent to the "c" in Method-2 and $\rho[Cp\Delta T + C_L\Phi]$ in Method-1. However, C_{rad} is dependent on the silica content of the lava (not its crystal content or cooling interval, as in Method-1) and the value has an error of +/-50%. In Method-1, $\rho[Cp\Delta T + C_L\Phi]$ is constant with a value of 7.9×10^8 J m^{-3}, which compares to a maximum value of 3.8×10^8 J m^{-3} for C_{rad}. Therefore, the amount of heat available to the flow estimated using Method-3 is between 2 and 15 times lower than the estimate using Method-1, which yields TADR values generally higher using Method-3 than Method-1 (as found in our results in section 4.3.1). The error associated with C_{rad} estimation always produces a wider range of discharge rate estimates when using Method-3 (the maximum TADR is exactly 3 times the minimum TADR) than when using Method-1 (the maximum TADR is generally ~1.7 times the minimum TADR). To study the relative differences in TADR derived from Method-1 and 3 in more detail, we define here a ΔTADR to express the change in our TADR time-series for different eruptions between Method-3 and Method-1 ($\Delta\text{TADR} = TADR_{M-3} - TADR_{M-1}$).

When ΔTADR is positive, the time-averaged discharge rate obtained using Method-3 is higher than Method-1, and when ΔTADR is negative the opposite is true.

For each method used to retrieve TADR, we input the same anomalous pixels from MODVOLC. We assume here that by using the same input pixels for each method, the influence of clouds on the estimated TADR cancels out. However, these methods still have some limitations. Satellite-based TADR estimates are dependent on the amount of spectral radiance from the active lava flow surface that can be detected from space, which is highly dependent on the cloud coverage and/or eruptive plumes. Clouds can easily hide the surface of an active lava flow and decrease the radiance detected by the instrument, which will underestimate the correct TADR, if the underlying assumption (that TADR is a function of active flow area) is valid. Patrick et al. (2003) and Harris and Neri (2002) also mention more limitations from the remote sensing technique for time-averaged discharge rate estimates, which arise from the assumptions that were made to establish these methods. The main assumptions are i) the eruption temperature is constant, ii) the lava flow is cooling-limited, and iii) the maximum potential surface area is attained when flow motion ceases. Some eruptions, e.g., when a lava flow is topographically controlled or growing by inflation, may violate some of these assumptions.

TADR derived using Method-2 (the coefficient method), as a simplification of Method-1, always follows exactly the same trend as the latter (based on the same active lava flow area A_{tot}). As is shown in Figure 4.5, there is a perfect correlation between Method-1 and 2 (low estimate) with a R^2 of 1. Therefore, in the rest of the next two section of this chapter we comment only on the relative difference in TADR and final flow volumes obtained using Method-1 and Method-3.

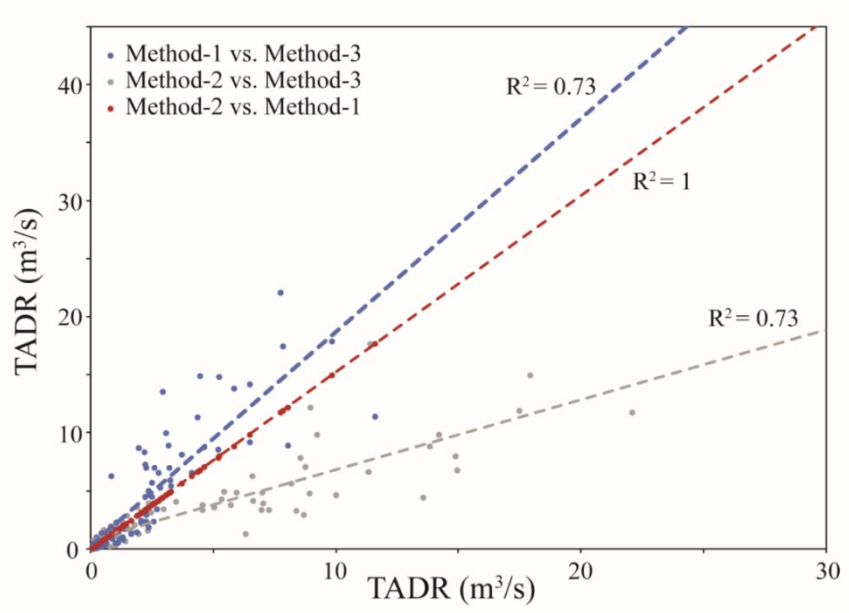

Figure 4.5. Correlation between the three methods for Fogo 2014-2015 eruption to estimate discharge rates, showing only the low estimates for clarity. This relationship is found for all eruptions.

4.2.2 Validating the accuracy of the space-based estimates

While comparing the shape and magnitude of the TADR time-series obtained from Method-1 (Harris et al., 1997a) and Method-3 (Coppola et al., 2012) provides insight into the satellite method and its general applicability, we can also quantify the accuracy of these approaches. Ground-based estimates of instantaneous lava discharge are relatively sparse or may be unavailable during an eruption, and have unknown errors. To validate which of the two space-based methods is most accurate, we integrate the satellite-derived TADR to estimate final flow volume and compare that to measurements of final flow volume made in-situ, which in many cases is well constrained via InSAR or GPS measurements. We looked for published estimates of the final lava flow volume for each of our 104 eruptions, which we will refer to as "literature" volumes. These volumes were derived using a variety of methods (including InSAR and geodetic surveys or sometimes from an unspecified method; recorded in Table A.3 in the Appendix). Unfortunately, not all volcanoes are accessible or intensively studied and so final flow volumes were available in the literature for only slightly more than 50% of the eruptions (58 of our 104 eruptions). For the remaining 46 eruptions, we used other remote sensing instruments such as

ASTER (Advanced Spaceborne Thermal Emission and Reflection Radiometer) and Landsat. We map the final flow outlines in these 30 × 30 m spatial resolution images, and use an estimate of the mean thickness (either from the literature or assumed based on other information) to obtain an estimate of volume. We compiled the estimated lava flow volumes from these satellite sensors with the assumed flow thicknesses (Table A.4 in the Appendix); we refer to these volumes as "inferred" volumes. Hereafter, when discussing final flow volumes estimated with both the literature and inferred from thermal satellite images, we refer to them as "recorded" volumes.

Based on our TADR time-series we can integrate the area under the curve over time to retrieve the lava flow volume estimated using the different methods (both minimum and maximum TADR from Method-1 and Method-3), and compare these estimates with the literature/inferred volumes. To do so, we identify all local maxima or peaks in each discharge rate time-series to remove low TADR values that are most probably induced by the presence of clouds in the image (reducing the spectral radiance detected by MODIS), or result from large satellite zenith angles (Bonny and Wright, 2017). We found that the peaks that were one standard deviation (one *nsig*) above the median of all maxima usually worked best for our eruptions. However, in the case where the number of TADR data points available for an eruption was small, we used all the possible peaks to avoid losing too much information. Then, we used a simple trapezoidal integration from the first to last hot spot detected by MODVOLC. We consider the volume that we retrieved from integration of TADR curves to be the Dense Rock Equivalent (DRE).

4.3 An assessment of relative changes in TADR determined using Method-1 and Method-3

First, we present several examples showing that the TADR time-series retrieved using the different methods differ (in Appendix all the eruptions studied are shown), to illustrate some important trends and systematic differences. The focus here is to highlight instances where Method-1 (Harris et al., 1997a) or Method-3 (Coppola et al., 2012) yield systematically higher or lower TADR than the other, and where the relative TADR derived by these methods changes in a more complex manner during an eruption. We use the following three eruptions to illustrate these points: Fogo 2014-2015, Nyamuragira 2004, Chirpoi 2012.

4.3.1 Three eruptions as examples of relative differences in TADR

4.3.1.1 Fogo 2014-2015

Fogo is an island in Cape Verde, a cluster of islands north-west of Africa, located at 14.95°N and 24.35°W. It is composed of a single stratovolcano, Pico, which erupted on November 23, 2014 for about 76 days. It produced Strombolian explosions, lava fountains from a fissure feeding lava flows (both ʻaʻā and pāhoehoe), and an ash plume that was visible almost 100 km away (GVP, 2014). This volcano, which had been quiescent since 1995, sits close to a couple of villages and caused about 1,000 people to be evacuated at the start of the eruption. The lava flows destroyed many homes, schools and roads and forced the airport to close. The TADR time-series for Pico do Fogo (Figure 4.6) demonstrates how Method-3 (Coppola et al., 2012) yields discharge rates that are higher than Method-1 (Harris et al., 1997a) for most of the eruption, which is the case for 90% of the eruptions in our database. The maximum TADR was found at slightly different time with the different methods. For Method-1 it was found on November 24 at 3:35 UTC with a maximum TADR of 18 m^3/s, and for Method-3 the maximum discharge rate (66 m^3/s) was found a day later on November 25, 2014 at 2:40 UTC.

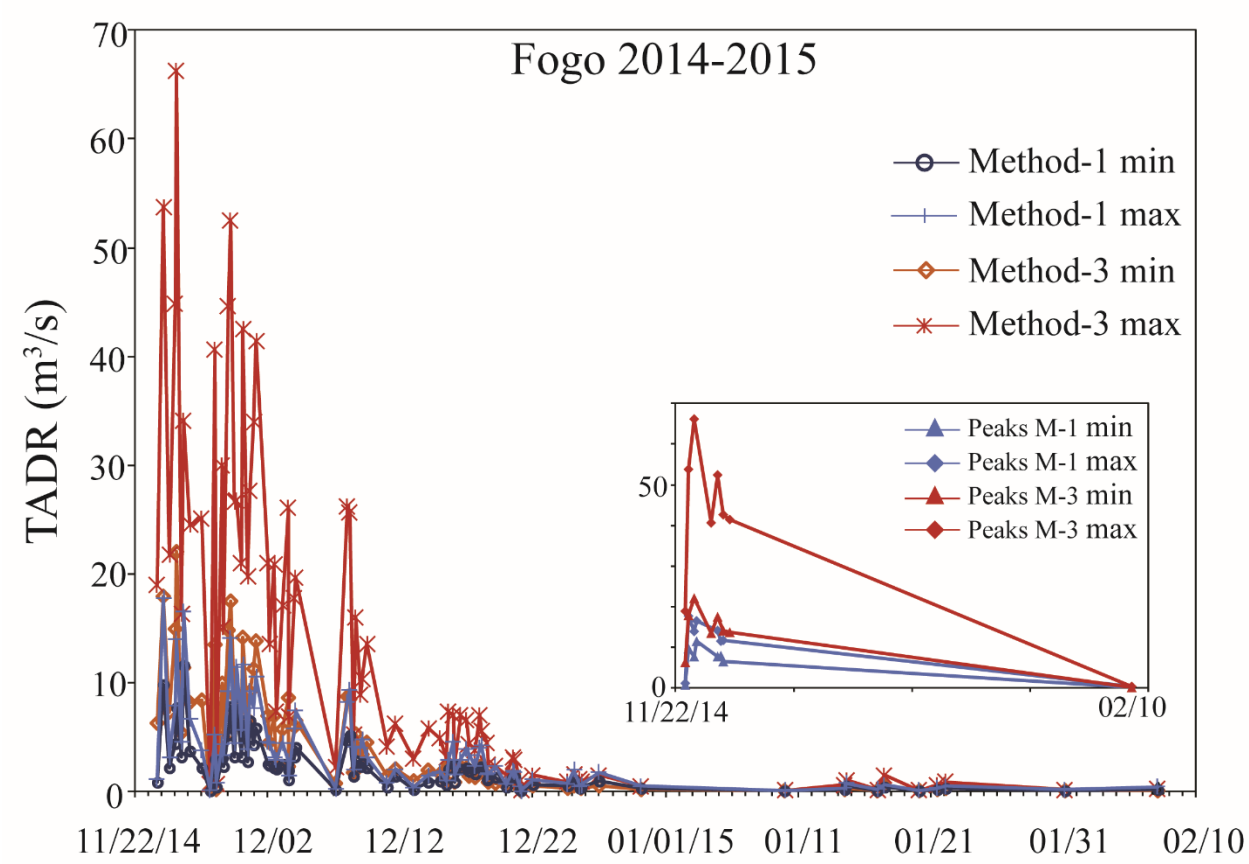

Figure 4.6. A) TADR time-series for Fogo 2014-2015 eruption using Method-1 and Method-3. Each method yields a minimum and maximum TADR values from the cold and hot cases for Method-1, and the low and high C_{rad} values for Method-3; inset shows the peaks selected to estimate the final volume (one *nsig*). The volume estimated is 2.5-4.4 × 10^7 m^3 from Method-1, 0.5-1.6 × 10^8 m^3 from Method-3, and 6-6.5 × 10^7 m^3 using ASTER images.

4.3.1.2 Nyamuragira 2004

Nyamuragira (also called Nyamulagira) is a shield volcano located in D.R. of Congo and is the most active volcano in Africa (Smets et al., 2010). The 2004 eruption emplaced both lava flow types (‘a‘ā and pāhoehoe) at the summit and on the NNW flank, and lasted for about 48 days based on the MODIS detections (May 11 to June 28). According to Smets et al. (2010), the eruption lasted only 24 days, starting on May 8; however, MODIS detected that the eruption continued up to 27 days longer. Figure 4.7 shows the results of our discharge rate calculations. We see that the maximum TADR is on May 15 23:10 UTC with 52 m^3/s estimated using

Method-1 (Harris et al., 1997a) and 203 m^3/s using Method-3 (Coppola et al., 2012). Method-3 yields higher TADR during the early part of the eruption, but Method-1 becomes higher towards the end of the eruption when Method-3 drops close to zero. We observed this trend for many eruptions at Nyamuragira.

4.3.1.3 Chirpoi 2012

Chirpoi is a small, uninhabited island located in the center of the Kuril Islands, Russia. This island comprises many volcanic edifices inside a partially submerged caldera, with the youngest volcano named Snow (GVP, 2017). Here we examine the eruption from Snow, and due to its remoteness, most of the information available about this eruption comes from satellite data. This eruption started on November 11, 2012, about 30 years after its last eruption. It was suspected that the eruption produced a lava flow on the south-east flank of the volcano (although there was no visual confirmation) and steam-and-gas emissions. According to MODIS satellite data, this eruption lasted about 37 days until December 17. In Figure 4.8, the TADR time-series shows that Method-1 (Harris et al., 1997a) yields discharge rates that are higher than Method-3 (Coppola et al., 2012) for most of the duration of the eruption; this is one of only two eruptions in our database where this is the case. This difference is produced by an estimate of VRP from Method-3 that is 10 times lower than the radiative heat loss from Method-1. The maximum TADR is reached on the first day (11/11) at 12:25 UTC with 1.6 m^3/s for Method-1, and 0.8 m^3/s for Method-3.

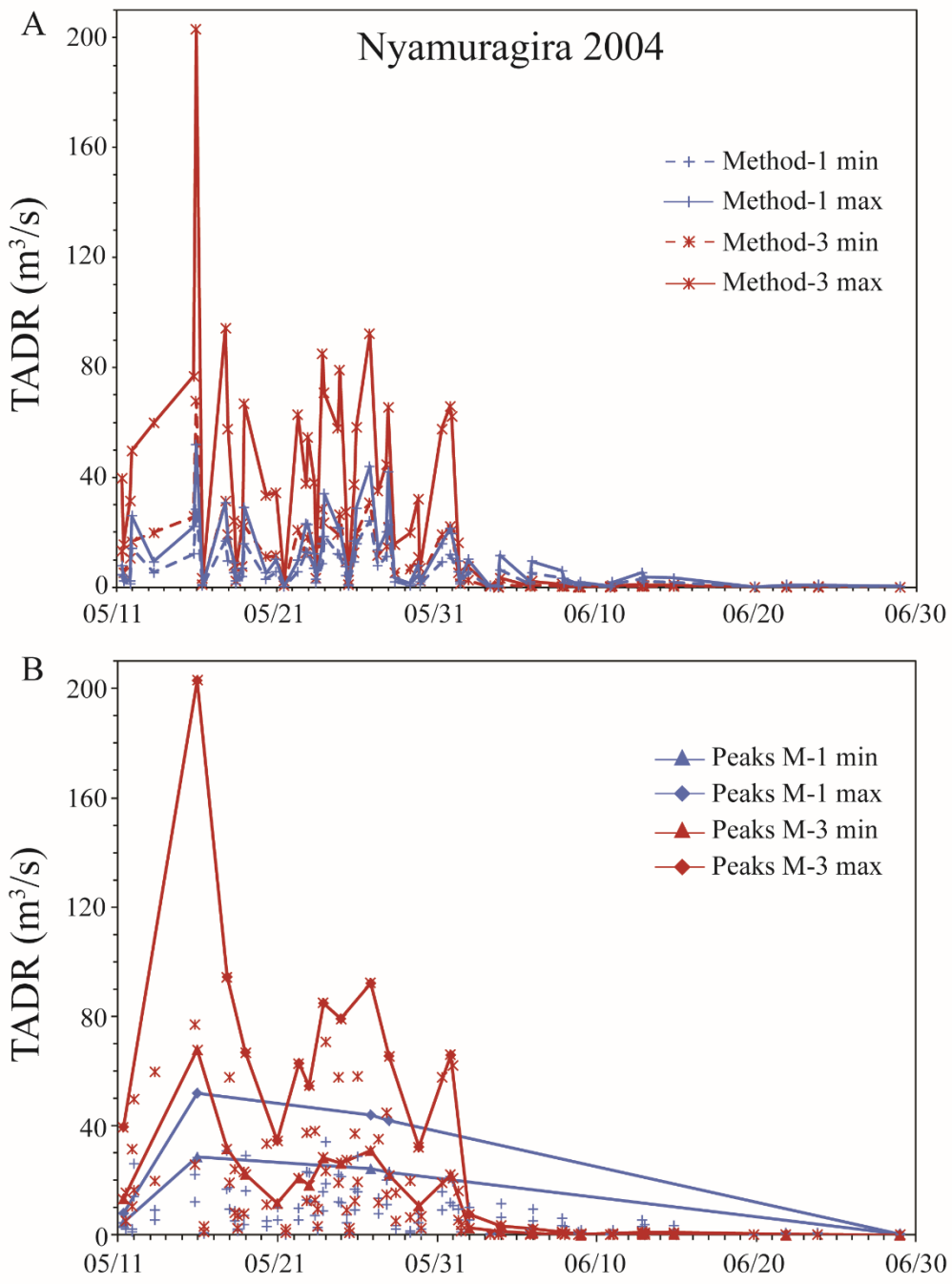

Figure 4.7. A) Nyamuragira TADR time-series using Method-1 and Method-3 from the May 2004 eruption; B) Identified peaks that were used to estimate a total flow volume of 0.65-1.2×10^8 m^3 with Method-1 (one *nsig*), 0.5-1.55×10^8 m^3 with Method-3 (all peaks), and 0.57-0.8×10^8 m^3 from Smets et al. (2010).

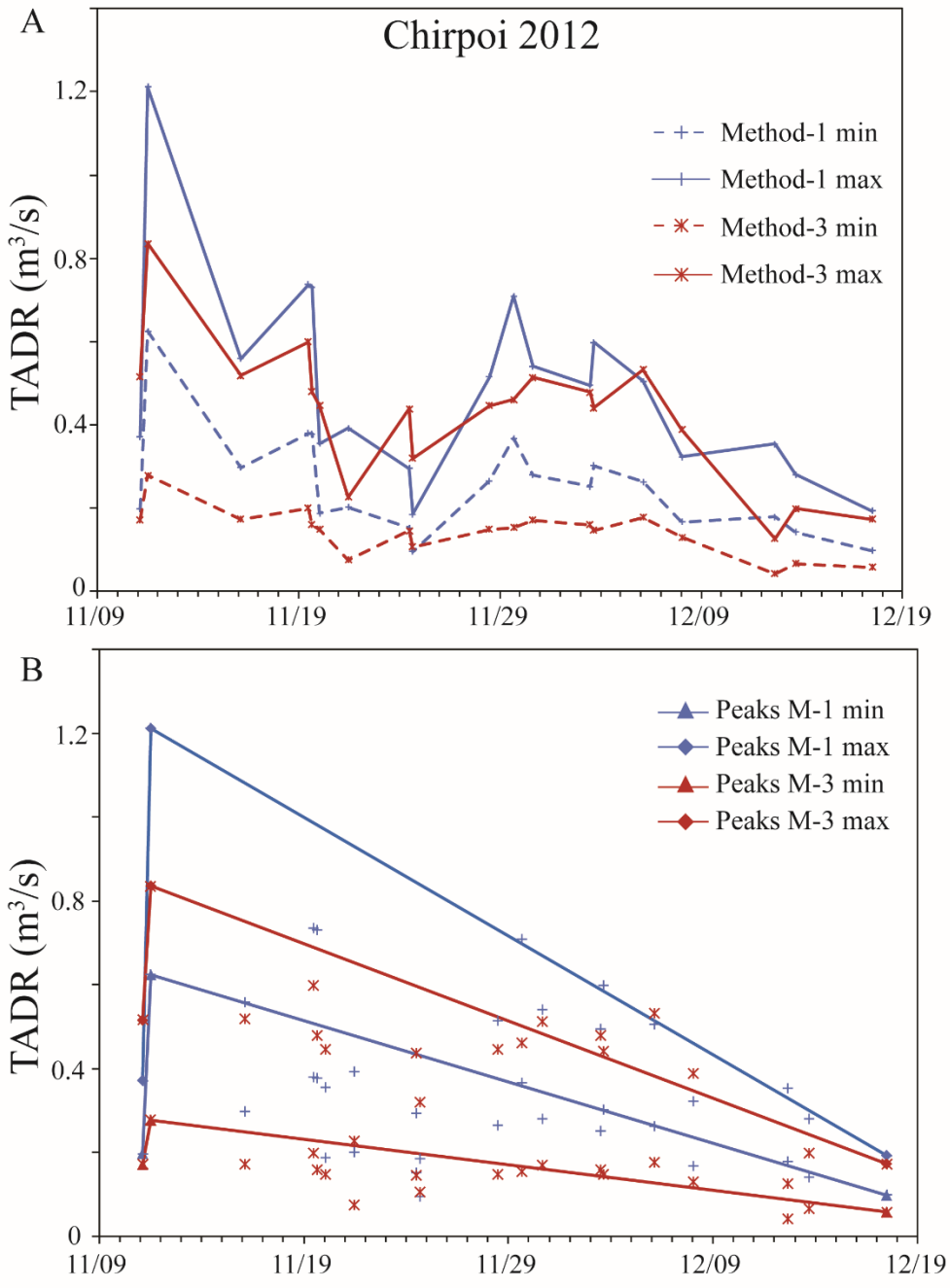

Figure 4.8. A) Chirpoi TADR time-series using Method-1 and Method-3 for its 2012 eruption; B) Same TADR with the identified peaks (one *nsig*) that allowed us to retrieve the total flow volumes. The final flow volume estimated with Method-1 is 1.1-2.2×10^6 m^3, 0.5-1.6×10^6 m^3 with Method-3, and 0.6-2.0×10^6 m^3 from ASTER images.

4.3.2 Discussion of the relative differences in TADR obtained using Method-1 and Method-3

All TADR time series from the 104 eruptions in our dataset can be organized in three different groups: a) the discharge rates from Method-3 (maximum) are higher than Method-1 during most of the eruption; b) Method-1 TADR (maximum) is higher than Method-3; and c) the relative difference in TADR reported by Method-3 and Method-1 (ΔTADR) switches from positive to negative during the eruption. We found that 90% of the eruptions fit into group a) where the lava discharge rates calculated using Method-3 are higher than Method-1 due to the large difference in the value used as heat available to the flow (section 4.2.1.4) . In the second group, we found only two eruptions (Chirpoi 2012 and Hekla 2000) where Method-1 gives higher discharge rate due to the underestimation of radiant heat loss using Method-3. Finally, 11 eruptions fit into group c).

Here we highlight the fact that each method yields different results and analyze when those methods actually differ from each other. Interestingly, out of the 11 eruptions in group c, we see that 70% of these eruptions exhibit a switch in ΔTADR from positive to negative at about 50% of the eruption duration. This is common for eruptions at Nyamuragira volcano (three eruptions) and Manda Hararo (two eruptions), where the maximum discharge rates estimated with Method-1 become higher than Method-3 toward the end of the eruption (Figure 4.7). The difference between Method-3 and Method-1 (ΔTADR) for the Nyamuragira 2004 eruption highlights this inversion in the TADR results. This pattern can probably be explained by the different wavelengths used in the two methods, because the sensitivity to high temperature surfaces is greater at the 4 μm spectral radiance than at 11 μm, which is better for detecting lower surface temperatures). During the early part of a vigorous channel-fed eruption, the average surface temperature of the flow is likely to be higher, leading to a larger increase in 4 μm spectral radiance than 11 μm spectral radiance. Towards the end of an eruption, a decrease in highly radiant incandescent cracks at the surface of the flow, and an increase of cooler crust will reduce the 4 μm spectral radiance disproportionately (Aries et al., 2001). When lava discharge rates determined using Method-3 are greater than Method-1 during the entire eruption, it is harder to discern such a pattern, but in some cases the minimum estimate of Method-3 becomes equal or lower to Method-1 maximum. We suspected this happens for the same reason but it is hard to distinguish in our dataset.

While we tried to apply strictly the original methods published in the literature, some small modifications were required. For example, in Method-1 (Harris et al., 1997a) we used MODTRAN instead of LOWTRAN values for the atmospheric corrections, while for Method-3 (Coppola et al., 2012) we did not resample the pixels to a 1 × 1 km. Furthermore, while we have strictly applied the methods of Harris et al. (1997a) and Coppola et al. (2012), in order to make direct comparisons, we recognize that the application of Method-1 has evolved over time. For example, in the two 1997 papers by Harris et al., there was no reference to vesicularity coming into play in the equations for density ρ and heat capacity C_p (i.e., see Equation 4.8). Only in the 1998 paper, do Harris et al. mention vesicularity and that the density and heat capacity should be corrected for void spaces. In terms of rate of heat loss (radiation M_{rad} and convection M_{conv} in Equations 4.5 and 4.6), we used the same equations as Harris et al. (1997a) even though these equations were later updated (both changed first in the Harris et al., 2005b paper noted as Q_{rad} and Q_{conv}), with additional heat losses coming from conduction or rain that could also be taken into account (see Harris et al., 1998). The calculation of radiant flux changed from using only T_{lava}^4 to T_{lava}^4-T_{back}^4 (although this update does not have any substantial impact since T_{back} is much smaller than T_{lava}, Equation 4.10). In terms of convective heat loss though, the change to a simpler equation depending on the convective heat coefficient h_c does make a difference and increases the total heat loss and therefore the final discharge rate that would result from application of a more recent formulation of the Harris et al. approach (Equation 4.10). The cooling range ΔT has also evolved since the original Harris et al. (1997a) paper and different values were tested from 150 K to 350 K in different papers from Harris et al. (2000, 2005a) and Haris and Neri (2002). We also note that the assumed surface temperature of active lava (T_{lava}) changed (tested with values from 100-1000°C, Harris and Neri, 2002, Harris et al., 2011), as well as the vesicularity values, crystal content Φ and the latent heat of crystallization C_L (Harris et al., 1999; Harris et al., 2000). In short, more recent updates to the Harris et al. method would result in different TADRs to those we report here. Another mode in which Method-1 has been used in the past (which belies the physics-based derivation) is to use field measurements to "fine-tune" the TADR calculation (Harris and Neri, 2002; Harris et al., 2010). In essence, an initial TADR estimation is made from the satellite data. If a coincident ground-based estimate (or series of such estimates) is known then values for parameters like vesicularity or crystal fraction can be

altered to force better agreement between the satellite and in-situ estimates (this can in a way be seen as changing the coefficient values, equivalent to applying Method-2).

In summary, the reason for our strict adherence to the methods originally published by Harris et al. (1997a) and Coppola et al. (2012) is to highlight the relative differences in TADR they return and we feel that those shown above are robust. However, we recognize that the first approach has evolved over time. The fact that Method-1 uses 11 μm radiance measurement and Method-3 uses 4 μm measurements has not changed over time, so relative differences in TADR due to this will still be apparent.

4.4 How accurately can TADR be derived from low spatial resolution infrared satellite data?

In this section, we focus on assessing the accuracy of Method-1 and Method-3 (by final flow volume comparison between MODIS-derived and recorded volumes) to investigate whether one method might work better overall, or for different flow types, eruption duration, or a specific volcano.

4.4.1 An examination of all 104 eruptions

We were able to compile estimates of the total lava flow volume based on our TADR time-series with the satellite methods described above, as well as from values published in the literature using different techniques, ranging from field studies to satellite images to DEMs and InSAR (accuracy of the estimate increasing in this order). Table A.3 shows final volumes estimated from Method-1 (Harris et al., 1997a) and Method-3 (Coppola et al., 2012) with both maximum and minimum estimates, as well as the literature values that we compiled (identifying the method used for this published final flow volume). Following from the TADR results, we found that, out of all eruptions, just four show a slightly higher volume estimate with Method-1 than Method-3. We found the final flow volumes for about 55% of our eruptions in the literature (58 eruptions) and used ASTER or Landsat images (following section 4.2.2) to estimate the final flow volume for the remaining eruptions (Table A.4). Unfortunately, for two eruptions it was not possible to estimate a final volume even using the Landsat/ASTER method (Reventador 2005

and Lopevi 2003) due to very cloudy images that obscured the lava flow, and subsequent eruptions that buried the flow of interest.

In Figures 4.9 and 4.10 we plot the minimum and maximum estimates of final flow volume for each eruption estimated by both Method-1 and Method-3, as well as the literature values (Fig. 4.9) and volumes inferred from ASTER or Landsat analysis (Fig. 4.10). This lets us see how all these recorded final flow volumes compare to the range of volumes estimated from the thermal remote sensing method of lava discharge rate retrieval. We found that for 35 eruptions (out of the 58 that had literature volumes available) the satellite-derived minimum and maximum volumes encompassed the literature final flow volume with one or two of the methods. Of these, Method-3 (Coppola et al., 2012) correctly encompasses the final flow volume for 22 eruptions, versus 20 eruptions for Method-1 (Harris et al., 1997a). The Coppola et al. (2012) method therefore encompassed the literature value slightly more often than does the Harris et al. (1997a) method. In addition to whether the infrared satellite method encompassed the "true" volume, we also noted which method allows us to accurately retrieve this volume. Since each satellite method retrieves a range of volumes (minima and maxima within which the true volume is assumed to lie), we identified whether the literature volume is better resolved by the final flow volume derived with the minimum or maximum TADR estimate. For Method-3 it is a clear that the minimum satellite-derived volume estimates are closer to the literature volumes than the maximum satellite-derived volumes (70% of eruptions are closer to the minimum volume estimate), which highlights the usual overestimation of final flow volume by this method. However, with Method-1 we did not find a systematic difference, and both minimum and maximum volume estimates are equally likely to fall close to the literature volume. It is important to remember that the range in TADR is larger with Method-3, therefore the range of volumes is also larger, and the probability of encompassing the published volume is also higher. For volumes inferred from satellite images (ASTER or Landsat), the same trend is visible as for the literature estimates (Figure 4.10). For 26 eruptions (out of the 44 eruptions without literature volumes available) the satellite-derived volumes encompassed the inferred final flow volume with one or two of the methods (almost all of them are identified with Method-1 and only half with Method-3).

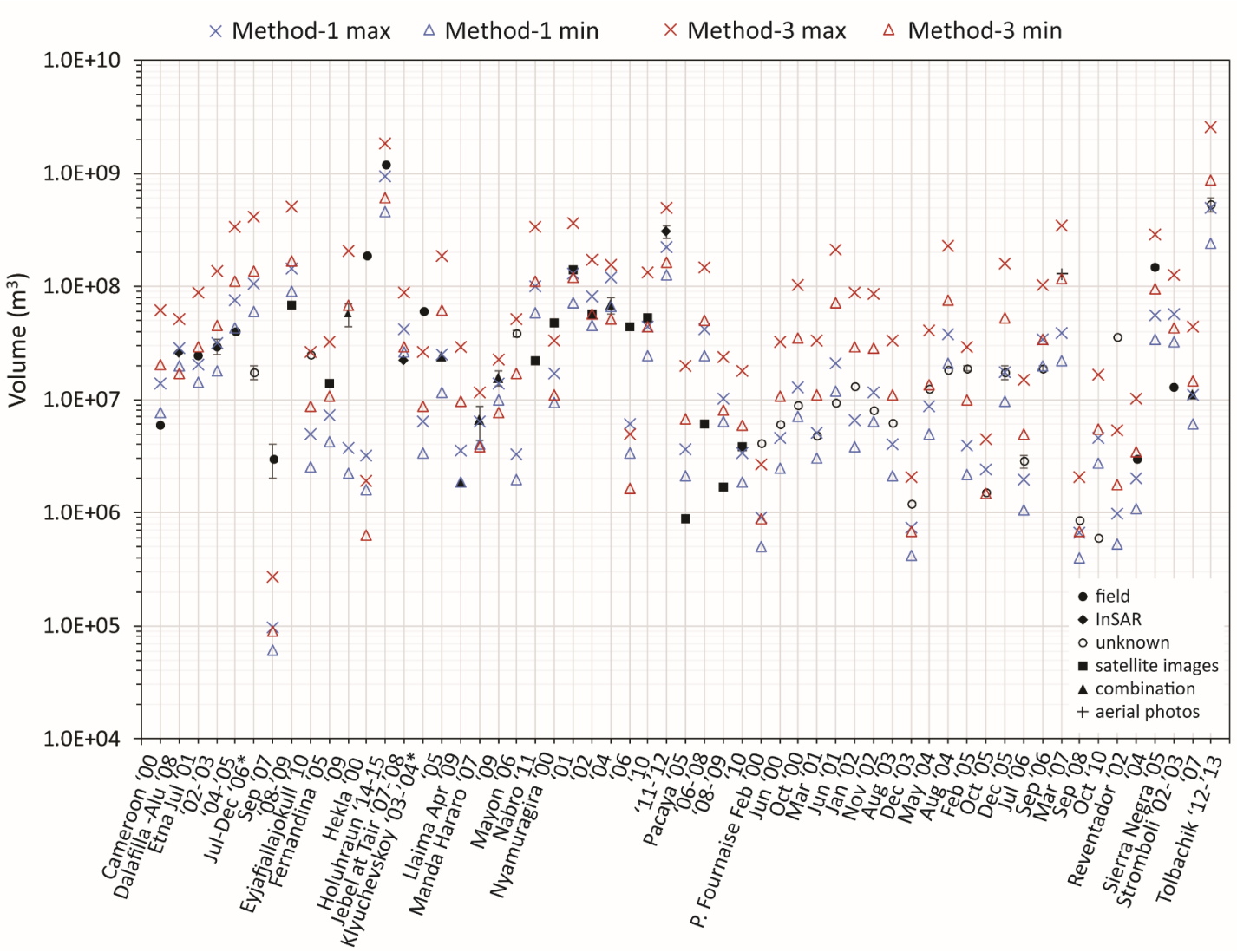

Figure 4.9. Final flow volumes derived from both Method-1 and Method-3, together with literature estimates for all available eruptions. It is important to note that the y-axis uses a log scale. Events that comprised two eruptions are shown with asterisks.

Figure 4.10. Final flow volume comparisons between the different methods and volume estimates from ASTER or Landsat for the eruptions with no published volumes available. The black lines are the errors associated with our estimates due to the range of flow thickness used. It is important to note that the y-axis uses a log scale.

We also tested the correlation between our satellite-derived volumes and all the recorded volumes (both literature and image-based estimates). When plotting the recorded estimates against the minimum or maximum satellite-derived volumes, we found that including the two most voluminous eruptions skewed our results. Therefore, we chose to remove those two influential points, Tolbachik 2012-2013 and Holuhraun 2014-2015, to better represent the dataset. Using this dataset of recorded volumes, Figure 4.11 shows how the final flow volume lies with respect to the 1:1 linear relationship between the recorded and satellite-derived final flow volumes (only minimum estimates are shown for clarity, as the same trend is found when using the with the maximum satellite-derived TADR estimates). When a data point is below that line, the final flow volume estimated from thermal remote sensing lava discharge rate is overestimated compared to reality, and if it is above this line, the satellite-derived volume is underestimated. We see that Method-3 more often overestimates the final flow volume (~60%) than Method-1 (~30%), and that the volumes derived from Method-1 are typically closer to the 1:1 line. This is confirmed by the correlation coefficient, between our minimum satellite-derived volume estimate and the recorded volume, being higher with Harris et al. (1997a) method than Coppola et al. (2012) method (R^2 is 0.41 for Method-1 against 0.26 for Method-3). This would suggest that Method-1 is more accurate than Method-3, although Method-3 encompasses slightly more often the literature final flow volumes (due to the larger range of TADR it generates).

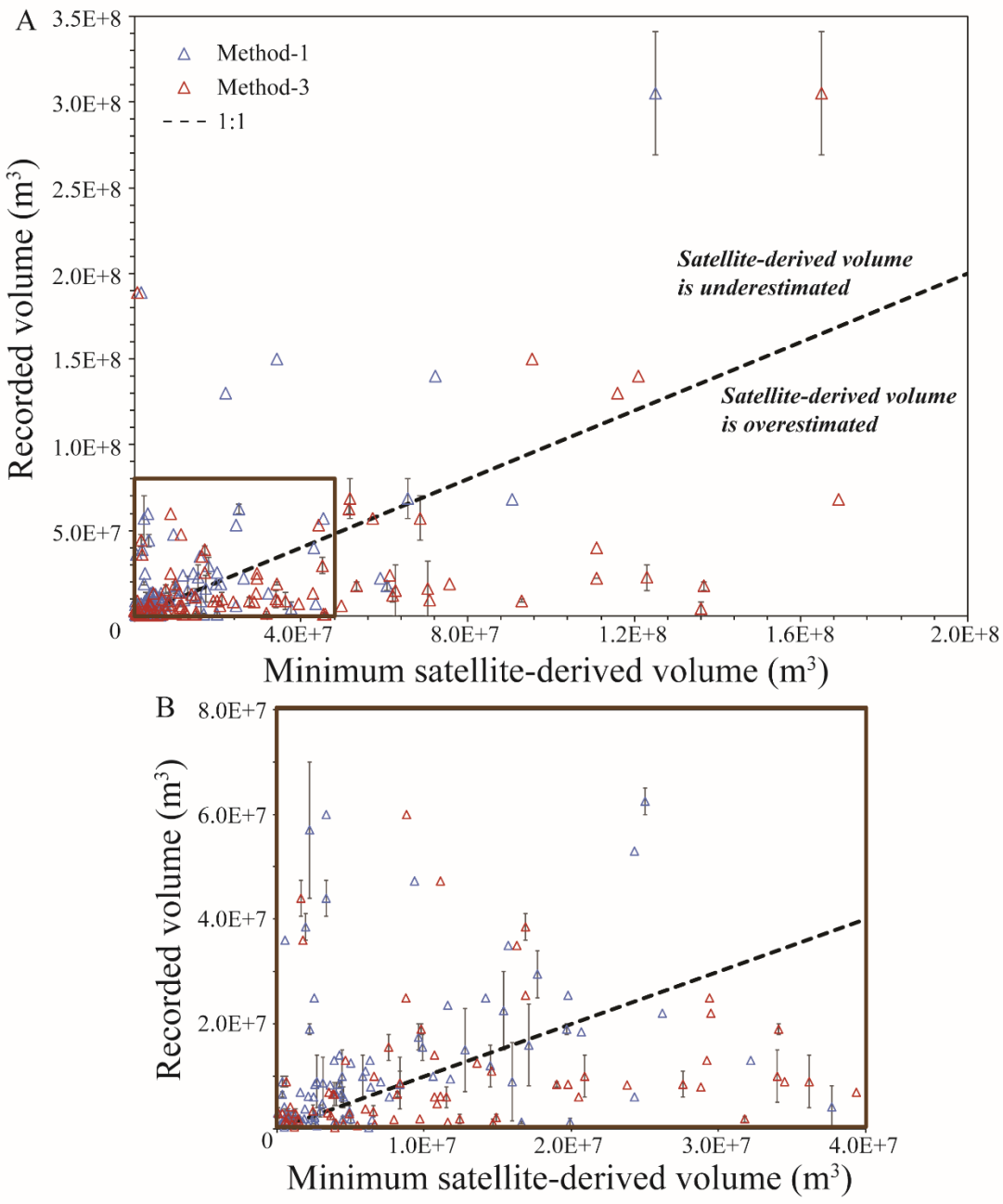

Figure 4.11. A) Correlation between satellite-derived and recorded volumes obtained with Method-1 and Method-3 used to retrieve TADR. This includes all the volumes found in the literature as well as the inferred volumes from ASTER/Landsat estimates for 100 eruptions. Not shown are two most voluminous eruptions from Holuhraun 2014-2015 and Tolbachik 2012-2013, as well as Reventador 2005 and Lopevi 2003, for which no have satellite images were available to allow a volume retrieval. B) Same graph focused on the brown rectangle zone in A with the same legend.

4.4.2 Evaluating the performance of the satellite-based methods for eruptions of different duration, of different lava flow types, and at different volcanoes

To investigate further the relationships between the different TADR retrieval methods and volume data, we divided our dataset into subsets based on different characteristics. First, we grouped our eruption dataset into different eruption durations (short, medium and long duration), different lava flow types (predominantly ʻaʻā versus pāhoehoe flow types, or a combination of both/indeterminate) and different volcanoes (for volcanoes that had more than one eruption during our study period). We then reexamined the correlation between our satellite-derived volumes and the recorded volumes (both literature values and volumes inferred from imaging data). We define an eruption to be of long duration when it lasted longer than 90 days, of short duration when it lasted less than 10 days, and medium duration when it was in between, based on the MODIS detection (the start of the eruption is the first hotspot detected and the end of eruption is the last hotspot detected). We see that generally the longer the eruption is, the better is the correlation (Figure 4.12a, b and c), and that Method-1 (Harris et al., 1997a) has a higher correlation coefficient in most cases. Method-3 (Coppola et al., 2012) has a higher correlation coefficient for medium eruption durations. This confirms that the longer an eruption lasts, the more TADR data are generally available, and the closer the final flow satellite-derived volume estimate is to reality. This is because the effects of clouds are ameliorated with higher temporal resolution and a longer measurement record, allowing the true variation of TADR to be better constrained from space. For short duration eruptions so little data may be available that reliable estimates of TADR (and hence volume) are not possible.

In the case of the different lava flow types (Figure 4.12d, e and f), the best volume correlation is for the combination of both ʻaʻā and pāhoehoe flows produced during a single eruption using either one of the methods, but Method-1 is overall better correlated with final flow volumes. For ʻaʻā flows, the correlation coefficient is again slightly better with Method-1 (when removing influential eruptions like Hekla due to its large final flow volume), although the coefficient is the lowest of all the lava flow types (R^2 is about 0.3). However, for pāhoehoe flows the correlation is better than ʻaʻā flows (R^2 is about 0.5 for both methods), which seems counter-intuitive based on how the methods were defined. Early papers from Walker (1973) and Wadge (1978) expressed the relationship between lava flow lengths and effusion rates mainly based on

ʻaʻā flows from Etna. However, Malin (1980) analyzed mainly pāhoehoe Hawaiian flows and found that the relationship between flow rate and length is not maintained. Pieri and Baloga (1986) combined all the previous ideas to show that the linear relationship is between the effusion rate and the area of the flow rather than its length. They defined two different quantitative relationships for a thermally mixed and unmixed-case (most Hawaiian lava flows are not thermally mixed; both channel-fed ʻaʻā and tube-fed pāhoehoe with the former being radiation limited instead of conduction limited for the latter). Method-1 and Method-3 are derived from the unmixed radiation limited case and should therefore be more accurate for ʻaʻā flow types rather than pāhoehoe flows. The main reason we expected the satellite-based TADR method to be more accurate for ʻaʻā flow types rather than pāhoehoe is because the surface of a pāhoehoe flow usually forms lava tubes that insulate the flow, and can travel to greater distances for a given discharge rate. We suspect that the correlation for pāhoehoe flows is improved in comparison to ʻaʻā flows because all pāhoehoe flows recorded here are from the same volcano, Piton de la Fournaise in Réunion Island, for which eruption conditions (i.e., lava flow composition, slope, topography) vary very little. In contrast, the ʻaʻā flow correlation is based on 14 different volcanoes. We conclude that satellite-derived lava discharge rates yield more accurate values in the case of an eruption producing both lava flow types and of a longer duration.

We also analyze the results for each volcano with more than one eruption recorded during the 15-year time period. For Etna (Figure 4.13a), Stromboli, Klyuchevskoy and Pacaya, it is clear that Method-1 is more appropriate than Method-3, with satellite-derived volumes closer to the final flow volumes found in the literature. These volcanoes tend to erupt predominantly channel-fed ʻaʻā flows and we showed previously that Method-1 performs better in this case. For Piton de la Fournaise, Nyamuragira (Figures 4.13b and c) and Manda Hararo, both methods perform well. Therefore, interest in a given volcano might help in choosing the best method to retrieve TADR.

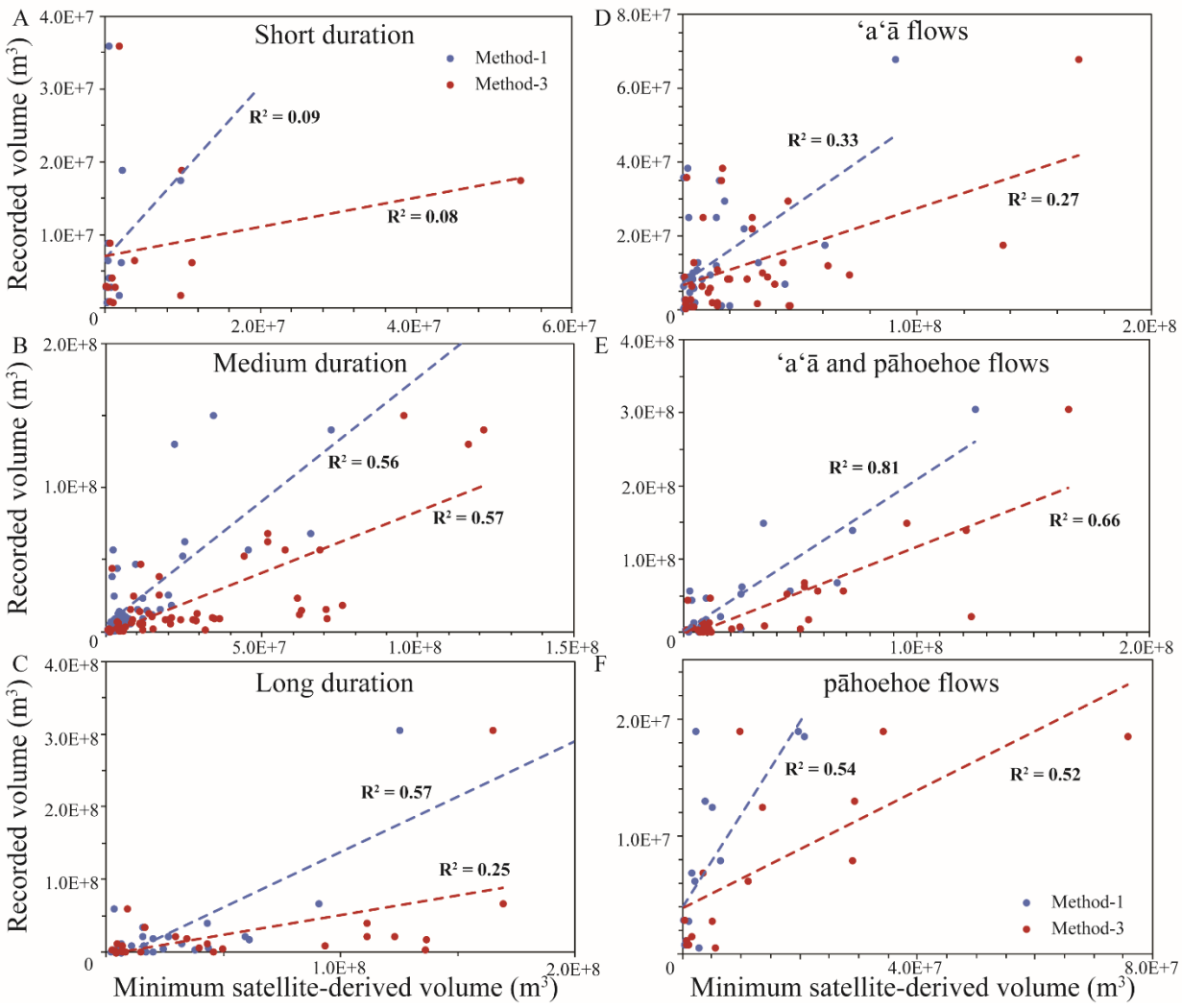

Figure 4.12. Comparison of volume correlations for different eruption durations, A) short duration, B) medium duration, and C) long duration. And different lava flow types , D) ʻaʻā flows (excluding Hekla), E) ʻaʻā and pāhoehoe flows (excluding Tolbachik and Holuhraun), F) pāhoehoe flows (excluding P. Fournaise April 2007). We chose to show only the minimum satellite-derived volume estimate because of similar results with the maximum values. Holuhraun and Tolbachik have been excluded from the long duration eruption group and Hekla from the short duration group. The same legend is valid for each figure.

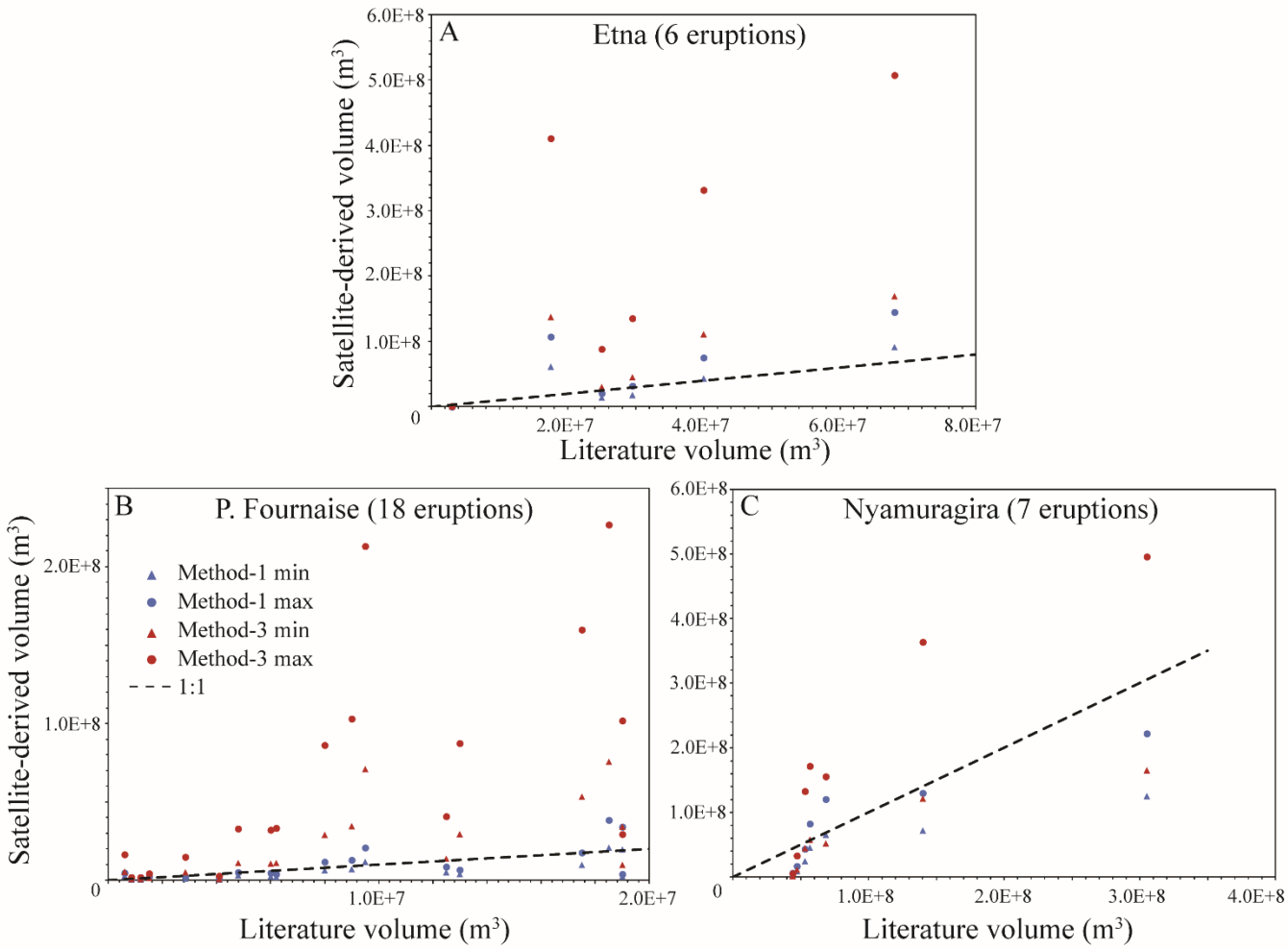

Figure 4.13. Correlation between satellite-derived volumes and literature volumes for some volcanoes. We are showing both maximum and minimum volume estimates derived from MODIS TADR for both Method-1 and Method-3. A) Mount Etna, B) Piton de la Fournaise, and C) Nyamuragira. The same legend is valid for each figure and the black dotted line is the 1:1 relationship.

4.4.3 Possible reasons for discrepancies between the satellite-based and recorded lava flow volumes

We used the identification of maxima in each TADR time-series to estimate the final flow volume by integrating the area under the curves, assuming we eliminated cloud-contaminated values by using a criterion of one standard deviation above the median of all peaks in the time series. However, it is possible that this technique would be eliminating valid data and low TADRs that were not produced by cloudy images but by real lower magma fluxes. This would be the case if a real low TADR is followed closely by an increase in discharge rate that is large enough to be higher than the one standard deviation criterion, and would therefore be overlooked. This could result in an overestimation of the total lava volume produced during the eruption. However, for eruptions where the number of TADR data points was too small to effectively identify peaks, or the peaks were misidentified, we used all maxima in the time series (47 eruptions**)** to estimate the final flow volume. Using every maximum could lead to an underestimate of flow volume by including more cloud-contaminated points. There is no real way to tell which technique is more appropriate, so we decided on a case-by-case basis by examining the results of the peak identification for each eruption. Eruptions of short duration are more likely to have fewer TADR data points available, possibly worsened by cloud-contamination, which suggests that the TADR time-series would be less reliable, and thus the final flow volume would also be less accurate. A longer eruption duration would likely increase the number of TADR data points, allowing for good peak identification, suppressing the effect of cloud-contaminated images, and hence yielding a more accurate final flow volume.

4.5 Improved estimation of satellite-derived TADR by deriving new coefficients relating A_{tot} to TADR from a global, multi-decadal time scale dataset

We now have an internally consistent dataset for which the area of active lava has been derived (A_{tot}, Equations 4.3 and 4.4) for all eruptions at all volcanoes in our database. We also have an independently derived dataset of final flow volumes. By combining these two datasets, we can go back to a simple relationship like Method-2 (the coefficient method) and define a new coefficient for each eruption, which best relates A_{tot} and volume (and hence TADR). Based on all

the literature volumes we compiled, for every eruption the satellite-derived volume is different from the literature volume, but we can tune the value of a coefficient X until the satellite-derived TADR is such that the volume derived from a time-series of those values matches the literature volume (e.g., Figure 4.14). In general, an increase in the coefficient X means that for a given active lava area the TADR required will be higher. We tested how well a single, globally applicable coefficient value would perform (i.e., can a single value of X improve our ability to estimate TADR from measurements of A_{tot}?) by using an average of all coefficients (only using the literature values of final volume for their better accuracy, not the recorded values). We found that a single value for all basaltic eruptions would not be helpful and instead would yield a final flow volume that is commonly further away (74% of the 58 eruptions) from the literature values. As Harris et al. (2007) mentioned, it is important to define coefficients that are valid on a case-by-case basis due to different properties, such as lava temperature, background temperature, crystallinity and volcano slope, that would influence the coefficient values (i.e., the relationship between A_{tot} and TADR). Unlike his work, we did not rely on establishing a range of values for the thermo-physical properties of lava playing a role in Method-1 (Harris et al., 1997a, Equations 4.7 and 4.8) but used literature final flow volumes to estimate new coefficients that yield final volumes matching the literature values. Therefore, we chose to define a coefficient for each volcano by averaging or using the resulting range of coefficient X that we derived for its eruptions.

In Table 4.4, we show the new coefficients that we compiled (X_{new}). We could not define a new coefficient for each volcano for which literature volumes were available (20 volcanoes), because it was clear that some coefficients were not reliable due to a large difference between the satellite-derived volume and the literature volumes. It is especially difficult when, for a given volcano, we have only two eruptions and the coefficients are too different from each other. In general, we feel confident that we derived a valid coefficient value for 14 volcanoes (37 eruptions). In some cases, the range of the coefficient X can be decreased, such as for Manda Hararo where we estimated X to be 2.25 - 27.5 $\times 10^{-6}$ m/s instead of the previous 0.9 - 29 $\times 10^{-6}$ m/s (Harris et al., 2007). For cases like Mt Etna, we decided to define two coefficients, one for summit eruptions and one for flank eruptions, because of different topographic constraints that can influence the lava flow propagation. We found a coefficient of 1.1 - 13 $\times 10^{-6}$ m/s for summit

eruptions and 2.35 - 27.5 × 10^{-6} m/s for flank eruptions, instead of 2.1 - 33 × 10^{-6} m/s in Harris et al. (2007). This illustrates that a lower coefficient value for summit eruptions where lava is flowing on steeper slopes is more appropriate than for gentler flank eruptions.

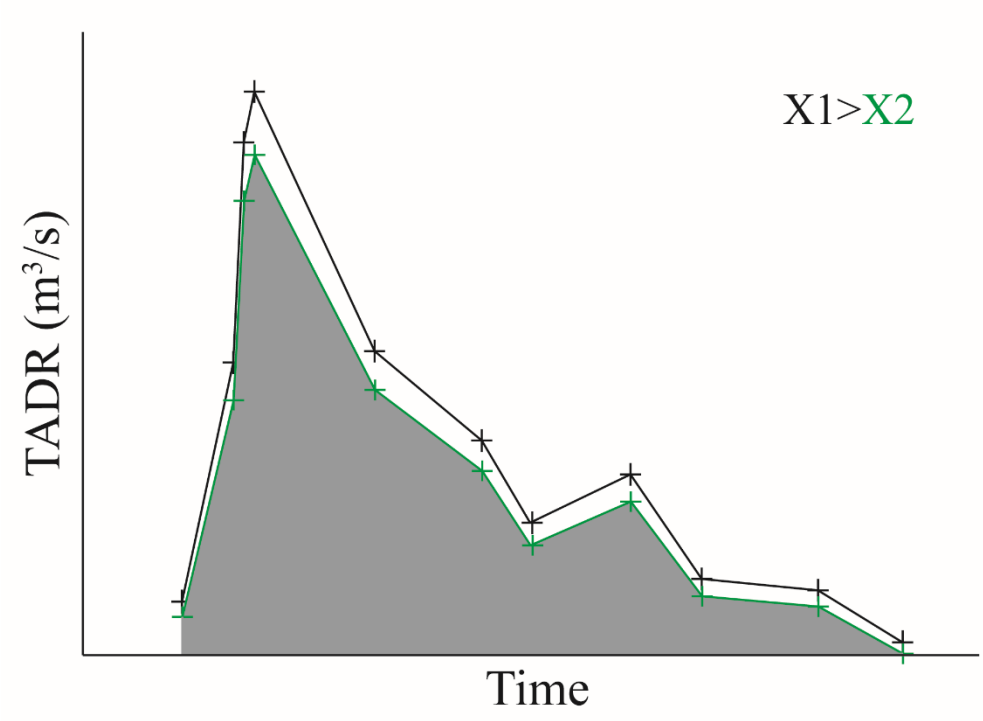

Figure 4.14. Schematic showing different TADR time-series for different coefficient values (each color corresponds to a different coefficient X). In this case X1>X2. By modifying the value of X, we can tune it until the integration of TADR over time (in grey shaded area) matches the final flow volume taken as a reference for each eruption.

Another conclusion is that the value of the coefficient X is mainly influenced by parameters from the environment into which the lava is erupted (elevation, slope, pre-existing topography) rather than small differences in the silica content of the flow. Figure 4.15 illustrates the improvement obtained using new coefficient values for all the eruptions, compared to the previously defined coefficients from Harris et al. (2007; X_{2007}). It is clear that the range of final flow volume decreases with the new coefficients, which improves the estimated volume most of the time, but also sometimes perversely yield volume further from the literature values (e.g., Piton de la Fournaise because the final flow volume estimated with X_{2007} is split almost evenly

between higher or lower volumes estimates with respect to the literature volumes, therefore their effect counteracts when taking the average). In summary, the new coefficients in Table 4.4 would, if used with values of area of active lava calculated using the method described in section 4.2.1, improve TADR estimates by an average of 30-50% overall.

Table 4.4. New coefficients estimated based on the literature volume values. In parentheses are the number of eruptions used for each volcano. All the silica weight percentages are the same as Table 4.2. Asterisks denote coefficients estimated from the range of coefficient values available for a given volcano instead of an average.

Volcano	**X_{2007} ($\times 10^{-6}$ m/s)** ***Harris et al., 2007***	**X_{new} ($\times 10^{-6}$ m/s)** ***This study***	**$XSiO_2$ (wt%)**
Nyamuragira flank **(5)**	0.9 - 29	2.7 - 71*	45.4
Summit and flank (2)		1.4 - 18*	
Etna summit **(3)**	2.1 - 33	1.1 - 13	47.9
flank (2)		2.35 - 27.5	
Manda Hararo (2)	0.9 - 29	2.25 - 27.5	48.5
Fernandina (2)	0.9 - 29	4.1 - 80*	48.5
P. Fournaise (19)	2.1 - 33	3.7 - 39	49.4
Pacaya (4)	2.1 - 33	0.3 - 6.1*	50
Holuhraun (1)	2.1 - 33	3.6 - 33	46.5
Dalafilla-Alu (1)	0.9 - 29	1.8 - 22	48.5
Cameroon (1)	0.9 - 29	1.1 - 11	48.5
Jebel at Tair (1)	0.9 - 29	1.2 - 13	48.5
Nabro (1)	0.9 - 29	0.5 - 5.7	48.5
Sierra Negra (1)	0.9 - 29	6 - 69	48.5
Tolbachik (1)	2.1 - 33	3.9 - 35	53
Llaima (1)	2.1 - 33	1.3 - 13	53

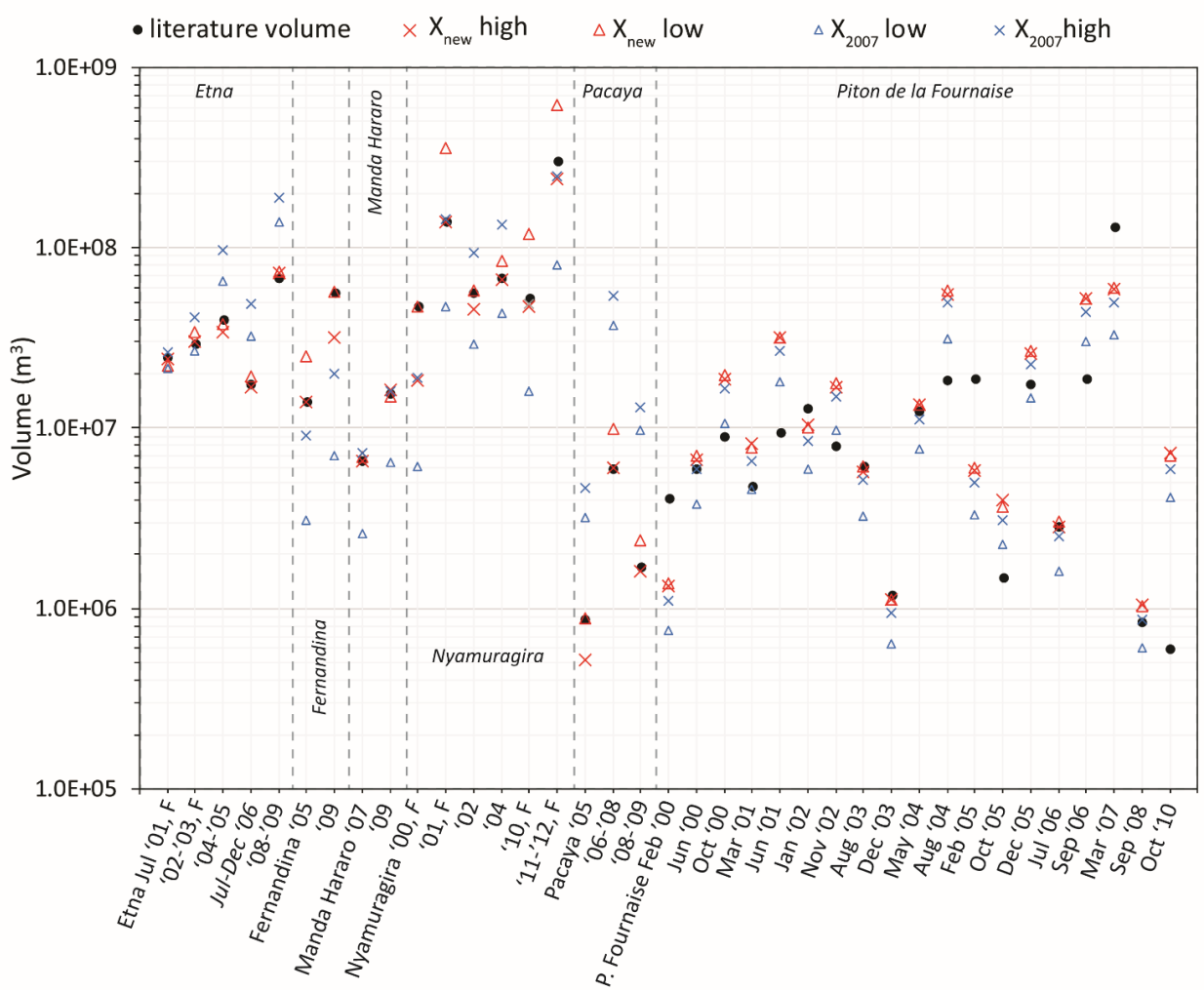

Figure 4.15. New volumes estimated with the new coefficients (X_{new} in red) for the six volcanoes with more than one eruption, as compared with the volumes estimated using the previously defined coefficients from Harris et al. 2007 (X_{2007} in blue). F specified on the x-axis indicates that the new coefficient is specific for flank eruptions instead of summit eruptions.

4.6 Conclusions

We have analyzed thermal infrared satellite data acquired by MODIS for all basaltic lava flow-forming eruptions on Earth since 2000. We created a database of TADR time-series for each of 104 effusive eruptions at 34 volcanoes and applied three thermal remote-sensing methods to retrieve lava discharge rate (Appendix). Each method, defined in the literature (and often used interchangeably), was assessed and compared to investigate their performance and demonstrate to what extent they give comparable results. The two physics-based thermal remote-sensing methods (Method-1 and 3) give different values of TADR, as suspected (Figures 4.6, 4.7 and 4.8). Investigating the relative differences in TADR between these two methods, we found different behaviors for different eruptions, which we divided into three groups. First, Method-3 (Coppola et al., 2012, 2013) gives TADR higher than Method-1 (Harris et al., 1997a, b, 1998) for the entire eruption duration for 90% of the eruptions we studied. Second, only two eruptions exhibit a higher TADR estimated with Method-1 than Method-3 for the entire eruption duration. Last, an interesting feature was observed when the TADR results from both methods are mixed. We found that 70% of these eruptions demonstrate a switch in the discharge rate difference between each method (ΔTADR) from positive to negative about half way through the eruption (Figure 4.7, i.e., Method-1 values become higher than those of Method-3 due to the former method higher sensitivity to lower lava surface temperatures).

Our results indicate that Method-1 is in better agreement with ground-based measurements than Method-3 because it yields better correlation with independently estimated final flow volumes (derived from either the literature or inferred from satellite images; Figure 4.11). However, Method-3 encompasses the recorded volumes more often than Method-1 due to its greater range between minimum and maximum estimated volumes (Figures 4.9, 4.10). For this method, the minimum satellite-derived volume estimates are closer to the literature volumes than the maximum satellite-derived volumes (70% of eruptions are closer to the minimum volume estimate), which highlights the usual overestimation of final flow volume of Method-3. We also confirmed that the longer an eruption is, the more accurate is the satellite-derived final flow volume (and hence TADR), due to the typically larger number of TADR points, which reduces the potential effects of cloud (Figure 4.12). We also found that both volumes derived from both satellite-based methods are more accurately correlated with the recorded volumes in

the case of eruption producing both lava flows types (‘a‘ā and pāhoehoe) rather than pāhoehoe flows or, as we would expect, ‘a‘ā flows (Figure 4.12). Lastly, we found that in some cases, one satellite-based method to estimate TADR works better for a given volcano, such as Method-1 for Etna (Figure 4.13).

The method to retrieve lava discharge rates from infrared satellite data has evolved over time from the original physics-based model (that claims to relate heat flux to the cooling and energy content of the mass of lava; Method-1) to a simple empirical relationship between satellite-derived active flow area and time-averaged discharge rate (Method-2), back to a new physics-based model (Method-3). However, the physics-based models do not capture the complexities of the lava discharge rate retrieval. The final flow volume estimates (minimum and maximum) encompass the recorded volumes (literature and inferred volumes) for just over 60% of all the eruptions in our database (irrespective of which method is used; Figures 4.19 and 4.10). After Wright et al. (2001a), we know that the discharge rate is proportional to the active lava area with a coefficient X following Equation 4.10. Therefore, we revisited this simpler explanation for the satellite-derived estimation of TADR and estimated new coefficients for more effusive basaltic volcanoes (14) using the literature volumes we compiled. We were able to refine some coefficients for volcanoes that were already compiled (Harris et al., 2007) and differentiate values for summit or flank eruptions (Figure 4.14 and Table 4.4). Using the new coefficients for these 14 volcanoes allows an improvement in TADR estimation and would therefore be recommended for use during future eruptions.

CHAPTER 5

CONCLUSIONS

The multi-decadal analyses of basaltic effusive eruptions presented in this dissertation show the importance of thermal infrared satellite remote-sensing measurements of lava discharge rates to help understand how these eruptions work, and in some cases how long the eruption will last. Thermal satellite remote sensing is well suited for studying many lava flow parameters such as temperature, cooling rate, and lava discharge rates. I focus on basaltic effusive eruptions in this dissertation because they are the most common features on the surface of the Earth. The MODVOLC archive provides a unique database that quantifies every such eruption around the globe since 2000.

Chapter 2 relies upon the theory defined by Wadge (1981) who suspected that most episodic basaltic effusive eruptions would exhibit a typical asymmetric waxing-waning trend of effusion rate over time. This work is based on a simple elastic model of the volcanic system, which during an eruption results in the fast increase of effusion rate at the beginning of an eruption (waxing phase) due to the release of magma chamber overpressure until it reaches a maximum. The effusion rate then slowly decreases exponentially over time (waning phase) from the elastic release of energy until the magma chamber re-equilibrates with the lithostatic pressure. Previous effusion rate studies highlighted that this typical asymmetric behavior was commonly observed for basaltic lava flow-forming eruptions. An initial idea for this project was to use this theoretical behavior to 1) see how commonly we could find it in a worldwide volcanic eruption database and 2) use this theory as an application for creating a predictive tool to know how long an eruption will last and test how well it can perform. I used the MODIS database of 104 eruptions since 2000, creating a TADR time-series for each of them using Harris et al. (1997a) method, to show that only 30% of the eruptions followed this waxing/waning trend. Another 12% of the eruptions showed a shorter waxing period that I called Half-Wadge type and 8% showed a double-pulse style of discharge rate. However, the 50% of the eruptions remaining did not demonstrate any specific curve shapes. For 16 eruptions that behaved ideally (and had enough satellite-derived TADR data points), I tested this waning model to predict, in a

retrocasting manner, when the eruption would end. I fit an exponential curve to the TADR waning phase, starting at the maximum discharge rate and updating the prediction as the number of TADR data points increased, to mimic a near-real time predictive capability during the monitoring of an eruption. I found that when this ideal shape of discharge rate time-series was attained, we could generally predict accurately when an eruption would end before half the eruption duration was reached. The double pulse style was not tested here but I think it could also be used in a predicting fashion by simply updating the exponential decay curve after the point when the new, secondary, maximum is reached. Predicting when an eruption would stop would be very valuable during multi-month effusive eruptions for the population living nearby to have a better constraint on how long they will be displaced. Satellite TADR measurements would improve with the availability of thermal satellite instruments with higher temporal and spatial resolutions.

Chapter 3 focuses on the case of the Holuhraun eruption in Iceland. This basaltic effusive eruption was the largest in Iceland since the Laki eruption in 1783-1784. This was an exceptional opportunity to study a lava flow-forming eruption that spread over almost flat ground, and was well monitored by many volcanologists in the field, with geophysical methods, and with satellite images. I chose to use MODIS data to estimate lava discharge rate for this six month-long eruption and compared the TADR evolution with in-situ discharge rates estimated through mapping of the flow front advance and volume estimates. I compared 866 TADR values retrieved by MODIS data with 33 TADRs retrieved from the ground over the entire eruption. Even for such a well-studied eruption, the temporal resolution attained in the field is still much lower than that available from space. I used a second method, a simplification from Harris et al. (1997a), to estimate TADR based on Wright et al. (2001a) and Harris et al. (2007), using a predefined coefficient for another Icelandic volcano to test how well the thermal satellite-based method was applicable for this case study. I found that due to the highly radiant and large area covered by the flow field, the range of lava surface temperature of 100°C and 500°C commonly assumed to cover the full range of possible surface temperatures when estimating TADR was not appropriate during the first 30 days of this eruption (the TADR estimated based on in-situ measurements is 2-3 times higher than the upper satellite-based estimate). However, agreement between the satellite and field-based estimates could be forced by raising the upper limit of the

assumed temperature range to 1000°C. Although the exact TADR values were different at the beginning of the eruption, the general TADR trend from both satellite- and ground-based measurements follow the same pattern. The final flow volume we retrieve from ground-based measurements is in good agreement with the upper volume estimate derived from the satellite-based method based on the typical high lava surface temperature (500°C). I notice the presence of a change in the TADR between the two methods at about day 50 when the ground-based estimate becomes lower than the upper satellite-based estimate (at 500°C) and similar to the low space-based TADR (at 100°C). Thus, this turnover compensates for the TADR discrepancies and yields flow volume in good agreement.

Chapter 4 aims to investigate the three thermal infrared remote sensing methods available in the literature that are commonly used to estimate lava discharge rate (Harris et al., 1997a; Wright et al., 2001a; Coppola et al., 2012). It is common for published papers to refer to any one of these methods as if they give similar results. However, I suspected that they actually yield different time-averaged discharge rates values since they use different wavelengths (11 μm versus 4 μm) and rely on slightly different theory. I used the same 104 basaltic effusive eruptions TADR time-series database as in Chapter 2 but estimated TADR with all three methods for each eruption. The first method was developed using a physics-based model depending on heat loss properties of lava flows. The second method then simplified Method-1 by identifying that the only variable parameter in all the equations of this physics-based model was the area of active lava present in each pixel. Method-2 is therefore based on a coefficient of proportionality between active lava area and time-averaged discharge rate defined for a volcano on a case-by-case basis. Finally, the third method returned to a physics-based model but is based on a different heat loss model, and uses an empirical parameter, the radiant density. This radiant density is defined as the amount of radiative energy that can be lost by the lava flow per unit volume, and is dependent on the silica content of the flow. I first concentrated on the relative differences in TADR between the different methods and found that Method-3 yields TADR values that are higher than Method-1 in 90% of the eruptions. Method-2 is a simplification of Method-1, so the TADR follows the same trend but is slightly lower or higher than the first method depending on the coefficient used. I also identified a behavior, where TADR from Method-3 becomes lower than Method-1 towards the last half of the eruption, which was observed mainly for Nyamuragira

volcano. This results from the different wavelengths used, since the midwave infrared (Method-3) is more sensitive to higher surface temperature than the long wave infrared (Method-1), and the prevalence of incandescent cracks at the surface of a flow decreases as it cools over time and ultimately ceases to flow. The second goal of this study is to estimate the accuracy of each method. Since in-situ measurement of discharge rates are hard to estimate and have large errors associated with them, instead of comparing our satellite-derived TADR with published ground-based TADR, I decided to use the final flow volume of each eruption as a way to validate each method. Final flow volumes can be very well constrained at the end of an eruption especially when using geophysical methods such as DEM subtraction or InSAR. Although only 50% of the eruptions I studied had published final flow volumes, I used other satellite instruments and inferred flow volumes based on the area covered by the flow and an assumed thickness. I found that Method-1 was closer to all the recorded volumes and therefore is more accurate than Method-3. However, Method-3 encompasses the recorded final flow volumes more often than Method-1 due to the larger range of TADR estimates. The final step of this project was to use the final flow volume database (literature volumes and satellite-derived volumes) to return to a coefficient method similar to Method-2. Knowing the final flow volume as found in the literature, I can tune the value of the coefficient to estimate TADR and yield final flow volume to match that of the published flow volume. Therefore, with our database I was able to define coefficients for 14 volcanoes (10 more basaltic volcanoes than Harris et al., 2007) and refine the coefficients for the four volcanoes already published, which improves the discharge rate and final flow volume measurements by approximately 30-50%.

Although we know that estimating lava discharge rate is difficult with every method and it is hard to know what the real value is, thermal remote sensing is a great tool available to volcanologists to help understand effusive eruptions, monitor an eruption in near-real time and help predict the eruption cessation. The data used here through MODIS and the MODVOLC algorithm is received between six and 18 hours after the satellite acquisition was made. However, having real time lava discharge rates is needed to have a fast response during an eruption and to help model where the flow will go. Such a system already exists for Mount Etna, Sicily, with the Lav@hazard (Vicari et al., 2011). The INGV-Catania science team was able to develop an automatic system that greatly improves lava flow monitoring, based on the approach

published by Wright et al. (2008). They combined two algorithms: a) HOTSAT (Ganci et al., 2011 and 2012) that automatically detects hotspot using MODIS and SEVIRI (Spinning Enhanced Visible and Infrared Imager) images and estimate TADR that updates every 15 minutes, and b) MAGFLOW (Vicari et al., 2007; Del Negro et al., 2008), a thermo-rheological model for lava flow path modelling that inputs lava discharge rate and takes into account its variation over time. This has been tested and proved reliable for Etna eruptions but unfortunately there is not equivalent here in Hawai‘i. However, such a system would be very valuable for both Kīlauea and for any future eruption at Mauna Loa.

There are many different satellite platforms with instruments of different performance in terms of spatial, temporal and spectral resolution. It is important to understand the advantages and limitations of individual instruments. However, in the future the synergetic use of data taken from multiple satellite instruments can greatly ameliorate resolution. The continuous technological improvement of the instruments themselves could be very useful for the volcanology community, although Ramsey and Harris (2013) highlighted that most new missions do not focus on volcanological applications. The exception is the HyspIRI instrument (Hyperspectral Infrared Imager), which has an increase in spatial resolution to 60 m in the thermal infrared, an increase in spectral resolution, and a higher saturation temperature up to 770°C. However, the launch date for this instrument has been delayed and could be later than 2020. Another source of improvement will come from the development of small satellites launched by universities or businesses like our very own Hawai‘i Space Flight Lab. For example, the Thermal Hyperspectral Imager (THI; Crites et al., 2011) has been developed with about 100 wavelength bands between 7 μm and 13 μm. These previous instruments show an improvement in terms of spatial and spectral resolution but not in terms of temporal resolution. The latest GOES satellites (Geostationary Operational Environmental Satellite): GOES-16 and GOES-17 ameliorate the temporal resolution. As geostationary instruments, they scan the same area over the Americas (GOES-East) or the Pacific Ocean (GOES-West) every 5-15 minutes (15-30 minutes with GOES-14 and GOES-15) and have a resolution of 2 km per pixel in the thermal infrared (4 km with GOES-14 and GOES-15). GOES satellites have been used mostly in the late 1990s to study volcanic activity (Davies and Rose, 1998; Harris and Thornber, 1999; Harris et al., 2001) allowing for detailed chronology of an eruption. Therefore, the latest improvement of

GOES satellites, with better spatial and temporal resolution, can greatly improve real time monitoring of volcanoes.

APPENDIX

Supporting Information for

AN ASSESSMENT OF THREE SATELLITE-BASED METHODS TO ESTIMATE LAVA DISCHARGE RATES DURING EFFUSIVE BASALTIC ERUPTIONS

A1. Introduction

This supporting information file is for Chapter 4. It contains the compilation of the constant values used to retrieve TADR using Method-1, the final flow volumes and all time-averaged discharge rate time-series estimated using MODIS infrared data. I show here two tables of constant values for Method-1, two tables of the recorded final flow volumes from the literature and the values we inferred from satellite images, and TADR time-series estimated with the three different thermal satellite remote sensing methods for the 104 basaltic effusive eruptions at 34 volcanoes over a 15-year time period.

A2. Supporting data for estimating TADR using Method-1

Method-1 requires to input many parameters that are constant for different volcanoes and I compiled them in the first two tables (Tables A.1. and A.2.)

A3. Final flow volumes for our entire volcano database

Here, I present the compilation of the final flow volumes integrated from our TADR time-series based on the three satellite-derived methods. First, I show all 104 eruptions with the final flow volumes found in the literature (Table A.3.). Second, the results of our inferred final flow volumes based on satellite images (estimate of lava area) and an assumption of lava flow thickness are shown (Table A.4.).

A4. TADR time-series

Here, I present all TADR time-series for all the eruptions studied in this dissertation. For most eruptions, the maximum and minimum TADR are shown in blue for Harris et al. (1997a) method (Method-1), in grey for Wright et al. (2001a) method (Method-2), and in red for Coppola et al. (2012) method (Method-3). The maximum TADR trends are shown by solid lines and the minimum TADR trends are shown by dotted lines. I included one legend in each figure and specified in case where this was different. The y-axis changes in each figure.

Table A.1. The values of atmospheric transmissivity and upwelling radiance for each volcano based on their elevation, as taken from Harris 2013 (Figures 2.15 and 2.17).

Volcano	**Transmissivity $\tau(\lambda)$**	**Upwelling radiance $Lu(\lambda)$**
Barren Island, Jebel at Tair	0.86	1.0×10^{-2}
Holuhraun	0.87	9.0×10^{-3}
Chirpoi, Dalafilla-Alu, Manda Hararo, Tinakula	0.88	8.5×10^{-3}
Sierra Negra, Stromboli	0.9	6.25×10^{-3}
Cerro Azul, Eyjafjallajokull, Fernandina, Hekla, Karangetang, Lopevi, Montagu Island, Tolbachik	0.915	5.0×10^{-3}
Cameroon, Etna, Fogo, Heard, Kizimen, Llaima, Mayon, Nabro, Nyamuragira, Pacaya, Pavlof, Piton de la Fournaise, Rinjani, Veniaminof	0.95	4.5×10^{-3}
Fuego, Reventador	0.96	2.0×10^{-3}
Klyuchevskoy	0.97	1.25×10^{-3}

Table A.2. Parameters used to calculate TADR with Method-1 for all volcanoes.

	Values used		***References***
T_{lava} (°C)	100	500	Harris et al., 1997a
T_{back} (°C)	Varying by month, sensor, time of day		MODIS Land Surface Temperature
σ (W m^{-2} K^{-4})	5.67×10^{-8}		Boltzmann constant
k (W m^{-1} K^{-1})	27.80×10^{-3}	39.51×10^{-3}	Kays and Crawford, 1980
ρ_{air} (kg m^{-3})	1.0928	0.706	Kays and Crawford, 1980
μ (Pa.s)	19.57×10^{-6}	26.82×10^{-6}	Kays and Crawford, 1980
α (K^{-1})	3.09×10^{-3}	2.03×10^{-3}	Kays and Crawford, 1980
κ (m^2 s^{-1})	2.50×10^{-2}	5.40×10^{-2}	Kays and Crawford, 1980
DRE ρ (kg m^{-3})	2600		Harris et al., 1997a
DRE Cp (J kg^{-1} K^{-1})	1150		Harris et al., 1997a
ΔT (°C)	150		Harris et al., 1997a
Φ (%)	45		Harris et al., 1997a
C_L (J kg^{-1})	2.9×10^{5}		Harris et al., 1997a
ε	0.989		Harris et al., 1997a

Table A.3. Summary of volume estimates derived using the two different thermal remote-sensing methods of TADR retrieval, and together with literature values when available (if not we specify whether we used ASTER or Landsat data) for all the 104 basaltic effusive eruptions in our database. The durations are estimated from MODIS and all volumes are in m^3. Asterisks represent volumes estimated from all peaks instead of one *nsig*.

Volcano name	**Eruption**	**Duration (days)**	**Volume Harris**		**Volume Coppola**		**Literature volumes**
			Max	Min	Max	Min	
Barren Island	2005-2006*	281	2.68×10^7	1.66×10^7	1.37×10^8	4.58×10^7	ASTER
	2008*	43.5	3.91×10^6	2.47×10^6	1.36×10^7	4.53×10^6	ASTER
	2009*	44	2.39×10^6	1.52×10^6	4.26×10^6	1.42×10^6	ASTER
Cameroon *Suh et al., 2003*	2000*	48.5	1.39×10^7	7.62×10^6	6.13×10^7	2.05×10^7	6.00×10^6 field
Cerro Azul	2008*	11	7.69×10^6	4.44×10^6	1.02×10^8	3.40×10^7	ASTER
Chirpoi	2012	36.5	2.21×10^6	1.14×10^6	1.59×10^6	5.30×10^5	ASTER
Dalafilla-Alu *Pagli et al., 2012*	2008	55	2.88×10^7	1.98×10^7	5.08×10^7	1.69×10^7	2.54×10^7 InSAR
Etna	May 2001	26	7.75×10^6	5.02×10^6	3.71×10^7	1.24×10^7	ASTER
Behncke and Neri, 2003	July 2001	21.5	2.06×10^7	1.42×10^7	8.82×10^7	2.94×10^7	2.50×10^7 field
Andronico et al., 2005	2002-2003	93.5	3.15×10^7	1.77×10^7	1.35×10^8	4.51×10^7	$2.5\text{-}3.4\times10^7$ thermal maps
Allard et al., 2006	2004-2005	200.5	7.52×10^7	4.30×10^7	3.32×10^8	1.11×10^8	4.00×10^7 field
GVP, 2007	2006 (2)	~150	3.79×10^7	2.15×10^7	4.11×10^8	1.37×10^8	$1.5\text{-}2.0\times10^7$ unknown
	Mar 2007*	32.5	8.00×10^6	4.46×10^6	9.54×10^7	3.18×10^7	ASTER

Andronico et al., 2008	Sept 2007*	1.5	9.66×10^{4}	6.16×10^{4}	2.70×10^{5}	9.01×10^{4}	$2.0\text{-}4.0\times10^{6}$ field
	Nov 2007	1	1.43×10^{6}	7.68×10^{5}	3.72×10^{6}	1.24×10^{6}	ASTER
Harris et al., 2011	2008-2009	439	1.44×10^{8}	9.06×10^{7}	5.07×10^{8}	1.69×10^{8}	6.80×10^{7} satellite images
	Jan 2014	69.5	2.64×10^{7}	1.45×10^{7}	1.86×10^{8}	6.19×10^{7}	ASTER
	June 2014*	66.5	1.32×10^{7}	8.37×10^{6}	8.29×10^{7}	2.76×10^{7}	ASTER
Eyjafjallajokull *Gudmundsson et al., 2010*	Mar 2010	19	5.00×10^{6}	2.53×10^{6}	2.62×10^{7}	8.74×10^{6}	2.50×10^{7} unknown
Fernandina							
Chadwick et al., 2011	2005*	19	7.20×10^{6}	4.25×10^{6}	3.21×10^{7}	1.07×10^{7}	1.40×10^{7} satellite images
GVP, 2009	2009	16.5	3.70×10^{6}	2.23×10^{6}	2.05×10^{8}	6.85×10^{7}	$4.4\text{-}7.0\times10^{7}$ combined (5)
Fogo	2014-2015	75.5	4.44×10^{7}	2.50×10^{7}	1.55×10^{8}	5.16×10^{7}	ASTER
Fuego	2011-2013*	748	2.54×10^{7}	1.54×10^{7}	3.68×10^{8}	1.23×10^{8}	ASTER
Heard	2000*	242	1.30×10^{7}	6.23×10^{6}	1.18×10^{7}	3.95×10^{6}	ASTER
	2006-2007	323	1.01×10^{7}	4.91×10^{6}	1.96×10^{7}	6.55×10^{6}	ASTER
	2012-2013*	199	5.10×10^{6}	2.52×10^{6}	1.09×10^{7}	3.64×10^{6}	ASTER
Hekla *Hoskuldsson et al., 2007*	2000	4	3.22×10^{6}	1.59×10^{6}	1.89×10^{6}	6.31×10^{5}	1.89×10^{8} field
Holuhraun *Gíslason et al., 2015*	2014-2015	176.5	9.31×10^{8}	4.63×10^{8}	1.82×10^{9}	6.08×10^{8}	1.2×10^{9} field
Jebel at Tair *Xu and Jonsson, 2014*	2007-2008*	231	4.16×10^{7}	2.62×10^{7}	8.85×10^{7}	2.95×10^{7}	2.20×10^{7} InSAR, bulk volume

Karangetang	2001*	100.5	4.79×10^{6}	2.94×10^{6}	7.27×10^{6}	2.42×10^{6}	ASTER
Kizimen	2011 p1	212	8.60×10^{7}	4.35×10^{7}	1.18×10^{8}	3.94×10^{7}	ASTER
	2011 p2	174	3.30×10^{7}	1.57×10^{7}	4.90×10^{7}	1.63×10^{7}	ASTER
	2012-2013	210	1.33×10^{7}	6.32×10^{6}	1.39×10^{7}	4.65×10^{6}	ASTER
Klyuchevskoy	'03-'04*	~217	6.41×10^{6}	3.32×10^{6}	2.63×10^{7}	8.79×10^{6}	6.0×10^{7} field
Fedotov and Zharinov, 2007	2005	72	2.48×10^{7}	1.16×10^{7}	1.84×10^{8}	6.13×10^{7}	2.35×10^{7} field, sat images
Rose and Ramsey, 2009 (2005)	2007	102	3.25×10^{7}	1.60×10^{7}	2.79×10^{8}	9.30×10^{7}	Landsat
	2008-2009	67.5	2.79×10^{7}	1.28×10^{7}	1.88×10^{8}	6.27×10^{7}	ASTER
	2009-2010	365	7.68×10^{7}	3.77×10^{7}	4.07×10^{8}	1.36×10^{8}	Landsat
	2013	60	3.53×10^{7}	1.71×10^{7}	2.11×10^{8}	7.04×10^{7}	Landsat
Llaima	Jan 2008*	42	6.63×10^{6}	3.60×10^{6}	7.15×10^{7}	2.38×10^{7}	ASTER
Romero Moyano et al., 2014	July 2008*	26	3.50×10^{6}	1.78×10^{6}	3.48×10^{7}	1.16×10^{7}	ASTER
	April 2009*	10	3.53×10^{6}	1.87×10^{6}	2.91×10^{7}	9.71×10^{6}	1.80×10^{6} field and OLI
Lopevi	2003*	2.5	1.98×10^{5}	1.19×10^{5}	9.15×10^{5}	3.05×10^{5}	
	May 2006*	24.5	1.51×10^{6}	9.13×10^{5}	1.21×10^{7}	4.03×10^{6}	ASTER
	June 2006*	33.5	7.50×10^{6}	4.53×10^{6}	3.44×10^{7}	1.15×10^{7}	ASTER
	2007	21	4.25×10^{6}	2.56×10^{6}	4.48×10^{7}	1.49×10^{7}	ASTER
Manda Hararo	2007*	20	6.40×10^{6}	4.00×10^{6}	1.16×10^{7}	3.86×10^{6}	$4.4\text{-}8.8\times10^{6}$ field, sat image
Ferguson et al., 2010	2009*	49	1.38×10^{7}	9.91×10^{6}	2.27×10^{7}	7.57×10^{6}	$1.3\text{-}1.8\times10^{7}$ field, sat image
Mayon	2006*	66	3.24×10^{6}	1.94×10^{6}	5.08×10^{7}	1.69×10^{7}	$3.6\text{-}4.1\times10^{7}$ unknown
GVP, 2006	2009	14.5	4.39×10^{6}	2.70×10^{6}	1.09×10^{8}	3.62×10^{7}	ASTER

Montagu Is.	2005*	19	1.14×10^{6}	5.61×10^{5}	2.24×10^{6}	7.48×10^{5}	ASTER
Nabro *Sealing, 2013*	2011	143.5	9.90×10^{7}	5.90×10^{7}	3.34×10^{8}	1.11×10^{8}	2.21×10^{7} satellite images
Nyamuragira	2000	58	1.70×10^{7}	9.34×10^{6}	*3.33×10^{7}*	*1.11×10^{7}*	4.73×10^{7} satellite images
Smets et al., 2010	2001	44.5	1.30×10^{8}	7.22×10^{7}	3.64×10^{8}	1.21×10^{8}	1.40×10^{8} satellite images
Smets et al., 2010	2002	64	8.20×10^{7}	4.54×10^{7}	1.72×10^{8}	5.73×10^{7}	5.67×10^{7} satellite images
Smets et al., 2010	2004	48.5	1.20×10^{8}	6.56×10^{7}	*1.55×10^{8}*	*5.18×10^{7}*	$5.7\text{-}8.0\times10^{7}$ InSAR
Smets et al., 2010 *Albino et al., 2015*	2006	16	6.14×10^{6}	3.36×10^{6}	*4.92×10^{6}*	*1.64×10^{6}*	$4.1\text{-}4.7\times10^{7}$ satellite images
Smets et al., 2010	2010	29.5	4.38×10^{7}	2.43×10^{7}	1.33×10^{8}	4.43×10^{7}	5.30×10^{7} satellite images
Albino et al., 2015	2011-2012	148.5	2.22×10^{8}	1.25×10^{8}	4.96×10^{8}	1.65×10^{8}	$2.7\text{-}3.4\times10^{8}$ InSAR
Pacaya	2005*	196.5	3.66×10^{6}	2.12×10^{6}	2.00×10^{7}	6.66×10^{6}	8.80×10^{5} satellite images
Morgan et al., 2013 (all)	2006-2008	746	4.14×10^{7}	2.43×10^{7}	1.49×10^{8}	4.97×10^{7}	6.00×10^{6} satellite images
	2008-2009*	204.5	1.02×10^{7}	6.45×10^{6}	2.39×10^{7}	7.97×10^{6}	1.70×10^{6} satellite images
	2010*	21	3.38×10^{6}	1.88×10^{6}	1.80×10^{7}	5.99×10^{6}	3.80×10^{6} satellite images
	2014	12	5.45×10^{6}	3.10×10^{6}	2.50×10^{7}	8.34×10^{6}	ASTER
Pavlof	2007	26.5	8.52×10^{6}	4.40×10^{6}	2.46×10^{7}	8.19×10^{6}	ASTER
	2013*	45	8.39×10^{6}	4.26×10^{6}	5.70×10^{7}	1.90×10^{7}	ASTER
	May 2014	4.5	7.01×10^{5}	3.58×10^{5}	1.13×10^{7}	3.77×10^{6}	ASTER
	Nov 2014*	3	7.34×10^{5}	3.64×10^{5}	1.89×10^{6}	6.30×10^{5}	ASTER
Piton de la	Feb 2000*	7	8.95×10^{5}	5.00×10^{5}	2.64×10^{6}	8.79×10^{5}	4.10×10^{6} unknown
Fournaise	June 2000*	30	4.59×10^{6}	2.50×10^{6}	3.21×10^{7}	1.07×10^{7}	6.00×10^{6} unknown

Observatoire Volcanologique du Piton de la Fournaise	Oct 2000	36.5	1.29×10^{7}	7.03×10^{6}	1.03×10^{8}	3.45×10^{7}	9.00×10^{6} unknown
	Mar 2001*	12	5.08×10^{6}	3.06×10^{6}	3.28×10^{7}	1.09×10^{7}	4.80×10^{6} unknown
	June 2001*	26	2.07×10^{7}	1.18×10^{7}	2.13×10^{8}	7.09×10^{7}	9.50×10^{6} unknown
	Jan 2002*	11.5	6.54×10^{6}	3.87×10^{6}	8.75×10^{7}	2.92×10^{7}	1.30×10^{7} unknown
	Nov 2002*	14.5	1.16×10^{7}	6.35×10^{6}	8.63×10^{7}	2.88×10^{7}	8.00×10^{6} unknown
	Aug 2003	7	4.00×10^{6}	2.14×10^{6}	3.34×10^{7}	1.11×10^{7}	6.20×10^{6} unknown
	Dec 2003*	13	7.38×10^{5}	4.21×10^{5}	*2.04×10^{6}*	*6.79×10^{5}*	1.20×10^{6} unknown
	May 2004	12	8.75×10^{6}	4.99×10^{6}	4.09×10^{7}	1.36×10^{7}	1.25×10^{7} unknown
	Aug 2004	61.5	3.82×10^{7}	2.07×10^{7}	2.27×10^{8}	7.57×10^{7}	1.85×10^{7} unknown
	Feb 2005	7	3.91×10^{6}	2.19×10^{6}	2.93×10^{7}	9.78×10^{6}	$1.8\text{-}2.0\times10^{7}$ unknown
	Oct 2005	13.5	2.38×10^{6}	1.49×10^{6}	4.44×10^{6}	1.48×10^{6}	1.50×10^{6} unknown
	Dec 2005	10	1.75×10^{7}	9.64×10^{6}	1.60×10^{8}	5.33×10^{7}	$1.5\text{-}2.0\times10^{7}$ unknown
	July 2006	21.5	1.98×10^{6}	1.06×10^{6}	1.48×10^{7}	4.93×10^{6}	$2.5\text{-}3.2\times10^{6}$ unknown
	Sep 2006	121.5	3.42×10^{7}	1.97×10^{7}	1.02×10^{8}	3.41×10^{7}	$1.8\text{-}2.0\times10^{7}$ unknown
	Mar 2007	29	3.89×10^{7}	2.19×10^{7}	3.47×10^{8}	1.16×10^{8}	1.30×10^{8} unknown
	Sep 2008*	7.5	6.70×10^{5}	3.93×10^{5}	2.04×10^{6}	6.80×10^{5}	8.50×10^{5} aerial photos
GVP, 2009	Dec 2008	44.5	2.46×10^{6}	1.56×10^{6}	1.05×10^{7}	3.51×10^{6}	ASTER
	Jan 2010*	9	4.40×10^{5}	2.44×10^{5}	3.13×10^{6}	1.04×10^{6}	ASTER
	Oct 2010*	21	4.60×10^{6}	2.72×10^{6}	1.64×10^{7}	5.48×10^{6}	6.00×10^{5} unknown
GVP, 2012	Dec 2010*	2	1.19×10^{5}	6.57×10^{4}	1.08×10^{6}	3.61×10^{5}	ASTER
Reventador	2002*	7	9.73×10^{5}	5.30×10^{5}	5.30×10^{6}	1.77×10^{7}	3.60×10^{7} unknown

Samaniego et al., 2008 *GVP, 2004*	2004* 2005* 2007*	36 26 62	2.01×10^{6} 3.19×10^{6} 4.78×10^{6}	1.09×10^{6} 1.71×10^{6} 2.59×10^{6}	1.02×10^{7} 2.74×10^{7} 5.93×10^{7}	3.41×10^{6} 9.14×10^{6} 1.98×10^{7}	3.00×10^{6} field ASTER
Rinjani	2009	149	1.91×10^{7}	1.06×10^{7}	1.98×10^{7}	6.60×10^{6}	ASTER
Sierra Negra *Geist et al., 2008*	2005	24	5.54×10^{7}	3.42×10^{7}	2.86×10^{8}	9.55×10^{7}	1.50×10^{8} field
Stromboli *Calvari et al., 2005* *Marsella et al., 2009*	2002-2003 2007 2012-2013* 2014	203 34 20 151	5.74×10^{7} 1.10×10^{7} 8.94×10^{5} 3.35×10^{7}	3.22×10^{7} 6.01×10^{6} 4.94×10^{5} 1.99×10^{7}	1.28×10^{8} 4.39×10^{7} 3.47×10^{6} 1.36×10^{8}	4.28×10^{7} 1.46×10^{7} 1.16×10^{6} 4.54×10^{7}	1.30×10^{7} field 1.10×10^{7} DEM ASTER ASTER
Tinakula	2006*	110	6.26×10^{6}	3.89×10^{6}	4.40×10^{7}	1.47×10^{7}	Landsat
Tolbachik *Kubanek et al., 2015*	2012-2013	272	4.95×10^{8}	2.38×10^{8}	2.58×10^{9}	8.60×10^{8}	$4.6\text{-}6.0\times10^{8}$ InSAR
Veniaminof	2013	80.5	1.10×10^{7}	5.84×10^{6}	6.27×10^{7}	2.09×10^{7}	ASTER

Table A.4. For eruptions with no published volume in the literature, we used different remote sensing instruments (from ASTER except when specified for Landsat) to estimate final flow volumes assuming a mean thickness depending on the volcano.

Volcano Name	Year of eruption	Volumes in m^3	Flow thickness (m)
Barren island	2005-2006	1.2×10^6 +/- 0.2	2-3
GVP, 2003	2008	9.6×10^5 +/- 0.2	2-3
	2009	1.8×10^6 +/- 0.4	2-3
Cerro Azul	2008	1.0×10^7 +/- 0.5	5-15 *GVP, 2008*
Chirpoi	2012	1.3×10^6 +/- 0.7	3-10
Etna	May 2001	1.9×10^6 +/- 0.9	1-3
Behncke and Neri, 2003	March 2007	1.8×10^6 +/- 0.6	3-6
	November 2007	2.85×10^6 +/-0.95	5-10
Andronico et al., 2008	January 2014	1.2×10^7 +/- 0.4	5-10
	June 2014	8.5×10^6 +/- 2.5	5-10
Fogo	2014-2015	6.25×10^7 +/-0.25	18-20 *GVP, 2014*
Fuego	2011-2013	2.25×10^7 +/-0.75	10-20
Heard	2000	2.4×10^5 +/-0.8	10-20
	2006-2007	3.3×10^6 +/- 1.1	10-20
	2012-2013	2.55×10^6 +/- 0.85	10-20
Karangetang	2001	3.4×10^6 +/- 1.1	5-10
Karymsky	2002	4.2×10^6 +/- 1.0	6-10
Kizimen	2011 p1	6.9×10^6	50
	2011 p2	3.5×10^7	50
	2012-2013	1.3×10^7	50
Klyuchevskoy	2007 (Landsat)	9.0×10^6 +/- 0.9	2-25
Rose and Ramsey, 2009	2008-2009	1.5×10^7 +/- 1.5	2-25
	2009-2010 (Landsat)	4.15×10^6 +/- 4.0	2-25
	2013 (Landsat)	1.6×10^7 +/- 1.6	2-25
Llaima	January 2008	8.3×10^6	10
	July 2008	1.20×10^6	10

Lopevi	May 2006	1.0×10^6 +/- 0.4	3-6
	June 2006	6.0×10^6 +/- 2.0	3-6
	2007	2.1×10^6 +/- 0.7	3-6
Mayon	2009	9.0×10^6 +/- 5.0	5-20
Montagu Island	2005	2.2×10^6 +/- 1.5	1-5
Pacaya	2014	8.7×10^6 +/- 5.0	2-8
Pavlof	2007	6.5×10^6 +/- 0.5	6-7
GVP, 1981	2013	8.5×10^6 +/- 0.5	6-7
	May 2014	6.5×10^6 +/- 0.5	6-7
	November 2014	9.0×10^6 +/- 1.0	6-7
Piton de la Fournaise	December 2008	6.9×10^6	75 *GVP, 2010*
	January 2010	8.1×10^5	5
	December 2010	2.9×10^6	5
Reventador	2007	8.5×10^6	15 *GVP, 2008*
Rinjani	2009	1.0×10^7	15
Stromboli	2012-2013	2.9×10^5 +/- 1.9	1-5
	2014	1.2×10^6 +/- 0.8	1-5
Tinakula	2006	1.1×10^6 +/- 0.7	5-25
Veniaminof	2013	1.0×10^7 +/- 0.4	20-50 *GVP, 1984*

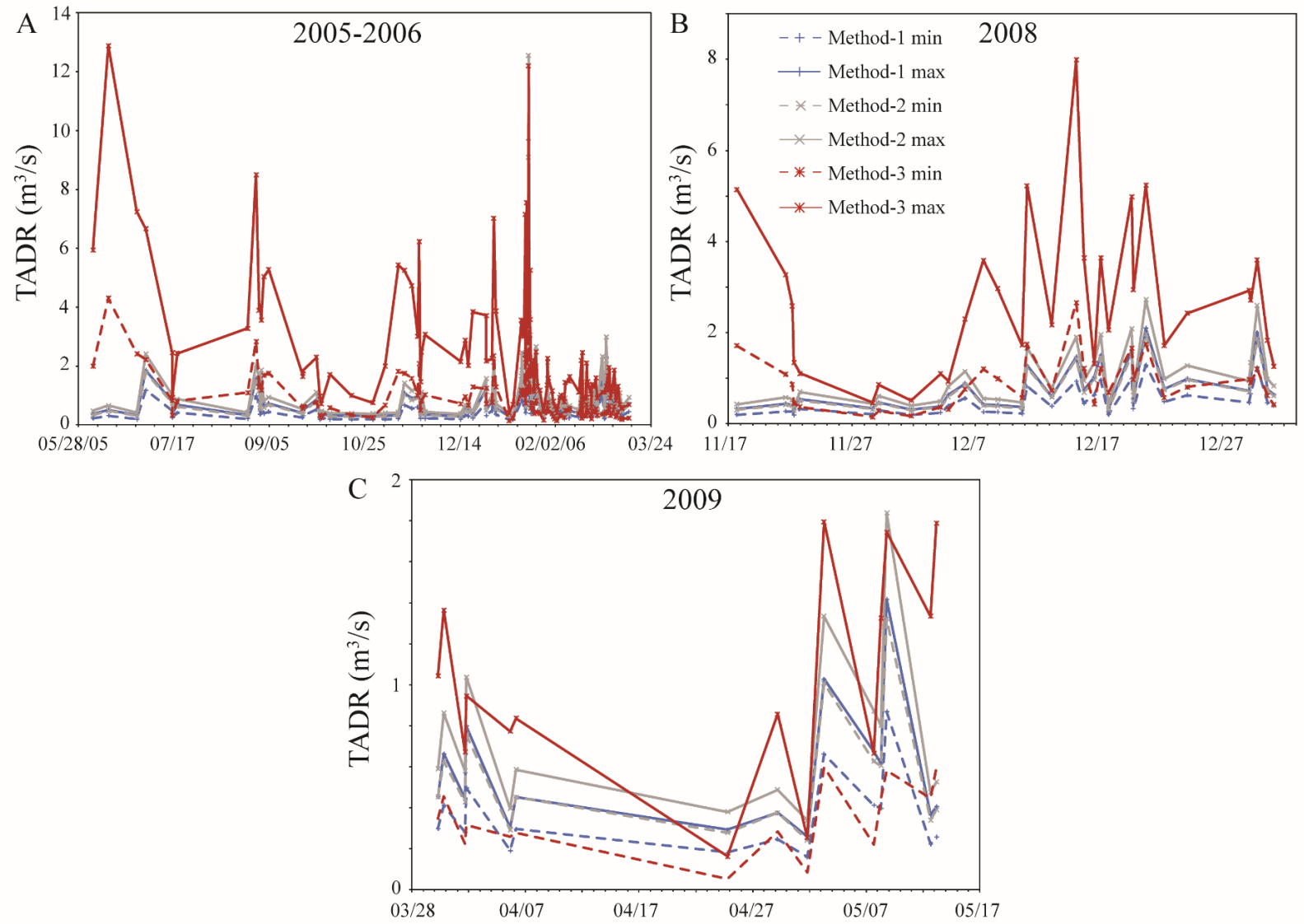

Figure A.1. TADR time-series for Barren Island eruptions in A) 2004-2005; B) 2008; and C) 2009.

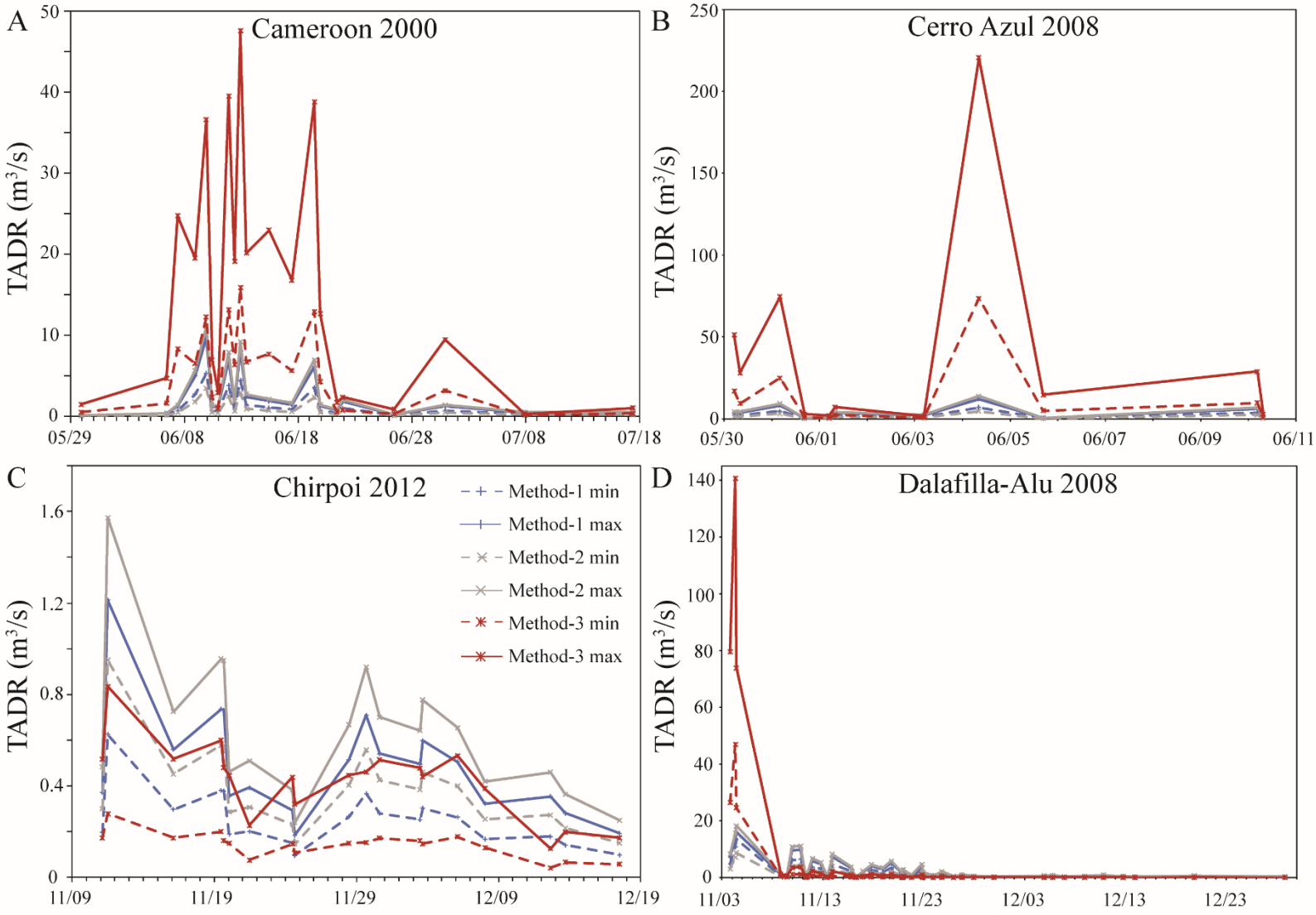

Figure A.2. A) TADR time-series for Cameroon eruption in 2000; B) Cerro Azul eruption in 2008; C) Chirpoi eruption in 2012; and D) Dalafilla-Alu in 2008.

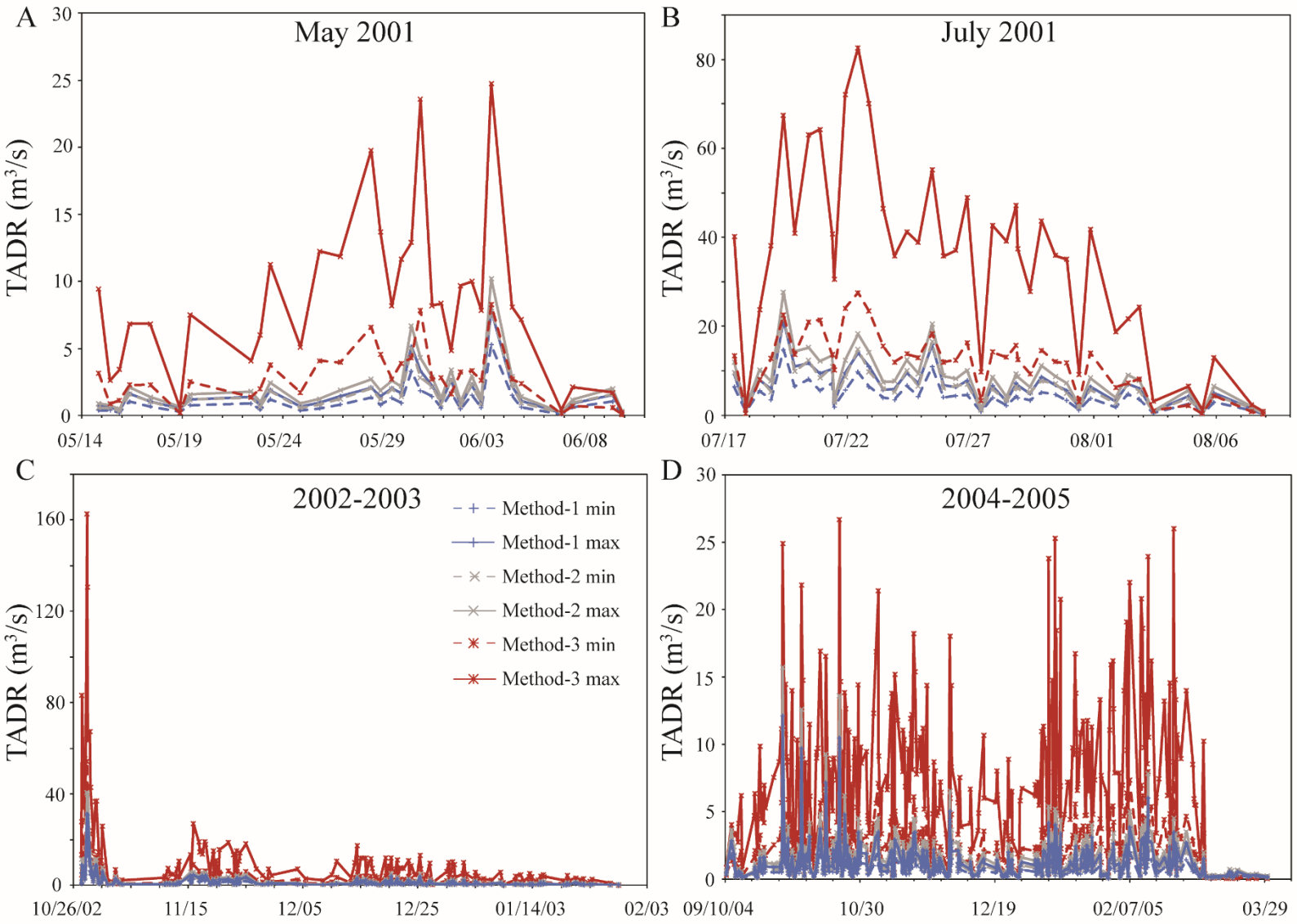

Figure A.3. TADR time-series for Etna eruption in A) May 2001; B) July 2001; C) 2002-2003; and D) 2004-2005.

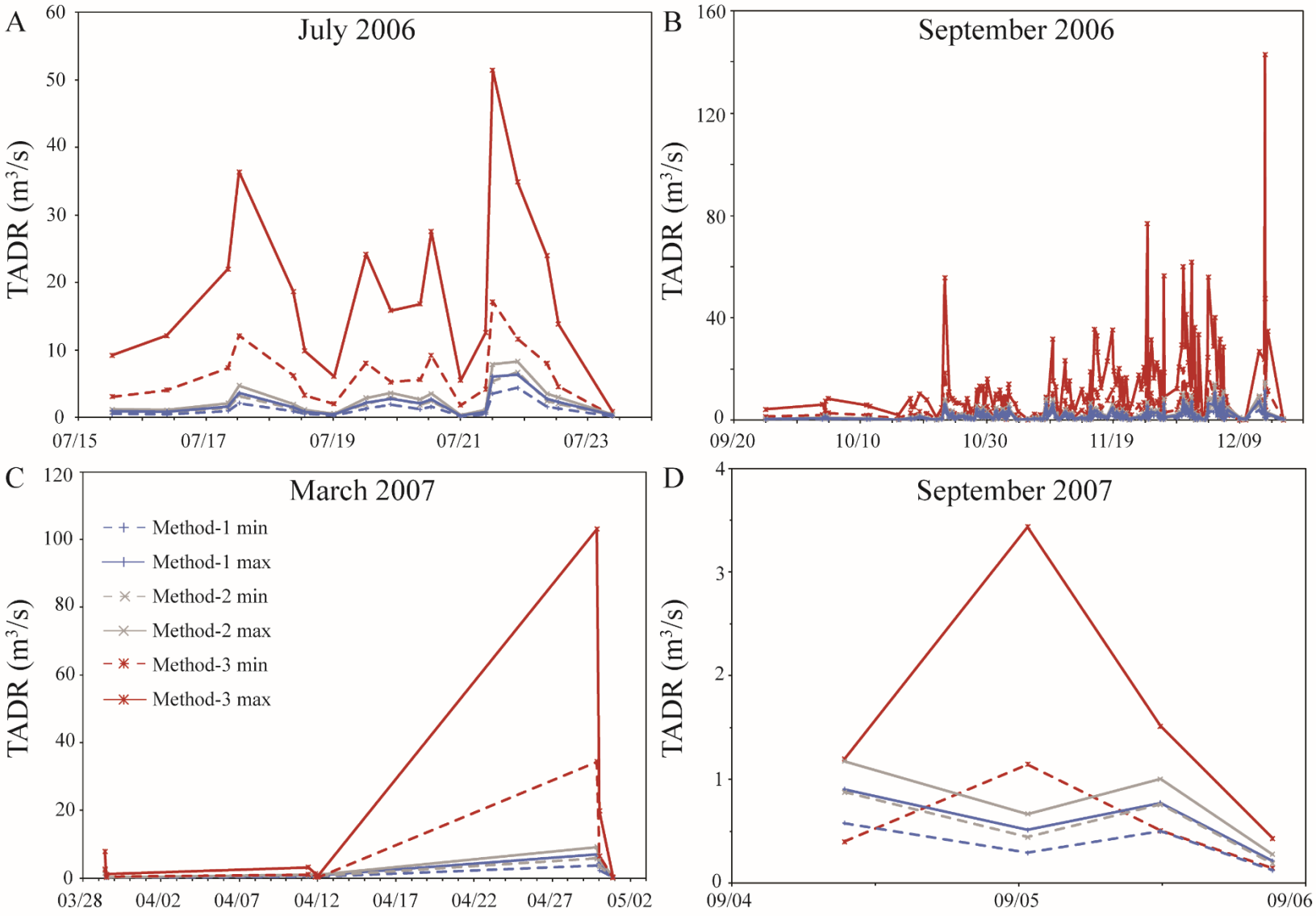

Figure A.4. TADR time-series for Etna eruption in A) July 2006; B) September 2006; C) March 2007; and D) September 2007.

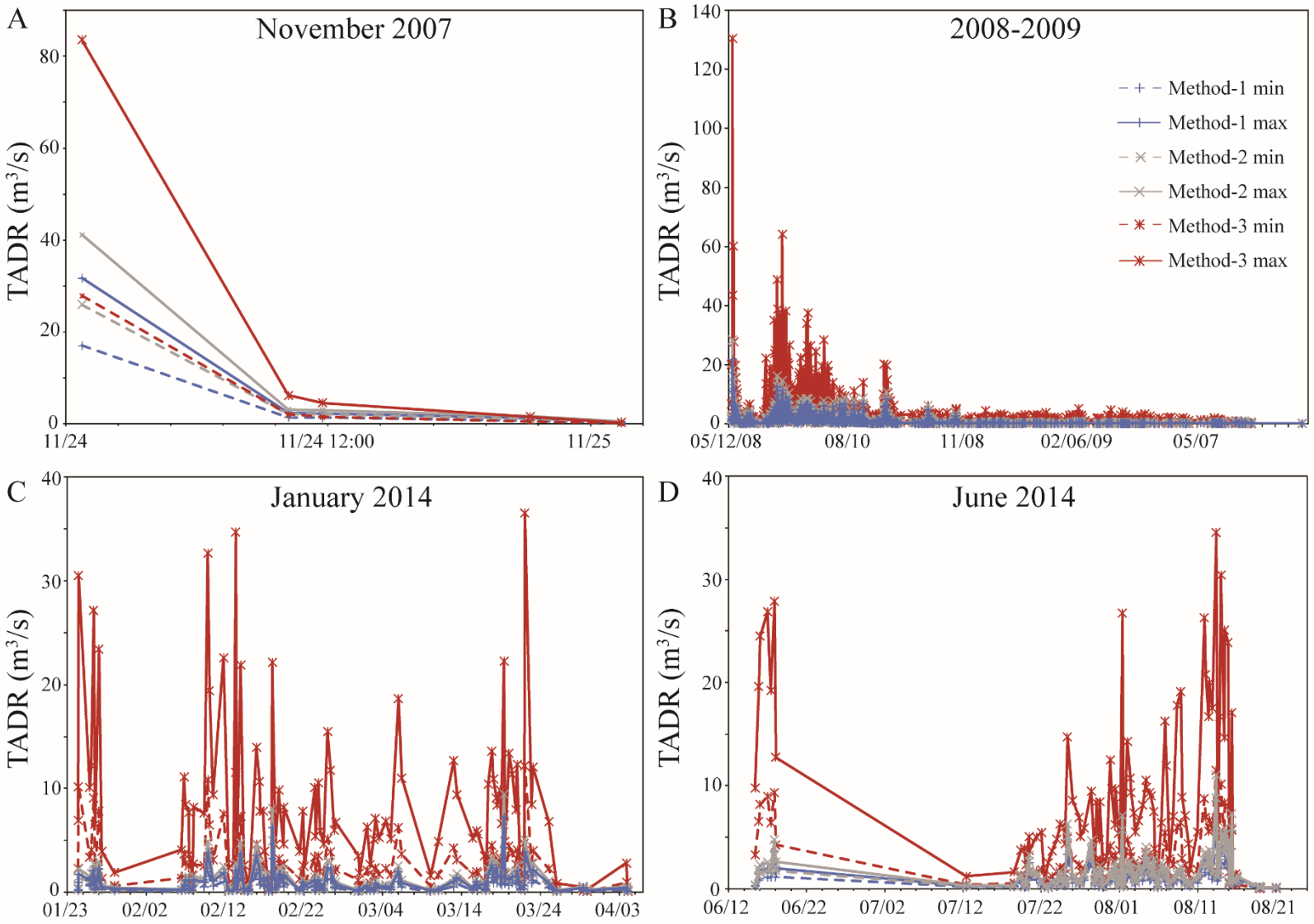

Figure A.5. TADR time-series for Etna eruption in A) November 2007; B) 2008-2009; C) January 2014; and D) June 2014.

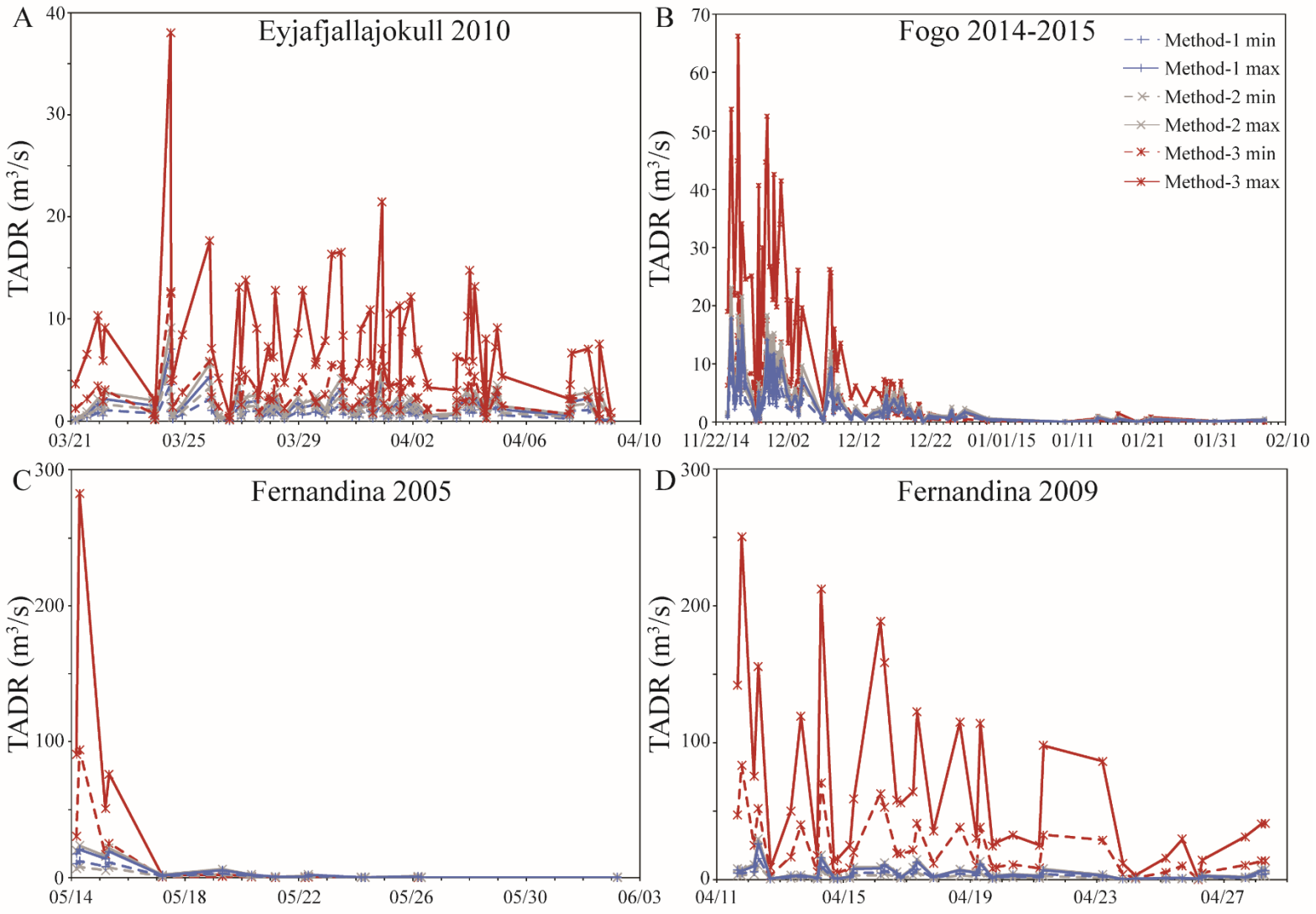

Figure A.6. TADR time-series for A) Eyjafjallajokull eruption in 2010; B) Fogo eruption in 2014-2015; C) Fernandina eruption in 2005; and D) Fernandina eruption in 2009.

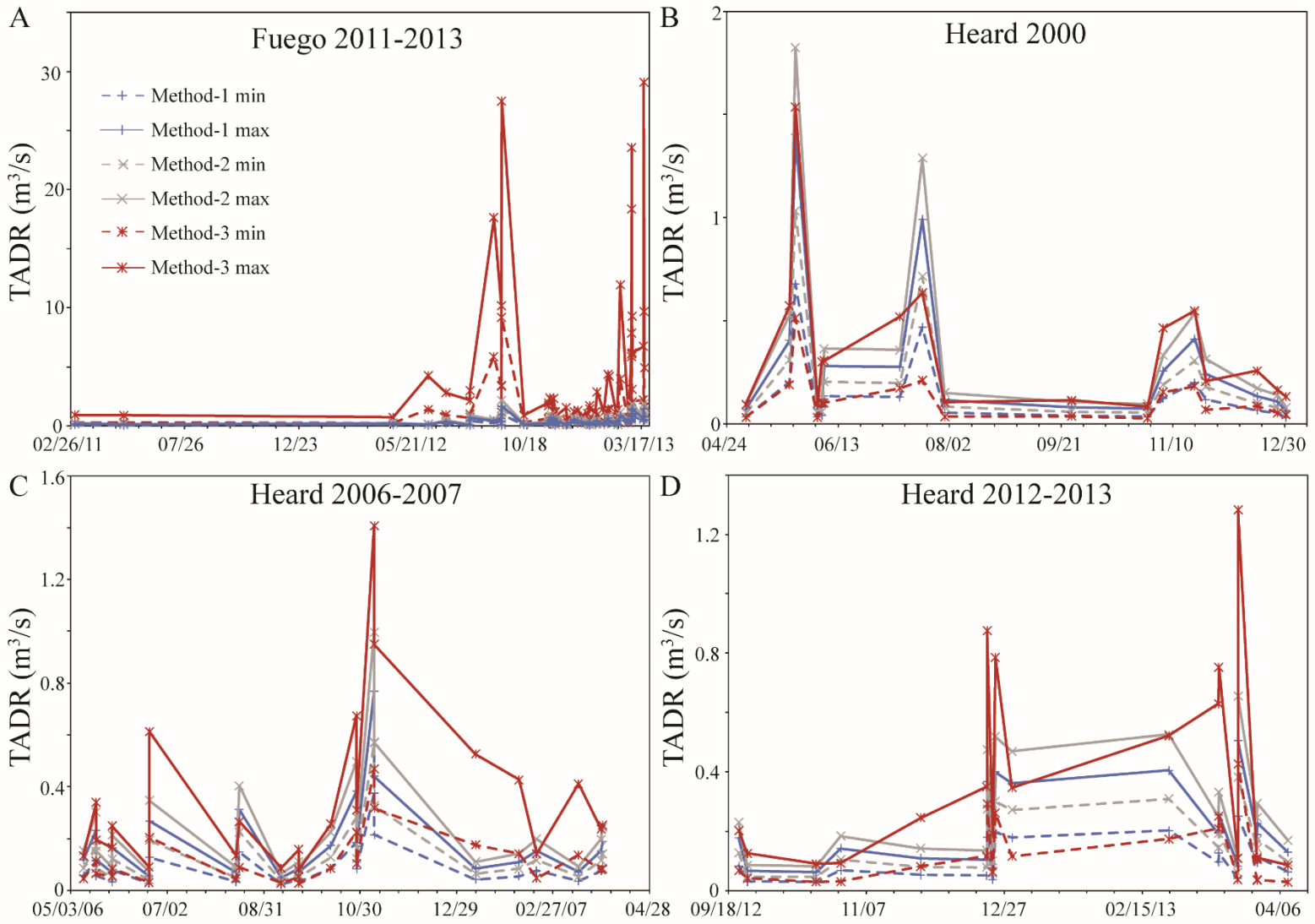

Figure A.7. TADR time-series for A) Fuego eruption from 2011-2013; B) Heard Island eruption in 2000; C) Heard Island eruption in 2006-2007; and D) Heard Island eruption in 2012-2013.

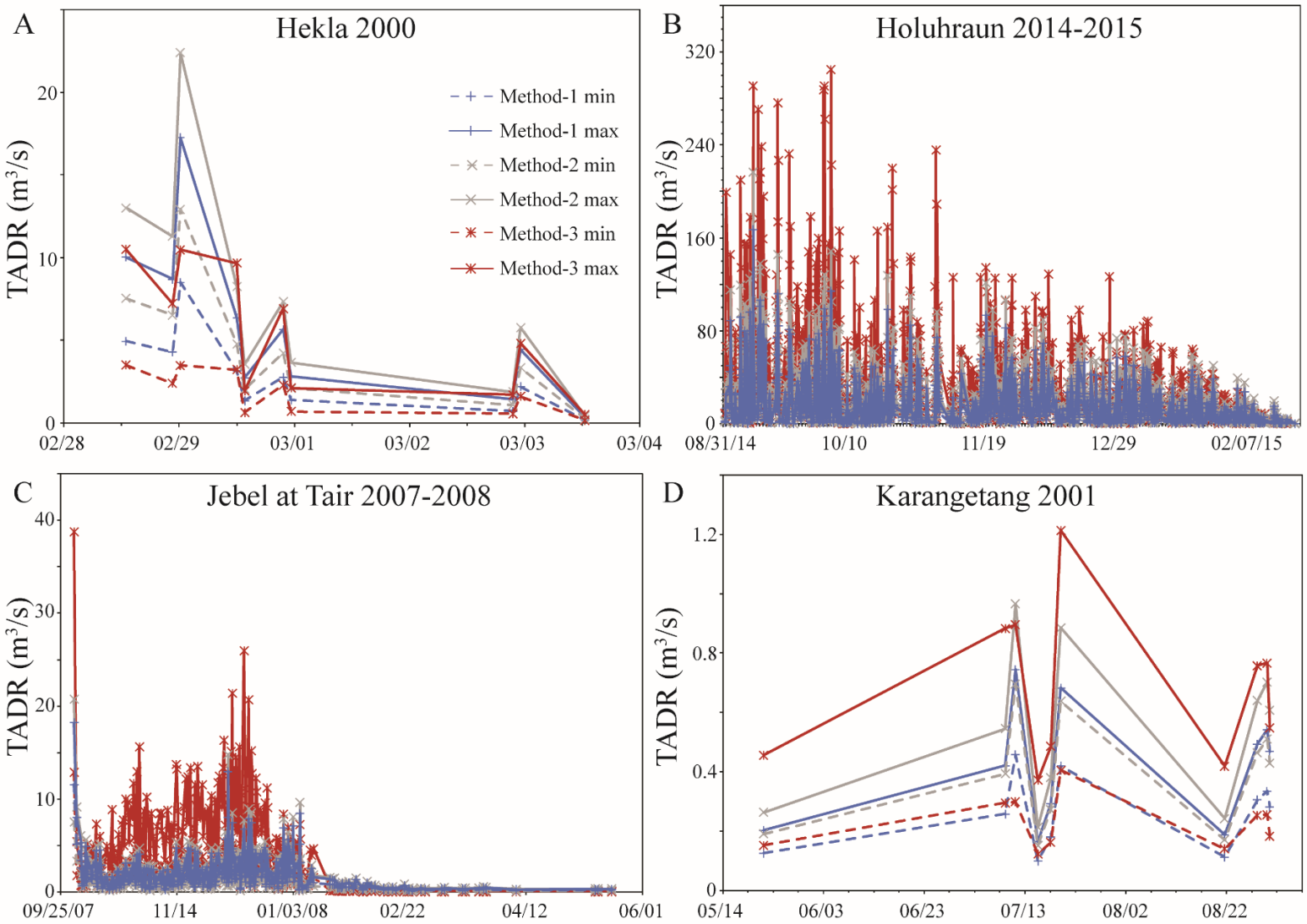

Figure A.8. TADR time-series for A) Hekla eruption in 2000; B) Holuhraun eruption in 2014-2015; C) Jebel at Tair eruption in 2007-2008; and D) Karangetang eruption in 2001.

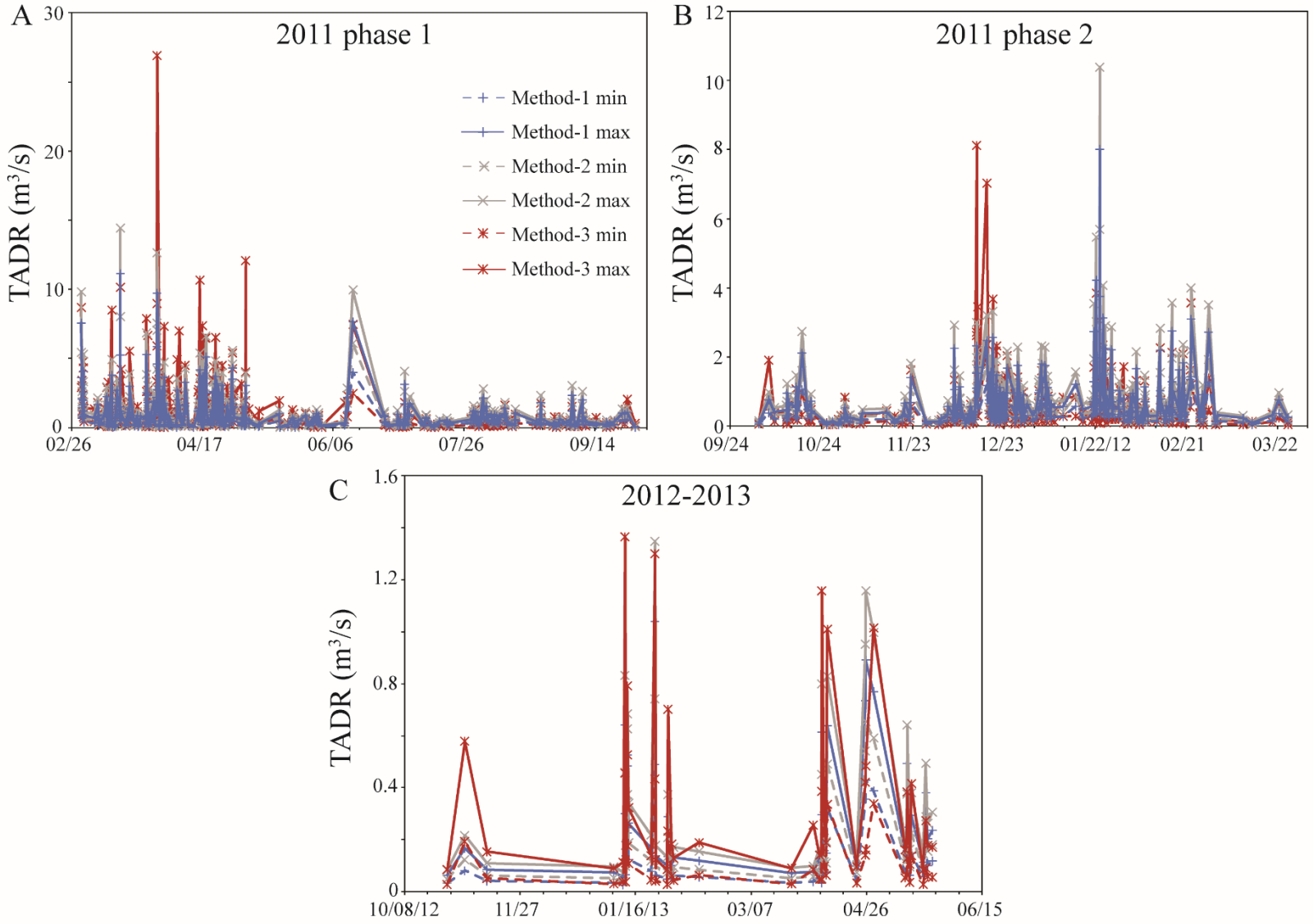

Figure A.9. TADR time-series for all Kizimen eruptions. A) 2011 phase 1; B) 2011 phase 2; and C) 2012-2013.

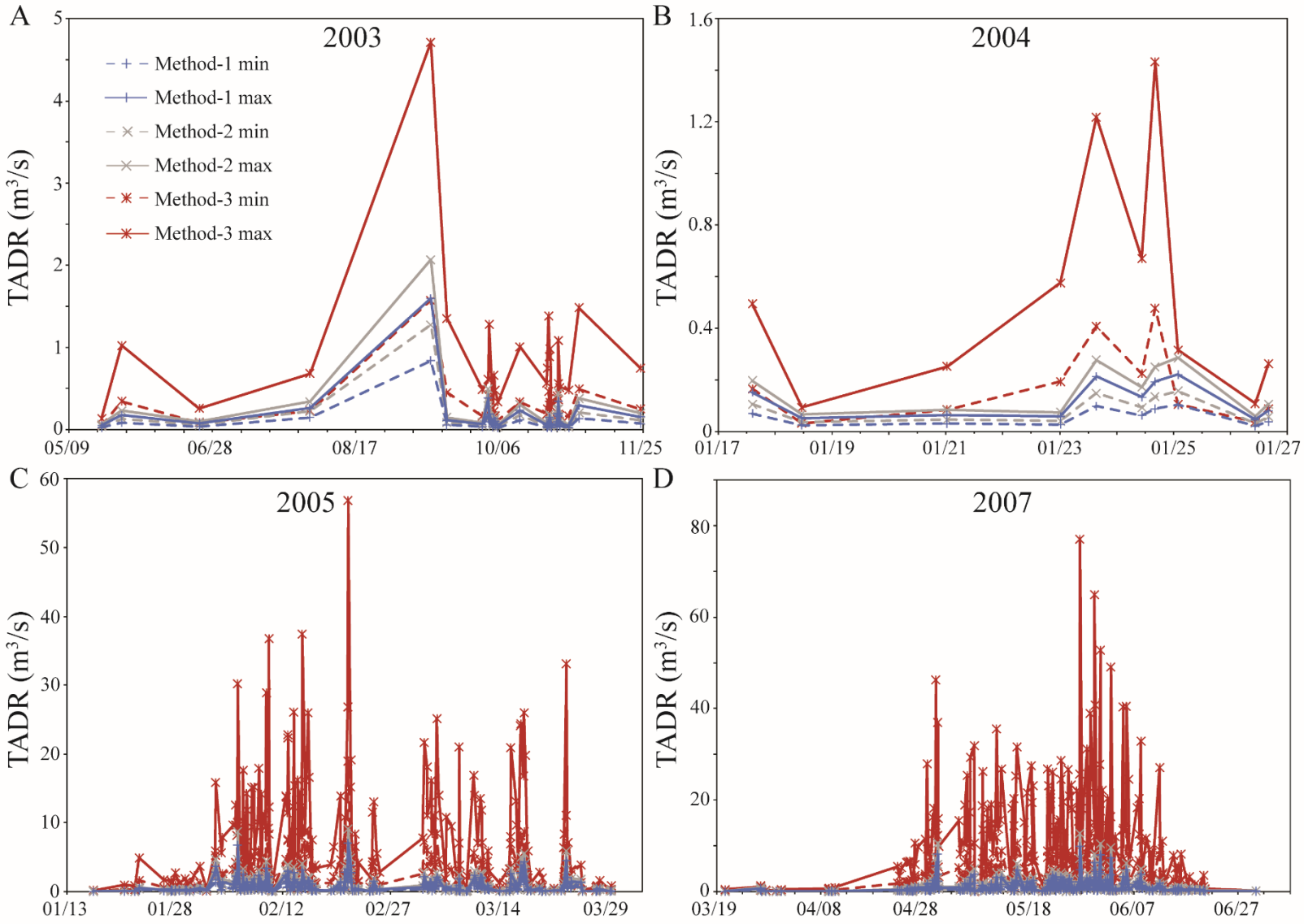

Figure A.10. TADR time-series for Klyuchevskoy eruptions. A) 2003; B) 2004; C) 2005; and D) 2007.

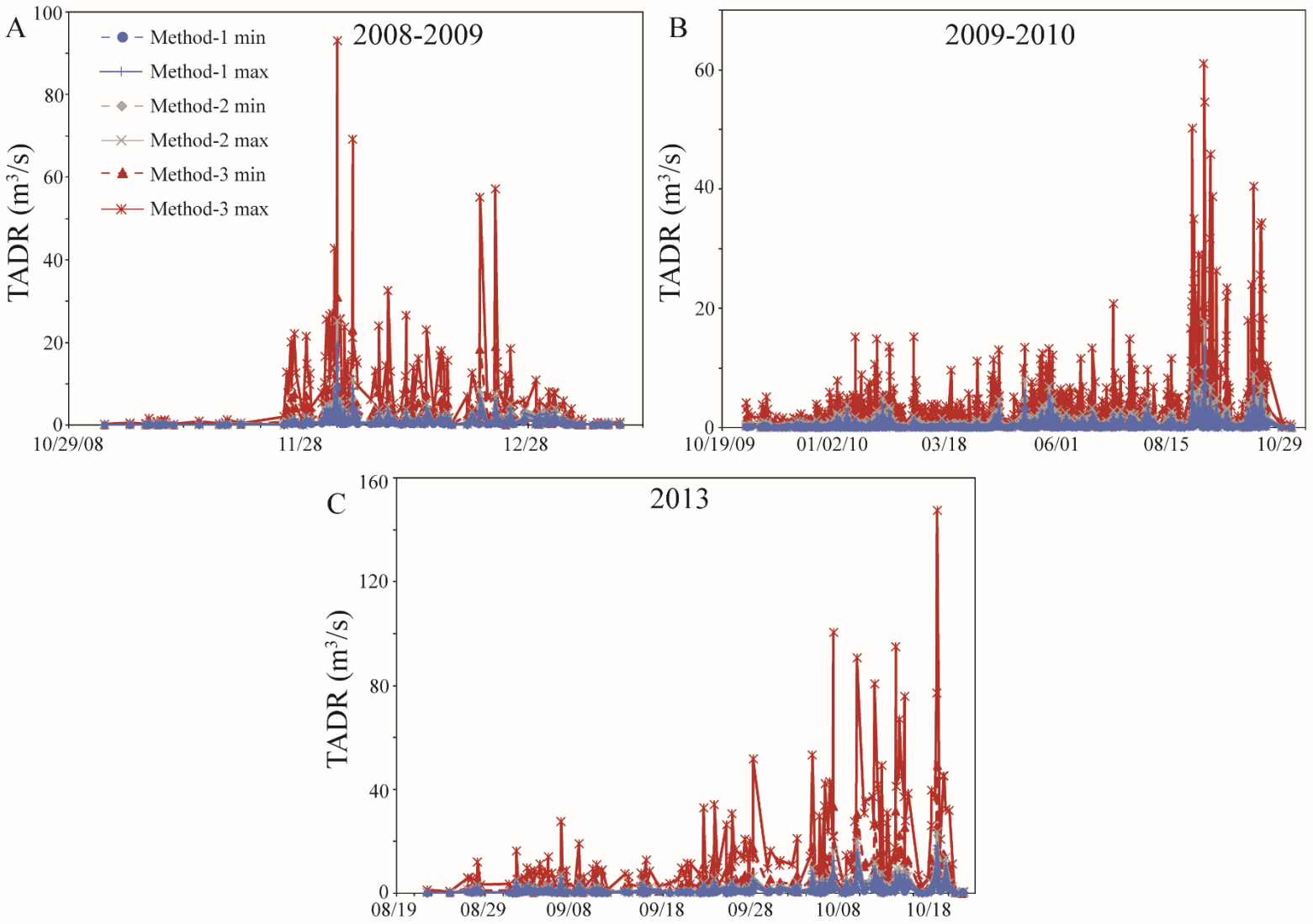

Figure A.11. TADR time-series for Klyuchevskoy eruptions. A) 2008-2009; B) 2009-2010; and C) 2013. Note a slightly different legend.

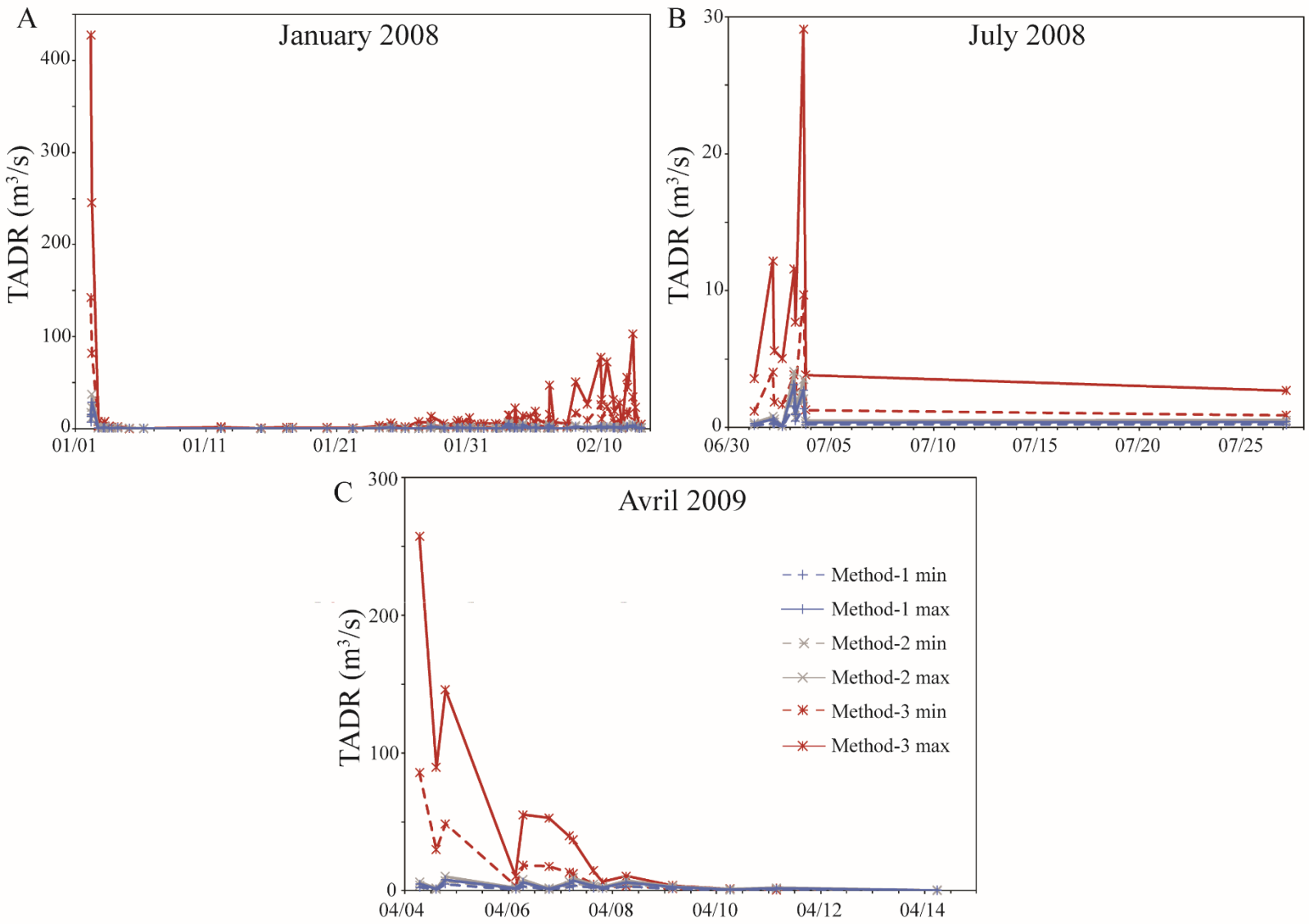

Figure A.12. TADR time-series for Llaima eruptions. A) January 2008; B) July 2008; and C) April 2009.

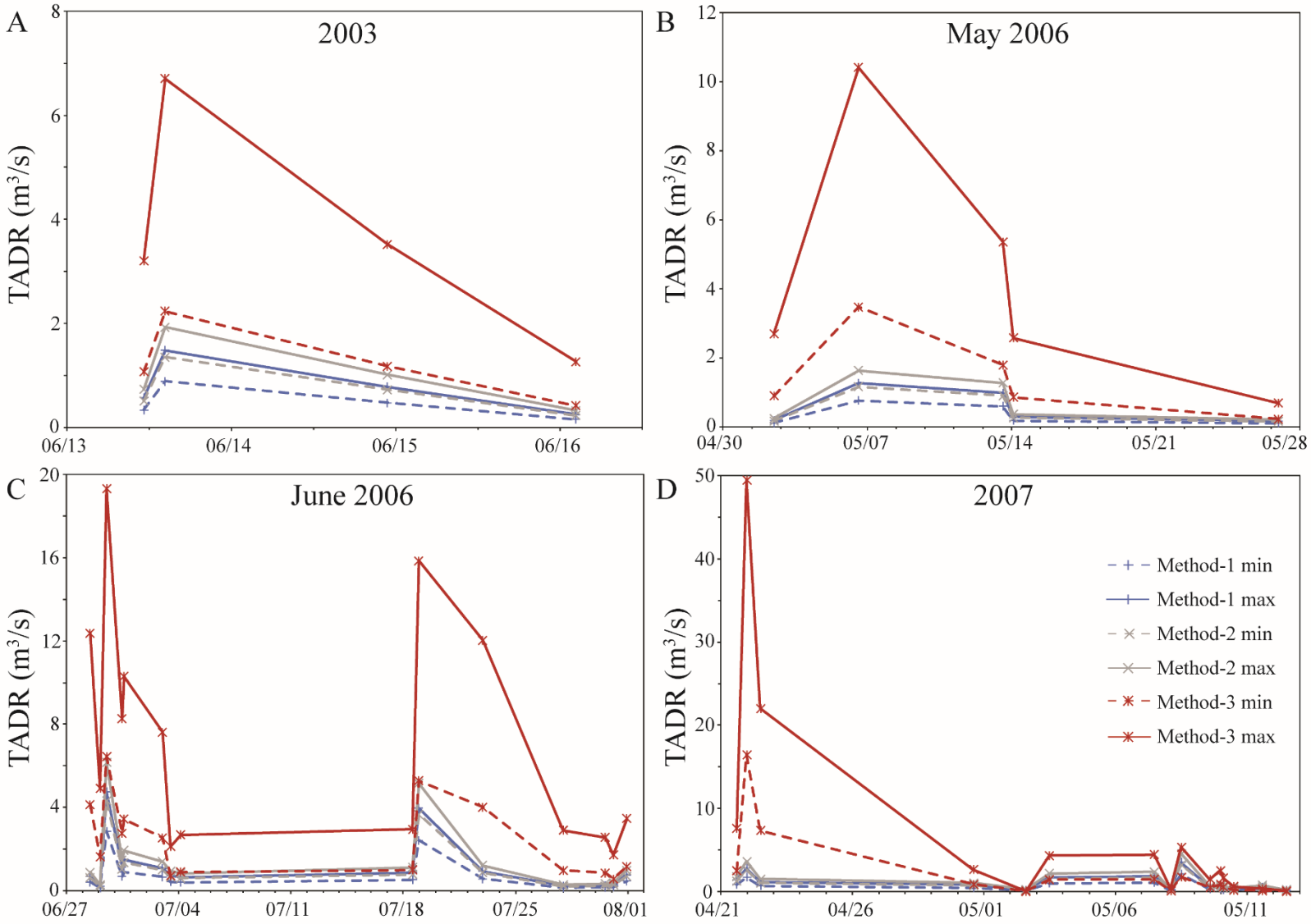

Figure A.13. TADR time-series for Lopevi eruptions. A) 2003; B) May 2006; C) June 2006; and D) 2007.

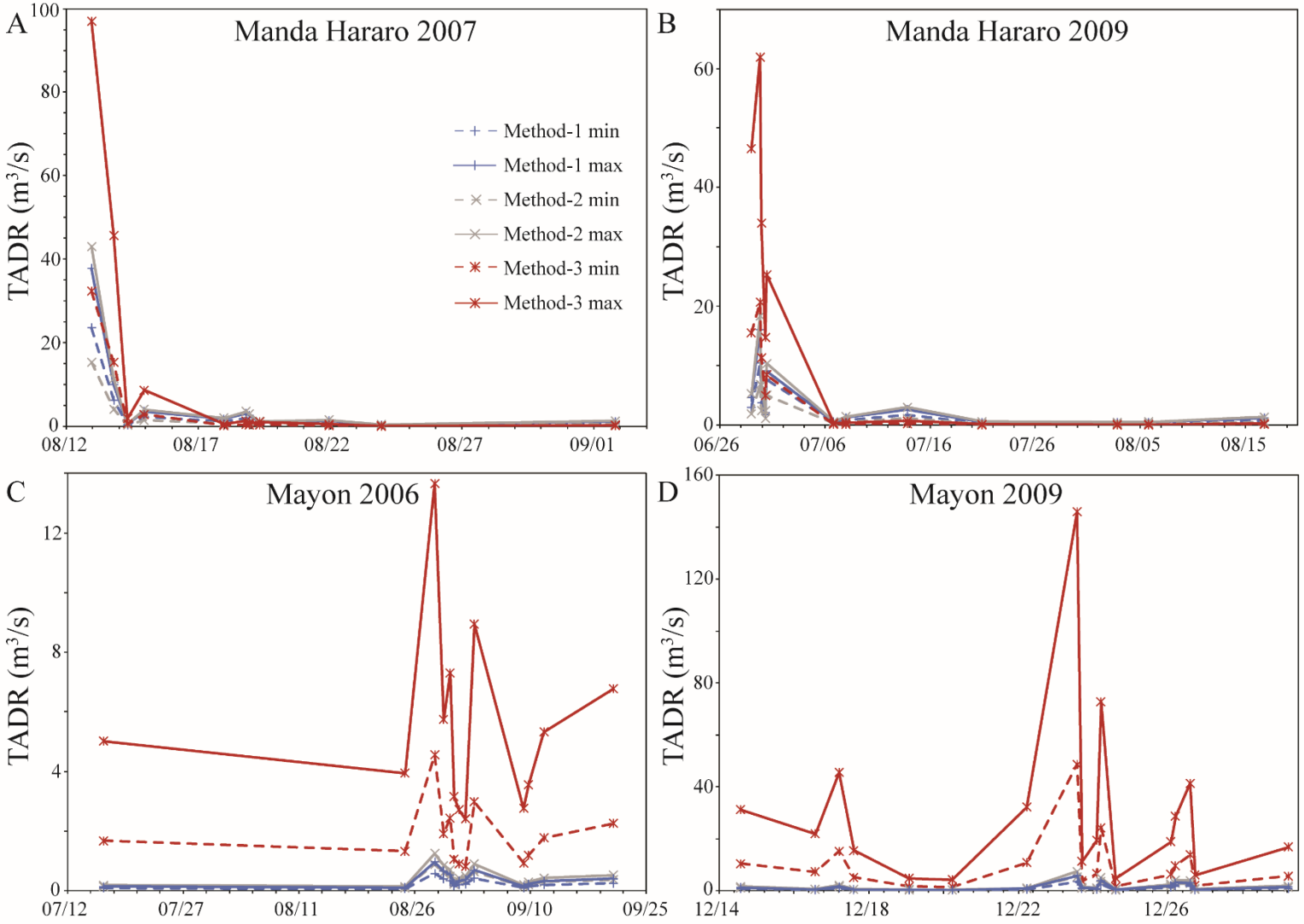

Figure A.14. TADR time-series for A) Manda Hararo eruption in 2007; B) Manda Hararo eruption in 2009; C) Mayon eruption in 2006; and D) Mayon eruption in 2009.

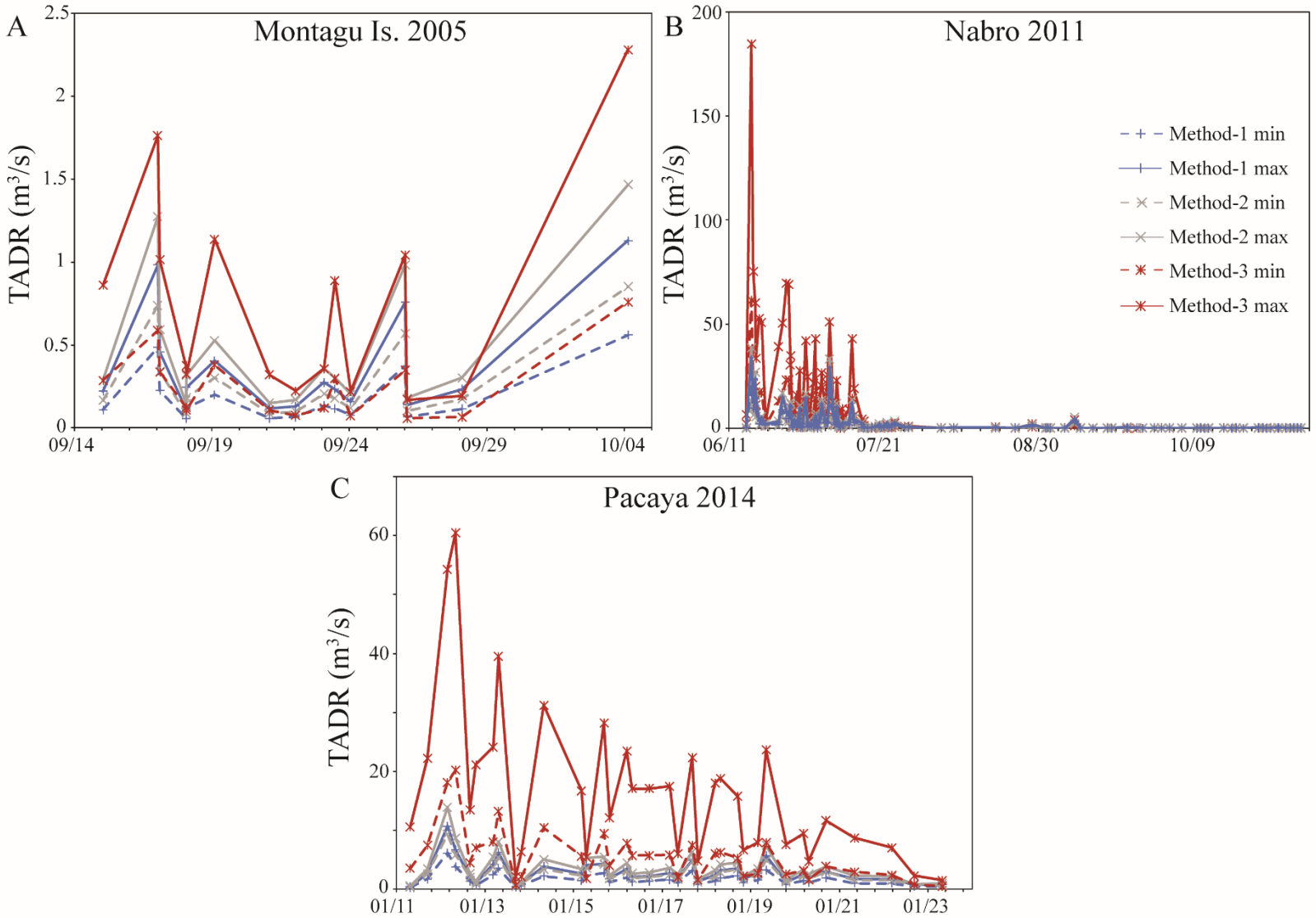

Figure A.15. TADR time-series for A) Montagu Island eruption in 2005; B) Nabro eruption in 2011; and C) Pacaya 2014.

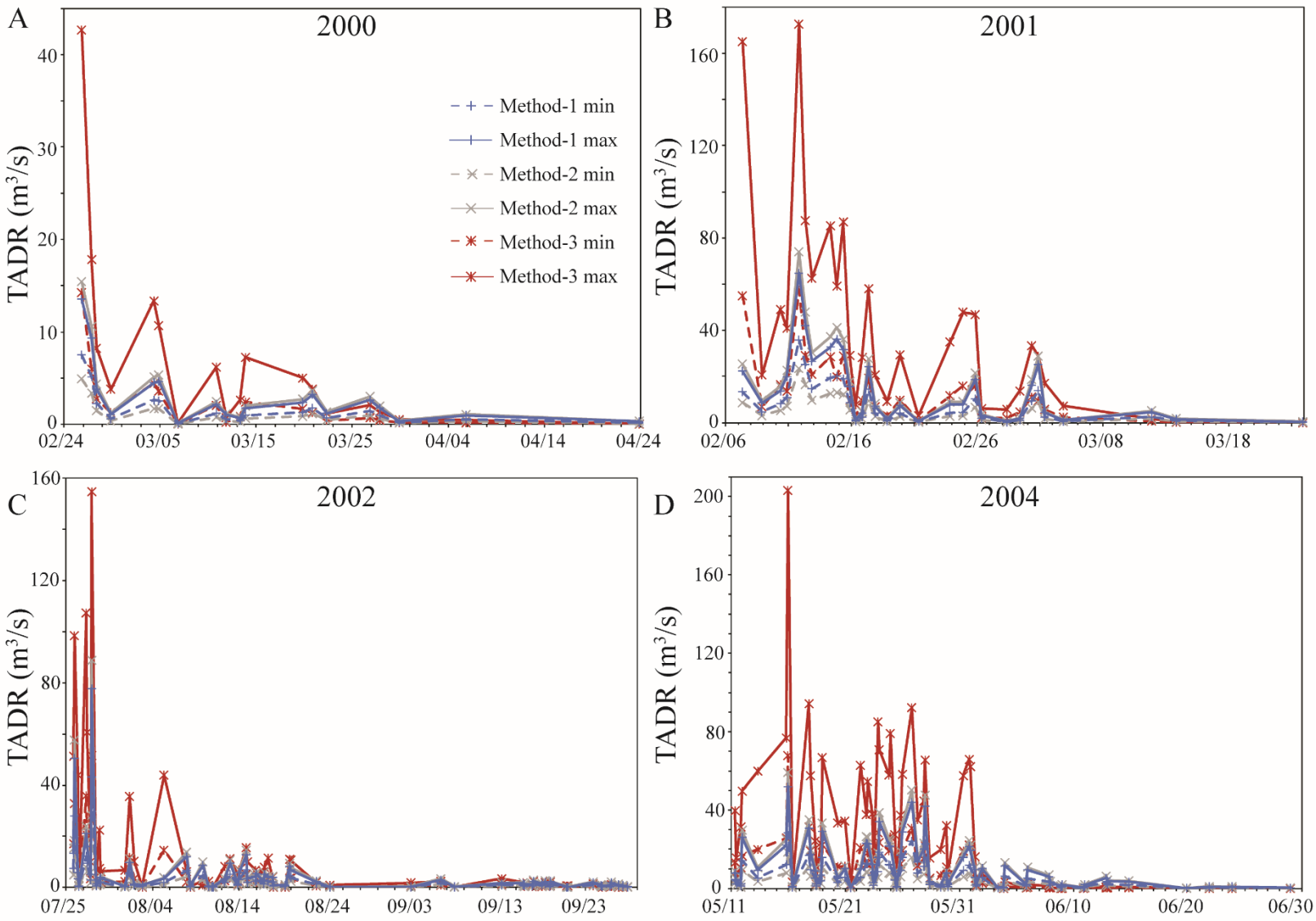

Figure A.16. TADR time-series for Nyamuragira eruptions. A) 2000; B) 2001; C) 2002; and D) 2004.

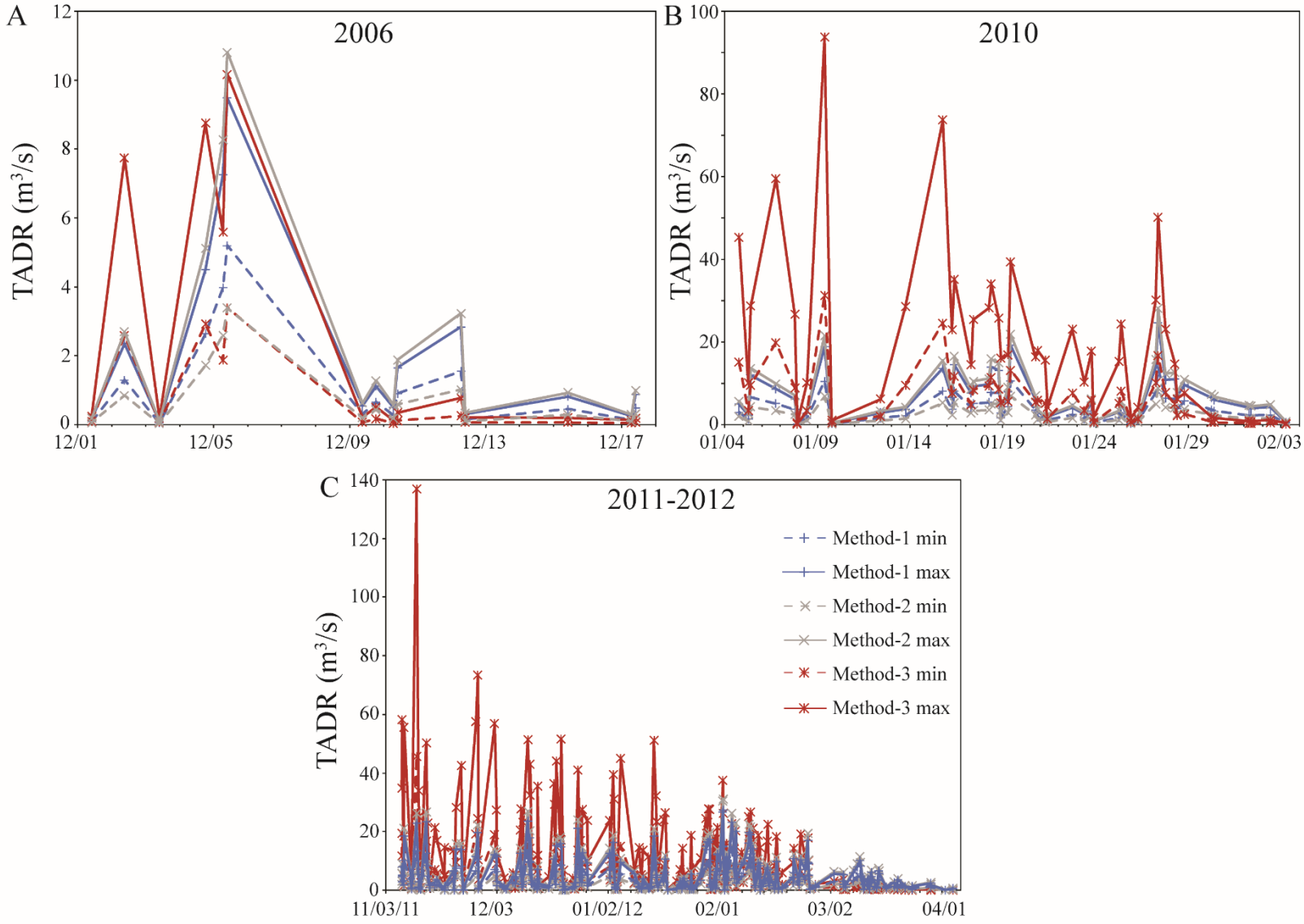

Figure A.17. TADR time-series for Nyamuragira eruptions. A) 2006; B) 2010; and C) 2011-2012.

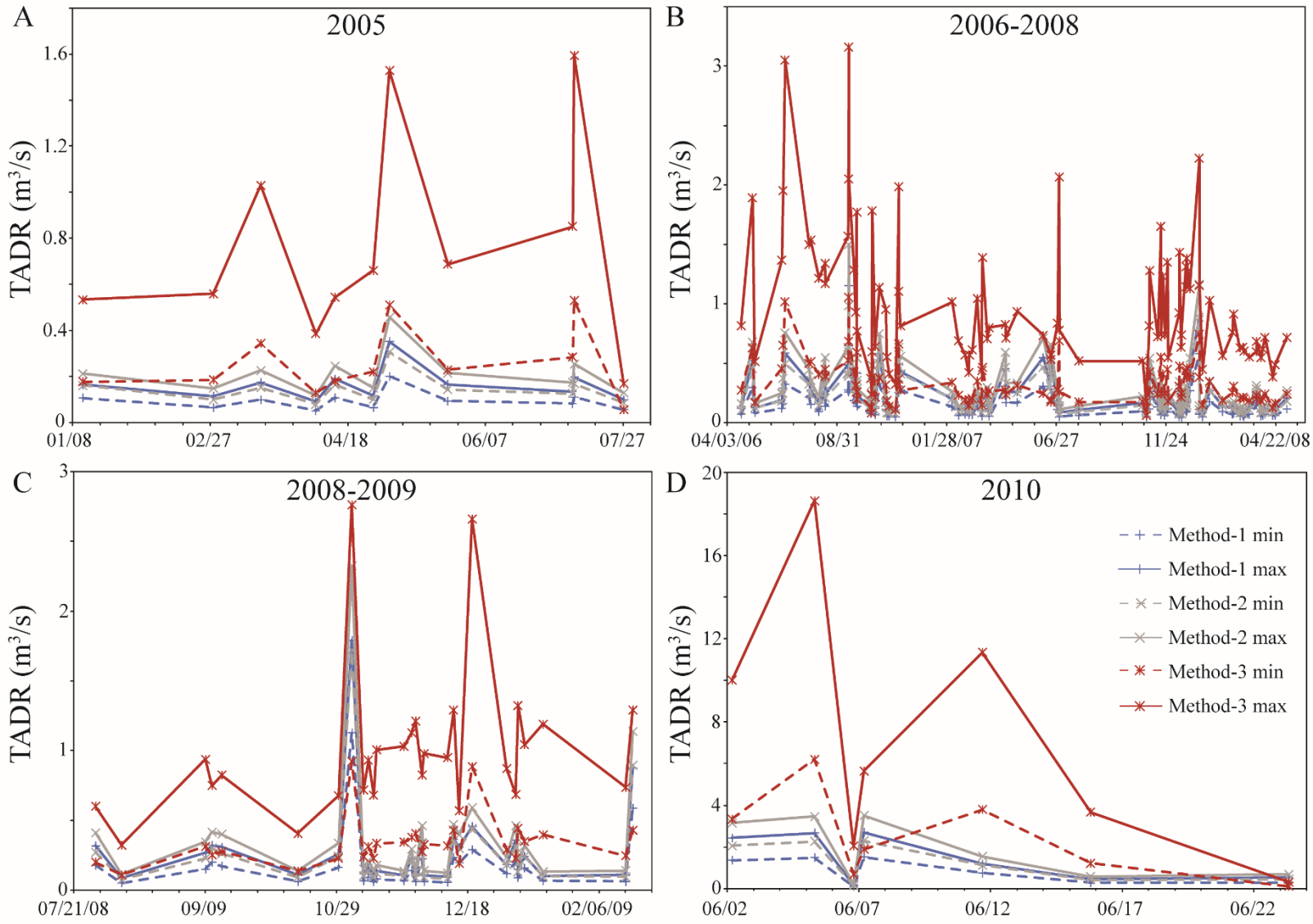

Figure A.18. TADR time-series for Pacaya eruptions. A) 2005; B) 2006-2008; C) 2008-2009; and D) 2010.

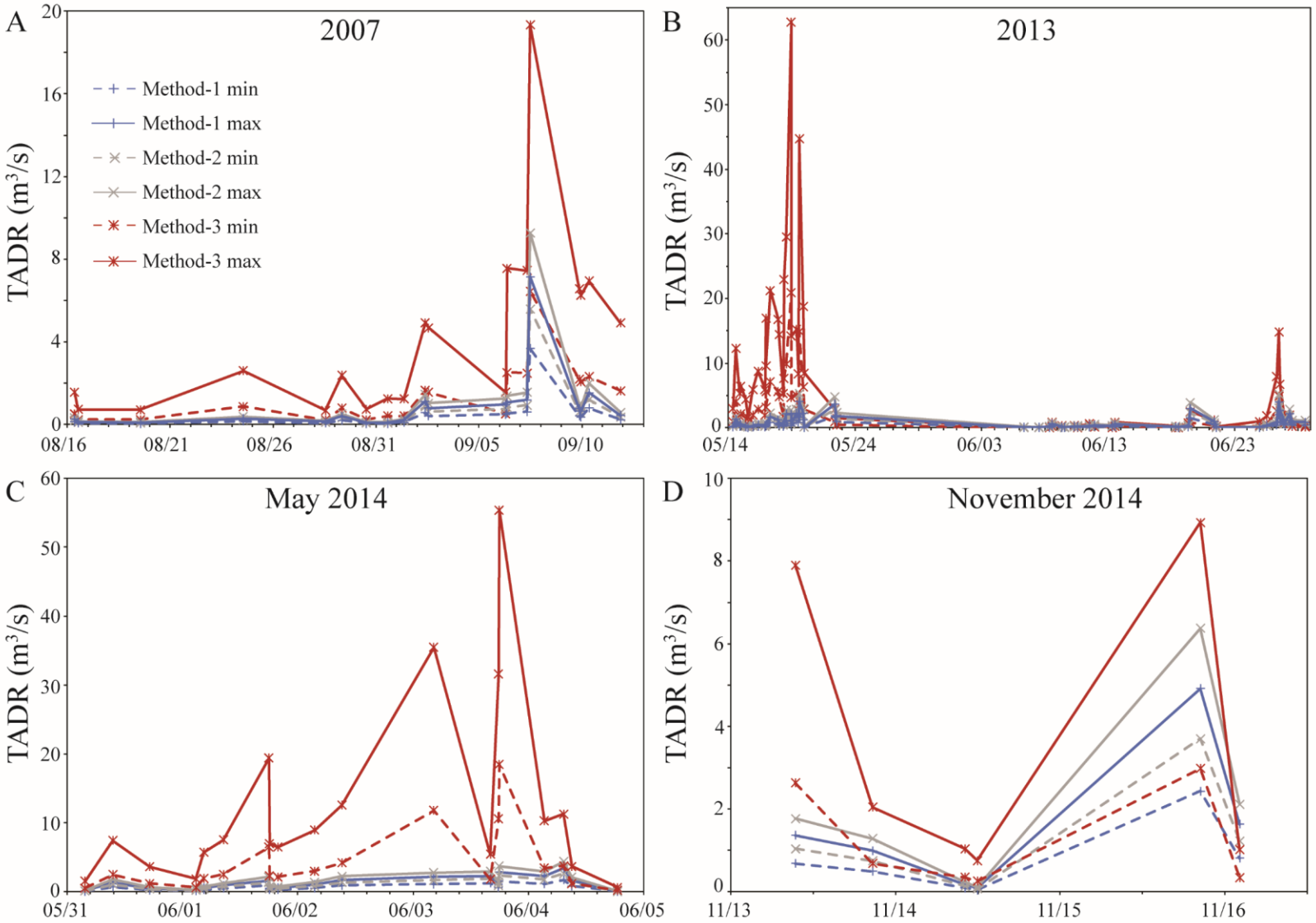

Figure A.19. TADR time-series for Pavlof eruptions. A) 2007; B) 2013; C) May 2014; and D) November 2014.

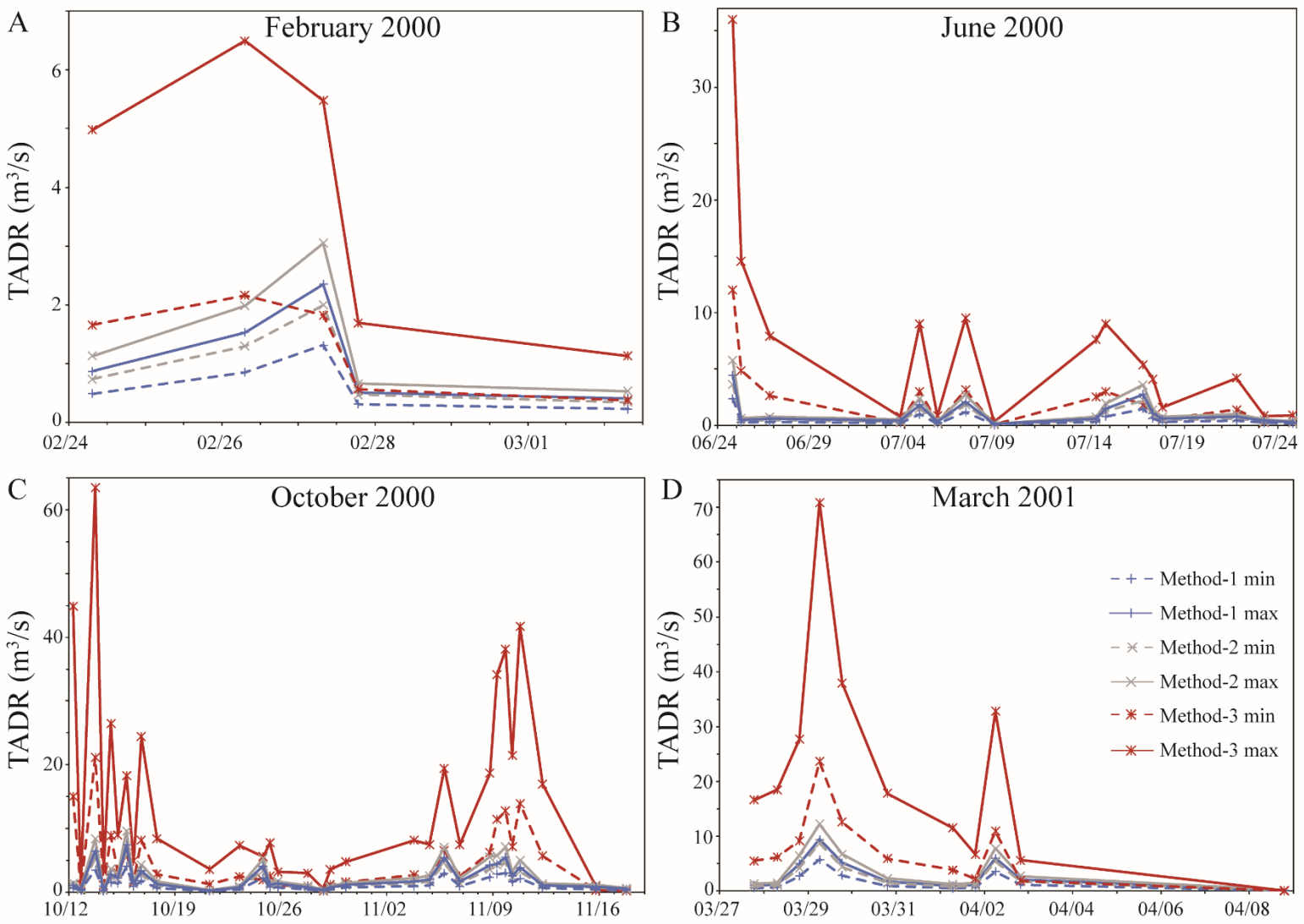

Figure A.20. TADR time-series for the Piton de la Fournaise eruptions. A) February 2000; B) June 2000; C) October 2000; and D) March 2001.

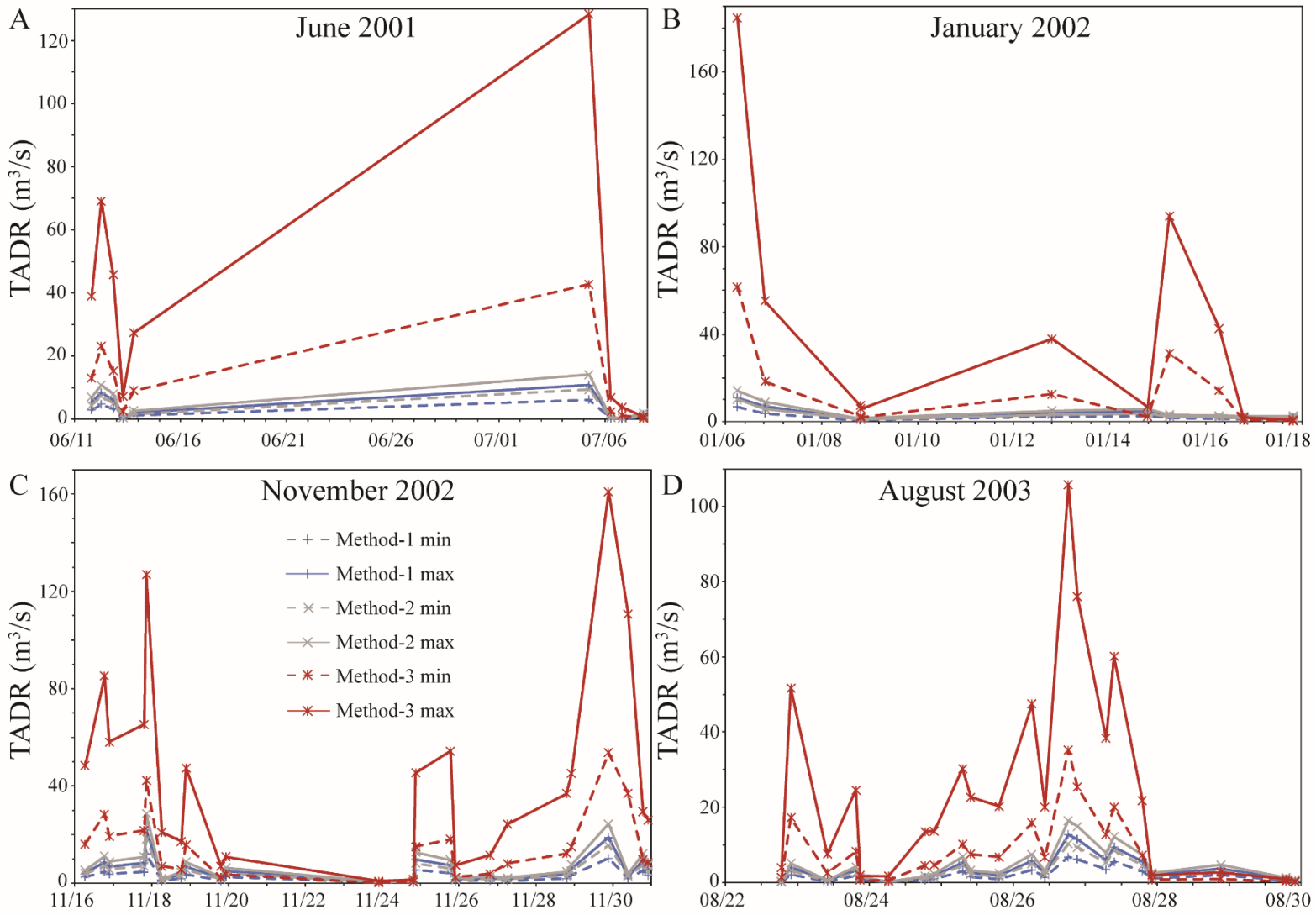

Figure A.21. TADR time-series for the Piton de la Fournaise eruptions. A) June 2001; B) January 2002; C) November 2002; and D) August 2003.

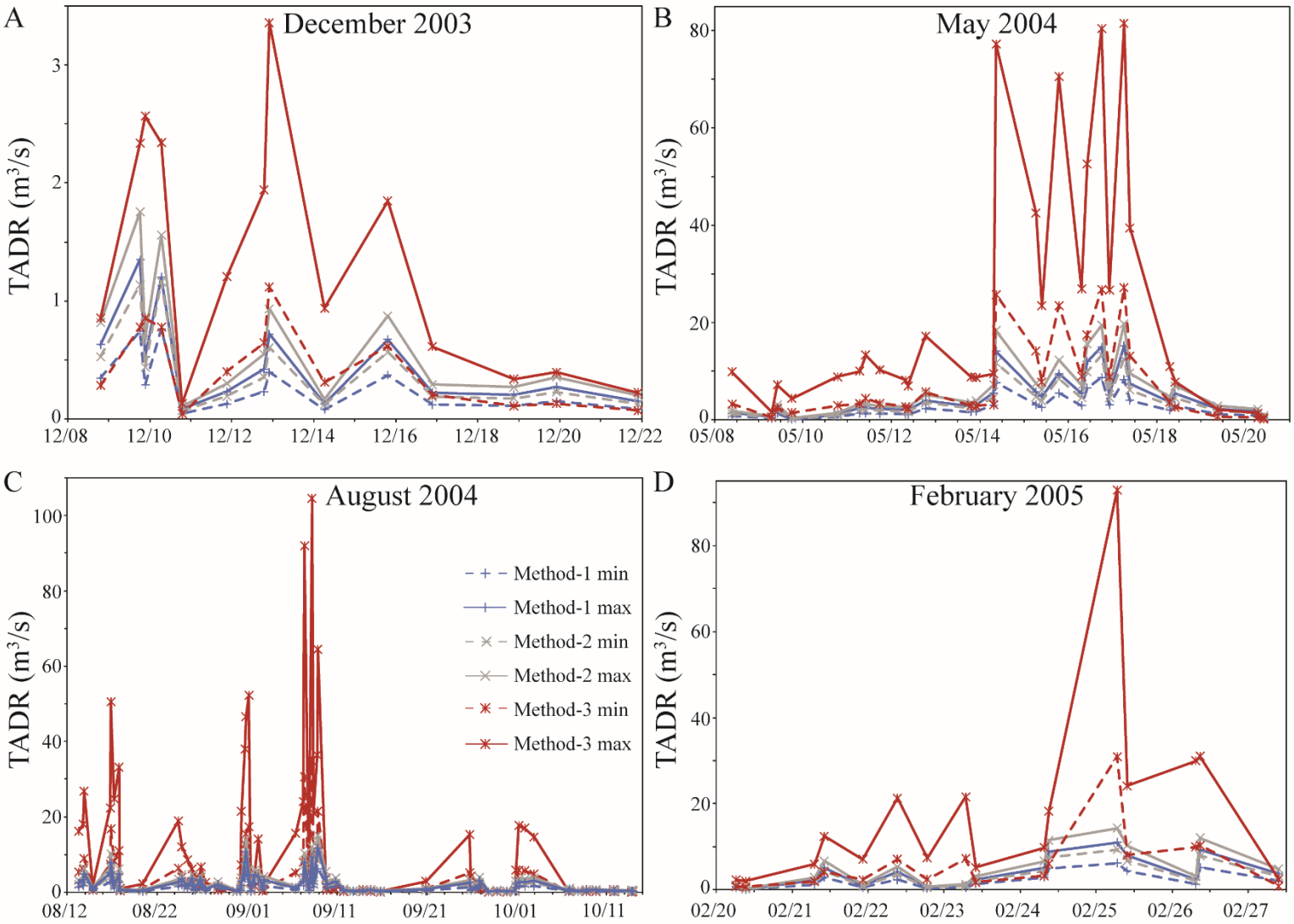

Figure A.22. TADR time-series for the Piton de la Fournaise eruptions. A) December 2003; B) May 2004; C) August 2004; and D) February 2005.

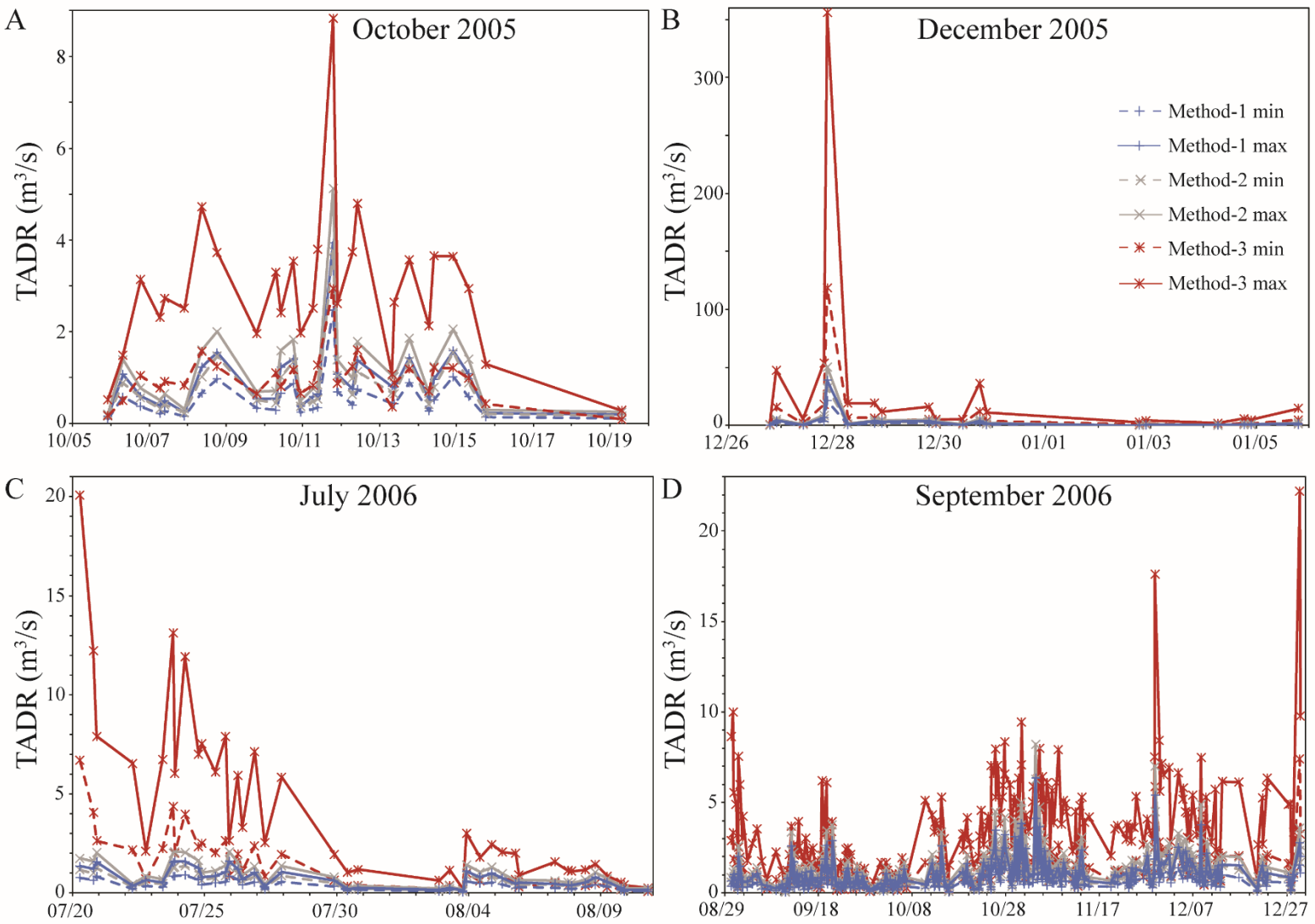

Figure A.23. TADR time-series for the Piton de la Fournaise eruptions. A) October 2005; B) December 2005; C) July 2006; and D) September 2006.

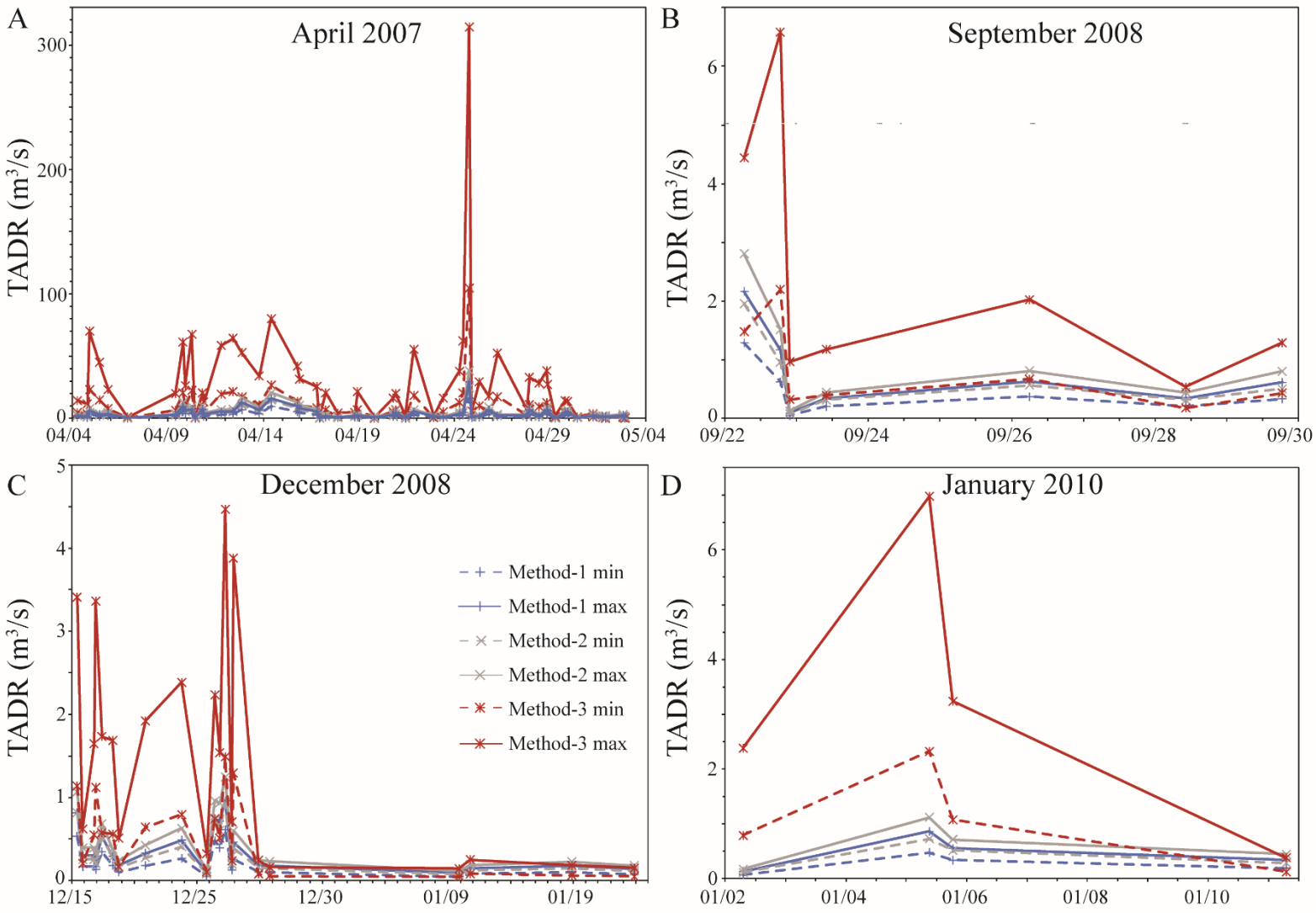

Figure A.24. TADR time-series for the Piton de la Fournaise eruptions. A) April 2007; B) September 2008; C) December 2008; and D) January 2010.

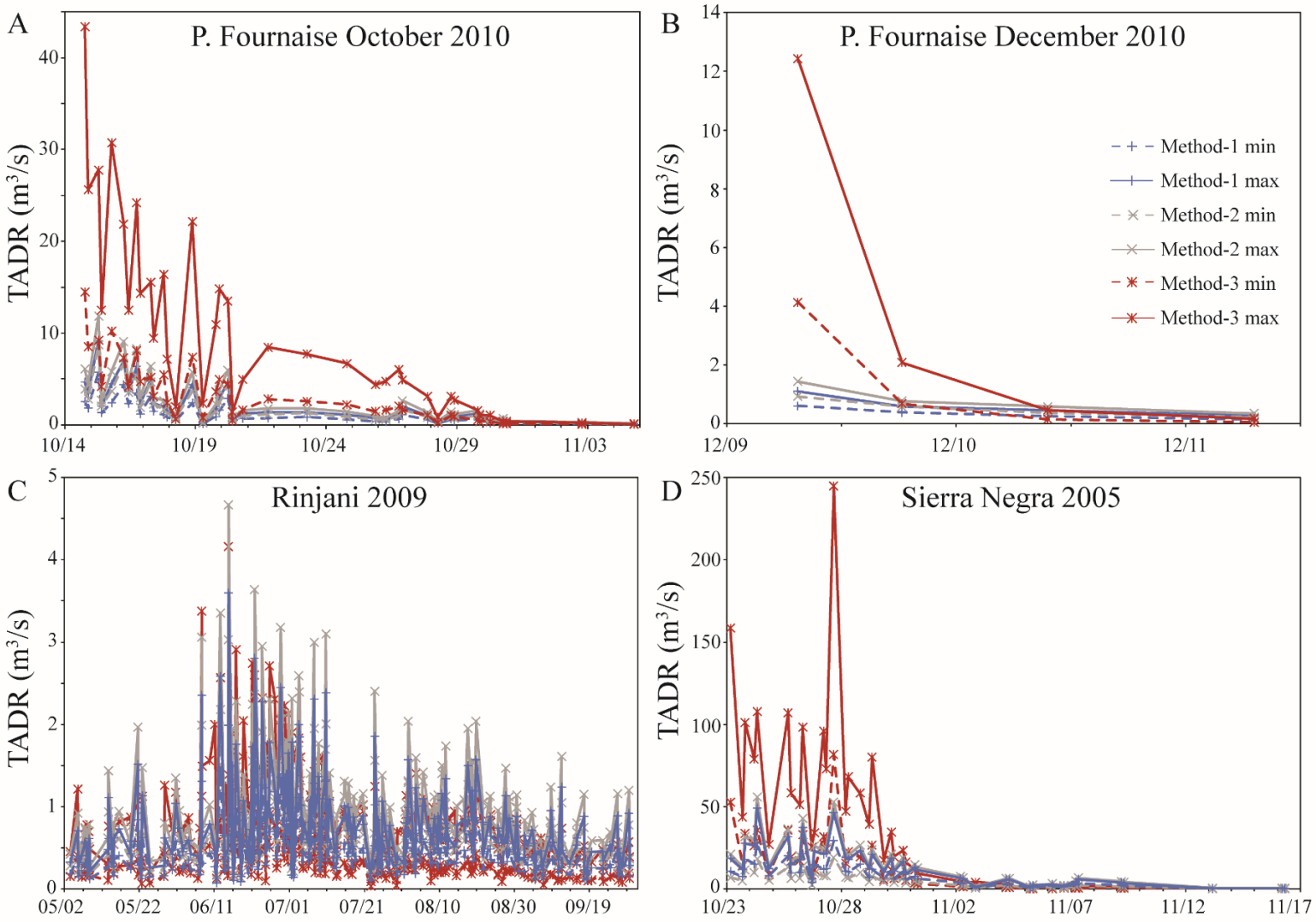

Figure A.25. TADR time-series for A) Piton de la Fournaise eruption in October 2010; B) Piton de la Fournaise eruption in December 2010; C) Rinjani eruption in 2009; and D) Sierra Negra eruption in 2005.

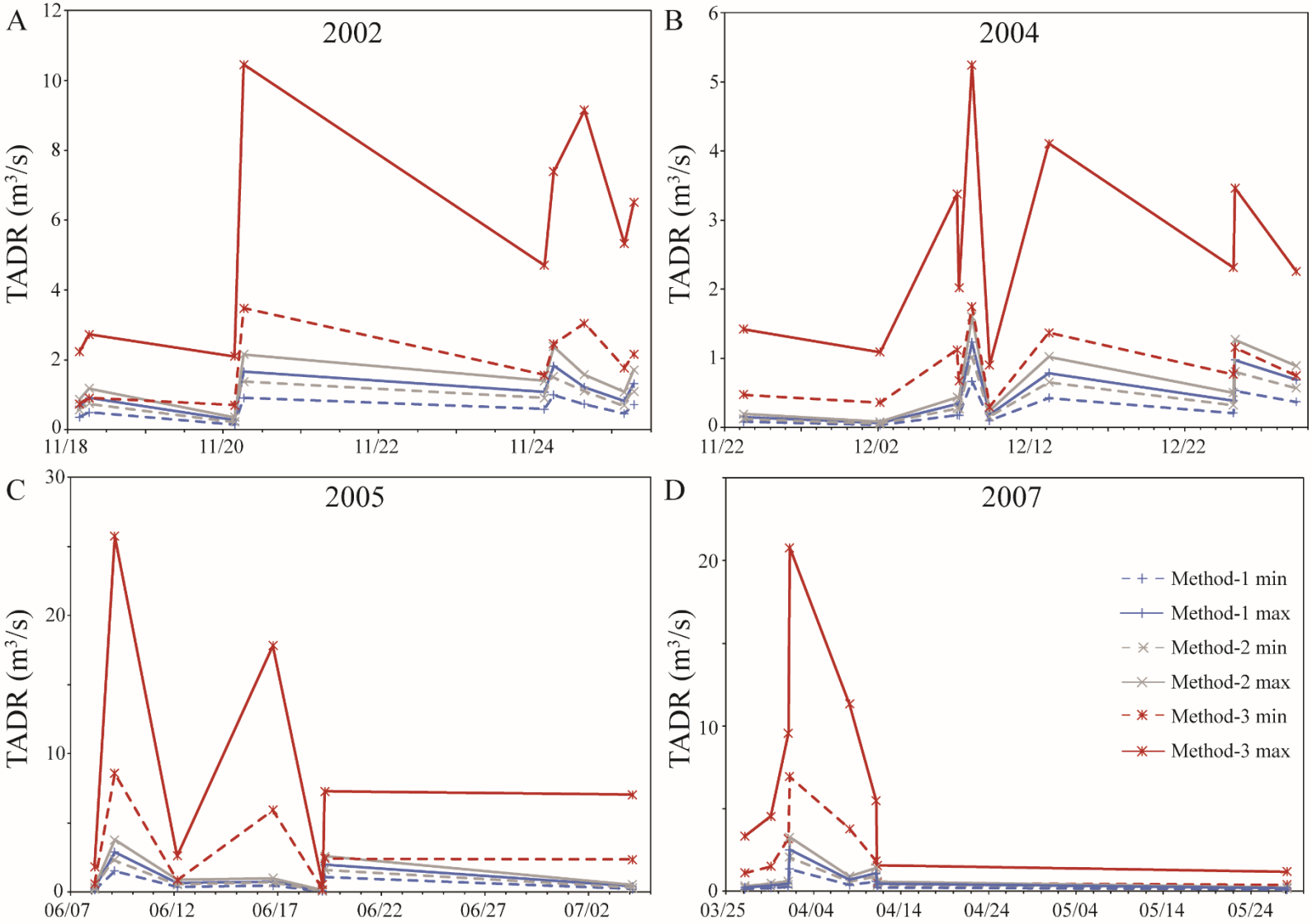

Figure A.26. TADR time-series for Reventador eruptions. A) 2002; B) 2004; C) 2005; and D) 2007.

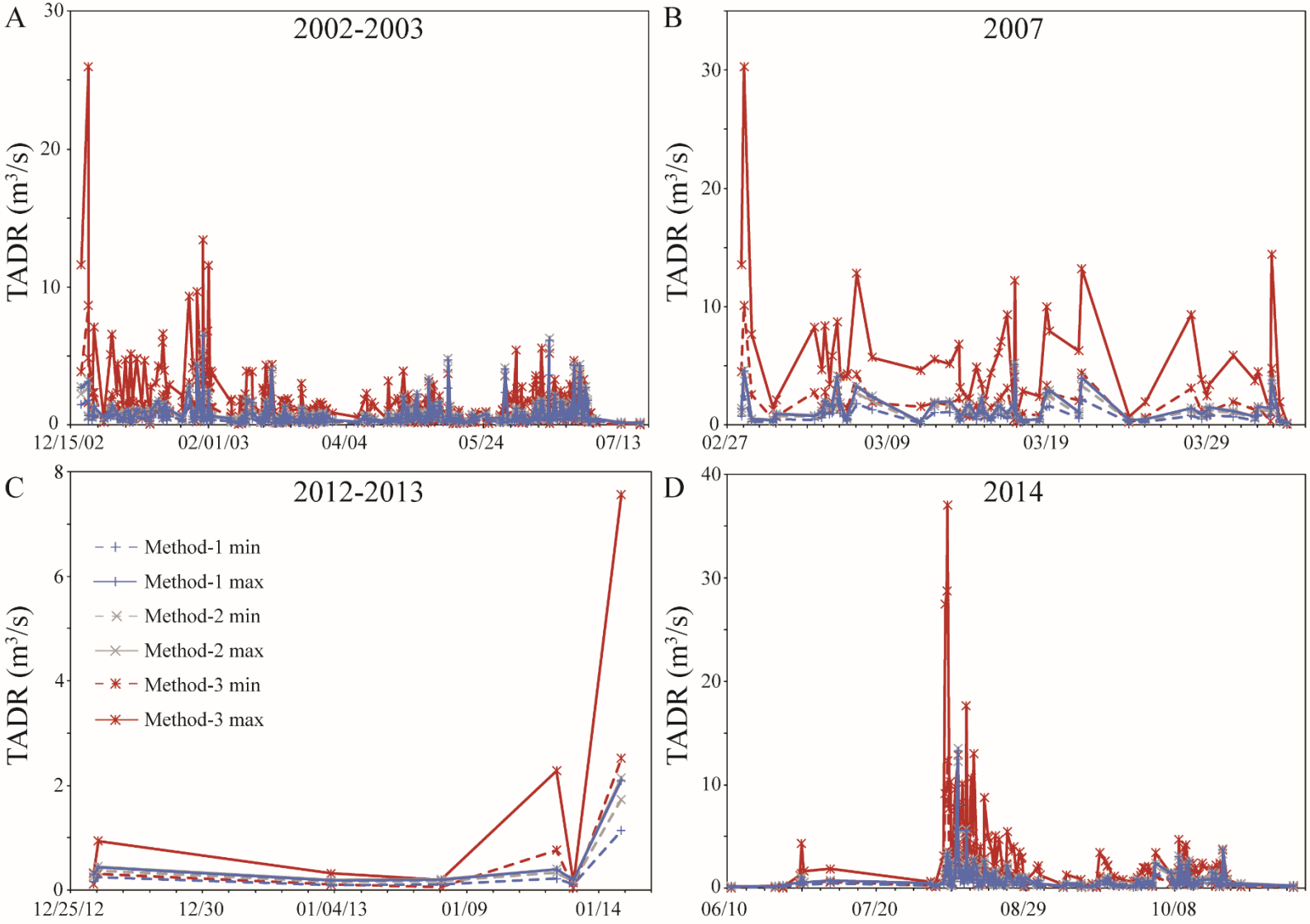

Figure A.27. TADR time-series for Stromboli eruptions. A) 2002-2003; B) 2007; C) 2012-2013; and D) 2014.

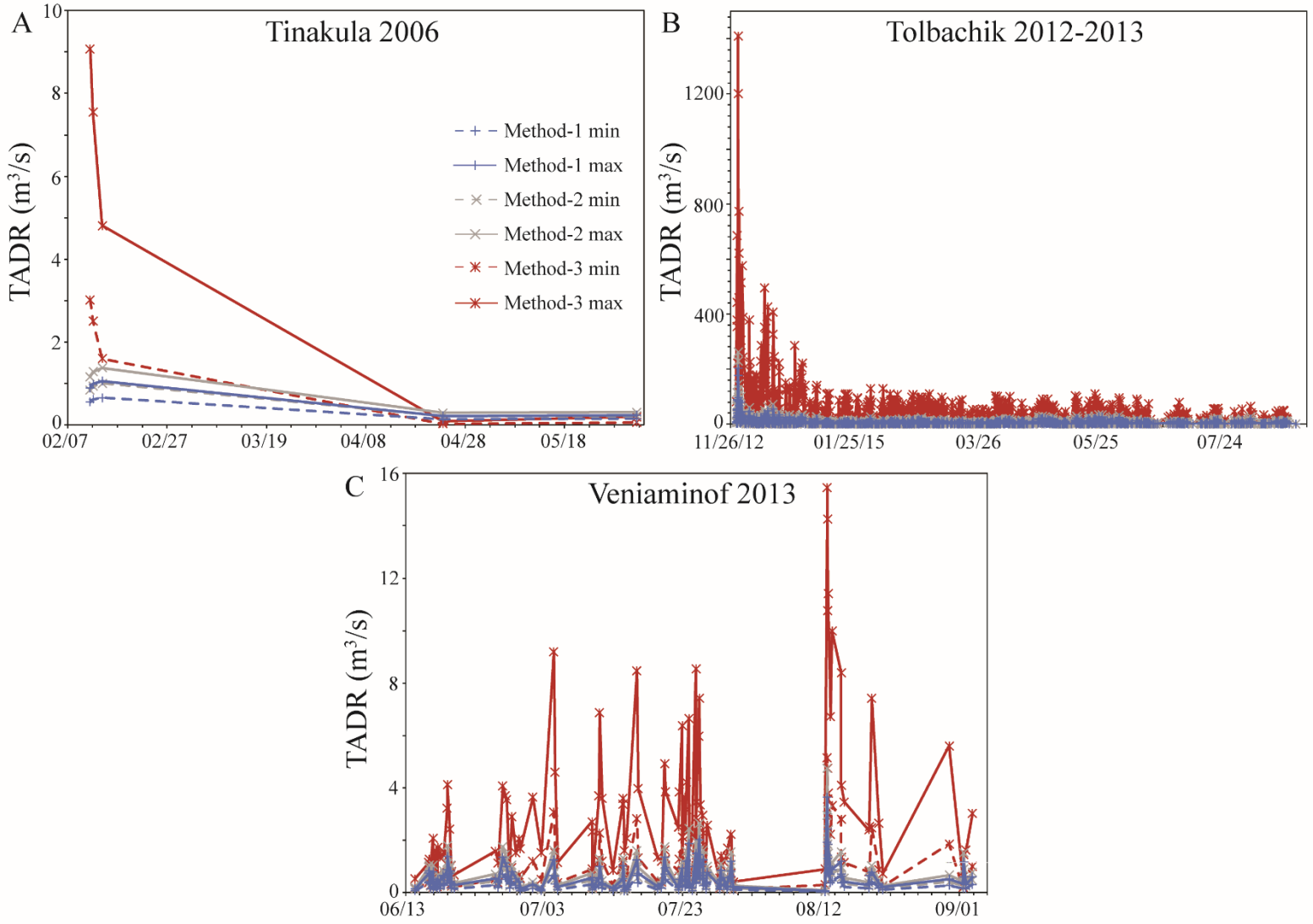

Figure A.28. TADR time-series for A) Tinakula eruption in 2006; B) Tolbachik eruption in 2012-2013; and C) Veniaminof eruption in 2013.

REFERENCES

Ágústsdóttir, T., J. Woods, T. Greenfield, R. G. Green, R. S. White, T. Winder, B. Brandsdóttir, S. Steinthórsson and H. Soosalu (2016), Strike-slip faulting during the 2014 Bárðarbunga-Holuhraun dike intrusion, central Iceland, *Geophys. Res. Lett.,* 43(4), 1495-1503.

Aiuppa, A., R. Moretti, C. Federico C, G. Giudice, S. Gurrieri, M. Liuzzo, P. Papale, H. Shinohara and M. Valenza (2007), Forecasting Etna eruptions by real-time observation of volcanic gas composition, *Geology,* 35(12), 1115-1118, doi: 10.1130/G24149A.1.

Albino, F., B. Smets, N. d'Oreye and F. Kervyn (2015), High-resolution TanDEM-X DEM: An accurate method to estimate lava flow volumes at Nyamulagira volcano (D. R. Congo), *J. Geophys. Res. Solid Earth*, 120, 4189–4207, doi:10.1002/2015JB011988.

Allan, J. F. and T. Simkin (2000), Fernandina Volcano's evolved, well-mixed basalts: Mineralogical and petrological constraints on the nature of the Galapagos plume, *J. Geophys. Res. Solid Earth*, 105(B3), 6017-6041.

Allard, P., B. Behncke, S. D'Amico, M. Neri and S. Gambino (2006), Mount Etna 1993–2005: anatomy of an evolving eruptive cycle, *Earth-Science Reviews,* 78(1), 85-114, doi:10.1016/j.earscirev.2006.04.002.

Andronico, D., S. Branca, S. Calvari, M. Burton, T. Caltabiano, R.A. Corsaro, P. Del Carlo, G. Garfi, L. Lodato, L. Miraglia, F. Mure, M. Neri, E. Pecora, M. Pompilio, G. Salerno and L. Spampinato (2005), A multi-disciplinary study of the 2002–03 Etna eruption: insights into a complex plumbing system, *Bull. Volcanol.,* 67, 314–330, doi:10.1007/s00445-004-0372-8.

Andronico, D., A. Cristaldi and S. Scollo (2008), The 4–5 September 2007 lava fountain at South-East Crater of Mt Etna, Italy, *J. Volcanol. Geotherm. Res.,* 173, 325–328, doi:10.1016/j.jvolgeores.2008.02.004.

Aries, S. E., A. J. L. Harris and D. A. Rothery (2001), Remote infrared detection of the cessation of volcanic eruptions, *Geophys. Res. Lett.,* 28(9), 1803-1806.

Bali, E., M. E. Hartley, S. A. Halldórsson, G. H. Gudfinnsson and S. Jakobsson (2018), Melt inclusion constraints on volatile systematics and degassing history of the 2014–2015 Holuhraun eruption, Iceland, *Contrib. Miner. Petrol.*, 173(2), 9.

Barmin, A., O. E. Melnik and R. S. J. Sparks (2002), Periodic behavior in lava dome eruptions, *Earth Planet. Sci. Lett.,* 199, 173-184.

Baubron, J. C., P. Allard, J. C. Sabroux, D. Tedesco and J. P. Toutain (1991), Soil gas emanations as precursory indicators of volcanic eruptions, *J. Geol. Soc. London,* 148, 571-576.

Behncke, B. and M. Neri (2003), The July–August 2001 eruption of Mt. Etna (Sicily), *Bull. Volcanol.,* 65, 461–476, doi:10.1007/s00445-003-0274-1.

Bonny, E. and R. Wright (2017), Predicting the end of lava flow-forming eruptions from space, *Bull. Volcanol.,* 79, 52, doi:10.1007/s00445-017-1134-8.

Brenguier, F., N. M. Shapiro, M. Campillo, V. Ferrazzini, Z. Duputel, O. Coutant and A. Nercessian (2008), Towards forecasting volcanic eruptions using seismic noise, *Nature Geoscience,* 1(2), 126-130, doi:10.1038/ngeo104.

Calvari, S., M. Neri and H. Pinkerton (2003), Effusion rate estimations during the 1999 summit eruption on Mount Etna, and growth of two distinct lava flow fields, *J. Volcanol. Geotherm. Res.*, 119(1-4), 107-123.

Calvari, S., L. Spampinato, L. Lodato, A. J. L. Harris, M. R. Patrick, J. Dehn, M. R. Burton and D. Andronico (2005), Chronology and complex volcanic processes during the 2002–2003 flank eruption at Stromboli volcano (Italy) reconstructed from direct observations and surveys with a handheld thermal camera, *J. Geophys. Res.,* 110, B02201, doi:10.1029/2004JB003129.

Chadwick, W. W. Jr, S. Jónsson, D. J. Geist, M. Poland, D. J. Johnson, S. Batt, K. S. Harpp and A. Ruiz (2011), The May 2005 eruption of Fernandina volcano, Galápagos: The first circumferential dike intrusion observed by GPS and InSAR, *Bull. Volcanol.,* 73, 679–697, doi:10.1007/s00445-010-0433-0.

Cigolini, C., M. Laiolo and S. Bertolino (2008), Probing Stromboli volcano from the mantle to paroxysmal eruptions, *Geol. Soc. London, Special Publications*, 304(1), 33-70.

Coltelli, M., P. Del Carlo and L. Vezzoli (1998), Discovery of a Plinian basaltic eruption of Roman age at Etna volcano, Italy, *Geology*, 26(12), 1095–1098.

Coppola, D., M. R. James, T. Staudacher and C. Cigolini (2010), A comparison of field- and satellite-derived thermal flux at Piton de la Fournaise: implications for the calculation of lava discharge rate, *Bull. Volcanol.,* 72, 341–356, doi:10.1007/s00445-009-0320-8.

Coppola, D., D. Piscopo, M. Laiolo, C. Cigolini, D. Delle Donne and M. Ripepe (2012), Radiative heat power at Stromboli volcano during 2000–2011: Twelve years of MODIS observations, *J. Volcanol. Geotherm. Res.,* 215-216, 48-60, doi:10.1016/j.jvolgeores.2011.12.001.

Coppola, D. and C. Cigolini (2013), Thermal regimes and effusive trends at Nyamuragira volcano (DRC) from MODIS infrared data, *Bull. Volcanol.,* 75, 744, doi: 10.1007/s00445-013-0744-z.

Coppola, D., M. Laiolo, D. Piscopo and C. Cigolini (2013), Rheological control on the radiant density of active lava flows and domes, *J. Volcanol. Geotherm.,* 249, 39-48, http://dx.doi.org/10.1016/j.jvolgeores.2012.09.005.

Coppola, D., A. Di Muro, A. Peltier, N. Villeneuve, V. Ferrazzini, M. Favalli, P. Bachèlery, L. Gurioli, A. J. L. Harris, S. Moune, I. Vlastélic, B. Galle, S. Arellano and A. Aiuppa (2017), Shallow system rejuvenation and magma discharge trends at Piton de la Fournaise volcano (La Réunion Island), *Earth Planet. Sci. Lett.,* 463, 13–24.

Coulson, I. M., F. M. Stuart and N. J. MacLean (2010), Assessing the link between mantle source and sub-volcanic plumbing in the petrology of basalts from the 2001 and 2002/2003 eruptions of Mount Etna, Sicily: evidence from geochemical and helium isotope data, *Lithos.,* 123, 254–261, http://dx.doi.org/10.1016/j.lithos.2010.11.013.

Cracknell, A. P. and L. W. B. Hayes (1991), Introduction to Remote Sensing, *London: Taylor & Francis*, 293.

Davies, M. A. and W. I. Rose (1998), GOES imagery fills gaps in Montserrat volcanic cloud observations, *Eos, Transactions American Geophys. Union,* 79(42), 505-507.

De Maisonneuve, C. B., M. A. Dungan, O. Bachmann and A. Burgisser (2012), Insights into shallow magma storage and crystallization at Volcán Llaima (Andean Southern Volcanic Zone, Chile), *J. Volcanol. Geotherm. Res.,* 211, 76-91.

Del Negro, C., L. Fortuna, A. Herault and A. Vicari (2008), Simulations of the 2004 lava flow at Etna volcano by the MAGFLOW cellular automata model, *Bull. Volcanol.*, doi:10.1007/s00445-007-0168-8.

Doglioni, C., F. Innocenti and G. Mariotti (2001), Why Mt Etna? *Terra Nova,* 13(1), 25-31.

Dozier, J. (1981), A method for satellite identification of surface temperature fields of subpixel resolution, *Remote Sens. Envir.,* 11, 221-229.

Edwards, B., A. Belousov, M. Belousova, A. Volynets, D. Melnikov, S. Chirkov, S. Senyukov, E. Gordeev, Y. Muraviev, P. Izbekov and Y. Demianchuk (2013), Another "Great Tolbachik" Eruption? *Eos, Transactions American Geophys. Union*, 94(21), 189-191.

Eibl, E. P. S., C. J. Bean, I. Jónsdóttir, A. Höskuldsson, T. Thordarson, D. Coppola, T. Witt and T. R. Walter (2017), Multiple coincident eruptive seismic tremor sources during the 2014–2015 eruption at Holuhraun, Iceland, *J. Geophys. Res. Solid Earth,* 122, doi:10.1002/2016JB013892.

Fedotov, S. A. and Y. K. Markhinin (1983), The Great Tolbachik Fissure Eruption: Geological and Geophysical Data 1975–1976, *Cambridge Univ. Press, Cambridge, U. K.*

Fedotov, S. A. and N. A. Zharinov (2007), On the Eruptions, Deformation, and Seismicity of Klyuchevskoy Volcano, Kamchatka in 1986–2005 and the Mechanisms of Its Activity, *J. Volcanol. Seismol.,* 1(2), 71–97, doi: 10.1134/S0742046307020017.

Ferguson, D. J., T. D. Barnie, D. M. Pyle, C. Oppenheimer, G. Yirgu, E. Lewi, T. Kidane, S. Carn and I. Hamling (2010), Recent rift-related volcanism in Afar, Ethiopia, *Earth Planet. Sci. Lett.,* 292, 409–418, doi:10.1016/j.epsl.2010.02.010.

Finch, R. H. and G. A. Macdonald (1953), Hawaiian volcanoes during 1950.

Francis, P. and C. Oppenheimer (2004), Volcanoes, 2nd edition, Oxford University Press, Oxford.

Ganci, G., A. Vicari, A., L. Fortuna and C. Del Negro (2011), The HOTSAT volcano monitoring system based on a combined use of SEVIRI and MODIS multispectral data, *Annals of Geophys.*, 54, doi:10.4401/ag-5338 5.

Ganci, G., A. Vicari, A. Cappello and C. Del Negro (2012), An emergent strategy for volcano hazard assessment: from thermal satellite monitoring to lava flow modeling, *Remote Sens. Envir.*, 119, 197-207.

Geist, D. J., K. S. Harpp, T. R. Naumann, M. Poland, W. W. Chadwick, M. Hall and E. Rader (2008), The 2005 eruption of Sierra Negra volcano, Galápagos, Ecuador, *Bull. Volcanol.,* 70, 655–673, doi:10.1007/s00445-007-0160-3.

Gíslason, S. R., et al. (2015), Environmental pressure from the 2014–15 eruption of Bárðarbunga volcano, Iceland, *Geochem. Perspect. Lett.,* 1, 84–93, doi:10.7185/geochemlet.1509.

Glaze, L., P. W. Francis and D. A. Rothery (1989), Measuring thermal budgets of active volcanoes by satellite remote sensing, *Nature*, 338(6211), 144.

Global Volcanism Program (1981), Report on Pavlof (United States). In: McClelland, L. (ed.), Scientific Event Alert Network Bulletin, 6:9. Smithsonian Institution. http://dx.doi.org/10.5479/si.GVP.SEAN198109-312030.

Global Volcanism Program (1984), Report on Veniaminof (United States). In: McClelland, L. (ed.), Scientific Event Alert Network Bulletin, 9:1. Smithsonian Institution. http://dx.doi.org/10.5479/si.GVP.SEAN198401-312070.

Global Volcanism Program (2000), Report on Nyamuragira (DR Congo). In: Wunderman, R. (ed.), *Bull. Glob. Volcanism Netw.* 25:1. Smithsonian Institution. http://dx.doi.org/10.5479/si.GVP.BGVN200001-223020.

Global Volcanism Program (2002), Report on Etna (Italy). In: Wunderman, R. (ed.), Bulletin of the Global Volcanism Network, 27:12. Smithsonian Institution. http://dx.doi.org/10.5479/si.GVP.BGVN200212-211060.

Global Volcanism Program (2003), Report on Barren Island (India). In: Venzke, E. (ed.), Bulletin of the Global Volcanism Network, 28:2. Smithsonian Institution. http://dx.doi.org/10.5479/si.GVP.BGVN200302-260010.

Global Volcanism Program (2004), Report on Reventador (Ecuador). In: Wunderman, R. (ed.), Bulletin of the Global Volcanism Network, 29:11. Smithsonian Institution. http://dx.doi.org/10.5479/si.GVP.BGVN200411-352010.

Global Volcanism Program (2006), Report on Mayon (Philippines). In: Wunderman, R. (ed.), Bulletin of the Global Volcanism Network, 31:7. Smithsonian Institution. http://dx.doi.org/10.5479/si.GVP.BGVN200607-273030.

Global Volcanism Program (2007), Report on Etna (Italy). In: Wunderman, R. (ed.), Bulletin of the Global Volcanism Network, 32:2. Smithsonian Institution. https://doi.org/10.5479/si.GVP.BGVN200702-211060.

Global Volcanism Program (2008), Report on Cerro Azul (Ecuador). In: Wunderman, R. (ed.), Bulletin of the Global Volcanism Network, 33:5. Smithsonian Institution. http://dx.doi.org/10.5479/si.GVP.BGVN200805-353060.

Global Volcanism Program (2008), Report on Reventador (Ecuador). In: Wunderman, R. (ed.), Bulletin of the Global Volcanism Network, 33:4. Smithsonian Institution. http://dx.doi.org/10.5479/si.GVP.BGVN200804-352010.

Global Volcanism Program (2009), Report on Fernandina (Ecuador). In: Wunderman, R. (ed.), Bulletin of the Global Volcanism Network, 34:10. Smithsonian Institution. http://dx.doi.org/10.5479/si.GVP.BGVN200910-353010.

Global Volcanism Program (2009), Report on Piton de la Fournaise (France). In: Wunderman, R. (ed.), Bulletin of the Global Volcanism Network, 34:2. Smithsonian Institution. http://dx.doi.org/10.5479/si.GVP.BGVN200902-233020.

Global Volcanism Program (2010), Report on Piton de la Fournaise (France). In: Wunderman, R. (ed.), Bulletin of the Global Volcanism Network, 35:3. Smithsonian Institution. http://dx.doi.org/10.5479/si.GVP.BGVN201003-233020.

Global Volcanism Program (2011), Report on Kizimen (Russia). In: Wunderman, R. (ed.), *Bull. Glob. Volcanism Netw.* 36:10. Smithsonian Institution. http://dx.doi.org/10.5479/si.GVP.BGVN201110-300230.

Global Volcanism Program (2012), Report on Piton de la Fournaise (France). In: Wunderman, R. (ed.), Bulletin of the Global Volcanism Network, 37:3. Smithsonian Institution. http://dx.doi.org/10.5479/si.GVP.BGVN201203-233020.

Global Volcanism Program (2012), Report on Tolbachik (Russia). In: Wunderman, R. (ed.), Bulletin of the Global Volcanism Network, 37:12. Smithsonian Institution. http://dx.doi.org/10.5479/si.GVP.BGVN201212-300240.

Global Volcanism Program (2014), Report on Fogo (Cape Verde). In: Wunderman, R. (ed.), Bulletin of the Global Volcanism Network, 39:11. Smithsonian Institution. http://dx.doi.org/10.5479/si.GVP.BGVN201411-384010.

Global Volcanism Program (2017), Report on Chirpoi (Russia). In: Venzke, E. (ed.), Bulletin of the Global Volcanism Network, 42:1. Smithsonian Institution.

Gudmundsson, M. T., R. Pedersen, K. Vogfjörd, B. Thorbjarnardóttir, S. Jakobsdóttir and M. J. Roberts (2010), Eruptions of Eyjafjallajökull Volcano, Iceland, *Eos, Transactions American Geophys.,* 91(21), 190-191.

Gudmundsson, M. T., et al. (2016), Gradual caldera collapse at Bárdarbunga volcano, Iceland, regulated by lateral magma outflow, *Science*, 353, aaf8988, doi: 10.1126/science.aaf8988.

Guðfinnsson, G. H., S. A. Halldórsson, E. Bali, S. Jakobsson, G. Sverrisdóttir, Á. Höskuldssson, M. S. Riishuus, Þ. Þórðarson and the 2014 Nornahraun Eruption Team (2015), Petrography and petrology of the Nornahraun eruption of the Bárðarbunga volcanic system, Iceland, in *EGU General Assembly Conference Abstracts* (Vol. 17).

Halldórsson, S., G. Guðfinnsson, I. Bindeman, G. Sverrisdóttir, E. Bali, S. Jakobsson, A. Höskuldsson, M. Riishuus, G. Sigurðsson, T. Thórðarson and the 2014 Nornahraun Eruption Team (2015), Geochemistry of the Nornahraun eruption in the Bárðarbunga volcanic system, Iceland, in *EGU General Assembly Conference Abstracts* (Vol. 17).

Harlow, D. H., J. A. Power, E. P. Laguerta, G. Ambubuyog, R. A. White and R. P. Hoblitt (1996), Precursory seismicity and forecasting of the June 15, 1991, eruption of Mount Pinatubo, *Fire and Mud: eruptions and lahars of Mount Pinatubo, Philippines,* 223-247.

Harris, A. J. L. (2013), Thermal remote sensing of active volcanoes: a user's manual, Cambridge University Press.

Harris, A. J. L. and C. R. Thornber (1999), Complex effusive events at Kīlauea as documented by the GOES satellite and remote video cameras, *Bull. Volcanol.,* 61(6), 382-395.

Harris, A. J. L. and S. K. Rowland (2001), FLOWGO: a kinematic thermo-rheological model for lava flowing in a channel, *Bull. Volcanol.,* 63, 20-44, doi:1O.1007/s004450000120.

Harris, A. J. L. and M. Neri (2002), Volumetric observations during paroxysmal eruptions at Mount Etna: pressurized drainage of a shallow chamber or pulsed supply?, *J. Volcanol. Geotherm. Res*., 79-95.

Harris, A. J. L. and S. Baloga (2009), Lava discharge rates from satellite-measured heat flux, *Geophys. Res. Lett.*, 36(19), doi:10.1029/2009GL039717.

Harris, A. J. L., S. E. J. Swabey and J. Higgins (1995a), Automated thresholding of active lavas using AVHRR data, *Int. J. Remote Sens.*, 16(18), 3681-3686.

Harris, A. J. L., R. A. Vaughan and D. A. Rothery (1995b), Volcano detection and monitoring using AVHRR data: The Krafla eruption, 1984, *Int. J. Remote Sens*., 16(6), 1001-1020.

Harris, A. J. L., D. A. Rothery, R. W. Carlton, S. Langaas and H. Mannstein (1995c), Non-zero saturation of AVHRR thermal channels over high temperature targets: Evidence from volcano data and a possible explanation, *Int. J. Remote Sens.,* 16(1), 189-196.

Harris, A. J. L., S. Blake, D. A. Rothery and N. F. Stevens (1997a), A chronology of the 1991 to 1993 Etna eruption using advanced very high resolution radiometer data: implications for real-time thermal volcano monitoring, *J. Geophys. Res.,* 102, 7985-8003.

Harris, A. J. L., A. L. Butterworth, R. W. Carlton, I. Downey, P. Miller, P. Navarro and D. A. Rothery (1997b), Low-cost volcano surveillance from space: case studies from Etna, Krafla, Cerro Negro, Fogo, Lascar and Erebus, *Bull. Volcanol.,* 59, 49-64.

Harris, A. J. L., L. P. Flynn, L. Keszthelyi, P. J. Mouginis-Mark, S. K. Rowland and J. A. Resing (1998), Calculation of lava effusion rates from Landsat TM data, *Bull. Volcanol.,* 60, 52–71.

Harris, A. J. L., J. B. Murray, S. E. Aries, M. A. Davies, L. P. Flynn, M. J. Wooster, R. Wright and D. A. Rothery (2000), Effusion rate trends at Etna and Krafla and their implications for eruptive mechanisms, *J. Volcanol. Geotherm. Res.,* 102, 237-270.

Harris, A. J. L., E. Pilger, L. P. Flynn, H. Garbeil, P. J. Mouginis-Mark, J. Kauahikaua, and C. R. Thornber (2001), Automated, high temporal resolution, thermal analysis of Kilauea volcano, Hawai'i, using GOES satellite data, *Int. J. Remote Sens.,* 22, 6, 945-967.

Harris, A. J. L., J. Dehn, M. Patrick, S. Calvari, M. Ripepe and L. Lodato (2005a), Lava effusion rates from hand-held thermal infrared imagery: an example from the June 2003 effusive activity at Stromboli, *Bull. Volcanol.,* 68(2), 107-117.

Harris, A. J. L., J. Bailey, S. Calvari and J. Dehn (2005b), Heat loss measured at a lava channel and its implications for down-channel cooling and rheology, *Geol. Soc. Amer. Spec. Paper* 396, 125–146. doi:10.1130/2005.2396(09).

Harris, A. J. L., J. Dehn and S. Calvari (2007), Lava effusion rate definition and measurement: a review, *Bull. Volcanol.,* 70,1–22, doi:10.1007/s00445-007-0120-y.

Harris, A. J. L., M. Massimiliano, A. Steffke, A. Fornaciai and E. Boschi (2010), A relation between lava discharge rate, thermal insulation, and flow area set using lidar data, *Geophys. Res. Lett.,* 37(20), doi:10.1029/2010GL044683.

Harris, A. J. L., A. Steffke, S. Calvari and L. Spampinato (2011), Thirty years of satellite-derived lava discharge rates at Etna: Implications for steady volumetric output, *J. Geophys. Res.* 116(B8), doi:10.1029/2011JB008237.

Hartley, M. E. and T. Thordarson (2013), The 1874–1876 volcano-tectonic episode at Askja, North Iceland: Lateral flow revisited, *Geochem. Geophys. Geosyst.,* 14(7), 2286-2309.

Hartley, M. E., E. Bali, J. Maclennan, D. A. Neave and S. A. Halldórsson (2018), Melt inclusion constraints on petrogenesis of the 2014–2015 Holuhraun eruption, Iceland, *Contrib. Miner. Petrol.*, 173(2), 10.

Head, E. M., A. M. Shaw, P. J. Wallace, K. W. Sims and S. A. Carn (2011), Insight into volatile behavior at Nyamuragira volcano (DR Congo, Africa) through olivine-hosted melt inclusions, *Geochem., Geophys., Geosystems,* 12(10), doi:10.1029/2011GC003699.

Hooper, A. J., M. T. Gudmundsson, M. Bagnardi, A. H. Jarosch, K. Spaans, E. Magnússon, M. Parks, S. Dumont, B. Ofeigsson, F. Sigmundsson and S. Hreinsdottir (2015), Forecasting of flood basalt eruptions: lessons from Bárðarbunga, *AGU Fall Meeting Abstracts.*

Hoskuldsson, Á., N. Óskarsson, R. Pedersen, K. Grönvold, K. Vogfjörð and R. Ólafsdóttir (2007), The millennium eruption of Hekla in February 2000, *Bull. Volcanol.,* 70, 169–182, doi:10.1007/s00445-007-0128-3.

Höskuldsson, A., I. Jónsdóttir and T. Thordarson (2016), Futurevolc and the Bardarbunga Eruption 2014–15 Iceland, success in the field and laboratory, in *European Geosciences Union, General Assembly,* vol. 18, 13687.

James, M. R., S. J. Lane and B. A. Chouet (2006a), Gas slug ascent through changes in conduit diameter: Laboratory insights into a volcano-seismic source process in low-viscosity magmas, *J. Geophys. Res.,* 111(B5), doi:10.1029/2005JB003718.

James, M. R., S. Robson, H. Pinkerton and M. Ball (2006b), Oblique photogrammetry with visible and thermal images of active lava flows, *Bull. Volcanol.,* 69(1), 105-108.

James, M. R., H. Pinkerton and S. Robson (2007), Image-based measurement of flux variation in distal regions of active lava flows, *Geochem., Geophys., Geosyst.*, 8(3).

Jónsdóttir, I., Á. Höskuldsson, T. Thordarson, S. Bartolini, L. Becerril, J. Marti Molist, S. Þorvaldsson, D. Björnsson and F. Höskuldsson (2016), The eruption in Holuhraun, NE Iceland 2014-2015: Real-time monitoring and influence of landscape on lava flow, in *European Geosciences Union*, *General Assembly*, Vol. 18, 11031.

Kauahikaua, J., D. R. Sherrod, K. V. Cashman and C. Heliker (2003), Hawaiian lava-flow dynamics during the Pu ‘u “O” o, *The Pu ‘u ‘O ‘o–Kupaianaha eruption of Kilauea volcano, Hawai ‘i: the first*, 20, 63-87.

Kaufman, Y. J., C. O. Justice, L. P. Flynn, J. D. Kendall, E. M. Prins, L. Giglio, D. E. Ward, W. P. Menzel and A. W. Setzer (1998), Potential global fire monitoring from EOS-MODIS, *J. Geophys. Res. Atmospheres*, 103(D24), 32215-32238.

Kays, W. M. and M. E. Crawford (1980), Convective heat and mass transfer, 2nd edition, McGraw-Hill series in mechanical engineering.

Kilburn, C. R. (2000), Lava flows and flow fields, *Encyclopedia of volcanoes*, 291-305.

Koeppen, W. C., E. Pilger and R. Wright (2011), Time series analysis of infrared satellite data for detecting thermal anomalies: a hybrid approach, *Bull. Volcanol.,* 73, 577–593, doi:10.1007/s00445-010-0427-y.

Kubanek, J., J. A. Richardson, S. J. Charbonnier and L. J. Connor (2015), Lava flow mapping and volume calculations for the 2012–2013 Tolbachik, Kamchatka, fissure eruption using bistatic TanDEM-X InSAR, *Bull. Volcanol.,* 77, 106, doi:10.1007/s00445-015-0989-9.

Lautze, N. C, A. J. L. Harris, J. E. Bailey, M. Ripepe, S. Calvari, J. Dehn, S. K. Rowland and K. Evans-Jones (2004), Pulsed lava effusion at Mount Etna during 2001, *J. Volcanol. Geotherm. Res.,* 137, 231– 246.

Linde, A. T., K. Agustsson, I. S. Sacks and R. Stefansson (1993), Mechanism of the 1991 eruption of Hekla from continuous borehole strain monitoring, *Nature* 365(6448), 737-740.

Lipman, P. W. and N. G. Banks (1987), Aa flow dynamics, Mauna Loa 1984, *US Geol. Surv. Prof. Pap*., 1350, 1527-1567.

Lyons, J. J., G. P. Waite, W. I. Rose and G. Chigna (2010), Patterns in open vent, strombolian behavior at Fuego volcano, Guatemala, 2005–2007, *Bull. Volcanol.,* 72, 1–15, doi:10.1007/s00445-009-0305-7.

Malin, M. C. (1980), Lengths of Hawaiian lava flows, *Geology*, 8(7), 306-308.

Marsella, M., C. Proietti, A. Sonnessa, M. Coltelli, P. Tommasi and E. Bernardo (2009), The evolution of the Sciara del Fuoco subaerial slope during the 2007 Stromboli eruption: Relation between deformation processes and effusive activity, *J. Volcanol. Geotherm. Res.,* 182, 201–213, doi:10.1016/j.jvolgeores.2009.02.002.

Marzocchi, W. and Woo G. (2007), Probabilistic eruption forecasting and the call for an evacuation, *Geophys. Res. Lett.*, 34(22), doi:10.1029/2007GL031922.

Marzocchi, W. and M. S. Bebbington (2012), Probabilistic eruption forecasting at short and long time scales, *Bull. Volcanol.,* 74, 1777-1805, doi:10.1007/s00445-012-0633-x.

Masuoka, E., A. Fleig, R. E. Wolfe and F. Patt (1998), Key characteristics of MODIS data products, *IEEE Trans. Geosci. Remote Sens.*, 36(4), 1313-1323.

Matson, M. and J. Dozier (1981), Identification of subresolution high temperature sources using a thermal IR sensor, *Photogramm. Engr. Remote Sens.*, 47(9), 1311-1318.

McDermott, F., F. G. Delfin Jr., M. J. Defant, S. Turner and R. Maury (2005), The petrogenesis of volcanics from Mt. Bulusan and Mt. Mayon in the Bicol arc, the Philippines, *Contrib. Mineral. Petrol.,* 150, 652–670, doi:10.1007/s00410-005-0042-7.

Melnik, O. E. and R. S. J. Sparks (1999), Non-linear dynamics of lava dome extrusion, *Nature,* 402, 37-41.

Melnik, O. E. (2000), Dynamics of two-phase conduit flow of high-viscosity gas-saturated magma: Large variations of sustained explosive eruption intensity, *Bull. Volcanol.,* 62, 153-170.

Morgan, H. A, A. J. L Harris and L. Gurioli (2013), Lava discharge rate estimates from thermal infrared satellite data for Pacaya Volcano during 2004–2010, *J. Volcanol. Geotherm. Res.,* 264, 1–11.

Mouginis-Mark, P. J., et al. (1991), Analysis of active volcanoes from the Earth Observing System, *Remote Sens. Environ.,* 48, 51– 60.

Mouginis-Mark, P. J., J. A. Crisp and J. H. Fink (2000), Remote Sensing of Active Volcanism Monograph, *Am. Geophys. Union,* Washington, DC.

Oppenheimer, C., P. W. Francis, D. A. Rothery, R. W. Carlton and L. S. Glaze (1993), Infrared image analysis of volcanic thermal features: Lascar Volcano, Chile, 1984–1992, *J. Geophys. Res. Solid Earth*, 98(B3), 4269-4286.

Oppenheimer, C. (1998), Volcanological applications of meteorological satellites, *Int. J. Remote Sens.,* 19(15), 2829-2864.

Pagli, C., T. J. Wright, C. J. Ebinger, S. H. Yun, J. R. Cann, T. Barnie and A. Ayele (2012), Shallow axial magma chamber at the slow-spreading Erta Ale Ridge, *Nature Geoscience,* 5(4), 284.

Pallister, J. S., D. J. Schneider, J. P. Griswold, R. H. Keeler, W. C. Burton, C. Noyles, C. J. Newhall and A. Ratdomopurbo (2013), Merapi 2010 eruption—Chronology and extrusion rates monitored with satellite radar and used in eruption forecasting, *J. Volcanol. Geotherm. Res*., 261, 144-152.

Parcheta, C., S. Fagents, D. A. Swanson, B. F. Houghton and T. Ericksen (2015), Hawaiian fissure fountains: Quantifying vent and shallow conduit geometry, episode 1 of the 1969-1974 Mauna Ulu eruption, *Hawaiian Volcanoes: From Source to Surface*, 208, 369-391.

Parfitt, L. and L. Wilson (2008), Fundamentals of physical volcanology, Blackwell, Oxford Paperback, ISBN: 978-0-632-05443-5.

Patrick, M. R., J. Dehn, K. R. Papp, Z. Lu, K. Dean, L. Moxey, P. Izbekov and R. Guritz (2003), The 1997 eruption of Okmok Volcano, Alaska: a synthesis of remotely sensed imagery, *J. Volcanol. Geotherm. Res.,* 127, 87-105.

Patrick, M. R., J. L. Smellie, A. J. L. Harris, R. Wright, K. Dean, P. Izbekov, H. Garbeil and E. Pilger (2005), First recorded eruption of Mount Belinda volcano (Montagu Island), South Sandwich Islands, *Bull. Volcanol.,* 67, 415–422, doi:10.1007/s00445-004-0382-6.

Pedersen, G. B. M., A. Höskuldsson, T. Dürig, T. Thordarson, I. Jonsdottir, M. S. Riishuus, B.V. Óskarsson, S. Dumont, E. Magnússon, M. T. Gudmundsson and F. Sigmundsson (2017), Lava field evolution and emplacement dynamics of the 2014–2015 basaltic fissure eruption at Holuhraun, Iceland, *J. Volcanol. Geotherm. Res.,* 340, 155-169.

Peterson, D. W. and R. I. Tilling (2000), Lava flow hazards, *Encyclopedia of Volcanoes, editado por Haraldur Sigurdsson*, 957-972.

Pieri, D. C. and S. M. Baloga (1986), Eruption rate, area, and length relationships for some Hawaiian lava flows, *J. Volcanol. Geotherm. Res*., 30, 29-45.

Pieri, D. C. and M. Abrams (2005), ASTER observations of thermal anomalies preceding the April 2003 eruption of Chikurachki volcano, Kurile Islands, Russia, *Remote Sens. Environ.,* 99(1), 84-94.

Planck, M. (1901), On the law of distribution of energy in the normal spectrum. *Annalen der physik*, 4(553), 1.

Ramsey, M. S. and L. P. Flynn (2004), Strategies, insights, and the recent advances in volcanic monitoring and mapping with data from NASA's Earth Observing System, *J. Volcanol. Geotherm. Res.*, 135(1-2), 1-11.

Ramsey, M. S. and A. J. L. Harris (2013), Volcanology 2020: How will thermal remote sensing of volcanic surface activity evolve over the next decade? *J. Volcanol. Geotherm. Res.,* 249, 217-233, doi:10.1016/j.jvolgeores.2012.05.011.

Romero Moyano, J. E., W. K. Ulrich and V. Marfull (2014), Short chronological analysis of the 2007-2009 eruptive cycle and its nested cones formation at Llaima volcano, *J. Technological Possibilism,* 2(3), 1-9.

Rose, S. and M. Ramsey (2009), The 2005 eruption of Kliuchevskoi volcano: Chronology and processes derived from ASTER spaceborne and field-based data, *J. Volcanol. Geotherm. Res.,* 184(3), 367-380.

Rothery, D. A., P. W. Francis and C. A. Wood (1988), Volcano monitoring using short wavelength infrared data from satellites, *J. Geophys. Res.,* 93(B7), 7993-8008.

Samaniego, P., J. P. Eissen, J. L. Le Pennec, C. Robin, M. L. Hall, P. Mothes, D. Chavrit and J. Cotten (2008), Pre-eruptive physical conditions of El Reventador volcano (Ecuador) inferred from the petrology of the 2002 and 2004–05 eruptions, *J. Volcanol. Geotherm. Res.,* 176, 82–93, doi:10.1016/j.jvolgeores.2008.03.004.

Schott, J. R. (2007), Remote sensing: the image chain approach, Oxford University Press, Technology & Engineering.

Sealing, C. R. (2013), Characterizing the first historic eruption of Nabro, Eritrea: insights from thermal and UV remote sensing, Master thesis.

Segall, P. (2013), Volcano deformation and eruption forecasting. In: Pyle DM, Mather TA and Biggs J (eds) Remote Sensing of Volcanoes and Volcanic Processes: Integrating Observation and Modelling, *Geol. Soc. London Spec. Pub.,* 380, 85-106, doi:10.1144/SP380.4.

Sigmarsson, O. and S. A. Halldórsson (2015), Delimiting Bárðarbunga and Askja volcanic systems with Sr-and Nd-isotope ratios, *Jökull*, 65, 17-27.

Sigmarsson, O., I. Vlastelic, R. Andreasen, I. Bindeman, J. L. Devidal, S. Moune, J. K. Keiding, G. Larsen, A. Höskuldsson and Th. Thordarson (2011), Remobilization of silicic intrusion by mafic magmas during the 2010 Eyjafjallajökull eruption, *Solid Earth,* 2(2), 271.

Sigmundsson, F., A. Hooper, S. Hreinsdóttir, K. S. Vogfjörd, B. G Ófeigsson, E. R. Heimisson, S. Dumont, M. Parks, K. Spaans, G. B. Gudmundsson and V. Drouin (2015), Segmented lateral dyke growth in a rifting event at Bárðarbunga volcanic system, Iceland, *Nature,* 517(7533), 191-195, doi:10.1038/nature14111.

Simkin, T. and L. Siebert (1994), Volcanoes of the World, Second Edition. Geoscience Press, Inc., Tucson, Arizona, 1-349.

Sheth, H. C., J. S. Ray, R. Bhutani, A. Kumar and R. S. Smitha (2009), Volcanology and eruptive styles of Barren Island: an active mafic stratovolcano in the Andaman Sea, NE Indian Ocean, *Bull. Volcanol.,* 71(9), 1021.

Smets, B., C. Wauthier and N. d'Oreye (2010), A new map of the lava flow field of Nyamulagira (D.R. Congo) from satellite imagery, *J. Afr. Earth Sci.,* 58(5), 778-786, doi:10.1016/j.jafrearsci.2010.07.005.

Sparks, R. S. J. (2003), Forecasting volcanic eruptions, *Earth Planet. Sci. Lett.,* 210, 1-15, doi:10.1016/S0012-821X(03)00124-9.

Suh, C. E., S. N. Ayonghe, R. S. J. Sparks, C. Annen, J. G. Fitton, R. Nana and A. Luckman (2003), The 1999 and 2000 eruptions of Mount Cameroon: eruption behaviour and petrochemistry of lava, *Bull. Volcanol.,* 65(4), 267-281.

Thordarson, T. and S. Self (1993), The Laki (Skaftár Fires) and Grímsvötn eruptions in 1783–1785, *Bull. Volcanol.,* 55(4), 233-263.

Vicari, A., A. Herault, C. Del Negro, M. Coltelli, M. Marsella and C. Proietti (2007), Modeling of the 2001 lava flow at Etna volcano by a Cellular Automata approach, *Envir. Modelling & Software,* 22, 1465–1471.

Vicari, A., G. Bilotta, S. Bonfiglio, A. Cappello, G. Ganci, A. Hérault, E. Rustico, G. Gallo and C. Del Negro (2011), LAV@ HAZARD: a web-GIS interface for volcanic hazard assessment. *Annals Geophys.*, 54(5).

Vlastélic, I., A. Peltier and T. Staudacher (2007), Short-term (1998–2006) fluctuations of Pb isotopes at Piton de la Fournaise volcano (Reunion Island): Origins and constraints on the size and shape of the magma reservoir, *Chem. Geol.,* 244, 202–220, doi:10.1016/j.chemgeo.2007.06.015.

Voight, B., R. P. Hoblitt, A. B. Clarke, A. B. Lockhart, A. D. Miller, L. Lynch and J. McMahon (1998), Remarkable cyclic ground deformation monitored in real-time on Montserrat, and its use in eruption forecasting, *Geophys. Res. Lett.,* 25(18), 3405-3408.

Wadge, G. (1978), Effusion rate and the shape of aa lava flow-fields on Mount Etna, *Geology*, 6(8), 503-506.

Wadge, G. (1981), The variation of magma discharge during basaltic eruptions*, J. Volcanol. Geotherm. Res.,* 11(2-4), 139-168.

Walker, G. P. L. (1973), Lengths of lava flows, *Phil. Trans. R. Soc. Lond.* A, 274(1238), 107-118.

Walker, G. P. L. (2000), Basaltic volcanoes and volcanic systems, *Encyclopedia of volcanoes*, 283-289.

Wilson, L. and J. W. Head (1981), Ascent and Eruption of Basaltic Magma on the Earth and Moon, *J. Geophys. Res.,* 86(B4), 2971-3001.

Wooster, M. J. and D. A. Rothery (1997), Time-series analysis of effusive volcanic activity using the ERS Along Track Scanning Radiometer: The 1995 eruption of Fernandina Volcano, Galapagos Islands, *Remote Sens. Envir.*, 62, 109-117.

Wooster, M. J., B. Zhukov and D. Oertel (2003), Fire radiative energy for quantitative study of biomass burning: derivation from the BIRD experimental satellite and comparison to MODIS fire products, *Remote Sens. Envir.,* 86, 83-107.

Wright, R. (2015), MODVOLC: 14 years of autonomous observations of effusive volcanism from space, *Geol. Soc. London, Spec. Pub.,* 426, 23-53, http://doi.org/10.1144/SP426.12.

Wright, R. and L. P. Flynn (2004), Space-based estimate of the volcanic heat flux into the atmosphere during 2001 and 2002, *Geology*, 32(3), 189-192.

Wright, R. and E. Pilger (2008), Radiant flux from Earth's subaerially erupting volcanoes, *Int. J. Remote Sens.,* 29(22), 6443–6466, doi:10.1080/01431160802168210.

Wright, R., S. Blake, A. J. L. Harris and D. A. Rothery (2001a), A simple explanation for the space-based calculation of lava eruption rates, *Earth Planet. Sci. Lett.,* 192, 223-233.

Wright, R., L. P. Flynn and A. J. L. Harris (2001b), Evolution of lava flow-fields at Mount Etna, 27-28 October 1999, observed by Landsat 7 ETM+, *Bull. Volcanol.,* 63, 1-7, doi:10.1007/s004450100124.

Wright, R., L. P. Flynn, H. Garbeil, A. J. L. Harris and E. Pilger (2002), Automated volcanic eruption detection using MODIS, *Remote Sens. Environ.,* 82, 135-155.

Wright, R., L. P. Flynn, H. Garbeil, A. J. L. Harris and E. Pilger (2004), MODVOLC: near-real-time thermal monitoring of global volcanism, *J. Volcanol. Geotherm. Res.*, 135, 29–49, doi:10.1016/j.jvolgeores.2003.12.008.

Wright, R., H. Garbeil and A. J. L. Harris (2008), Using infrared satellite data to drive a thermo-rheological/stochastic lava flow emplacement model: A method for near-real-time volcanic hazard assessment, *Geophys. Res. Lett.,* 35(19), doi:10.1029/2008GL035228.

Wright, R., M. Blackett and C. Hill-Butler (2015), Some observations regarding the thermal flux from Earth's erupting volcanoes for the period of 2000 to 2014, *Geophys. Res. Lett.,* 42, doi:10.1002/2014GL061997.

Wylie, J. J., K. R. Helfrich, B. Dade, J. R. Lister and J. F. Salzig (1999), Flow localization in fissure eruptions, *Bull. Volcanol.,* 60, 432–440.

Xu, W. and S. Jonsson (2014), The 2007–8 volcanic eruption on Jebel at Tair island (Red Sea) observed by satellite radar and optical images, *Bull. Volcanol.,* 76(2), 795, doi:10.1007/s00445-014-0795-9.